論文 / 著書情報
Article / Book Information

題目(和文)	
Title(English)	Non-Intrusive Hand Trajectory Estimation Framework Utilizing Channel State Information of commodity Wi-Fi devices
著者(和文)	キラティウォラナン ノッポン
Author(English)	Nopphon Keerativoranan
出典(和文)	学位:博士(工学), 学位授与機関:東京工業大学, 報告番号:甲第11630号, 授与年月日:2020年9月25日, 学位の種別:課程博士, 審査員:髙田 潤一,髙橋 邦夫,山下 幸彦,秋田 大輔,青柳 貴洋,齋藤 健太郎
Citation(English)	Degree:Doctor (Engineering), Conferring organization: Tokyo Institute of Technology, Report number:甲第11630号, Conferred date:2020/9/25, Degree Type:Course doctor, Examiner:,,,,,
学位種別(和文)	博士論文
Type(English)	Doctoral Thesis

Non-Intrusive Hand Trajectory Estimation Framework Utilizing Channel State Information of commodity Wi-Fi devices

A dissertation submitted in partial fulfillment
of the requirements for the degree of
Doctor of Engineering

by

Nopphon Keerativoranan

Supervisor

Professor Jun-ichi Takada
Assistant Professor Kentaro Saito

School of Environment and Society
Department of Transdisciplinary Science and Engineering
Global Engineering for Development, Environment and Society Course
Tokyo Institute of Technology

September, 2020

Acknowledgments

First of all, I would like to express my gratitude and thankfulness toward my supervisor, Prof. Jun-ichi Takada, for his research guidance, suggestion, support, and providing me the opportunity to do great research work in his laboratory. I also would like to thank Asst. Prof. Kentaro Saito, Asst. Prof. Azril Haniz for their advice and tireless support. Without them, this work could not be finished or completed. In addition, I would like to thank my colleague Dr. Panawit Hanpinisak for providing the knowledge on the implementation of physical optics (PO) to complete the simulation part of my work. Likewise, I would like to thank Dr. Tossaporn Srisooksai for the support on the hardware implementation during my research student study.

Special thank to Prof. Jeffrey S. Cross who accepted me to work as teaching assitant in the online education development office (OEDO). This invaluable experience has enhanced my programming skill in the real-word problem as well as get to know a lot of awesome international people in the team.

I would also like to thank the Japanese government scholarship program for providing me the financial support during my research student study as well as PhD degree in such a wonderful country as Japan. Without this scholarship, it would be impossible to complete my study here in Japan.

Life in Japan might be tougher if I would have failed to know these awesome people. First I would like to express my deepest gratitude to my colleague in the Lab as well as many friend I have acquaintance with: Dr. Ceelia, Ek-amorn, Murakami, Traitip, Tan, Chen, Joko, Ahmad, Tontan, Max and many more. It makes my life here to be easier and funnier more than I expected.

This thesis could not be complete without my beloved mom and dad who always believe in my potential that I can eventually finish this work. Last but not least, I generously thanks to my friendliness girlfriend, Sasipa, for her love and patience, and also for her superb instincts as my private editor.

Nopphon Keerativoranan

June 2020

Abstract

This thesis presents the framework for hand trajectory tracking by utilizing commodity Wi-Fi devices without the need of body-equipped sensor.

Although commercially-available vision-based hand gesture motion sensing can achieve a promising accuracy and precision, it may not be able to fully operate or install in certain environments such as in the presence of obstacles between sensors and user, in the bright/dim light areas, and in the private places. Since radio frequency (RF) signal can work in the scenarios described above, utilizing RF signal can be an alternative solution for the non-intrusive motion sensing. While many studies could acceptably recognize a set of hand gesture using the pattern matching technique, their results could worsen drastically when gesture is performed at different positions.

Envision a ubiquitously device-free motion sensing, this research analyzes the possibility of Wi-Fi-based trajectory tracking of hand gesture by utilizing Doppler frequency obtained from channel state information (CSI). To achieve this goal, the novel calibration is firstly introduced to mitigate undesired components on a measured CSI so that Doppler spectrum can be correctly observed. Since a movement of human limb generates variant Doppler signatures caused by micro-Doppler effect to the spectrum, the estimation technique is proposed to extract the hand-only Doppler signature. With a set of signatures from different pairs of Wi-Fi antenna, hand trajectory can be traced by exploiting multi-static Doppler radar model. To validate the proposed method, deterministic Doppler CSI model is developed to simulate the movement of human limb and its Doppler. The model is based on the incorporation between the non-rigid body motion model of the human limb and electromagnetic scattering theory. The result from simulation and measurement conducted in the meeting room using commodity Wi-Fi devices with 3x2 MIMO setup showed that the shape of hand gestures could successfully reconstruct albeit a small offset in orientation and scale.

Contents

List of Figures

List of Tables

List of Acronyms

AR Augmented reality

CDF Cumulative density function

CFO Carrier frequency offset

CIR Channel Impulse response

CSD Cyclic shift diversity

CSI Channel state information

DPD Doppler power spectrum

EM Electromagnetic

EMD Empirical mode decomposition

HBT Hilbert transform

HCI Human-computer interaction

HT-LTF High throughput long training field

IMU Inertial measurement unit

IO Interacting object

IR Impulse response

LO Local oscillators

LoS Line-of-sight

MIMO Multiple-input-multiple-output

NIC Network interface card

NLoS Non line-of-sight

OFDM Orthogonal frequency division multiplexing

PBD Packet boundary delay

PDP Power-delay-profile

PEC Perfect electric conductor

PL Path loss

PLO Phase-locked-loop offset

PO Physical optics

RF Radio frequency

RFID Radio frequency identification detection

RMSE Root-mean-squared error

RSSI Received signal strength indicator

Rx receiver

SDR Software defined radio

SFO sampling frequency offset

SM Spatial matrix

STFT Short-time Fourier transform

TIV Time-invariant

TV Time-variant

Tx Transmitter

VNA Vector network analyzer

VR Virtual reality

WT Wavelet transform

WVD Wigner-ville distribution

Chapter 1

Introduction

1.1 Background

The advancement of communication technology in recent years has drastically influenced the mean of interaction between humans and computing devices. In particular, the evolution of human-computer interaction (HCI) interface is moving toward the contactless interaction where users could communicate with any computing devices by merely performing particular gestures or actions in the air. Motion sensing is one of the emerging technology that enables this interaction possible. Various commercial non-intrusive motion sensing such as Kinect, Orbbec, Leap motion can achieve a promising accuracy and precision by utilizing vision sensors. However, their performance could extremely worsen in the following scenarios and circumstances due to the physical limitation of the optical device. It operates only in the presence of line-of-sight (LoS) between device and user due to its high sensitivity to obstacle, the active sensing area is relatively small owing to the focal length of the lens in vision sensor [4, 5, 6, 7, 8, 9, 10]. Besides, a privacy concern due to images captured by vision-sensor would limit the usage of motion sensing in certain private locations such as restroom or office meeting room [11, 12]. These constraints may be a few of the reasons why commercial virtual reality (VR) and augmented reality (AR) handsets such as gear VR controller, data glove, or smartphone require a wearable device such as ineatial measurement unit (IMU) sensors for interaction. However, body-equipped sensors are intrusive and inconvenient, and may not be practical for specific applications such as elderly care, and intrusion detection [4, 9, 10, 13]. Hence, an alternative motion sensing approach which is non-intrusive, ubiquitous, and low-cost could be a good candidate in assisting or substituting the current system in these scenarios.

Leveraging commercial radio frequnecy (RF) system such as Wi-Fi, Bluetooth, radio-frequency identification (RFID) is one solution because RF-based motion sensing could theoretically operate with fewer privacy concerns in non line-of-sight (NLoS) scenario and with a larger sensing area owning to a longer wavelength. Many studies have investigated the

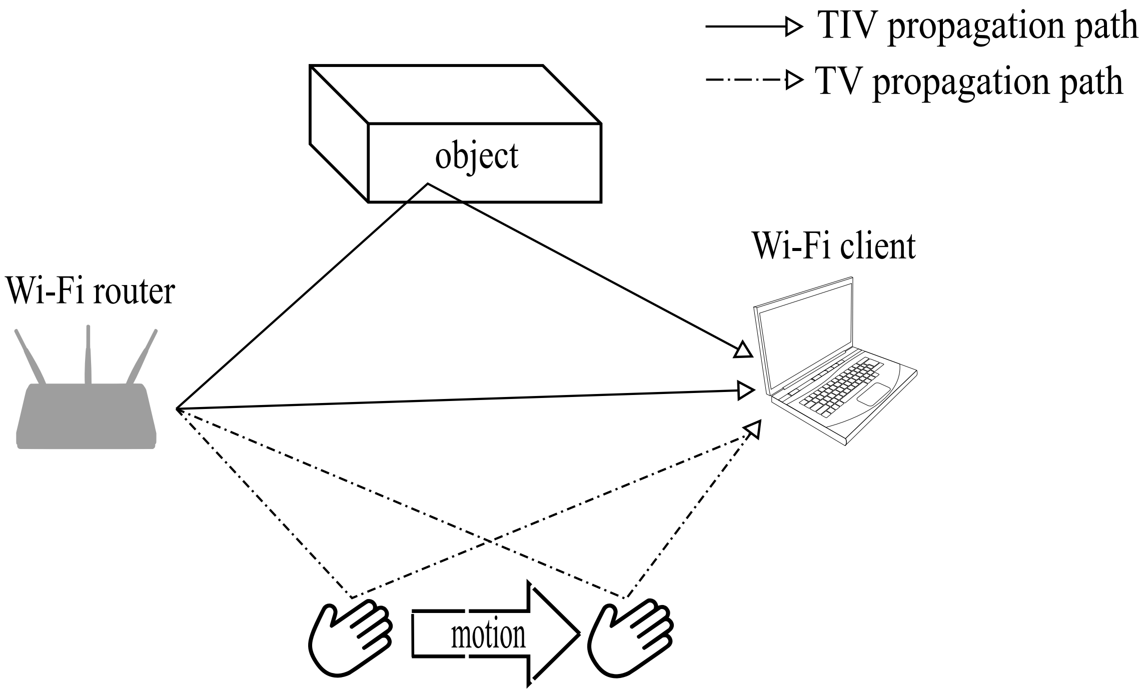

Figure 1.1: Propagation of Wi-Fi signal in multipath channel interacting with a static object and a moving hand.

applicability of RF signal for motion sensing [4, 14, 15, 16]. In fact, received signal strength identification (RSSI) of RF signal based motion sensing has been researched comprehensively in [17, 18, 19, 20]. Unfortunately, the nature of RSSI is highly interference-sensitive, device-dependent, and easily affected by external conditions such as temperature and humidity [21, 22, 23]. Therefore only simple gesture recognition would be achievable rather than performing tracking.

With respect to recent works in the extraction of channel state information (CSI) from the physical layer (PHY) of commodity Wi-Fi network interface card (NIC) [24, 25], which arguably contains a lot more information than RSSI, fine-grained motion sensing and indoor localization with Wi-Fi devices have gained much attention from researchers. In addition to its low-cost and ubiquitous, various works using CSI have increased drastically [26, 27, 28, 29, 30, 31, 32, 33, 34]. Generally, Wi-Fi chips estimate CSI which is represented by the complex channel frequency transfer function of the wireless channel between two Wi-Fi transceivers at each orthogonal frequency division multiplexing (OFDM) subcarrier. In the simple transmission depicted in Fig. 1.1, the Wi-Fi signal propagates through a wireless channel on different paths, and the superposition of multipath signals at receiver is translated onto CSI as channel fading, and it supposedly remains unchanged with the same configuration and environment. However, in the presence of motion, a certain path which interacts with the moving object will experience changes with time. This effect could be observed in the time-variant (TV) component of CSI as the rotation of phase components and a time-varying channel fading in the amplitude component. The rotation corresponds to the Doppler frequency shift which is directly proportional to the object's velocity in the direction concerning a link between Wi-Fi transceivers.

In actual measurements, unfortunately, the undesired temporal phase rotation of local oscillators (LO) between two Wi-Fi transceivers due to the absence of synchronization obscures the CSI phase component, and therefore Doppler frequency cannot be explicitly used. As a consequence, performing any motion analysis is infeasible without separation of the undesired phase rotation from the CSI. Besides, spatial mapping (SM) and cyclic shift diversity (CSD) modulated in the transmitter may remain attached to the extracted CSI when operating in multiple transmit streams configuration of multiple-input-multiple-output (MIMO) transmission [3, 35]. Many works have proposed various signal processing techniques for dealing with the phase rotation. Using CSI amplitude approach has been widely used to avoid the effect of phase rotation. However, without the CSI phase component, only a magnitude of Doppler frequency could be obtained. Without a sign of Doppler frequency, this approach is only suitable for analyzing motion with a periodic profile such as breathing detection [11, 36], or a small set of predefined human gestures [7, 32, 30, 31] and human activities [26, 28, 29, 37]. The phase sanitization approach compensates for the phase rotation by linearly removing the mean and slope of the measured CSI phase. This is a double-edged approach in which phase rotation is mitigated but simultaneously a part of the CSI is proportionally removed along with it. Although the resulting sanitized phase has been implemented in many works [27, 34, 38, 39], to the best of the author knowledge, there is no justification of what the sanitized phase physically represents. The phase difference method, applied in [9, 33, 40, 41], mitigates the phase rotation by using the CSI phase measured from another receive antenna. Since the phase rotation between both antennas was generated by the same Wi-Fi chip, it should be canceled out after subtraction. Although this method could remove the phase rotation, the result is still not yet the original CSI phase but a phase difference between two antennas. Even though various phase rotation mitigation techniques have been implemented in previous works, it is impossible to remove the phase rotation without sacrificing partial or entire phase information. Therefore the application is quite limited and mostly case-dependent.

1.2 Research Motivation

Majority of literature in Wi-Fi CSI based motion sensing suffered from the incomplete Doppler frequency information and thus could only detect and recognize certain motions via data-driven based approach. For example, the works in [6, 8, 42, 43] were able to distinguish a set of hand gestures moving in different directions which could be useful for contactless interaction with computing devices. With a similar goal, the study in [30, 32] could successfully classify plenty of finger gestures [14, 31] by recognizing a distinct pattern of keystroke while typing a keyboard and touching smartphone respectively. Although their works have empirically displayed the feasibility of the motion analysis even on a small movement of a human limb, it relies on the strong assumption that each gesture always reflects a unique pattern on the CSI streams. Unfortunately, the temporal pattern of CSI which causes by Doppler frequency depends on the position of the Wi-Fi transmitter and receiver relative to the user location according to the bistatic radar [44, 45, 46]. As a result, the usability of micro-motion sensing may not be able to generalize without further in-depth analysis.

Trajectory tracking could be another method for hand motion sensing as shown in Fig. 1.2 since the hand gesture is just a collection of temporal position moving through space. This approach could be regarded as the application of OFDM radar [47, 48, 49]. However, the implementation with commercial Wi-Fi system is a challenging task because the tracking requires accurately a knowledge of velocity and position. Without solving the undesired phase rotation issue, it is virtually difficult to extract velocity from Doppler frequency. Although one can theoretically extract the temporal position with CSI by exploiting the propagation delay information from its channel impulse response (CIR) [50], the commercially-available Wi-Fi systems are mostly narrowband resulting in the poor propagation delay resolution. For instance, typical 40-MHz Wi-Fi signal causes the position uncertainty around 7.5-meter which is unreliable for hand gesture tracking that needs at least sub-meter scale resolution.

Another challenge in hand motion sensing stems from the general assumption of radar. In the radar tracking problem [44], a moving target can be assumed as a point object because it is typically located far away relative to transmitter and receiver position. Unfortunately, this is not always the case for indoor motion sensing where the user could be positioned nearby Wi-Fi transceivers supposedly in the same room. Since human body could be consists of multiple components [51] with each part moving at different paces, multiple Doppler frequency components were correspondingly induced. These components are accumulated in CSI and expressed as Micro-Doppler effect in the Doppler power spectrum [51, 52, 53]. In case of CSI-based motion tracking in indoor environment [54, 55], Doppler component with the highest power is likely corresponding to the signature of human torso movement [51, 56]. The peak then was selected for tracking a human walking by utilizing OFDM radar concept. Likewise, during the motion of hand gesture, each part of the human limb is also moving at different pace due to non-rigid body motion [51]. The Doppler spectrum therefore experiences the micro-Doppler effect in this case as well. In [52, 53], distinct features of hand Micro-Doppler effect were utilized for hand gesture recognition applications. Regarding previous works on non-intrusive hand tracking with Wi-Fi CSI [57, 58], the Micro-Doppler signature has unfortunately not been taken into consideration. In fact, the work in [57] detected a 3D hand trajectory by observing the hand shadowing effect in the angular spectrum obtained from a minimum of 30 Wi-Fi devices. Despite a cm-scaled trajectory error, the performance

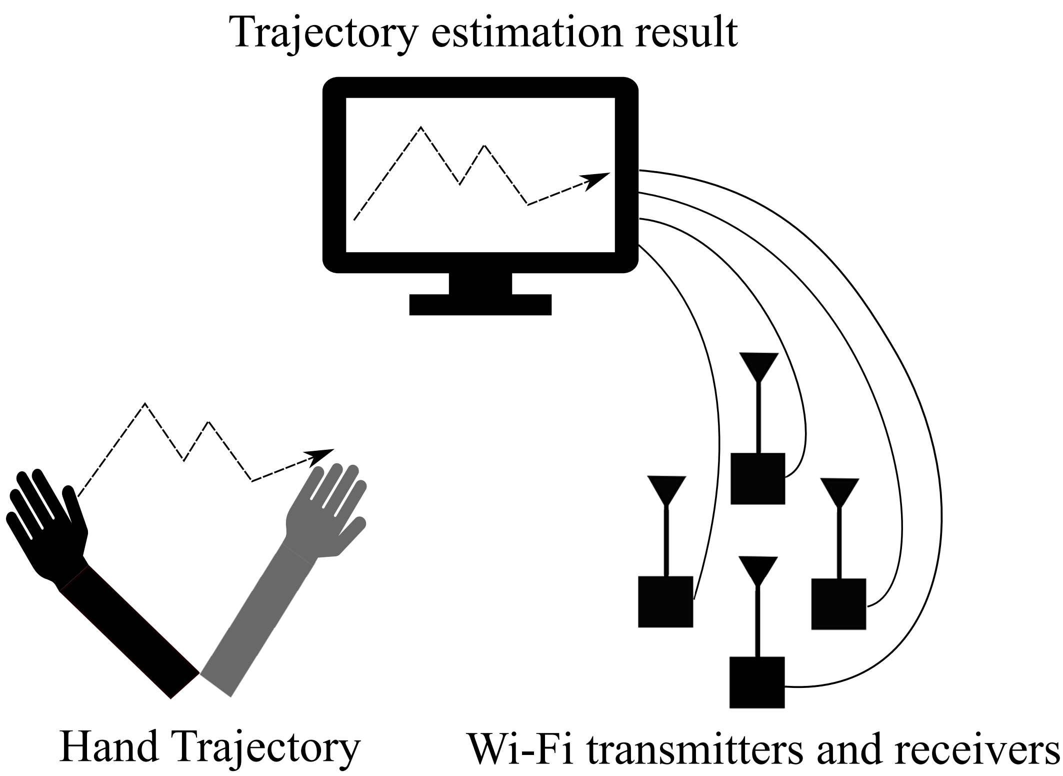

Figure 1.2: Concept of Wi-Fi based hand gesture trajectory estimation.

could still be location-dependent since it is sensitive to the position and distribution of sensors in a specific area. Other drawback in this work is the usability and scalability owing to a large number of Wi-Fi transceivers required. Another work in [58] proposed a 2D trajectory tracking system of hand gesture exclusively for the motion in horizontal plane. Their system utilized two Wi-Fi receivers to recursively track the absolute hand position from a phase component of CSI. Since the Wi-Fi signal was communicated between two synchronized software-defined radio (SDR) equipments, the undesired phase rotation has already been mitigated. By limiting the analysis in 2D, the elliptic geometry of bistatic propagation delay was utilized to calculate the temporal position of hand gesture. Because this system assumed a single component of Doppler frequency during hand gesture, the applicability is limited to a strict configuration of transmitter and receiver position relative to the hand gesture such that the micro-Doppler signature from the hand segment is strongly dominated other signatures.

To the best of our knowledge, there does not exist a Wi-Fi CSI based hand gesture trajectory tracking that successfully resolves the undesired phase rotation issue and addresses the impact of Micro-Doppler effect during hand gesture through theoretical model. By acknowledging these research gaps, this thesis aims to investigates the applicability of hand gesture trajectory estimation for the future ubiquitous Wi-Fi assisted motion sensing system by fully exploiting the Doppler frequency from Wi-Fi CSI.

1.3 Objective and Contributions

The objectives of this study are to investigate the possibility of utilizing the commodity Wi-Fi devices to trace hand gesture trajectory without the need of body-equipped sensor and to develop the deterministic CSI model as a tool for studying the mechanism of Micro-Doppler effect during hand gesture. To fulfil these goals, challenges described in the research motivation must be addressed in this thesis through the followings novelties and contributions:-

- The novel CSI calibration that mitigates the effect of the undesired phase rotation while preserving Doppler frequency information in the phase component of CSI (Chapters 3)
- Time-variant CSI model that physically simulates micro-Doppler effect caused by the movement of hand gesture (Chapters 4)
- Doppler component extraction technique that can estimate the target signature of hand Doppler in the presence of micro-Doppler effect during hand gesture (Chapters 5)
- Tracking framework that can reconstruct and preserve the original hand trajectory by utilizing only Doppler frequency of hand motion (Chapters 6)

1.4 Limitations of the Thesis

It should be noted that the CSI data of Wi-Fi signal utilizing in the thesis is obtained from the Linux-based CSI extraction tool developed by [24] which is compatible with the Intel 5300 NIC Wi-Fi chip. This implies that additional software and the Wi-Fi chip must be installed under the Linux operating system in order to capture the CSI. Moreover, detail hardware specification may not fully obtained since it may be classified to the chip's development company [35]. In fact, this is a common method among the CSI-based researches since the capability to extract CSI has not yet officially implemented in any commercial operating system. Another limitation is involved the undesired phase rotation that prevents us to obtain Doppler frequency without applying any processing. As will be discussed in chapter 3, the novel calibration technique unavoidably has to trade the need of hardware modification in order to correctly obtain Doppler frequency. These limitation are actually expected since Wi-Fi system is not originally designed for motion sensing. With many researchers showing the applicability of Wi-Fi for motion sensing, it would be beneficial for engineers to hopefully include the sensing capability to the future commercial wireless communication standard.

Regarding the motion tracking scenario, investigation in the thesis considers the special case scenario where it exists only one-handed gesture motion in the static environment. Although it is a very strong assumption in practical scenario, this is an ideal and simple case to investigate and validate the concept of hand motion tracking performance. Actually, this condition was widely-assumed in previous works for their CSI-based motion sensing research. In order to deal with multiple moving objects, additional information with sufficient precision such as high-resolution range information and angle-of-arrival and departure is needed to spatially separate different target objects. Nevertheless, be able to obtain these information comes with the cost of larger number of antennas and larger bandwidth. Once the future commercial device could obtain this requirement, it could be feasible to realize the hand tracking in the more realistic environment.

With respect to the motion tracking framework covered in chapter 6, it requires largely separated antennas to estimate the target velocity and position. In our measurement, the large antenna separation was realized by connecting widely-separated external antennas to the same Wi-Fi chip installed in the commercial laptop with the cable. This configuration was established to reduce number of laptop used in the measurement. In more practical scenario, we may substitute this system with the configuration similar to those of wireless sensor network. In this alternative case, each antenna is represented by separate device and can be widely placed without the need of external antenna connection.

1.5 Outline of the Thesis

The overall structure of this thesis is outlined as shown in Fig. 1.3. In this chapter, the motivation and background have already been provided.

Chapter 2 describes the modeling and structure of Wi-Fi CSI followed by the explanation of how the measurement CSI is extracted from the off-the-shelf Wi-Fi chip. Then, the concept of OFDM radar is explained in terms of velocity and range estimation followed by the detailed explanation of Micro-Doppler signature in general. Finally, state-of-art techniques of motion sensing with Wi-Fi are discussed in detail.

Chapter 3 firstly narrates the problem with the undesired phase rotation in the measurement CSI. In particular, the effect of spatial mapping in MIMO system is detailed followed by the source of undesired phase rotation and the consequence to the quality of Doppler frequency. Then the novel phase rotation calibration is introduced to mitigate the undesired phase rotation without destroying the desired rotation of Doppler frequency. The performance was finally validated with the CSI result measured from the vector network analyzer.

Chapter 4 describes the kinematic model of hand gesture through the non-rigid body motion of robot arm. With this knowledge, we then detail the construction of the human limb model based on surface point cloud that could naturally simulate the hand gesture movement. The scattering wave on the movement of human limb is later explained as a basis for the construction of deterministic CSI model. Specifically, the development of circular-mesh physical optics (PO) approximation for the practical usage of moving scatterer is addressed followed by the validation. In the end, this chapter introduces and validates the deterministic

CSI model that could simulate micro-Doppler effect from the hand gesture motion.

Chapter 5 explains the characteristic of micro-Doppler on the surface of human limb model. The analysis was conducted based on the Doppler and the scattered power distribution induced from each surface point on the human limb. Next, the proposed technique to extract the temporal profile of hand Doppler signature from the Doppler spectrum is presented followed by the validation of the algorithm in simulation scenario.

Chapter 6 firstly presents the trajectory estimation framework based on multi-static Doppler radar followed by the formulation of Kalman filter (KF) model in this problem with the goal to mitigate the accumulated tracking error. The concept of initial position estimation is later on addressed. Then, the validation of hand gesture trajectory estimation is conducted with the simulated CSI. Finally, the usability of the estimation is evaluated with the measurement CSI conducted in the meeting room.

Finally, Chapter 7 concludes the thesis findings and provides prospect directions for the future motion sensing application.

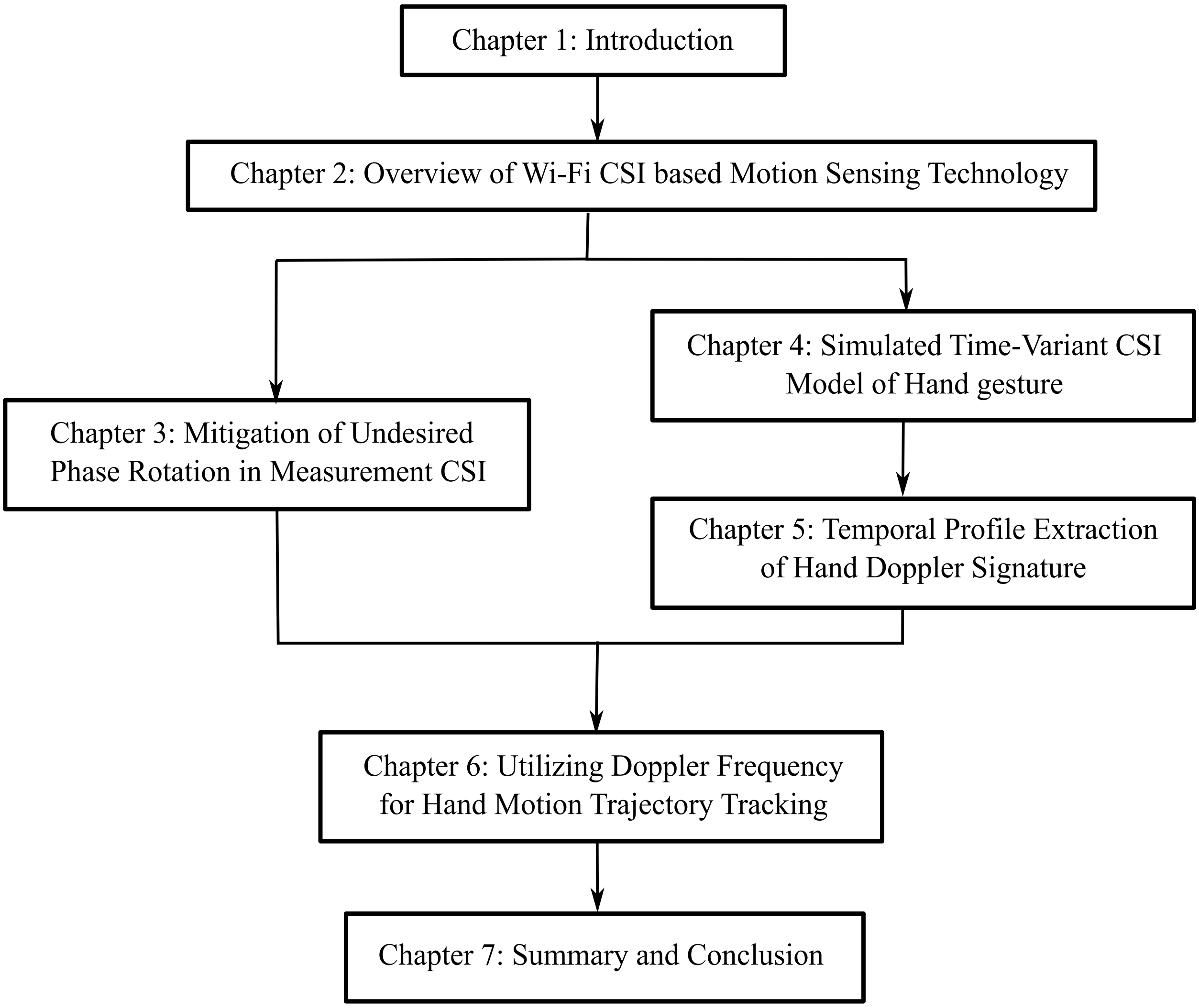

Figure 1.3: Structure of thesis

Chapter 2

Overview of Wi-FI CSI based Motion Sensing Technology

2.1 Introduction

In this chapter, the fundamental knowledge of motion sensing through the manipulating of Wi-Fi channel state information (CSI) will be discussed. The explanation firstly includes the structure and the extraction of CSI in Wi-Fi signal. since Wi-Fi motion can be categorized as one of the OFDM radar application, The general concept of OFDM radar will be further given in terms of range and velocity estimation. Micro-Doppler effect is also addressed as the movement of hand gesture can generally induce multiple Doppler signature especially in indoor environment. Finally, the hand motion sensing techniques used in literature will be categorically addressed to give a better understanding of the advancement in this topic.

2.2 Wi-Fi Channel State Information

2.2.1 CSI Modeling and Estimation

Multiple-input multiple-output (MIMO) transmission and beamforming have been introduced in many wireless communication systems in order to improve data transmission rate and reliability. They require a knowledge of real-time CSI to perform spatial multiplexing and diversity techniques. Therefore, a CSI frame has been included in the physical layer (PHY) of Wi-Fi systems since the IEEE 802.11n standard, specifically in the training symbols of the high throughput long training field (HT-LTF) preamble format [3]. According to the standard, a 4-μs duration HT-LTF which is a part of PHY high throughput (HT) packet purposely allows receiver to estimate MIMO channel-related parameters including CSI data. Since Wi-Fi signal utilizes OFDM scheme for the transmission, HT-LTF symbols are transmitted through K subcarriers simultaneously. Specifically, the payload data in the

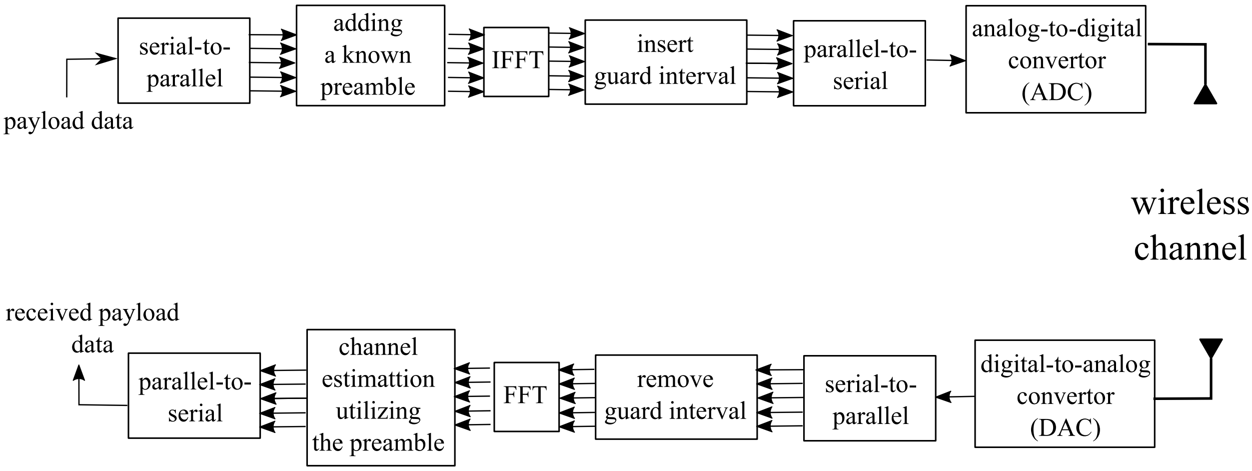

Figure 2.1: Simplified transmission flowchart of Wi-Fi OFDM signal.

OFDM scheme is parallelized, added with a known symbol sequence, and then modulated to the K orthogonal subcarrier frequencies by the mean of inverse fast Fourier transform (IFFT) as shown in Fig. 2.1 [50, 59, 60]. Guard interval interval T_{G} of 0.4 µs and 0.8 µs for short and normal guard band respectively is added to mitigate inter-symbol interference (ISI) between consecutive symbols. Accordingly, the OFDM receiver then performs the fast Fourier transform (FFT) to convert the received OFDM signal back into the original sequence. This multi-subcarrier modulation scheme is beneficially more robust than those with a single carrier to deal with the multipath channel environment such as frequency-selective fading [50]. In addition, orthogonality property of subcarrier enables the possibility of a faster and efficient transmission within a relatively smaller bandwidth in comparison with the single carrier transmission. Therefore it has been widely implemented in various communication systems such as Wi-Fi [59], 4^{th} generation (4G) of cellular network [60], digital television broadcasting [61], and digital audio broadcasting [62]. In Wi-FI OFDM, a total of K subcarrier frequency is 64 and 128 tones distributed over 20-MHz and 40-MHz bandwidth channel respectively. Each subcarrier frequency f_k is equally-spaced with a gap Δf of 312.5 kHz. Here k denote the index of subcarrier frequency. To avoid interference from the adjacent Wi-Fi channel, few subcarrier frequencies located near the border of the signal bandwidth as depicted in Fig. 2.2 contains no information which are also known as zero subcarriers. The 56-symbol sequence of HT-LTF is sent over 56 subcarrier frequencies of 20-MHz channel. Likewise, the 114 subcarrier frequencies are occupied for the 114-symbol sequence in 40-MHz channel. These sequences information can be found in [3] for IEEE 802.11n Wi-Fi standard.

Let us define $X_m(t, f_k)$ as the known transmitted Wi-Fi signal corresponding to HT-LTF training symbols in frequency domain measured at time t. Given a linear model of wireless communication system [50], the received HT-LTF signal $Y_n(t, f_k)$ which is being distorted

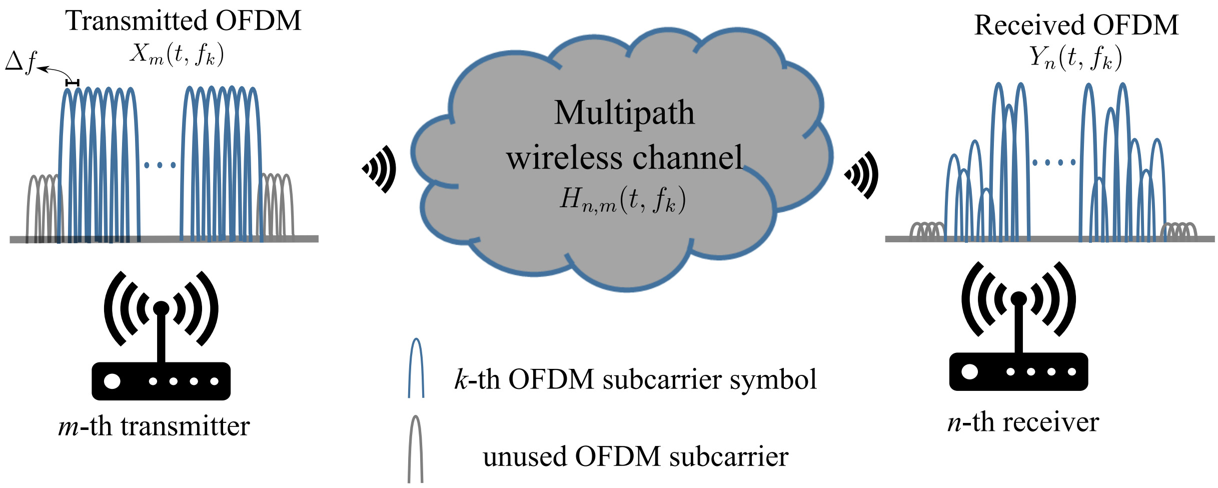

Figure 2.2: Transmission of OFDM signal in multipath wireless channel.

by the wireless channel as shown in Fig. 2.2 can be expressed by,

$$Y_n(t, f_k) = H_{n,m}(t, f_k)X_m(t, f_k) + \mathscr{N}(t, f_k) \tag{2.1}$$

The wireless channel at each subcarrier f_k can be represented as the CSI matrix $H_{n,m}(t, f_k)$. This channel matrix corresponds to the link between m-th transmit (Tx) antenna and n-th receive (Rx) antenna and has a dimension of $M \times N \times K$. Here the total number of Tx and Rx antenna are M and N respectively. An additive white Gaussian noise (AWGN) is assumed in the communication which is denoted by $\mathscr{N}(t, f_k)$. In an ideal noise-free scenario, CSI can be easily calculated by normalizing the received signal $Y_n(t, f_k)$ with the transmitted signal $X_m(t, f_k)$. However, to extract CSI matrix in a practical noisy scenario, further signal processing techniques such as a minimum mean square error (MMSE) [63], maximum likelihood (MLE) [64], least square (LS) [65] and time domain based Frequency Pilot Time Average (FPTA) [66] channel estimations are required to estimate CSI by minimizing $\mathscr{N}(t, f_k)$ at Rx as shown in Fig. 2.1. In Wi-Fi transmission, Tx and Rx are not physically synchronized and thus Rx generally utilizes the preamble received from the transmitted signal for the synchronization purpose [2]. Although the synchronization can be optimally yielded, it inevitably introduces the additionally phase offset and rotation to the CSI. The effect of these undesired phase terms to the motion sensing application will be discussed further in chapter 3.

In a nutshell, CSI is physically a collection of Wi-Fi OFDM signal propagated through multiple paths in the channel. Along the propagation, each signal experienced different attenuation, fading, and scattering effect from their interaction with th interacting objects (IOs). Suppose the time-variant (TV) component of the CSI defined as $H^{\mathrm{TV}}_{n,m}(t, f_k)$ represents a set of L_{TV} signal in which each i-th propagated signal interacts with moving IOs along their i-th differential propagation path length of $d^{(i),\mathrm{TV}}_{n,m}(t)$ and get attenuated by the constant complex attenuation $\alpha^{(i),\mathrm{TV}}_{n,m}(t, f_k)$. On the other hand, the time-invariant component (TIV-

CSI) defined as $H^{\text{TIV}}_{n,m}(f_k)$ represents L_{TIV} signal whose j-th signal comes into contact with static IOs along their j-th total propagation path length of $D^{(j),\text{TIV}}_{n,m}$ and thus contributes to an amplitude attenuation $\gamma^{(j),\text{TIV}}_{n,m}(f_k)$. Henceforth, according to [26, 67], the CSI corresponding to the channel between m-th transmit and n-th receive antenna could be modelled as,

$$H_{n,m}(t, f_k) = H^{\text{TIV}}_{n,m}(f_k) + H^{\text{TV}}_{n,m}(t, f_k) \tag{2.2}$$

$$H^{\text{TIV}}_{n,m}(f_k) = \sum_{j=1}^{L_{\text{TIV}}} \gamma^{(j),\text{TIV}}_{n,m}(f_k) \exp\left(\frac{-\text{j}2\pi}{\lambda_k} D^{(j),\text{TIV}}_{n,m}\right) \tag{2.2a}$$

$$H^{\text{TV}}_{n,m}(t, f_k) = \sum_{i=1}^{L_{\text{TV}}} \alpha^{(i),\text{TV}}_{n,m}(t, f_k) \exp\left(\frac{-\text{j}2\pi}{\lambda_k} d^{(i),\text{TV}}_{n,m}(t)\right) \tag{2.2b}$$

$$d^{(i),\text{TV}}_{n,m}(t) = \lambda_k \int_0^{t'} f^{(i)}_{\text{d}}(t')\, dt' \tag{2.2c}$$

where $\lambda_k = \frac{c}{f_k}$ is the wavelength of k-th subcarrier frequency given the c light speed. As clearly seen in the phase term of TV-CSI, any motion will cause a change of $d^{(i),\text{TV}}_{n,m}(t)$ resulting in the phase rotation or Doppler frequency shift $f^{(i)}_{\text{d}}(t)$. The speed of the moving target has an explicit relationship with $f^{(i)}_{\text{d}}(t)$ according to the radar model [51] which will be further discussed in section 2.3.1.

2.2.2 CSI Extraction Method

Typically, CSI cannot be obtained directly from commercial Wi-Fi devices. To utilize Wi-Fi CSI, the Initial idea was to implement the Wi-Fi communication structure onto any programmable RF board or software-defined radio (SDR) as the mean to simulate the general Wi-FI transmission. With the manual modification, they can successfully extract either received OFDM signal or CSI for further motion sensing analysis. For example, previous works in [4, 58, 68] extracted CSI and the received OFDM signal from universal software radio peripheral (USRP) [69] which is one of well-known SDR module for the analysing of motion sensing via Doppler frequency. Another work in [70] implemented the wireless open access research platform (WARP) toolkit onto the programmable RF module to analyze the motion via channel parameters.

Later on, open-source tools have become available allowing user to directly extract a stream of CSI matrices from network interface card (NIC) of commercial Wi-Fi chips corresponding to a set of consecutive OFDM packets. Linux 802.11n CSI tool developed by [24] is compatible with only Intel 5300 NIC, and only capture CSI from the sampled 30 OFDM subcarriers in both 20 and 40 MHz bandwidth. The sampled subcarrier is governed by the grouping method of CSI report field according to 802.11n stardard [3]. Five years later, Atheros CSI Tool was developed by [25] and is claimed to be compatible with any Atheros

NICs despite a few NICs being verified. In contrast with the former tool, it reports CSI from all OFDM subcarriers available, 56 and 114 for 20-MHz and 40-MHz bandwidth accordingly. Both tools run on Linux operating system and their software-modified firmware are licensed under MIT and GPL agreement respectively. Despite limitation on the former tool, it gains more popularity in the CSI-based motion sensing and indoor localization than the latter. One advantage in particular for the 802.11n CSI tool is that at least one Wi-Fi transceiver is required to capture CSI while the Atheros CSI Tool needs both Wi-Fi transceivers. Therefore, the former tool is able to directly work with any off-the-shelf Wi-Fi access point (AP) whereas the extra modification of AP firmware is necessary to capture CSI with the latter tool.

With these considerations, 802.11n CSI tool was finally chosen for the study of motion sensing in this thesis. Based on the Intel 5300 NIC specification, it supports up to 3 antenna ports and the CSI is estimated at the receiver side. Therefore, the maximum of $M \times 3$ MIMO channel matrix can be obtained. Aside from CSI matrix, this tool also provides other relevant information that are also contained in CSI report field such as RSSI of each antenna, local timestamp, adaptive gain control (AGC), noise floor, and transmission rate. The timestamp is in the decimal number representing a lower 32 bits of the NIC's 1 MHz local clock and therefore the number will rotate every 4,300 seconds. By setting the timestamp of the 1$^{\text{st}}$ received CSI data as reference, a relative time in a unit of second can be easily converted by factoring the time difference between each recorded CSI to that of the reference time by the ratio between 2^{32} and the clock cyclic period of 4,300. Cyclic-to-linear time unwrapping is necessary for the linearization of this relative time conversion when a duration of CSI recording exceeds a cycle of the local clock. The unit of the raw extracted CSI is normalized by the relative reference level of NIC. Fortunately, the tool's developer has provided a method to convert it back to the original unit by basically utilizing AGC and noise floor data. Rather than the usual infrastructure mode where both Wi-Fi stations operated as transceiver, the tool can capture CSI in the injection-and-monitor mode where the Wi-Fi station is operated as Tx and Rx respectively. Since it allows a full control of transmission configuration, this mode has been utilized in our experiment. Regarding the CSI transmission sampling rate, although it has not been explicitly mentioned in the literature, the preliminary experiment showed that the nearly-uniform sampling rate could still be achieved up to 2,500 Hz and thus the rate was heuristically set to this number in our measurement campaign on the hand motion sensing.

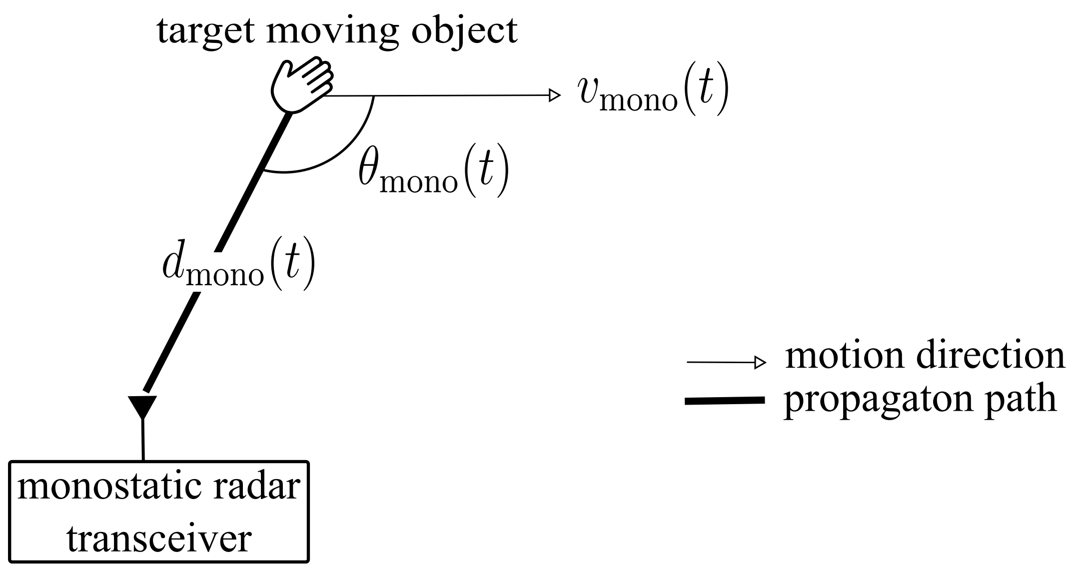

Figure 2.3: Monostatic radar system.

2.3 OFDM Radar

Before addressing the OFDM radar technology, it is necessary to understand a general concept of radar. In this section, we will focus our study to the range and speed estimation in radar since it directly contribute to the investigation in this thesis. The micro-Doppler effect will be later on explained especially how it impacts the analysis on velocity estimation.

2.3.1 Radar Technology

Radar technology is a well-established system for speed and range estimation of a moving object by analyzing the scattered RF signal. Generally, the target object is presumably maneuvering far away from radar sensors and thus can be assumed with a simplest point scatter with the received RF power proportional to the radar cross section (RCS) from the target object [44, 51]. Range and speed can be estimated from the the overall propagation delay $\tau(t)$ and Doppler frequency shift $f_{\text{d}}(t)$ at the radar Rx respectively. The former is described the time it takes for RF signal to arrive at the radar sensor after being scattered from the surface of moving object. The latter is manifested as the time-varying phase rotation of the scattered signal induced by a motion on the target surface where RF signal is interacted with [44]. Based on number of RF sensors used, radar can be categorized into monostatic, bistatic radar systems. The latter system also knows as mult-static radar system if number of sensors are more than two. Therefore, the range and speed of target are calculated differently according to their respective system.

- **Monostatic radar** [44] As shown in Fig. 2.3, Tx and Rx are situated in the same

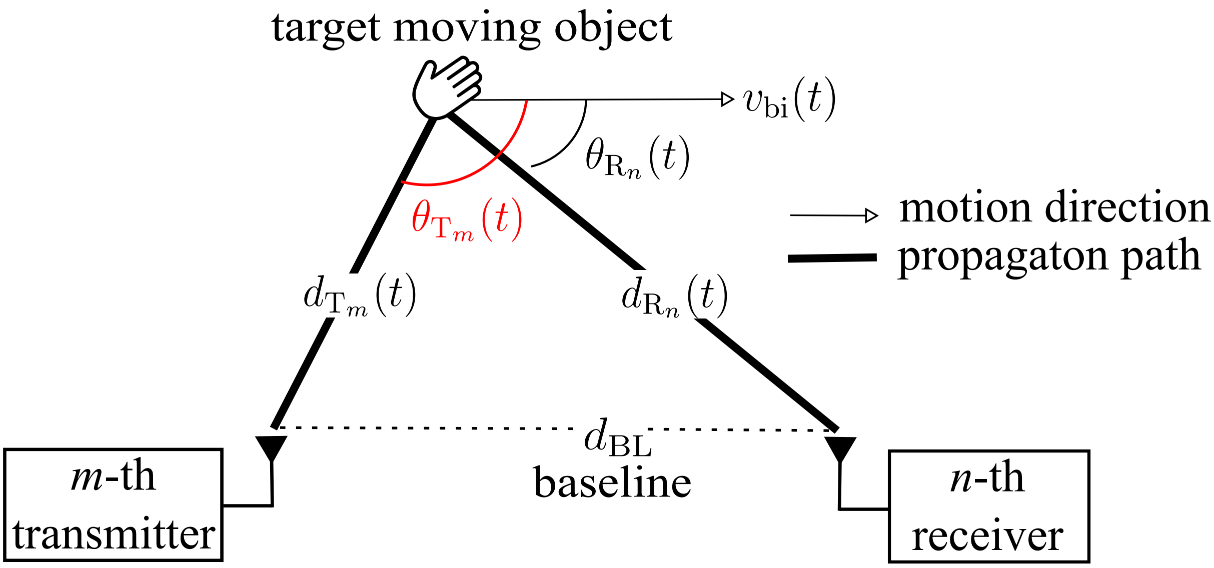

Figure 2.4: Bistatic radar system.

position for this radar system. Therefore, the distance of the target object relative to the sensor $d_{\mathrm{mono}}(t)$ can be easily computed by

$$d_{\mathrm{mono}}(t) = \frac{c}{2}\tau(t) \tag{2.3}$$

where c denotes a speed of light. Similarly, a speed $v(t)$ of the object in this system can be calculated from the measured Doppler frequency which is corresponded to the instantaneous path length change as,

$$\begin{aligned} v_{\mathrm{mono}}(t) &= \frac{d}{dt} d_{\mathrm{mono}}(t) \\ &= \frac{\lambda}{2\cos\theta_{\mathrm{mono}}(t)} f_{\mathrm{d}}(t) \end{aligned} \tag{2.4}$$

where $\theta_{\mathrm{mono}}(t)$ defines the angle between a direction of motion and a direction from the object to the radar sensor. Since speed is a scalar variable, a sign of Doppler frequency is proportional to a relative direction of target motion depending on $\theta_{\mathrm{mono}}(t)$. The Doppler gains a positive sign when the object is moving toward the radar sensor and vice versa for a negative sign. It should be noted that $\tau(t)$ will become constant if the target object is circling around the radar sensor. The range $d_{\mathrm{mono}}(t)$ effectively becomes its radius of the motion trajectory. In this scenario, motion direction is always perpendicular to the direction toward the radar sensor, $\cos\theta_{\mathrm{mono}}(t) = 0$, resulting in zero Doppler frequency regardless of the actual speed of the moving object.

- **Bistatic radar** [44, 71] Tx and Rx are at different position which are distanced away by the length of baseline d_{BL} in this system. As depicted in Fig. 2.4, the bistatic propagation path d_{bi} is the summation of range from the target object to the m-th Tx and that to the n-th Rx as

$$d_{\mathrm{bi}} = d_{\mathrm{T}_m}(t) + d_{\mathrm{R}_n}(t) \tag{2.5}$$

Suppose the angle between the direction of motion and a direction from the target to Tx and those to Rx are defined as θ_{T_m} and θ_{R_n} respectively, both $d_{\mathrm{T}_m}(t)$ and $d_{\mathrm{R}_n}(t)$ could be estimated by solving the following equations under the constraint that these ranges are greater than zero,

$$c\tau(t) = d_{\mathrm{T}_m}(t) + d_{\mathrm{R}_n}(t) \tag{2.6}$$

$$d^2_{\mathrm{BL}}(t) = d^2_{\mathrm{T}_m}(t) + d^2_{\mathrm{R}_n}(t) + d_{\mathrm{T}_m}(t) d_{\mathrm{R}_n}(t) \cos\left(\theta_{\mathrm{T}_m}(t) - \theta_{\mathrm{R}_n}(t)\right). \tag{2.7}$$

Likewise, the bistatic Doppler frequency shift can be used for the calculation of object's speed as a function of the instantaneous change of the total propagation path

$$\begin{aligned} v_{\mathrm{bi}}(t) &= \frac{d}{dt}\left[d_{\mathrm{T}_m}(t) + d_{\mathrm{R}_n}(t)\right] \\ &= \frac{\lambda}{\cos\theta_{\mathrm{T}_m}(t) + \cos\theta_{\mathrm{R}_n}(t)} f_{\mathrm{d}}(t) \end{aligned} \tag{2.8}$$

When either number of Tx or Rx are more than one, it is generally referred to as multi-static radar system. Moreover, the bistatic would gradually becomes the monostatic system if Tx and Rx position are relatively closer in comparison with their distance to the target object such that $d_{\mathrm{BL}} \ll d_{\mathrm{R}_n}(t)$ and $d_{\mathrm{BL}} \ll d_{\mathrm{T}_m}(t)$. With respect to a sign of bistatic Doppler frequency, it now depends on both $\cos\theta_{\mathrm{T}_m}$ and $\cos\theta_{\mathrm{R}_n}$. In other word, a positive and negative sign of Doppler frequency represents the object direction whether it moves toward to or away from the bistatic baseline respectively. Instead of the circular motion in monostatic, the overall propagation delay and distance are constant when the moving object has an elliptical trajectory around Tx and Rx whose positions are the foci of the ellipse. Consequently, the measured Doppler frequency becomes zero as the cosine of both angles are canceling out.

As clearly seen from these radar systems, range information could be easily determined in monostatic with the measured delay whereas the angular information is needed for the bistatic ranging according to eq. (2.3) and eqs. (2.6) - (2.7) respectively. Since the measured Doppler frequency only represents the radial speed component, angular information is necessary to infer the tangential component and therefore be able to estimate the actual speed of the object speed as stated in eq. (2.4) and eq. (2.8) for monostatic and bistatic radar respectively. With the radial component, speed estimation from Doppler frequency is virtually difficult in some certain motion directions which make the value of $\cos\theta_{\mathrm{mono}}(t)$ and $\cos\theta_{\mathrm{T}_m}(t) + \cos\theta_{\mathrm{R}_n}(t)$ approaches zero in monostatic and bistatic radar respectively. Considering the Wi-Fi CSI model in eq. (2.2), it can then be expressed in terms of the speed of moving object by substituting eq. (2.2c) with Doppler frequency in either eq. (2.4) or eq. (2.8) depending on the configuration of Wi-Fi Tx and Rx positions.

2.3.2 Wi-Fi based OFDM Radar and The Joint Range and Speed Estimation

The concept of utilizing multiple subcarrier frequencies in radar was firstly considered by [72] in 2000. It then has been further investigated in terms of the OFDM signal coding for radar application by [73] and the extension of OFDM radar in MIMO communication [47]. Later on, OFDM radar has been established by [48, 74] as the candidate system that could enable both data communication and radar simultaneously without the interference between each system. Since then, many researchers has been studied and formulated the usage of OFDM radar in various aspect such as OFDM signal structure [49, 73, 75], range and velocity ambiguity and resolution [48, 75, 76], and hardware and software complexity [73, 76]. The utilization of Wi-Fi CSI for motion sensing analysis can be regarded as one of the application in OFDM radar since OFDM signal is transmitted in the Wi-Fi communication system.

With the equally-spaced OFDM subcarrier frequencies, OFDM radar estimates range information by taking IFFT of the estimated CSI with respect to subcarrier f_k variable. Likewise, with sufficient consecutive OFDM symbols within a window period of W where T_P is the symbol duration, radial speed in terms of Doppler frequency can be computed from the FFT of CSI with respect to the temporal t variable [76, 77]. These transformations will result in the Doppler-variant impulse response, also known as the spreading function, which is a function of both propagation delay and Doppler frequency as shown in Fig. 2.5. The delay resolution $\Delta\tau(t)$ is restricted by a size of the signal bandwidth $K\Delta f$ due to the resolution trade-off with the subcarrier frequency. Since $d_\mathrm{bi}(t)$ and $d_\mathrm{mono}(t)$ in the bistatic and monostatic radar system are all proportionally to $\tau(t)$, their finest range resolution $\Delta d_\mathrm{max}(t)$ where the radar is able to tolerably distinguish multiple objects with the same speed given the maximum tolerable delay resolution $\tau_\mathrm{max}(t)$ can be expressed as,

$$\Delta d_\mathrm{mono,max}(t) = \frac{c}{2K\Delta f} \tag{2.9}$$

$$\Delta d_\mathrm{bi,max}(t) = \frac{c}{K\Delta f} \tag{2.10}$$

Similarly, Doppler frequency resolution Δf_d is depended on a length of the analyzed window W. Let us consider a scenario where the Doppler frequency shift is maximized $f_\mathrm{d,max}(t)$. In such condition, the $\theta_\mathrm{mono}(t)$, $\theta_{\mathrm{T}_m}(t)$, and, $\theta_{\mathrm{R}_n}(t)$ in both radar system are all either 0 or π and thus the achievable resolution of object's speed $\Delta v_\mathrm{max}(t)$ can be determined by

$$\begin{aligned}\Delta v_\mathrm{max}(t) &= \lambda\Delta f_\mathrm{d,max}(t) \\ &= \frac{\lambda}{2T_\mathrm{P}} \end{aligned} \tag{2.11}$$

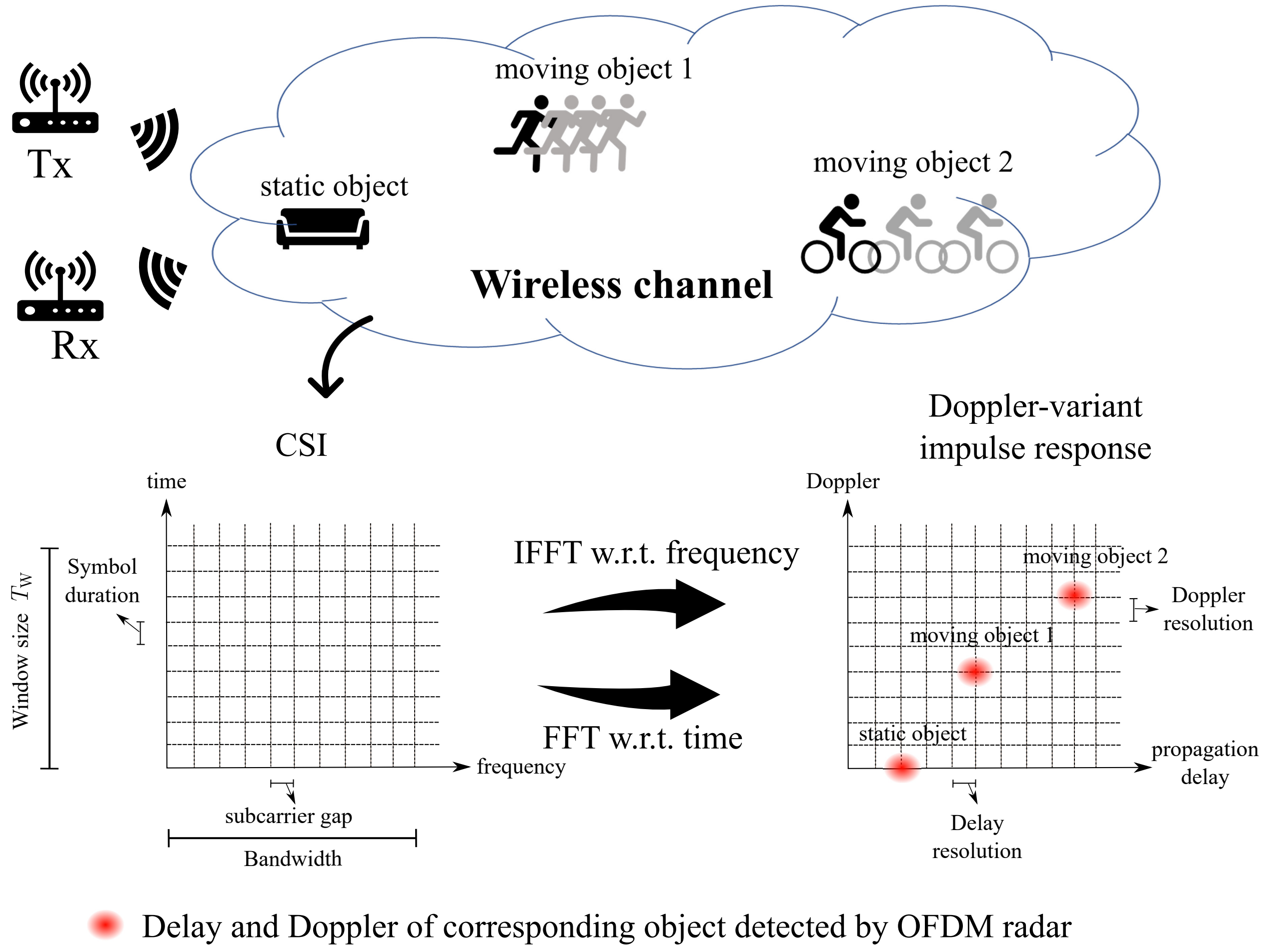

Figure 2.5: Range and speed estimation of multiple objects in terms of delay and Doppler frequency with OFDM radar.

Considering the aspect of OFDM communication, the allowance propagation delay τ_{max} that prevents the suffering of OFDM symbol from ISI should be shorter than OFDM guard band interval T_{G} [50, 60]. Therefore, the maximum radar detectable range for monostatic $d_{\mathrm{mono,max}}(t)$ and bistatic $d_{\mathrm{T}_m,\mathrm{max}}(t) + d_{\mathrm{R}_n,\mathrm{max}}(t)$ radar system can be computed by,

$$d_{\mathrm{mono,max}}(t) = \frac{cT_{\mathrm{G}}}{2} \tag{2.12}$$

$$d_{\mathrm{bi,max}}(t) = cT_{\mathrm{G}} \tag{2.13}$$

In frequency domain, the effect of Doppler frequency to the OFDM signal is manifested as inter-carrier interference (ICI) which effectively reduces the orthogonality among subcarrier [50, 77]. Although this results in the performance degradation for the communication, the OFDM radar ironically needs this Doppler frequency for the speed estimation. Since the impact of ICI fortunately could be reduced with a larger subcarrier spacing Δf relative to the maximum shift in Doppler frequency such that $f_{\mathrm{d,max}} \ll \Delta f$, the fastest speed

Table 2.1: Parameters of OFDM radar in case of utilizing 802.11n WI-Fi CSI [3]

Parameters	**Values (2.4 GHz)**	**Values (5 GHz)**
Finest speed resolution $\Delta v_{\max}(t)$	$0.0625/T_{\mathrm{W}}$ m/s	$0.03/T_{\mathrm{W}}$ m/s
Maximum achievable speed $v_{\max}(t)$	$\ll$ 19,531 m/s	$\ll$ 9,375 m/s
Monostatic radar system		
Finest range resolution $\Delta d_{\mathrm{mono,max}}(t)$	8.57 m	4.21 m
Maximum range $d_{\mathrm{mono,max}}(t)$	60 m ($T_{\mathrm{G}} = 0.4$ µs), 120 m ($T_{\mathrm{G}} = 0.8$ µs)	
Bistatic radar system		
Finest range resolution $\Delta d_{\mathrm{bi,max}}(t)$	17.14 m	8.42 m
Maximum range $d_{\mathrm{bi,max}}(t)$	120 m ($T_{\mathrm{G}} = 0.4$ µs), 240 m ($T_{\mathrm{G}} = 0.8$ µs)	

the OFDM monostatic and bistatic radar systems are able to detect while maintaining the communication quality [77] should be restricted by,

$$v_{\max}(t) \ll \frac{\lambda \Delta f}{2} \tag{2.14}$$

With the implementation of OFDM radar into the existing Wi-Fi communication by utilizing CSI tool mentioned in section 2.2.2, these radar parameters could be determined by considering the structure of HT-LTF symbol from 802.11n Wi-Fi standard discussed in section 2.2.1. As shown on Table 2.1, Wi-Fi motion sensing could theoretically have the operational range larger than 60 meters. These range, however, may drastically reduce owning to various variables such as obstacles, RCS of the moving IOs, transmitted power, antenna gain, and noise floor [77]. In terms of range resolution, few meters range uncertainty is unfortunately unreliable to track trajectory of micro-motion such as hand gesture. It is still challenging with this coarse-grained resolution even for the human walking tracking in indoor environment. With respect to the moving speed, it seems Wi-Fi CSI obviously can handle a speed of hand gesture or any human activities since those speed are tremendously slower than $v_{\max}(t)$ stated on Table 2.1. Although speed resolution is still inverse proportional to the window size, this centimeter per second uncertainty may be sufficiently fined for the hand motion analysis recognizing that the hand motion speed is still less than a few meter per second according to literature [78, 79, 80, 81].

Therefore, it could be argued that only speed information could likely be utilized via Doppler frequency for the Wi-Fi CSI based hand motion analysis. However, it is virtually challenging to apply the range information for motion analysis with WI-Fi CSI owing to its coarse-grained resolution.

2.3.3 Micro-Doppler Effect

Let's firstly discuss a type of moving object that induce Doppler frequency. The simplest model of moving object the point scatterer only exhibits a single component of Doppler frequency [51, 82]. As mentioned previously, this model is generally applicable in radar system where the distance between the target and radar sensors are larger. This range is regarded as far-field region can be defined based on the transmitted RF wavelength and the dimension of the object [44, 83]. In this region, the phase variation of RF signal scattered from different area on the target's surface is negligibly small, approximately less than 22.5°, and thus resulting in the detectable coherent Doppler frequency. In a context of human motion sensing, point scatter assumption could be impractical considering a shorter distance from the target to the sensors as well as the target size. The more realistic but complicated model would be a structural objects model consisting of multiple components. Each small movement of these parts can be regarded either a rigid body or non-rigid body motion [1]. For example, the former motion could be a subtle movement of torso while walking. Arm swinging, on the other hand, can be regarded as the non-rigid body motion which consists of the bulk rigid body movement of hand, forearm, and upperarm segment. These micro-motions could induce many frequency modulations to the scattered RF signal and thus contributing to multiple components of time-varying Doppler frequency upon the received signal and CSI [51, 52, 53, 56, 84]. This characteristic of micro-Doppler effect can be clearly seen in the joint time-Doppler frequency spectrum. In fact, a set of micro-Doppler signatures from each micro-motions is then superimposed in the spectrum. In general, Doppler frequency of objects are likely situated near the area with higher power in the spectrum. Because of this effect, it has been also exploited to analyze the kinematic properties of small components in the complex structure such as leg swinging in gait analysis [56], and the rotation of helicopter blades [51].

To understand the impact of micro-Doppler effect to the speed estimation in radar, let us consider the non-rigid body motion of 2R robot arm [1]. For simplification, a straight horizontal movement of the end-effector with a constant speed is assumed to simulate the micro-motion of non-rigid body as depicted in Fig. 2.6a . Inverse kinematic solution in [1] is applied to estimate the trajectory of the entire robot arm during a course of motion given the reference movement at the end-effector. Considering five sample points denoted as p_j where $j = 1, 2, ..., 5$ with distinct trajectories depicted as solid-line with arrowhead respectively in Fig. 2.6a, it is obvious that each point on the robot arm would generate various speed. By subjecting this setup into a bistatic Doppler radar given in the figure, micro-Doppler frequency induced from the movement of these points on the robot arm can be simulated by utilizing eq. (2.8) under the transmission of RF signal operated at 5-GHz carrier frequency. The five temporal profiles or signatures of micro-Doppler frequency marked in Fig. 2.6a which represent the end-effector, joints, and the points in the middle of each

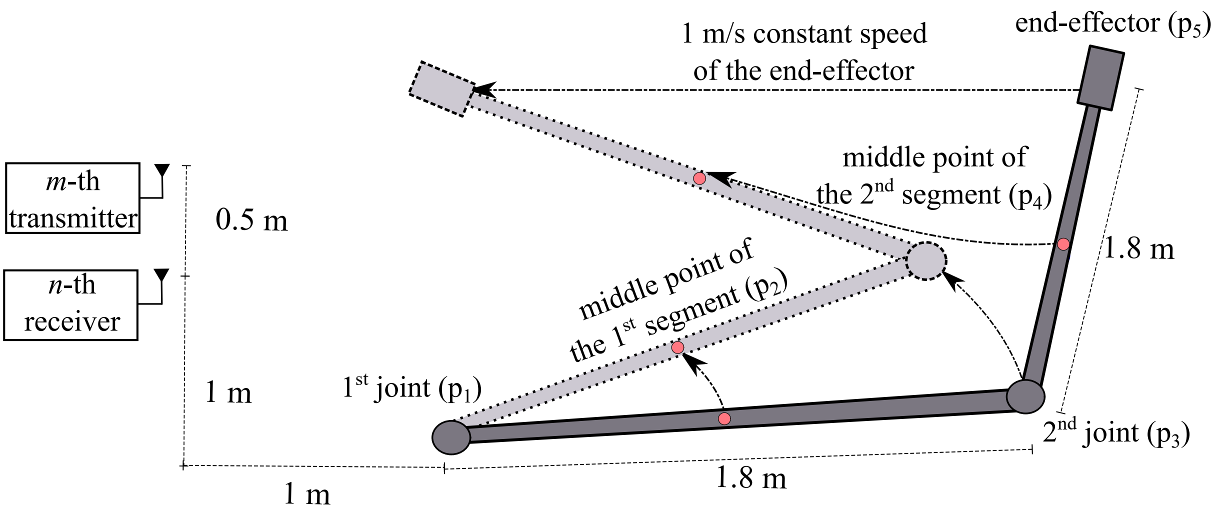

(a) Movement of the robot arm

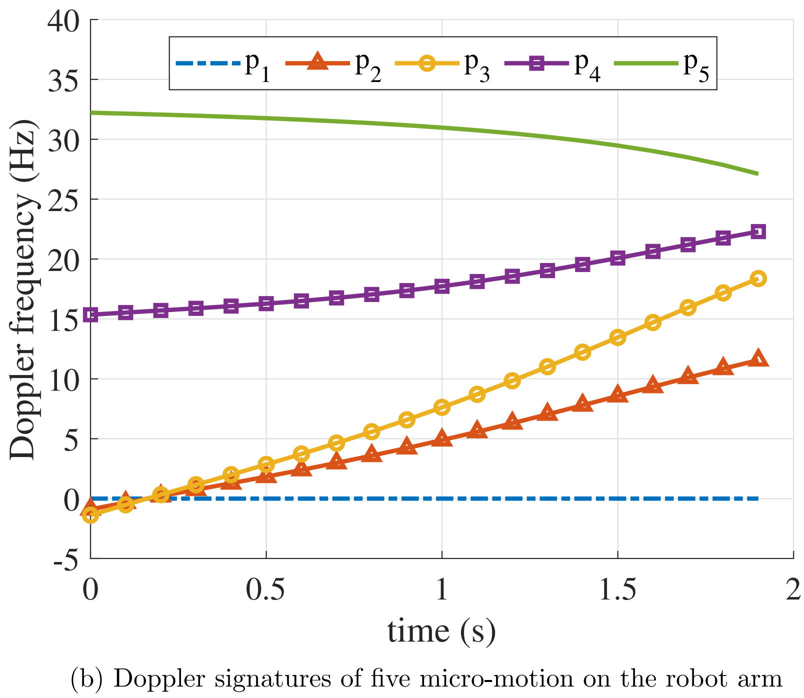

(b) Doppler signatures of five micro-motion on the robot arm

Figure 2.6: Simulation of non-rigid body motion of 2R robot arm [1] and five sample signatures of bistatic Doppler signatures from each segment, joints and end-effector

robot arm's segment were comparatively plotted in Fig. 2.6b. As expected, each of them induced different Doppler pattern regardless of the constant speed at the end-effector. The aggregation of these signatures in the received RF signal would be observed through the joint time-Doppler power spectrum as either multiple stripes or spreading which is commonly known as micro-Doppler effect [51, 56]. Suppose we want to estimate the velocity of the 2^{nd} joint (p_3). By simply observing Doppler profiles in Fig. 2.6b, it is still a challenging task to determine which signature is corresponding to the Doppler signature of the target joint without any supportive model. Having additional information such range and angular variables could help deciding the target signatures however it comes with the cost of the larger bandwidth and the need of array antennas [85, 86]. Inappropriate and unjustified selection of Doppler selection could without a doubt lead to the higher error in the tracking performance. Therefore, the investigation of micro-Doppler effect will be thoroughly covered in chapter 5 for the estimation of hand Doppler signature during the course of hand gesture. In fact, each profile here can be regarded as the i-th component of the TV-CSI expressed in eq. (2.2b) for the CSI-based motion analysis.

Temporal characteristic of Doppler frequency is necessary in the velocity estimation via radar. Table 2.2 lists various techniques that have been implemented to ease the analysis in this problem. Depending on the types of motion and scenarios, the selection of these tools is absolutely important for the motion analysis since each of them comes with both pros and cons which has been summarized accordingly in the table.

- **Hilbert transform (HBT)** This transformation enables the computation of a so-called instantaneous Doppler frequency through the the time derivative of time-varying signal [87, 88]. Although it can yield better time and Doppler resolution than other techniques, the applicability of HBT is restricted to only a monocomponent Doppler frequency for any given time since its output always contains only one value. In the presence of micro-Doppler frequency, HBT will obviously fail to provide an accurate representation of multiple components of Doppler frequency.

- **Empirical mode decomposition (EMD)** As the name suggest, this technique decomposes multi-component signal empirically into a set of time-varying monocomponent called intrinsic mode function (IMF) [89]. Since the estimated IMF ideally contains only one component at a time, HBT can be utilized to infer Doppler frequency [51, 89]. The decomposition criteria does not have the concrete model but it relies on empirical criteria based on the temporal characteristic of the signal such as maxima, minima, and zero crossing points. Each IMF is estimated iteratively ordering from higher to lower frequency components and are supposed to be a nearly orthogonal basis of the original signal [90]. Based on literature, EMD provides a good time-Doppler frequency resolutions and also performs well with the target signal containing a unique set of signatures. Nevertheless, the drawback of this tool lies on the empirical method. First of all, the performance of IMF could not be analytically validated due to the lack of theoretical formula [91]. Therefore, IMF estimation is highly depended on the variables adjustment during the decomposition. Mode mixing is another issue in EMD. The phenomena describes the undesired IMF characteristic that additionally contains high-frequency component in the lower-component IMF [92].

- **Short-time Fourier transform (STFT)** This classical joint time-frequency analysis is in fact the extension of the traditional Fourier transform (FT) [51, 93]. STFT utilizes a window function to localize multiple signatures of Doppler frequency within each short-time period. The decomposition is computed via the Fourier basis and thus could preserve the energy and spectral shape during the transformation. Therefore, this method has been widely implemented in various fields including the micro-Doppler analysis [8, 51, 53, 56, 84, 94, 95]. However, the localized energy within a short-time period is restricted by the uncertainty principle resulting in the spectrum spreading [93]. As a result, the STFT analysis inevitably is subject to the constant time and Doppler frequency resolutions which are reciprocal of each other. In a nutshell, a longer window size gains a better time resolution but reduces a resolution in Doppler frequency domain, and vice versa for the shorter window period. Although changing type of window functions have a direct consequence to the achievable trade-off resolution, Gaussian window has been analytically proven to yield the optimal value among these two quantities [94, 93, 96].

- **Wavelet transform (WT)** The idea of this transformation is motivated by a constant resolution trade-off in STFT. Conceptually, WT relaxes this constraint by varying the resolution at different frequency bands without violating the uncertainty principle [93, 97]. As a result, a better resolution of Doppler frequency (with a lower time resolution) at a lower frequency band can be achieved. This feature, however, is opposite at a higher frequency band with a higher time resolution but a poorer Doppler frequency resolution. This concept can be achieved by introducing the wavelet signal, a finite oscillating function, as the kernel instead of continuous signal as in STFT. Through the convolution of the target signal with the translating and scaling version of the wavelet signal, multi-resolution time-Doppler frequency spectrum can be obtained. Due to the scaling property, the wavelet spectrum represents the component of signal in terms of wavelet scale which is inverse proportional to Doppler frequency. Although the Doppler domain could be easily converted in WT, it will be arranged in a non-linear scale which is different from other techniques. Regardless, WT also becomes one of widely-implemented joint domain analysis in various field owning to resolution variety [97, 98, 99, 100, 43]. Similar to the window function in STFT, there are plenty of wavelet signal to be used in WT and thus also have a direct impact to the wavelet spectral shape and resolution. The incompatibility of a certain wavelet basis to the target signal features could lead to the poorer time and Doppler frequency resolution than its counterpart STFT.

- **Wigner-ville distribution (WVD)** This technique is similar to STFT in the sense that both decompose the spectral component with Fourier basis. Unlike STFT, this technique applies Fourier transform to the time-dependent autocorrelation function of the target signal [51, 93]. Henceforth, the short-time spectrum of WVD is one-sided owing to the autocorrelation. Mathematically, it has been shown that WVD could acquire a better resolution than either STFT and WT. Unfortunately, WVD strongly suffers from the cross-term interference which could be regarded as the undesired components occurred in the spectrum. The WVD drawback from this attenuation could make it difficult in the presence of micro-Doppler effect as the distortion to the shape of spectral. Although this interference could be mitigated by applying the appropriate filter, the smoothing WVD spectrum will unavoidably spread out thus losing the resolution in the process. In fact, STFT and WT can be considered as the special case of the smoothing WVD [93].

- **Subspace method** Rather than decomposing the target signal into the spectrum, this technique conceptually projects each temporal signal segment into an orthogonal subspace [101]. Each subspace may contain a single or multiple Doppler components depending on the coherency of Doppler signatures within a short-time period. The reconstruction technique of the pseudo-Doppler spectrum from each subspace is basically computed by utilizing the subspace basis function or the subspace array response. Famous subspace techniques such as multiple signal classification (MUSIC) [102] and estimation of signal parameters via rotation invariance (ESPRIT) [103] have also been implemented in the analysis of Doppler frequency [54, 104, 105, 106]. Because the mean of estimating Doppler frequency component could be categorized as the continuous search along the subspace plane, it could obtain a super resolution in both Doppler and temporal domain. However, the method assumes the known number of the signal subspace which is difficult to determine especially in the presence of micro-Doppler effect. The physical interpretation of signal subspace is also another issue in this method since again it does not always represent each Doppler signature. Moreover, it requires plenty of signal samples or sensors to construct the orthogonal subspace basis from the signal correlation matrix.

As far as micro-Doppler effect is concerned, HBT is obvious is not a preferable technique due to its inability to deal with multi-component signal. WVD and subspace may not be a suitable analysis tool as well since the former could have the spectrum shape distorted

Table 2.2: Comparison of the joint time-Doppler frequency analysis

Techniques	**Merit**	**Drawback**
HBT	high resolution, simplicity	feasible only a single component signal
EMD	high resolution	lack of mathematical framework, mode-mixing issue
STFT	preserving energy and spectral shape	fixed uncertainty trade-off
WT	multi-resolution	wavelet-dependent resolution, non-linear Doppler scale
WVD	high resolution, preserving spectral shape	cross-term interference, only one-sided spectrum
Subspace	super resolution	prerequisite number of incoherent signal component, large number of signal sample

resulting in the difficulty to handle the continuous spectrum spreading whereas number of Doppler coherency is hard to estimate in the latter technique. Considering the hand gesture motion sensing, it could be a challenging task to model the characteristic of Doppler signatures for all possible variety of gestures. Although the remaining techniques are able to handle the unknown pattern of Doppler frequency, STFT is finally chosen in this study because it could preserve the power and spectral shape which makes it easier for the physical interpretation of Doppler signatures in the join time-Doppler power spectrum.

2.4 RF-based Motion Sensing

Through extensive literature review, applications of human motion sensing with RF signal can be broadly categorized into three groups: detection, recognition, and tracking. The target motion is varied from a macro-motion such as human action and activity down to micro-motion of hand and finger gestures [13]. Typically, Doppler, delay, and angular information derived from either received RF signal or CSI are exploited for sensing the moving target [14, 107].

2.4.1 Motion Detection

Detection could be considered the basic application in comparison to other motion sensing analysis. In general, this study may be regarded as the two-state prediction in which the system attempts to passively perceive whether there exists any motion happening in vicinity based on the temporal phase change caused by Doppler frequency. Since only the presence of Doppler is sufficient for detection, previous works simply analyze the phase term of the signal without any decomposition techniques. Additional, it was mathematically shown in [26] that the effect of Doppler frequency manifested in the amplitude of the measured CSI as temporal fluctuation and thus is utilizable for the motion detection. In fact, most literature with Wi-Fi CSI preferred the use of amplitude since the time-varying phase caused by the motion is highly contaminated by the undesired phase rotation owning to non-synchronization between Tx and Rx [108].

Previous works in [34, 109, 110, 111] analyzed the temporal characteristic of the measured CSI from the human walking to realize the passive intrusion detection. Short-time variance profile is the common features for the intrusion detection application such as people entering the room since it directly capture signal variation. Amplitude variance of CSI was applied to hidden Markov model (HMM) and Gaussian mixture model (GMM) in [109, 110] respectively to train and predict the presence of human walking. [111] supplied the variance of CSI phase information together with the amplitude variance as the features into the support vector machine (SVM) model to increase the intrusion detection performance. Since the undesired phase rotation obscured the rotation from the motion, the phase difference between adjacent antennas was applied to partially mitigate the undesired phase rotation in CSI phase. On the other hand, [34] applied the widely-implemented phase sanitization technique to reduce the impact from the undesired rotation. In this work, the heuristic threshold was derived based on the sanitized phase variance to detect the presence of human motion.

The passive fall detection with RF signal has also been studied to improve the elderly care system [112, 113]. In a nutshell, the concept is closely related to the intrusion detection explained previously. Instead of the gradual temporal change in the RF signal due to human walking, this problem focuses on the micro-Doppler effect of human falling which is manifested as a harsh and rapid change of signal within a relatively shorter period [113]. The fall detection in [40, 112, 114] followed the same analysis as in intrusion detection which essentially trains the classifier model such as SVM or k-th nearest neighbor (kNN) with the statistical features extracted from either temporal profile of CSI amplitude or phase. On the other hand, the analysis in [115] conducted in 24-GHz radar system identified the micro-Doppler signature of human torso while falling from the STFT spectrum and then used it as the SVM feature to evaluate their fall detection performance. Aside from the fall detection, [113] has studied the characteristic of micro-Doppler effect when human falling. The study was conducted in simulation with a simple movement model consisting of 5 moving scatterers corresponding head, arms, and legs. The result has been verified with the measurement data obtained from channel sounder.

In the healthcare application, [9, 33] estimated breathing and heart rate by observing the subtle phase oscillation of received signal and CSI respectively which were caused by the subtle movement of human chest. In CSI phase preprocessing, linear phase sanitization technique was applied in [33] while the inter-antenna phase difference was utilizing in [9] to deal with the undesired phase rotation. In contrast, The time-variance CSI amplitude [11, 12, 36, 116] detected the vital signal for the remote sleep monitoring system. Since breathing generally generates a unique periodic pattern, these works could also retrieve and validate the rate of breathing by taking FT over the time-varying amplitude or phase. The concept of breathing detection has also been extended for the detection of human smoking in [29] which aimed to capture the temporal change of CSI amplitude caused by the smoker while inhaling and exhaling. Furthermore, as suggested in [20, 116], the usability of breathing detection could be applied in parallel with the intrusion detection framework to sense the presence of both dynamic and stationary scenarios.

2.4.2 Motion Recognition and Identification

Arguably, the could be considered the most popular application in RF-based motion sensing due to its simplicity and practical. Given statistical, time-series, and/or spectrum features obtained from measured CSI or received RF signal data, the unsupervised pattern matching based algorithm is applied to train the classification model. Depending on how distinguishable the features are, a group of gestures or activities can be correctly recognized. In comparison, this motion recognition aims to differentiate various actions based on the effect of micro-Doppler in amplitude and phase of either CSI or received signal whereas the motion detection attempts to simply find the presence of certain motion. Similar to the detection, recognition is the data-driven approach and does not directly require the knowledge in radar Doppler model which is, in contrast, essential for the motion tracking application. Therefore, the estimation of range and speed is not necessary as long as each action preserves the uniqueness of overall time-varying signal.

Device-free human action/activity recognition has been intensively researched since the benefit of non-intrusive system could help realizing the HCI system and enhancing internet-of-things (IoT) application [107]. Recognition systems in [26, 37] focused their analysis on the common human activities in the indoor environments such as running, walking, and sitting down by utilizing CSI amplitude. HMM was used in [26] to classify these activities based on features in both temporal and WT-based frequency domains. On the other hand, [37] applied the statistical features to SVM model for classification. The statistical features of CSI amplitude were also utilized in [28] to identify a certain person from different group of people while crossing the LoS between two Wi-Fi transceivers. Sparse Approximation based

Classification (SAC) commonly used in the face recognition problem was applied to handle multiple features in their study. RF-based human identification was also performed in the frequency modulated continuous wave (FMCW) multi-static radar system in [117]. With 4 Txs and 8 Rxs, joint range-angular spectrum could be estimated to visualize the strong scattered signal from any human standing nearby radar sensors. Principle components of this joint spectrum was then used to identify 10 persons with the SVM classifier model.

Many works also proposed the usage of RF-based hand gestures recognition since the micro-Doppler effect from a micro-motion of hand movement could still be detectable. On average, around 6-10 gestures could be distinguished in each previous work. While [43] still utilized a statistical features of CSI amplitude for classify hand gestures, other works have begun to analyse the micro-Doppler components of either received signal or CSI at different frequency bands since gesture is becoming harder to distinguish from the statistical feature alone. For instance, the temporal sequence features of Doppler sign was selected in [4] as motion features for recognizing simple hand gestures such as pushing, pulling, and swiping. Similarly, the WT-based high frequency component of the received Wi-Fi signal were applied as the motion features in [6, 19]. These works classified gesture with the primitive technique of time-series sequence matching. Inverse synthetic-aperture radar (ISAR) was applied in [42] to construct the MUSIC pseudo-spectrum of time and angular domains from the measured CSI under the pseudo-monostatic radar configuration [44]. This spectrum was then used as feature of SVM model to recognize hand gestures. In [52, 53], the envelope of micro-Doppler spectrum of CW radar were extracted as hand gesture features. Various classification models have been compared in these previous works with the agreement conclusion that the best classifier belongs to kNN. In addition, it has been shown that RF-signal could still perceive a tiny and subtle change of finger gesture [31, 30, 32] and the lip motion [7]. The objective of finger gesture recognition is similar to those of hand gesture. Lip recognition, on the other hand, recognized Doppler frequency signature corresponding to the fundamental English phonetic by using Multi-Cluster/Class Feature Selection (MCFS) classifier. By correctly recognize the phonetic sound, the system is able to reconstruct any word the target has spoken.

2.4.3 Motion Tracking

Unlike other sensing techniques, motion tracking requires an accurate kinematic information such as velocity, position, and angle to correctly estimate the target trajectory. Therefore, the radar model described in section 2.3 is commonly applied for the RF-based tracking problem. In comparison, motion detection and recognition can handle only a single motion and a set of motion respectively whereas the motion tracking application ideally could deal with any kind of motion. In literature, only a few motion tracking was proposed with the commercial Wi-Fi system in comparison with the detection and recognition applications. This is because the poor range resolution and the noisy Doppler measurement owing to the narrowband signal and the undesired phase rotation in the measured CSI respectively. Therefore, FMCW radar, USRP, and WARP based motion tracking platform were alternatively introduced to achieve a better range and Doppler quality than CSI data.

Intensive research has been conducted in RF-based indoor human tracking. Although the non-rigid body motion of human walking induced micro-Doppler effect, the strongest scattering usually contributes from the bulk human torso [51, 117]. Since most literature [5, 15, 54, 55, 68] detected the human motion based on the highest power in either Doppler, range, or angular domain, it is likely that their tracking systems implicitly traces the torso movement. In [68], 1D human tracking was implemented using the received Wi-Fi signal obtained from USRP. Here ISAR technique was applied to translate the Doppler frequency into the 1D angle-of-arrival (AoA) MUSIC pseudo-spectrum. With ISAR, the obtained AoA represents the angle relative to the direction between radar sensor and the human temporal position. For the 2d tracking, [54, 55] iteratively traced the human walking trajectory from the estimated Doppler profile by exploiting bistatic radar model between single Tx and multiple Rxs. Doppler frequency was estimated from MUSIC and STFT in the former and latter works respectively. In addition, the former proposed the use of the angular information to improve tracking accuracy. Space Alternating Generalized Expectation Maximization (SAGE), a high dimensional search algorithm, was implemented in [5] to estimate range, AoA, and Doppler with high resolution from Wi-Fi CSI. Although the resolution was improved, additional signal processing is needed to handle the noisy Doppler measurement and the range uncertainty of CSI. Multiple motion tracking has been achieved in [15]. They utilized multi-static FMCW radar to construct the fine-grained 2D range spectrum. By analyzing a pair of spectrum from the consecutive received signal, multiple movement could be localized.

In contrast to motion recognition, Device-free hand gesture tracking with Wi-Fi CSI has not been widely studied. In fact, only previous works in [57, 58] has investigated the possibility of hand motion tracking. As mentioned in [57], the change of angular spectrum profile due to the shadowing of hand at certain position could help tracing hand trajectory. To realize this concept, at least 30 Wi-Fi transmitters have to be distributed over the experiment scenario to track the 3D hand movement in terms of the change in AoA profiles. Despite the fruitful trajectory estimation result, it is applicable only when the gesture is performed around 0.6 meter nearby the Wi-Fi receiver. On the other hand, [58] has the capability to track 2D hand trajectory performed in horizontal direction with only 1 Tx and 2 Rxs. By utilizing the ellipse geometry of bistatic radar, the 2D temporal position was recursively estimated. However, this system needs the pre-determined gesture to estimate the initial position before the iterative process. Another drawback of this tracking system is that the Doppler frequency was estimated using HBT technique whose micro-Doppler effect does not take into account. Therefore, the usability might be limited to only the scenario where it exists only a single dominated scattered power in the entire gesture motion.

2.5 Summary

In this chapter, we have elaborately explained literature review regarding the technology in RF-based motion sensing specifically through the usage of Wi-Fi CSI. From the CSI modelling and estimation, it was showed that the CSI-based motion analysis could be considered as the application in OFDM radar. The review in OFDM radar has concluded that range information is unreliable with the narrowband signal of commercial Wi-Fi devices. Henceforth, only speed information could be utilized via Doppler frequency.

The non-rigid body motion of human action/activity inevitably induces micro-Doppler effect. Its consequence is manifested as the ambiguity in Doppler power spectrum. velocity profile estimation becomes challenging as the target Doppler signature is difficult to obtain from the superposition of multiple Doppler components in the spectrum. To ease the analysis, selecting the suitable joint time-Doppler transformation is essential. Since different hand gesture could produce various temporal characteristic, STFT was selected for the motion sensing analysing in our study since since it correctly preserve the Doppler spectral shape and energy in comparison with various techniques explained in this chapter.

According to the intensive literature review, RF-based motion sensing can be categorized based on applications into detection, recognition, and tracking. Data-driven approach is the core concept for the motion detection and recognition application. For that reason, their proposed models were not based on radar or EM scattering theory which describe the physical characteristic of Doppler frequency. In motion tracking system, majority focused their study on the indoor human trajectory tracking by utilizing radar model. Hand motion tracking, in contrast, has not gained much attention in comparison with the hand gesture recognition system. Although previous work in hand tracking utilized radar model, the impact of Micro-Doppler effect to the quality of estimated trajectory has not yet been addressed. Moreover, their system also required the manual calibration before imitating the hand tracking process. In the later chapter, we will explain our passive hand tracking system that addresses micro-Doppler effect and thus does not requires any manual calibration prior to the tracking.

Table 2.3: Summary of RF-based motion sensing technique

Sensing application	RF system	Frequency (GHz)	Analysing data	Sensing technique
Motion detection [109, 111, 110, 34, 116]	Wi-Fi	2.4	CSI amplitude and phase difference	Energy detection, GMM, SVM
Fall detection [113, 114, 112, 40, 115]	Wi-Fi	2.4, 5	CSI amplitude and phase difference	SVM
	Channel sounding radar	5	Channel transfer function	Doppler mean/spread
		5, 24	Radar waveform	SVM, kNN
Breathing detection [116, 41, 16, 9, 15]	Wi-Fi	2.4	CSI phase difference	Spectrum analysis
	FMCW radar	5 - 7	CW and its phase	Range difference, Spectrum analysis
Daily human activity recognition [118, 26, 37]	Wi-Fi	2.4, 5	CSI amplitude	SVM, HMM, Earth mover's distance
Human identification [117, 28]	Wi-Fi	5	CSI amplitude	SAC
	FMCW radar	5 - 7	CW	Angular spectrum
Hand gesture recognition [6, 19, 43, 42, 53, 52]	Wi-Fi	2.4, 5	CSI and its amplitude	SVM, sequence matching, Dynamic time wraping
	USRP	2.4	OFDM signal	Sequence matching
	CW radar	25	CW signal	kNN
Finger gesture recognition [30, 32]	Wi-Fi	2.4, 5	CSI amplitude	Dynamic time wrapping, kNN
Keystroke recognition [31, 119]	Wi-Fi	2.4	CSI amplitude	Dynamic time wrapping, kNN
Lip recognition [7]	Wi-Fi, USRP	2.4	CSI amplitude	MCFS
Human tracking [55, 68, 5, 15, 54]	Wi-Fi, USRP	2.4, 5	CSI	Bistatic Doppler radar, SAGE, MUSIC
	FMCW radar	5 - 7	CW	Range estimation
Hand gesture tracking [57, 58]	Wi-Fi, USRP	2.4	CSI phase and phase difference	Bistatic range estimation, AoA spectrum

Chapter 3

Mitigation of Undesired Phase Rotation in Measurement CSI

3.1 Introduction

In order to effectively suppress the phase rotation without contaminating the CSI, a calibration method by using a back-to-back (b2b) channel will be introduced in this chapter. The effect of the attached spatial mapping (SM) and cyclic shift diversity (CSD) matrices to the extracted CSI for multiple transmit streams configuration [3, 35] will also be discussed. Furthermore, it will show that in case of single-input-multiple-output (SIMO) configuration, the proposed calibration method can effectively remove SM and CSD matrices without requiring their knowledge and thus returning the channel matrix without distortion. For validation, the experiment was performed to compare between the calibrated CSI with the channel measured using a Vector Network Analyzer (VNA) as ground truth. Furthermore, the correctness of the estimated Doppler frequency is visualized from the simple movement of hand swiping and different position.

3.2 Effect of Spatial Mapping and The Effective CSI

In the case of MIMO configuration, each OFDM symbol $\tilde{X}(t, f_k)$ is firstly allocated into i_{SM} spatial stream. Suppose the OFDM symbol that will be transmitted with the S_{SM} spatial streams is denoted by,

$$\tilde{\boldsymbol{X}}(t, f_k) = \left[\tilde{X}^{(1)}(t, f_k) \quad \tilde{X}^{(2)}(t, f_k) \quad , \cdots , \quad \tilde{X}^{(i_{\mathrm{SM}})}(t, f_k)\right] \tag{3.1}$$

The vector is then being shifted and/or multiplied by the SM and CSD before transmission according to the IEEE 802.11n standard [3] as shown in Fig. 3.1. The SM matrix $\mathbf{Q}$ with a dimension of $M \times S_{\mathrm{SM}}$ modulates S_{SM} spatial streams into M transmit antennas. Although there exists plenty of $\mathbf{Q}$, the mapping matrix can be grouped into 4 categories according to the standard.

- **Direct mapping** This is a simple form of SM mapping in which each m-th transmit antenna is corresponded to only a single stream. Identity matrix is a special case that literally bypass the spatial mapping. The following SM is the example of direct mapping in case of $M = 4$ and $S_{\text{SM}} = 3$,

$$\mathbf{Q}_{\text{direct}} = \begin{bmatrix} 1 & 0 & 0 \\ 0 & 0 & 0 \\ 0 & 0 & 1 \\ 0 & 1 & 0 \end{bmatrix} \tag{3.2}$$

  With this mapping, three input spatial streams are directly mapped to the 1^{st}, 4^{th}, and 3^{rd} transmit antennas respectively whereas the 2^{nd} antenna is left unused.

- **Indirect mapping** All S_{SM} streams are somehow superimposed and sent concurrently through all M transmitter in this mapping. In order to correctly decouple these streams at the receiver, SM should be a square unitary matrix such as the Hadamard matrix [3]. According to [35], Intel 5300 NIC also applies the indirect mapping to the transmit OFDM signal. The following is the indirect SM matrix of Intel 5300 NIC provided by the CSI tool [24] when the Wi-Fi transmission is operated at 40 MHz bandwidth with three transmite antenna ($M = 3$),

$$\mathbf{Q}_{\text{indirect}} = \begin{bmatrix} e^{-\mathrm{j}2\pi(1/16)} & e^{-\mathrm{j}2\pi(80/13)} & e^{-\mathrm{j}2\pi(80/23)} \\ e^{-\mathrm{j}2\pi(80/37)} & e^{-\mathrm{j}2\pi(48/11)} & e^{-\mathrm{j}2\pi(240/107)} \\ e^{-\mathrm{j}2\pi(80/7)} & e^{-\mathrm{j}2\pi(240/83)} & e^{-\mathrm{j}2\pi(48/11)} \end{bmatrix} \tag{3.3}$$

- **Spatial expansion** This technique considers the direct and indirect mapping as the intermediate mapping. Spatial expansion further maps the S_{SM} spatial streams in to M transmit antenna such that $M > S_{\text{SM}}$ through the multiplication with the unitary matrix. the factor $\sqrt{S_{\text{SM}}/M}$ is applied to normalize the power spreading from asymmetry mapping. For example, considering the mapping from 1 spatial stream to 3 transmit antenna, the spatial expansion can be expressed as [35],

$$\mathbf{Q}_{\text{expand}} = \mathbf{Q}_{\{\text{direct,indirect}\}} \frac{1}{\sqrt{3}} \begin{bmatrix} 1 & 1 & 1 \end{bmatrix}^T \tag{3.4}$$

- **Beamforming steering matrix** Unlike other predetermined mapping technique, the element of the beamforming matrix is adjusted according to the channel condition estimated from the CSI at previous timestamp. Moreover, this mapping could be subcarrier frequency dependent in order to improve the transmission quality based on the estimated channel.

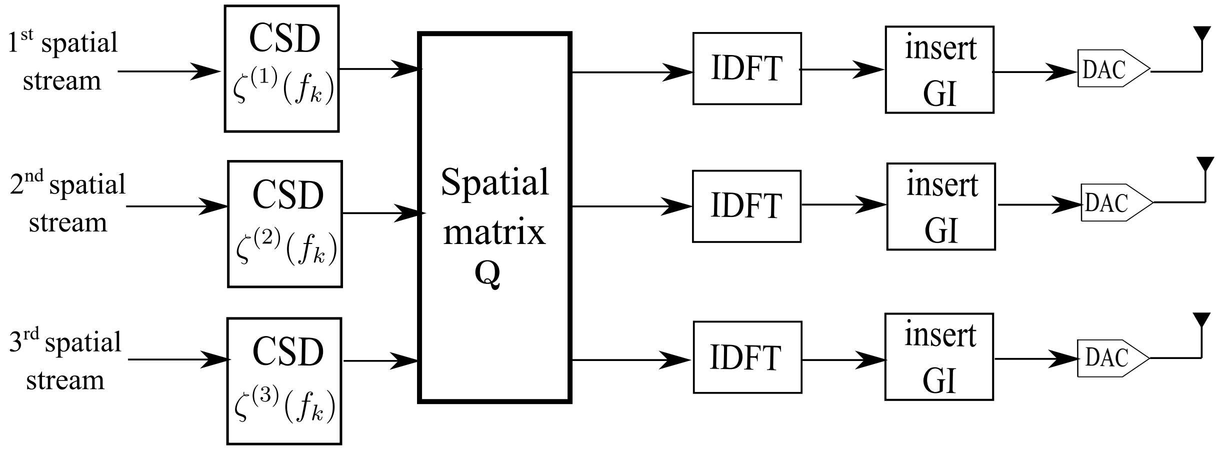

Figure 3.1: Partial Wi-Fi transmitter block diagram with 3 spatial streams being mapped by SM and CS according to IEEE 802.11n standard.

CSD is added in Wi-Fi communication to enable the spatial diversity. According to the standard, it is defined as a subcarrier-dependent diagonal matrix which can be given as

$$\boldsymbol{\zeta}_{\mathrm{CSD}}(f_k) = \begin{bmatrix} \zeta^{(1)}(f_k) & 0 & \cdots & 0 \\ 0 & \zeta^{(2)}(f_k) & \cdots & 0 \\ \vdots & \vdots & \ddots & 0 \\ 0 & 0 & \cdots & \zeta^{(i_{\mathrm{SM}})}(f_k) \end{bmatrix} \tag{3.5}$$

where each diagonal element of CSD is given by $\zeta^{(i_{\mathrm{SM}})}(f_k) = \exp\left(-\mathrm{j}2\pi k\Delta f \tau_{\mathrm{CSD}}^{(i_{\mathrm{SM}})}\right)$. In general, CSD rotates the spatial streams with different delay offsets $\tau_{\mathrm{CSD}}^{(i_{\mathrm{SM}})}$ which is given in [3] for Wi-Fi IEEE 802.11n standard. Consequently, this eases the receiver to distinguish incoming signal with multiple streams. As a result, the transmitted OFDM symbol can be written in terms of vector as,

$$\boldsymbol{X}(t, f_k) = \tilde{\boldsymbol{X}}(t, f_k)\mathbf{Q}\boldsymbol{\zeta}_{\mathrm{CSD}}(f_k) \tag{3.6}$$

In fact, the element of $\boldsymbol{X}(t, f_k)$ is the transmitted Wi-Fi signal from m-th transmitter $X_m(t, f_k)$ which has been described in eq. (2.1).

In IEEE 802.11n Wi-Fi standard, there are two procedures to obtain CSI depending on where CSI estimation is calculated which are called implicit and explicit methods. Suppose the CSI between transmitter and receiver with M and N antennas respectively is written in terms of channel matrix $\mathbf{H}(t, f_k)$ with $N \times M$ dimension. For consistency, the CSI model $H_{n,m}(t, f_k)$ addressed previously in eq. (2.1) is the element of this channel matrix. Considering a Wi-Fi communication scenario between ST1 and ST2 Wi-Fi transceiver. For the sake of explanation, let us assign m-th Wi-Fi transmitter and n-th Wi-Fi receiver to respresent ST1 and ST2 respectively.

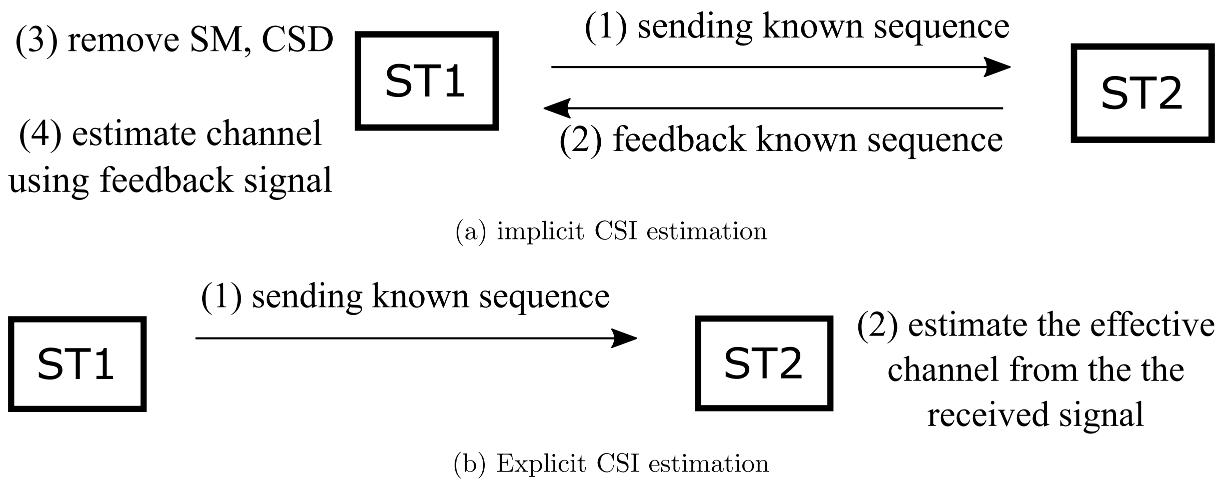

Figure 3.2: Diagram of Wi-Fi CSI estimation in 802.11n standard.

In the implicit method, the estimation of CSI matrix from ST1 to ST2 is calculated at ST1 by deriving its reverse channel based on a feedback signal sending from ST2 as depicted in Fig. 3.2a. The explicit method depicted in Fig. 3.2b estimates channel directly at the ST2 receiver. However, this method in practice cannot separate the SM matrix from CSI because the ST1 transmitter does not provide spatial mapping to the ST2 receiver. Additionally, it may not have removed CSD matrix from CSI despite having information of CSD defined in Wi-Fi standard. This type of CSI is called effective CSI [3, 35],

$$\mathbf{H}^{\text{eff}}(t, f_k) = \mathbf{H}(t, f_k)\mathbf{Q}\boldsymbol{\zeta}_{\text{CSD}}(f_k) \tag{3.7}$$

Note that the dimension of $\mathbf{H}^{\text{eff}}(t, f_k)$ is $N \times S_{\text{SM}}$ which clearly does not represent the wireless channel between a pair of antenna as described in eq. (2.2). For instance, an open-source Linux 802.11n CSI tool developed by [24] used the explicit method to capture the effective CSI per received Wi-Fi packet. Since the tool was applied in this work, our CSI calibration inevitably has to remove SM and CSD matrices aside from phase rotation in order to return the correct channel matrix $\mathbf{H}(t, f_k)$.

The phase component of CSI is the most significant feature for motion detection analysis. This is because when there is any motion, the set of signal that interacts with these dynamic IOs will physically experience change in their propagation paths. Specifically, $d_{n,m}^{(i),\text{TV}}(t)$ of the i-th propagation path in eq. (2.2b) keeps changing with time and therefore exhibited as a phase rotation in the measured CSI. Unfortunately, this phenomena could not be directly observed because it has been corrupted by the additional time-varying phase rotation $\psi(t, k)$ due to non-synchronized LOs. Here k is the subcarrier index. To visualize the effect of $\psi(t, k)$ on CSI phase, we connected two Wi-Fi stations with a cable and measured the back-to-back (b2b) channel of 30 subcarrier frequencies over 2000 snapshots. An attenuator was inserted in between to prevent damage to the Wi-Fi devices. In comparison, the channel without

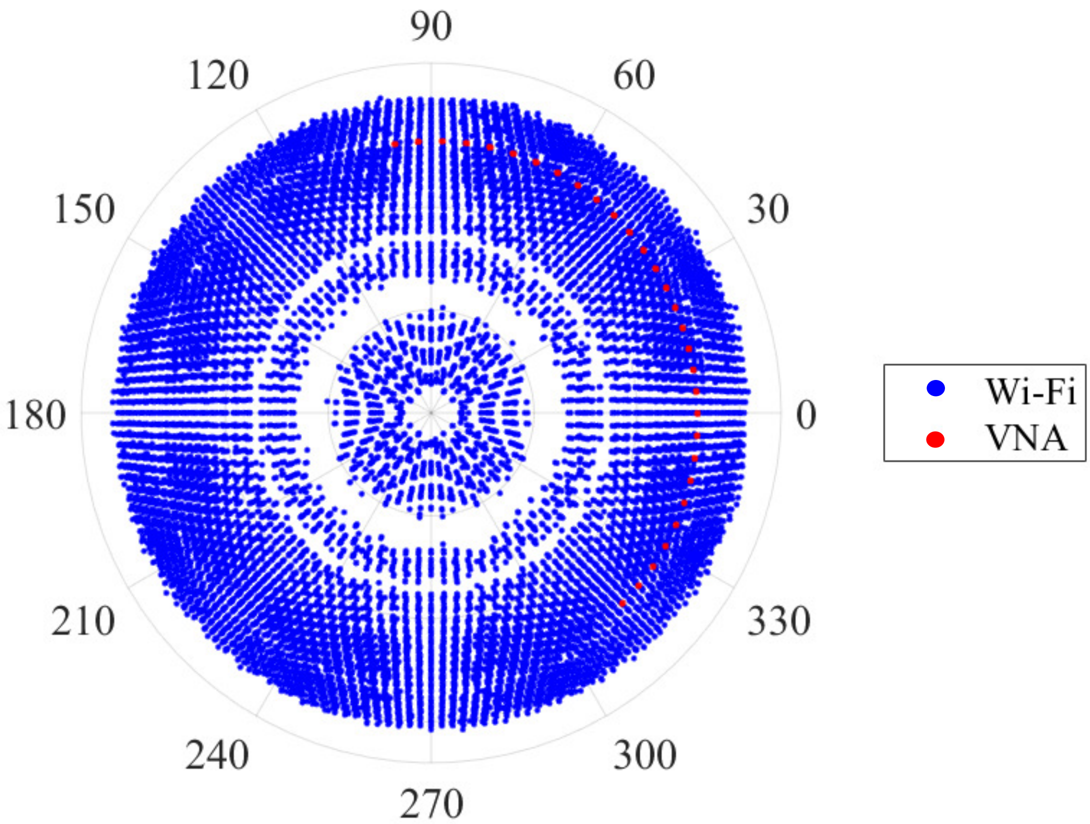

Figure 3.3: 2000 snapshots of the phase of Wi-Fi CSI (blue dots) and the phase of a channel measured by VNA (red dots) under the same b2b configuration plotted in polar coordinates.

phase rotation was measured using a VNA with the same configuration. Fig. 3.3 shows that Wi-Fi CSI phase (blue dot) appears to be spinning around the polar coordinate plane even in the static wired channel. In contrast, the channel measured using the VNA (red dot) has a relatively stable phase in all 30 frequencies with a constant phase shift between consecutive frequencies which seems to agree with eq. (2.2). Hence, it is a non-trivial task to mitigate the phase rotation term denoted as $\exp\left(-\mathrm{j}\psi(t,k)\right)$ in a measured Wi-Fi CSI before attempting any further motion analysis.

3.3 Source of Undesired Phase and The Effect to The Measured Doppler Frequency

The sources of phase rotation have been widely discussed throughout CSI phase related literature. There are at least four sources listed below that contribute to CSI phase information.

- **Carrier frequency offset (CFO)** [120, 2, 9, 25, 38, 108, 121] Although both Tx and

Rx operates in the same band during the communication, carrier frequency is generated from different local oscillators (LO) that are not ideal and therefore locally introduce an additional frequency shifting and varying to the desired carrier frequency over time. If their LOs are not perfectly synchronized, the received signal will be contaminated by the CFO which is the carrier frequency difference between Tx and Rx. In fact, OFDM is highly sensitive to CFO as it contributes to the inter-carrier interference (ICI). In CSI, the impact is consequently affected phase of all subcarrier equally in terms of the temporal phase offset $\psi_{\mathrm{C}}(t)$ as visualized in Fig. 3.4a.

- **Sampling frequency offset (SFO)** [2, 9, 25, 34, 38, 108, 122, 120] Similar to the CFO, both Tx and Rx use different ADC clocks which control the rate at which the signal is transmitted and received. These clocks are not ideal and will occasionally and separately introduce the temporal sampling drift. With this mismatch, a portion of OFDM signal in time domain observed by the Rx may not fall within the ideal Rx window. This effect contributes to the ICI the same as CFO. In the frequency domain, it distorts each subcarrier frequency differently at the phase term of CSI. Therefore, the characteristic of SFO can be represented by an additional phase rotation $\psi_{\mathrm{S}}(t)$ proportional to subcarrier index k as shown in Fig. 3.4b.

- **Packet boundary delay (PBD)** [2, 9, 25, 108, 121, 122, 123] After an OFDM packet which consists of a sequence of OFDM symbol passes through the ADC, the receiver must perform the symbol synchronization in order to correctly estimates the boundary of each OFDM packet out of the received transmission stream. As a sequence of OFDM symbol is orthogonally modulated at each subcarrier, the symbol synchronization attempts to search the packet boundary such that the orthogonality between consecutive symbols is preserved. Within the search interval restricted by guard interval, it is stated [2] that there exists multiple delay positions in this period where the synchronization can be yielded due to the shorter size of OFDM packet comparing to the search interval. Therefore, the received signal and thus CSI unavoidably suffer from the additional delay or PBD. This delay exhibits a similar effect to SFO in the frequency domain as another additional phase rotation $\psi_{\mathrm{P}}(t)$ proportional to subcarrier index as shown in Fig. 3.4b.

- **Phase-locked loop offset (PLO)** [9, 108, 121] When Wi-FI NIC is intiated, LO generates a random initial phase at the phase-locked loop circuit for generating a center frequency. The random phase offset for both Tx and RX are not the same because they each comes from different chips. The phase difference between them is referred as PLO. Similar to CFO, the impact contributes to the CSI such that the phase term is additionally leveled by a relatively constant phase offset ψ_{PLL} as shown in Fig. 3.4a.

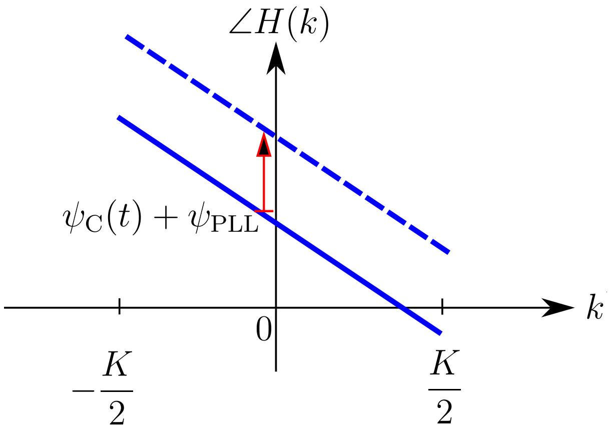

(a) Effect of CFO and PLO

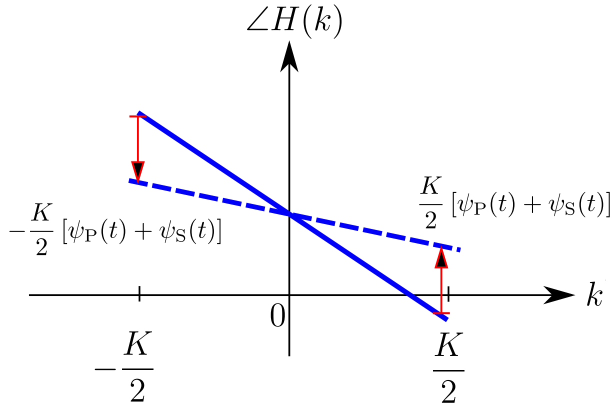

(b) Effect of SFO and PBD

Figure 3.4: Geometric representation of CSI phase with subcarriers before (solid line) and after (dash line) being shifted and rotated by phase offset sources according to [2]

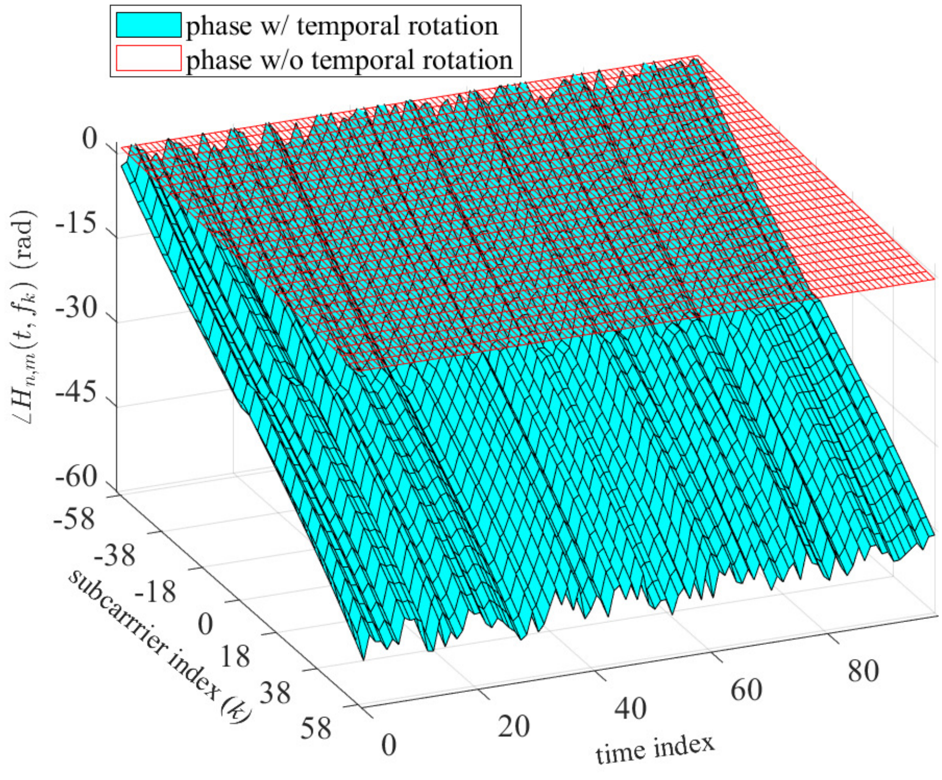

Figure 3.5: Effect of the temporal phase rotation to the CSI phase (cyan) in comparison with the original phase component (red).

The time-varying phase rotation $\psi(t,k)$ can be modeled as a summation of these four sources as follows.

$$\psi(t,k) = \left[\psi_{\mathrm{P}}(t) + \psi_{\mathrm{S}}(t)\right] k + \psi_{\mathrm{C}}(t) + \psi_{\mathrm{PLL}} \tag{3.8}$$

Fig. 3.5 visualizes the effect from the phase rotation's sources causing the time-varying shift and rotation of the CSI phase away from the channel without the phase rotation. Unfortunately, even though a model of $\psi(t,k)$ can be formed, it is a challenging task to filter out the rotations because we cannot directly obtain their parameters from the NIC. Hence, other indirect signal processing techniques are needed for calibration of CSI phase rotation. It is worth noting that, although NIC has implemented CFO and SFO correction, it may not be able to remove these rotations entirely [38, 108]. As clearly seen in Fig. 3.3, the result after correction would still be the residual phase rotation added to CSI phase.

To handle with this undesired phase rotation, various techniques have been introduce in literature. In general, their methods could be divided into three approaches in the followings.

- **Undesired phase mitigation with amplitude** One of the straightforward method is to utilize only the amplitude part of signal. As elaborated in [26], the influence of motion in terms of Doppler frequency is also manifested in the amplitude part. This can be explain by considering the CSI model described in eq. (2.2) contaminated by the undesired phase rotation $H_{n,m}(t,f_k)\exp\left(-\mathrm{j}\psi(t,k)\right)$. The model of CSI power in a noise-free condition can be given as,

$$\begin{aligned}\left|H_{n,m}(t,f_k)\right|^2 =& H_{n,m}(t,f_k)H^*_{n,m}(t,f_k)\\ =& \left[H^{\mathrm{TIV}}_{n,m}(f_k)\right]^2 + H^{\mathrm{TIV}*}_{n,m}(f_k)H^{\mathrm{TV}}_{n,m}(t,f_k)\\ &+ H^{\mathrm{TIV}}_{n,m}(f_k)H^{\mathrm{TV}*}_{n,m}(t,f_k) + \left[H^{\mathrm{TV}}_{n,m}(t,f_k)\right]^2\end{aligned} \tag{3.9}$$

  where $[\cdot]^*$ is the conjugate term. As clearly seen from the above equation that the effect of motion represented by TV-CSI still exists in the amplitude as the sinusoidal-like fluctuation where as the undesired phase rotation got cancelled out owing to its conjugation. However, since the amplitude is not an analytical signal, it only represents a magnitude of Doppler but not the sign which represents a relative 1D direction.

  Undesired phase mitigation with linear phase sanitization This is another well-implemented signal processing method [27, 34, 38, 39]. Basically, it assumes the slope and offset of the measured CSI phase are highly distorted by $\psi_{\mathrm{P}}(t) + \psi_{\mathrm{S}}(t)$ and $\psi_{\mathrm{C}}(t) + \psi_{\mathrm{PLL}}(t)$ respectively. By removing these linear variables, the residual should contains a temporal rotation signature of Doppler signature. The sanitized phase can be expressed by subtracting the overall slope β_{slope} and the mean from the measured

CSI as

$$\angle H_{n,m}^{\text{sani}}(t, f_k) = \angle H_{n,m}(t, f_k) - \left[k\beta_{\text{slope}} + \frac{1}{K} \sum_{k=-\frac{K}{2}}^{\frac{K}{2}} \angle H_{n,m}(t, f_k) \right] \tag{3.10}$$

The drawback of this approach is that the original phase rotation due to Doppler frequency shift is distorted. Nevertheless, this sanitized phase can be directly utilizing to detect a simple motion through the phase fluctuation. Some previous works such as [42] reconstructed the analytic CSI by simply combining the the sanitized phase with its amplitude. However, it is obvious that the analytic signal still suffer the distortion owing to the partial removal of CSI phase. To the best of our knowledge, there is no justification of what the sanitized phase physically represents. This is the reason why the sanitized phase-based application is quite limited and mostly case-dependent.

- **Undesired phase mitigation with the inter-antenna phase difference** The concept of this method stems from the assumption that both received antennas generated by the same Wi-Fi ship should experience the same undesired phase rotation. Theoretically, phase offset should be canceled out after taking the difference between two CSI data. This method, although, could filter out the majority of the offset, the remaining is not the original CSI phase but a relative phase difference between two antennas. Nevertheless, the output is relatively constant with time in a static scenario and varies strongly in the presence of motion as shown in [9, 33, 40, 41].

  Originally, this method is developed for the motion analysis with only CSI phase. However, the extension of this concept has been implemented in [54, 55] such that the analytic CSI can be directly utilized for motion analysis. The concept has a crude assumption that two antennas should be located nearby such that the they could experience the similar temporal multipath channel. By applying the cross-correlation between these pair of CSI, the undesired phase offset should be removed similar to the CSI amplitude approach.

$$\begin{aligned} H_{n,m}^{*}(t, f_k) H_{n+1,m}(t, f_k) &= H_{n,m}^{\text{TIV}\,*}(f_k) H_{n+1,m}^{\text{TIV}}(f_k) + H_{n,m}^{\text{TIV}\,*}(f_k) H_{n+1,m}^{\text{TV}}(t, f_k) \\ &+ H_{n,m}^{\text{TV}\,*}(t, f_k) H_{n+1,m}^{\text{TIV}}(f_k) + H_{n,m}^{\text{TV}\,*}(t, f_k) H_{n+1,m}^{\text{TV}}(t, f_k) \end{aligned} \tag{3.11}$$

  The cross correlation could preserve the Doppler frequency components located in the 4$^{\text{th}}$ term while the static component is contained in the 1$^{\text{st}}$ term. Unfortunately, similar to the WVD join-time Doppler analysis mentioned in section 2.3.3, the issue of this method is obviously the image of Doppler frequency owing to the cross terms generated by the 2$^{\text{nd}}$ and 3$^{\text{rd}}$ terms in the above equation. Another drawback is the ill-assumption regarding the position of a pair of antennas. A closer two antennas is, the higher antenna coupling effect they will experience which effectively distorted the quality of CSI. Therefore, it would be difficult that these two channels physically represents the same characteristic.

3.4 Novel Phase Rotation Calibration

Based on previous techniques, there is no such method that could mitigate the undesired phase rotation without sacrificing the original CSI phase. With this reason, the goal of our CSI calibration method is to virtually subdue phase rotation and thus maintain original CSI in both the amplitude and phase components.

3.4.1 CSI Calibration Model

The calibration should be able to analytically explain the effect of movement in a target CSI which is assumed to be the measured channel $H_{n,m}(t, f_k)$. Since it is infeasible to precisely acquire the parameters of phase rotation from NIC, the practical solution to remove them would be the normalization of the target CSI with a reference CSI that suffers the same rotations. Hence, it is argued that the ideal reference CSI for phase rotation removal should have the following properties. It should be a static channel which is independent from the target CSI, and both experience the same phase rotation which can be written as

$$H_{\mathrm{REF}}(t, f_k) = \left[\sum_{b=1}^{L_{\mathrm{B}}} \alpha^{(b)}(f_k) \exp\left(\frac{-\mathrm{j}2\pi}{\lambda_k} d^{(b)}\right)\right] \exp\big(-\mathrm{j}\psi(t, k)\big) \tag{3.12}$$

where L_{B} is a total number of path propagating in the reference channel. Subsequently, the calibrated CSI can be formulated as the CSI in eq. (2.2) being normalized by the transfer function of the reference channel,

$$\begin{aligned} H_{n,m}^{\mathrm{CAL}}(t, f_k) &= \frac{H_{n,m}(t, f_k)}{H_{\mathrm{REF}}(t, f_k)} \\ &= \frac{\sum_{j=1}^{L_{\mathrm{TIV}}} \alpha_{n,m}^{(j),\mathrm{TIV}}(f_k) \exp\left(\frac{-\mathrm{j}2\pi}{\lambda_k} d_{n,m}^{(j)\mathrm{TIV}}\right) + \sum_{i=1}^{L_{\mathrm{TV}}} \alpha_{n,m}^{(i),\mathrm{TV}}(t, f_k) \exp\left(\frac{-\mathrm{j}2\pi}{\lambda_k} d_{n,m}^{(i),\mathrm{TV}}(t)\right)}{\sum_{b=1}^{L_{\mathrm{B}}} \alpha_{\mathrm{b2b}}^{(b)}(f_k) \exp\left(\frac{-\mathrm{j}2\pi}{\lambda_k} d_{\mathrm{b2b}}^{(b)}\right)} \end{aligned} \tag{3.13}$$

This calibration, however, does not consider the effect of SM and CSD. In case of the effective CSI described by eq. (3.7), $\mathbf{Q}$ and $\boldsymbol{\zeta}^{i_{\mathrm{SM}}}(f_k)$ matrices must be separately detached prior to the calibration. In fact, the effect of CSD can be negligible for motion analysis because it only adds a constant phase due to the calibrated CSI although it will cause the

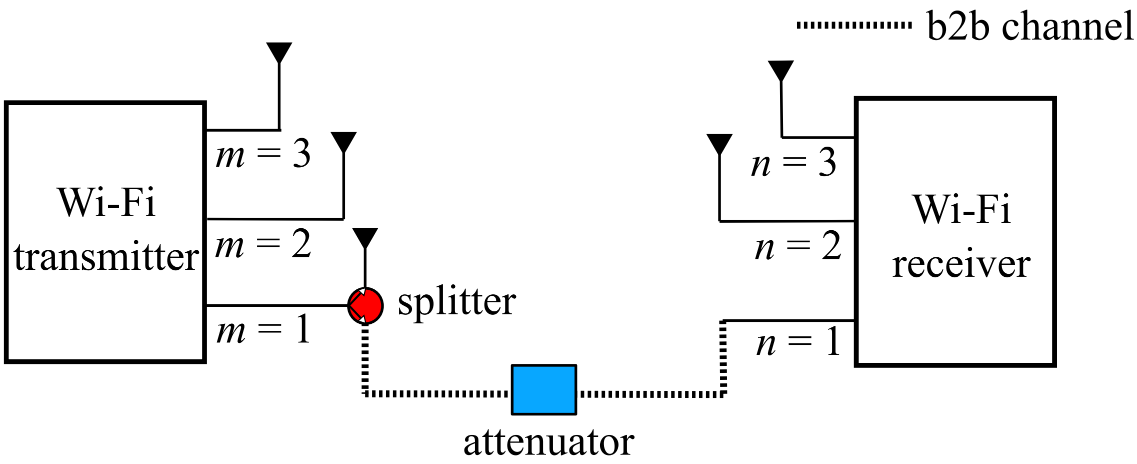

Figure 3.6: 3×3 MIMO configuration describing the implementation of the simplified CSI calibration technique in eq. (3.14)

delay offset in the channel impulse response. On the other hand, SM must unavoidably be removed beforehand if the transmitter does not use direct spatial mapping. This is because the m-th element of CSI does not represent the channel coming from a single transmit stream but the mixture between multiple streams.

Regarding the practical reference CSI for the implementation of our calibration method, the previous works of using CSI amplitude and the phase difference approaches also use the concept of reference CSI where the target CSI itself and the CSI measured from different antenna port are treated as the reference respectively. As it was mentioned in section 3.3, although both methods could remove the phase rotation, the partial or entire CSI phase is also inevitably removed because these reference channels are not independent from the target CSI. The CSI measured from a transmit antenna and the receive antenna located far away relative to the location of moving IOs could satisfy the condition of the reference CSI. Another candidate for the reference CSI could be the wireless channel whose environment is shielded by the RF absorber, thus resulting in the static and independent channel. Although these configurations may be feasible for our calibration conditions, we decided to apply the CSI obtained through the b2b channel as reference CSI because not only it fits all criteria stated previously, the propagation path of signal is also limited to a single path through the cable (0-th path) and consequently simplifies the reference CSI eq. (3.12). Moreover, we are able to practically calculate a constant phase shift due to path length $d_{\mathrm{b2b}}^{(0)}$ of the b2b channel. For the sake of explanation, this b2b connection is assigned to measure the channel corresponding to the channel coming from the 1$^{\mathrm{st}}$ Tx antenna port to the 1$^{\mathrm{st}}$ Rx antenna as depicted in Fig. 3.6. The RF splitter is introduced to allow the communication possible from the 1$^{\mathrm{st}}$ Tx antenna. Suppose SM and CSD matrices are already detached. The practical calibrated CSI in eq (3.13) can be simplified as below,

$$\begin{aligned} H'^{\mathrm{CAL}}_{n,m}(t,f_k) = &\sum_{j=1}^{L_{\mathrm{TIV}}} \frac{\alpha^{(j),\mathrm{TIV}}_{n,m}(f_k)}{\alpha^{(0)}_{\mathrm{b2b}}(f_k)} \exp\left(\frac{-\mathrm{j}2\pi}{\lambda_k}\left[d^{(j),\mathrm{TIV}}_{n,m} - d^{(0)}_{\mathrm{b2b}}\right]\right) \\ &+ \sum_{i=1}^{L_{\mathrm{TV}}} \frac{\alpha^{(i),\mathrm{TV}}_{n,m}(t,f_k)}{\alpha^{(0)}_{\mathrm{b2b}}(f_k)} \exp\left(\frac{-\mathrm{j}2\pi}{\lambda_k}\left[d^{(i),\mathrm{TV}}_{n,m}(t) - d^{(0)}_{\mathrm{b2b}}\right]\right) \end{aligned} \tag{3.14}$$

It is now clearly seen from the equation above that the calibration preserves CSI and removes the phase rotation term though with a constant scaling in amplitude and phase shifting by $\alpha^{(0)}_{\mathrm{b2b}}(f_k)$ and $d^{(0)}_{\mathrm{b2b}}$ respectively. However, these shift would not affect Doppler frequency since it produces the constant values.

In case of SIMO configuration ($M = 1$), both wireless and b2b channels will have the same SM and CSD matrices and thus automatically be canceled out together with the phase rotation during calibration. Therefore the calibrated CSI in this configuration, $H'^{\mathrm{CAL}}_{n,1}(t,f_k)$, does not need to remove those matrices separately.

3.5 Validation of The Calibrated CSI

This section explains the details of the experimental setting and phase rotation mitigation performance of the CSI calibration method explained in section 3.4. The capability to capture the bistatic Doppler frequency due to the motion of the calibrated CSI described in section 2.3 was also experimented by using short-time Fourier transform (STFT).

3.5.1 Measurement Setup

A testbed was implemented on commercial equipment. Two laptops equipped with Intel 5300 802.11n MIMO Wi-Fi NICs were used as Wi-Fi stations. Commercial Wi-Fi 6dBi-omnidirectional antennas operating in both 2.4 GHz and 5 GHz bands were externally connected to the Wi-Fi NICs through a coaxial cable with 0.77 velocity factor and U.FL-to-SMA adapter cables. A Mini-Circuits ZFSC-2-10G 2-way RF power splitter/combiner was applied at the first transmit antenna for dividing the signal into the b2b channel where a 40dB-attenuator was inserted at the cable connected to the first receive antenna. Fig. 3.7 shows the connection configuration and specific cable lengths. Linux 802.11n CSI tool developed by [24] was installed on both laptops that run Ubuntu version 12.04.1 to extract CSI from Wi-Fi packets. To control transmission parameters such as transmission rate and the number of active antennas, a Dell Latitude D530 laptop was set as the transmitter operating in the injection mode while an Acer Travelmate 5760 laptop was the receiver operating in the monitor mode. The distance between the first transmit antenna and the second receive antenna was 1 meter. In all measurements, 2,500 Wi-Fi packets were sent every second over the 5.31 GHz frequency band (Wi-Fi channel number 62) and 40 MHz bandwidth. Due to the CSI tool configuration, it only captures CSI with 30 subcarriers equally sampled every four subcarriers from a total of 114 which follows the CSI grouping number 4 according to standard [3] covering 36.25 MHz bandwidth.

For comparison, an E5071B VNA developed by Keysight Technologies (formerly known as Agilent's Electronic Measurement) was used as the standard for evaluating the performance of CSI after calibrating phase rotation. The S_{21} between ports S1 and S2 was assigned for the wireless channel while S_{31} was set to the b2b channel between ports S1 and S3. All physical connections are the same as those in the Wi-Fi configuration except for the absence of U.FL-to-SMA adapter cables and the use of a 20dB-attenuator as shown in Fig. 3.8. The reason a higher attenuation was used in Wi-Fi was to avoid the saturation of the received signal due to the vast difference of received signal strength between the b2b and wireless channels. Instead of sending 30 subcarriers, we set the VNA to sweep and equally transmit 30-tone frequencies over the same channel and bandwidth as Wi-Fi. A custom-made visual basic for applications (VBA) script was implemented inside the VNA to automatically measure the wireless channel and b2b channel every 4 ms under 70 kHz IFBW setting, the fastest sampling time the VNA can handle given this configuration. The script configured a bus trigger in the single mode for initiation and termination of each measurement. All channel information captured from both instruments were later processed in MATLAB

3.5.2 Evaluation of The Calibrated CSI

The performance of our calibration method is determined based on how close the calibrated CSI to channel measured using the VNA which represented the CSI without phase rotations. Although there is virtually no phase rotation in VNA, the calibration method was also applied on the channel measured from the VNA for a fair comparison. In this experiment, measurement was conducted in the room without people (static environment) using both instruments within a 10-s period, and was repeated three times for reproducibility of the calibration. Fig. 3.9a clearly depicted the effect of phase rotation in polar coordinate causing phase rotation similar to the b2b channel primarily tested in Fig. 3.3. After the CSI calibration was performed, CSI phase became indistinctly more stable as shown in Fig. 3.9b. The calibrated CSI has a similar trend to the VNA channel as depicted in Fig. 3.9c with distinguishable 30 clusters in polar coordinates corresponding to subcarrier frequencies separated by a comparably constant phase shift except for a few subcarriers with a high amplitude and phase variation. It was found that the distorted subcarriers are those located near the bandwidth boundary which have fairly smaller path gain relative to other subcarriers. According to the CSI tool developer, this distortion is unavoidable due to a filter function applied during channel estimation. Nevertheless, ignoring the distorted subcarriers, standard deviation of CSI phase is acceptably low at about 1.64° which is reasonably higher

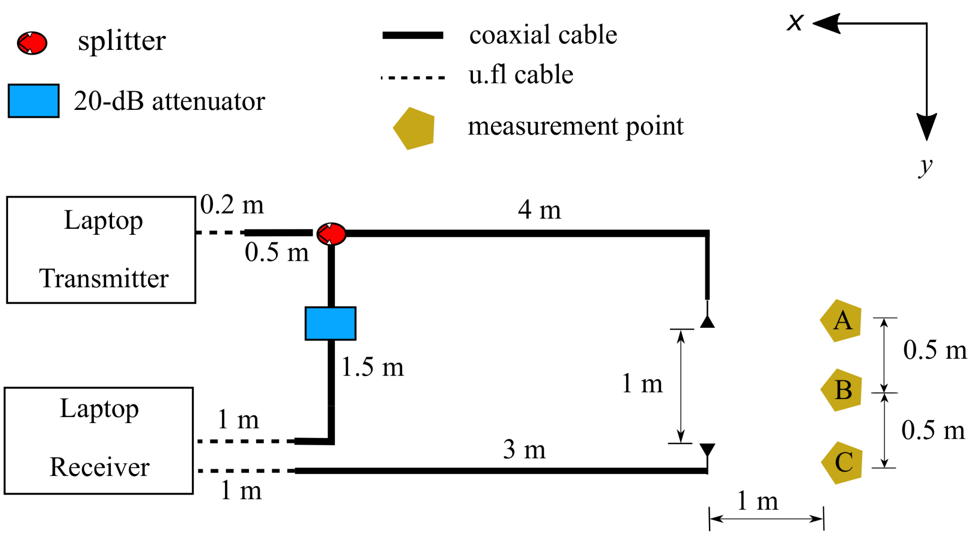

(a) Schematic configuration

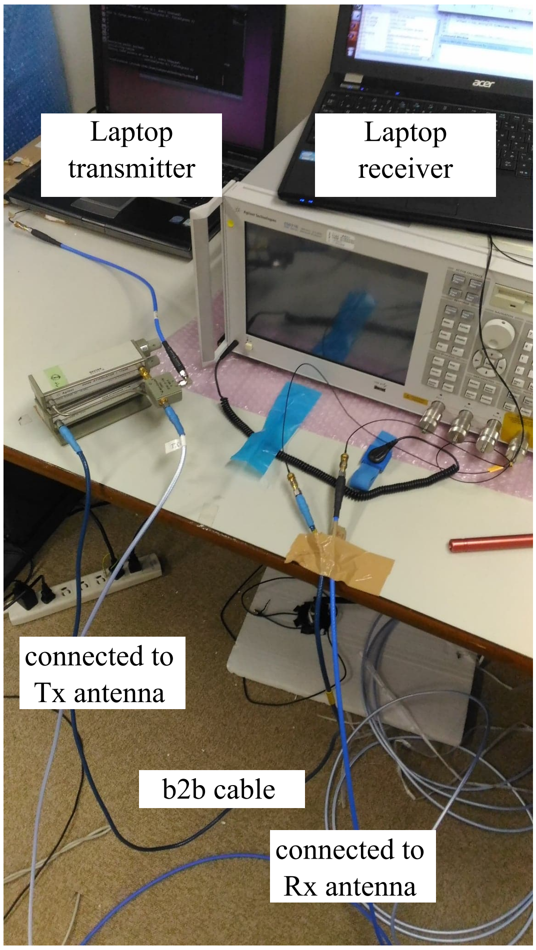

(b) Physical configuration

Figure 3.7: Wi-Fi measurement setup for b2b calibration

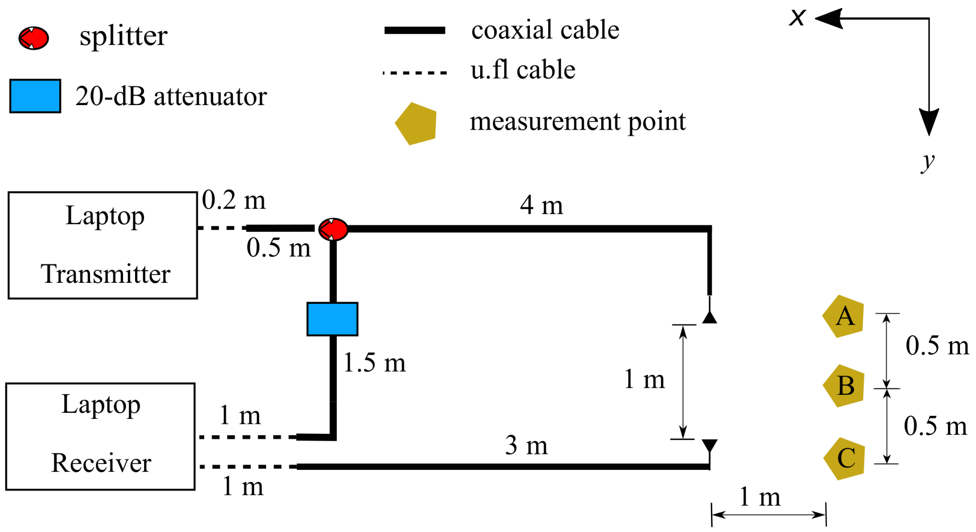

(a) Schematic

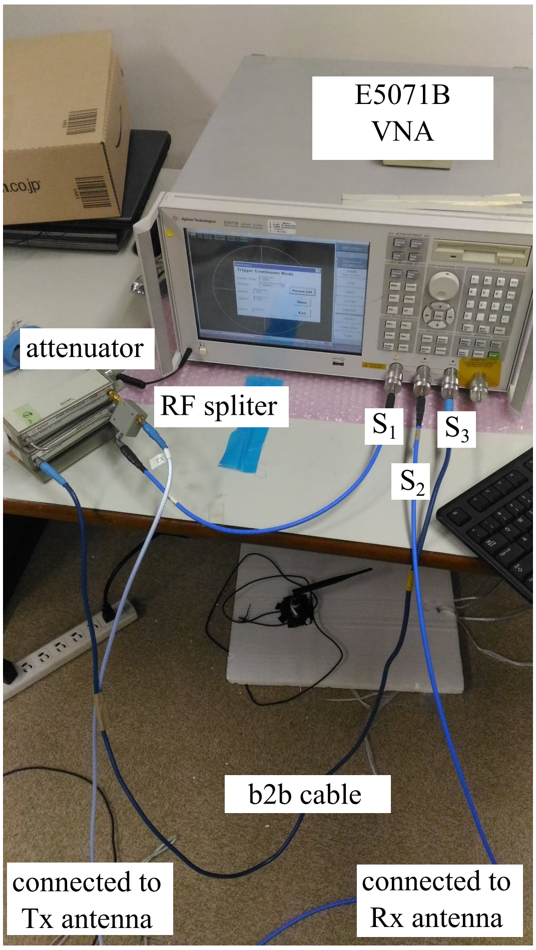

(b) Physical configuration

Figure 3.8: VNA measurement setup for b2b calibration

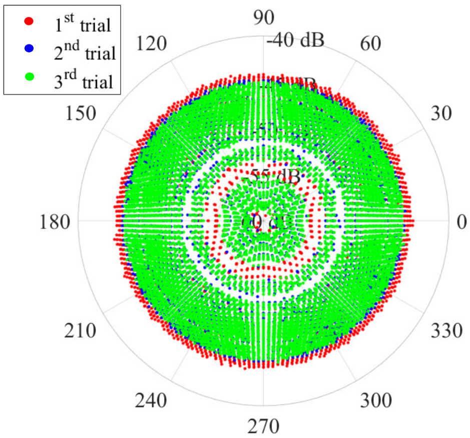

(a) CSI without calibration

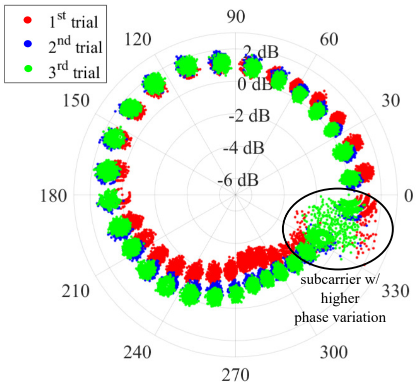

(b) Calibrated CSI

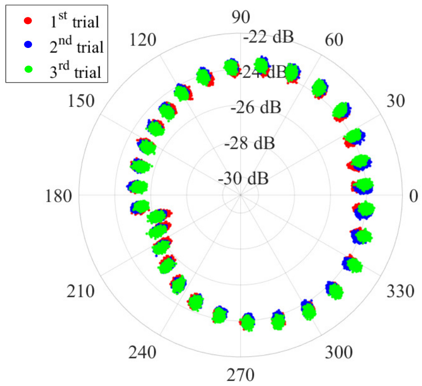

(c) Calibrated channel from VNA

Figure 3.9: Polar plot of Wi-Fi CSI before and after calibration in comparison with channel measured by VNA within a 10-second period.

than the variation in the calibrated channel by the VNA.

As it can be clearly observed in Fig. 3.9b that the calibrated CSI at all three measurements produced the similar trend, only the result from the 2nd measurement was illustrated in Fig. 3.10 to compare the performance of the calibrated CSI in a linear plot. In Fig. 3.10a, the measured CSI phase in a black line with circle markers became unstable owing to the phase drifting away from the channel measured by the VNA depicted as the solid line with triangle markers. The effect of phase rotation and shift could also be explained by the instantaneous phase rotation model introduced in Equation (3.8). Besides the similarity of the calibrated CSI with the result by the VNA depicted as a black line with circle markers and a magenta line with small triangle markers respectively in Fig. 3.10b, it also showed a constant phase offset around 3 radians relative to the calibrated channel measured by the VNA at all frequencies. After investigation, it was heuristically found that the additional offset was constantly changed every time the receiver was initialized. Hence we suspected

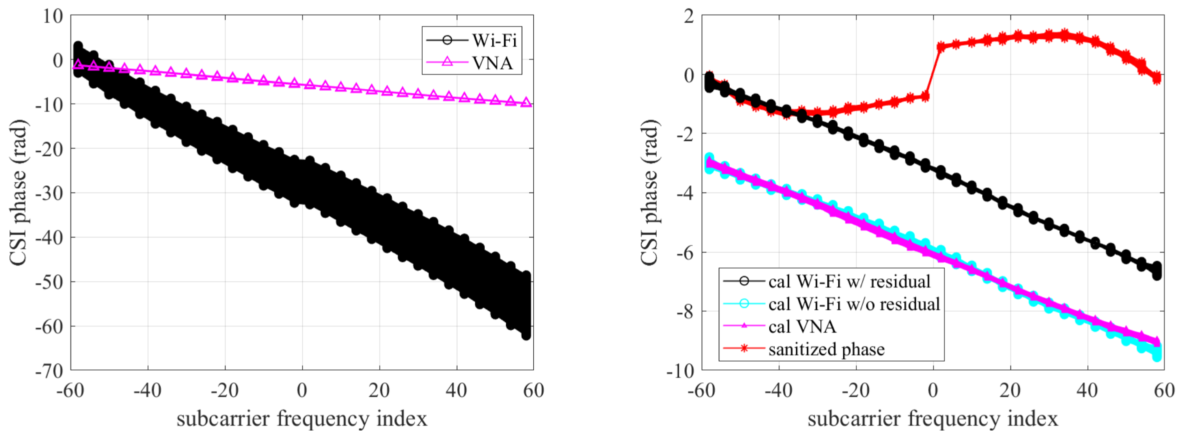

(a) Channel phase before calibration

(b) Channel phase after calibration

Figure 3.10: Comparison of phase of the calibrated CSI to the calibrated channel measured from VNA and phase sanitization method before and after calibration.

that the residual PLO would be the cause of preventing the alignment with the absolute phase without calibrating all the channels. For the fair comparison, it is necessary to remove the residual offset from the calibrated CSI. As the residual offset is constant, we could be able to statistically calculate this offset by averaging the difference between the calibrated CSI and the ones from VNA. The calibrated CSI after removing the residual offset shown as a cyan line with circle markers in Fig. 3.10b has virtually identical to the ones by the VNA at all frequencies with sightly small RMSE of 0.114, 0.123 and 0.116 radians which correspond to 6.50°, 7.04°, 6.62° for three measurements respectively. By comparison with the existing methods [27, 34, 38, 39], the result of CSI after applying the phase sanitization approach was plotted as the red line with asterisk markers in Fig. 3.10b. The sanitized phase obviously had a totally different phase pattern to the result measured using the VNA because the sanitation removed the part of CSI phase together with the phase rotation.

As it seems phase rotations are almost convincingly removed except for the residual PLO, it would be possible to compare the power delay profiles (PDP) of CSI which is simply the magnitude squared of channel impulse response. The Hanning window was multiplied with the channel before transformation to suppress the effect of the distorted subcarriers as well as the side lobes. As depicted in Fig. 3.11, both PDPs of calibrated CSI and the ones from VNA have a single-peak PDP which is due to the narrowband channel, and the similarity between two profiles can be seen with clarity. It should be noted that the small peak in VNA is in fact the sidelobe residual. Due to calibration, the power level of both profiles is the relative power with respect to the power of the b2b channel. In this case, the relative power offset between Wi-Fi and VNA is around 24 dB. As a result, this indicates the possibility of using the calibrated CSI for motion analysis at each delay bin separately from the channel impulse

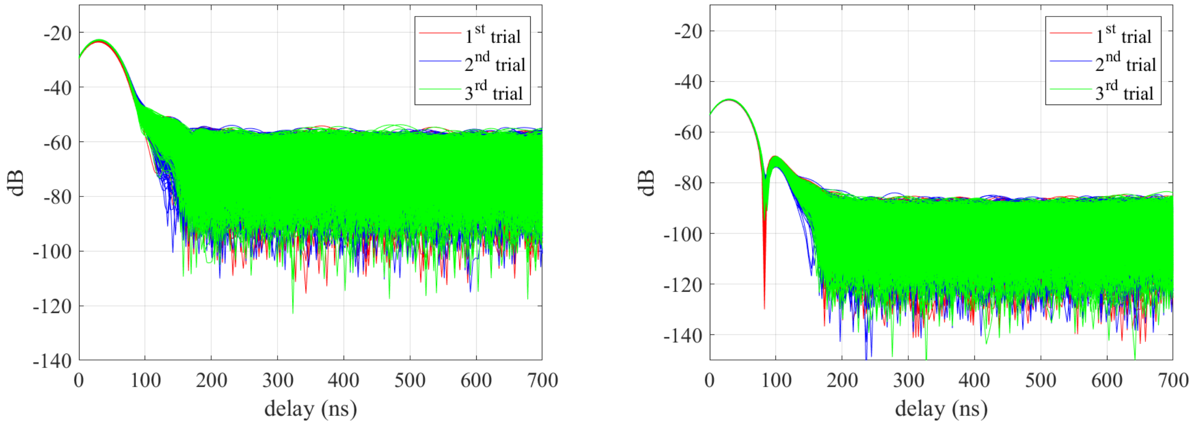

(a) PDP of calibrated CSI (b) PDP of calibrated VNA channel

Figure 3.11: Power delay profile of calibrated CSI and calibrated VNA channel.

response. Although the LoS path (the strongest path) is only 1 meter which corresponds to the propagation delay of around 3.3 ns, the LoS peak is located at the 30 ns in both profiles because the propagation path in the cable ($d^{(0)}_{\mathrm{b2b}}$) was not taken into account in these PDP.

3.6 Validation of The Doppler Power Spectrum Obtained from The Calibrated CSI

3.6.1 Measurement Setup

In this experiment, simple hand gestures were used for motion detection analysis performed at three marked points depicted in Fig. 3.12 while CSI was continuously estimated at the Wi-Fi receiver for 10 s in the room without other people. Before measurement began, a person stood facing in the $+x$ direction and raised his hand up to the same level as the transmitter and receiver. During the measurement, his right hand was moved horizontally towards the $+y$-direction for about 60 cm. After pausing for 2 s, his hand was pulled back ($-y$ direction) to the original position as depicted in Fig. 3.12. These gestures were performed twice in the single measurement. For analysis of bistatic Doppler, the time-varying channel impulse response at the delay bin with the highest power was chosen in this scenario. This is because both reflected path's signal from the moving hand and the LoS path were within the same delay bin. Therefore, by limiting our analysis to only this single delay bin, we are effectively focusing only on the LoS path and the strong reflected path from the hand, thus the Doppler frequency should be more easily observed. STFT explained in sec. 2.3.3 was applied to observe the joint time-Doppler spectrum. Gaussian window with standard deviation of 32

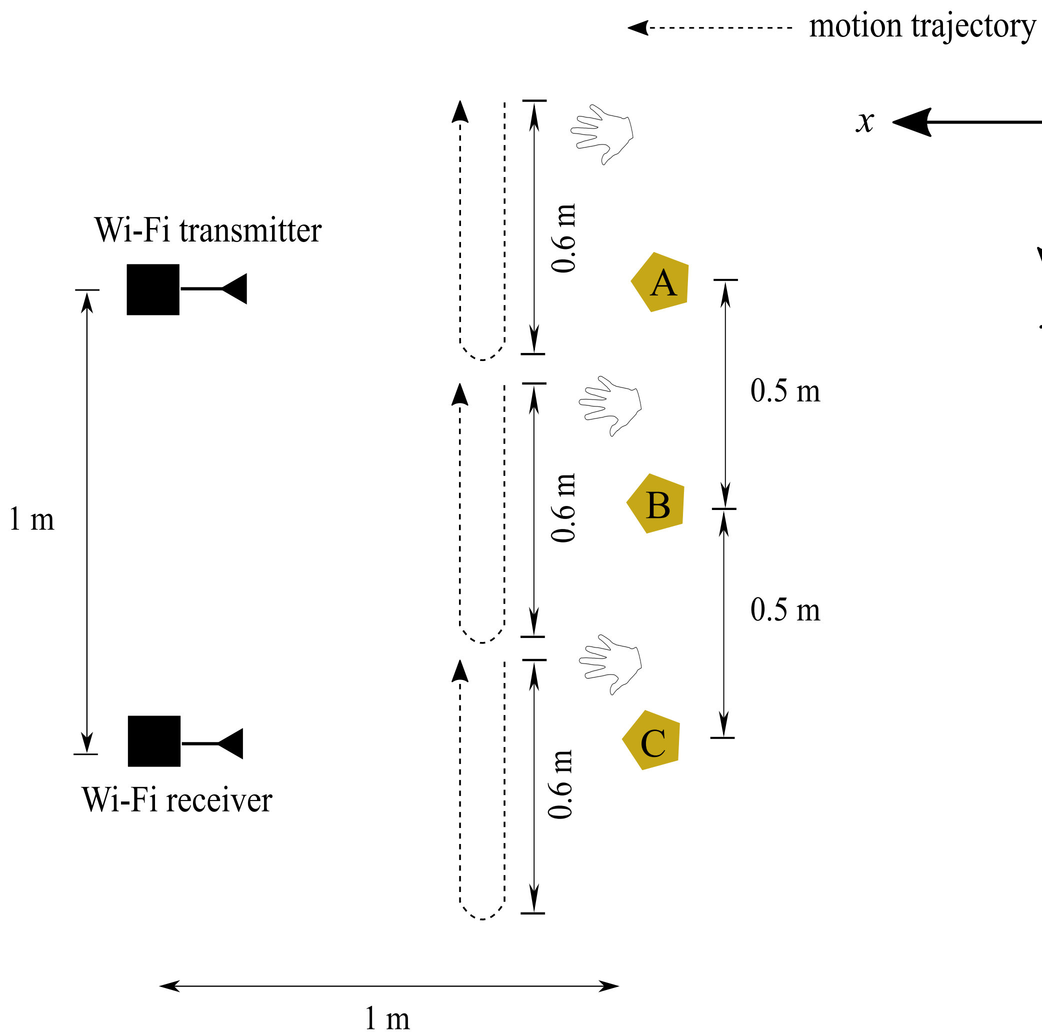

Figure 3.12: Experiment scenarios of hand motion detection at point A, B, and C.

ms was applied to increase the Doppler resolution and mitigated the sidelobe.

3.6.2 Result of Doppler Spectrum with The Calibrated CSI

The measurement was repeated six times at each marked point for reproducibility. Since the results at the same point are similar, one of the measurements at positions A, B, and C were illustrated in Fig. 3.13. It revealed the effect of motion where a stronger Doppler power spectrum represents bistatic Doppler frequency. In all cases, bistatic Doppler has a bell-shaped profile with a duration of around half a second on average. These gestures were similar to a speed profile of a wrist when handwriting as [124]. The highest bistatic Doppler frequency is about 60 Hz or roughly 1.7 m/s without factoring direction of the angles in bistatic Doppler equations, $\cos\theta_m(t) + \cos\theta_n(t)$, described in eq. (2.8). Although we were not able to calculate a precise motion trajectory in this measurement, these figures can tell the relative direction from the sign of bistatic Doppler. For instance, Doppler frequency at

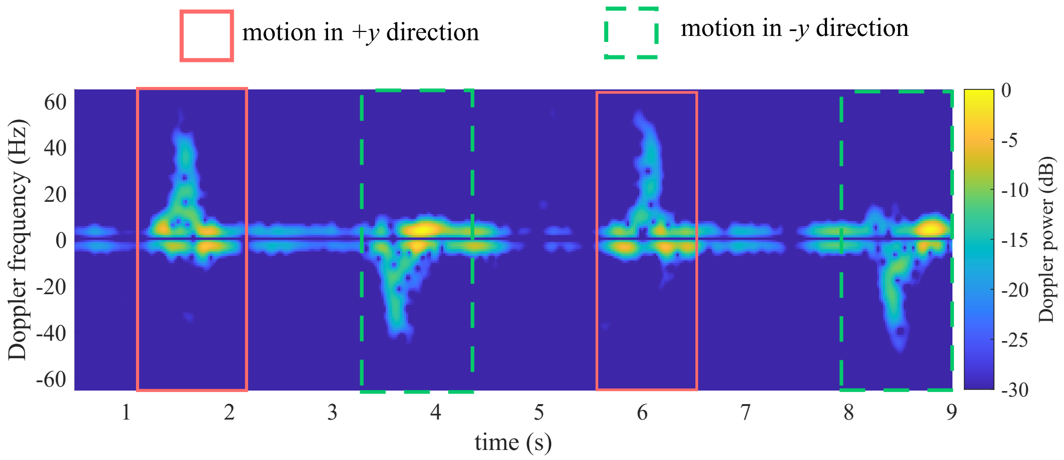

(a) Motion at position A

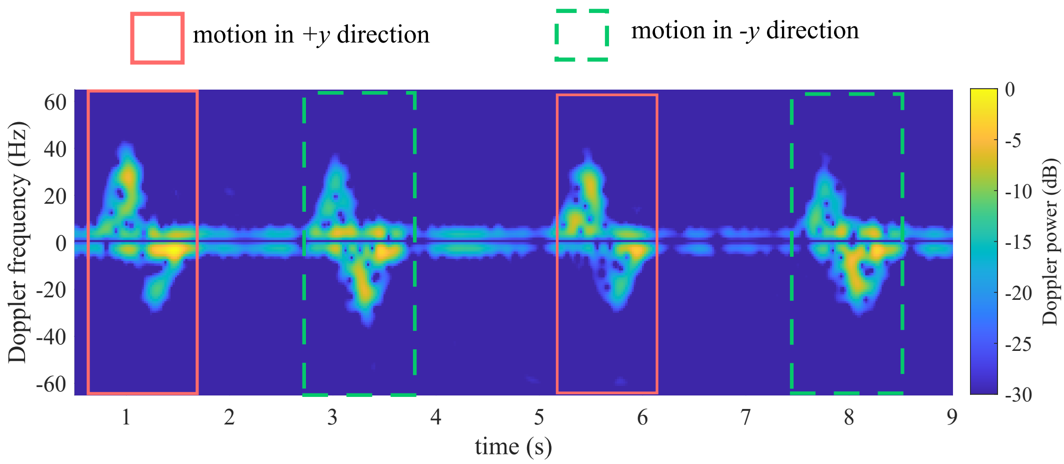

(b) Motion at position B

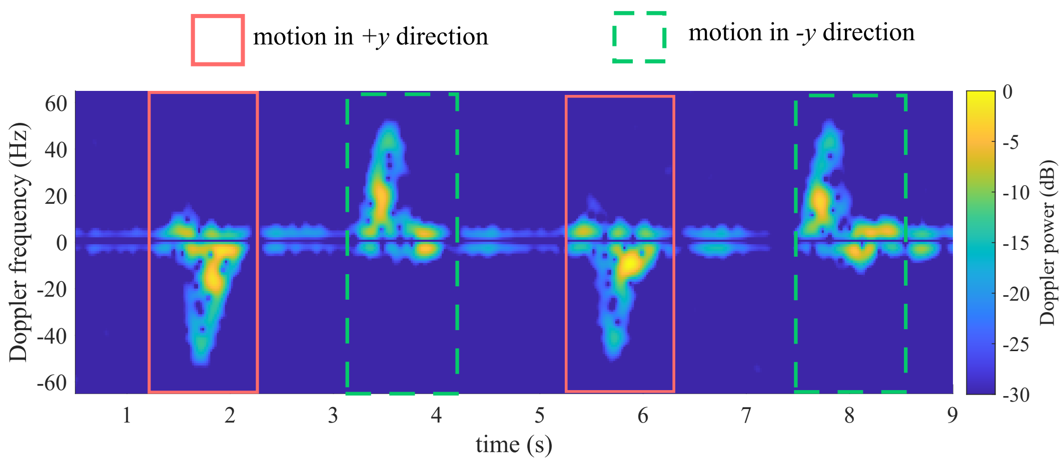

(c) Motion at position C

Figure 3.13: Bistatic Doppler spectrum produced by hand gestures at three different locations in terms of joint time-Doppler power spectrum of the calibrated CSI measurement.

point A had the positive sign when the hand was moving towards the $+y$ direction and a negative sign when moving in the $-y$ direction as shown in Fig. 3.13a because the direction factor $\cos\theta_m(t) + \cos\theta_n(t)$ is less than and higher than 90° respectively. Doppler sign was opposite at point C as shown in Fig. 3.13b where it was negative in the $+y$ direction and vice versa, and this can be explained $\cos\theta_m(t) + \cos\theta_n(t)$ with the same manner. This effect also explained a sudden change of Doppler sign within a single gesture at point B as shown in Fig. 3.13c from positive to negative in both $+y$ direction and $-y$ direction. Moreover, at point B, the magnitude of Doppler is comparatively smaller than others because of $\cos\theta_m(t) + \cos\theta_n(t) \to 0$ in this measurement.

This result could qualitatively confirm that the use of bistatic Doppler for motion analysis can be successfully achieved with calibrated CSI. Moreover, fine-grained or micro-motion detection can be used this calibration model as a basis for further investigation which will be applied for motion tracking in chapter 6. Although calibrated CSI does not remove the constant phase offsets from the residual PLO, it should not have any impact for motion analysis because any constant value will be added to zero Doppler frequency component during transformation. By comparison with related works, it would be difficult to produce correctly the Doppler frequency profiles as depicted in Fig. 3.13 for the result from the phase sanitization and the phase difference approach because they do not have the original phase information. Using only CSI amplitude may still able to analyze motion but has the limitation to observe the relative direction of motions from the sign of bistatic Doppler frequency.

Moreover, the spectrum result also confirmed that the uniqueness of Doppler signatures is not preserved when the gesture is performed at different position relative to the Tx and Rx. For instance, the hand swiping in $+y$ and $-y$ direction returned the opposite sign if the gesture is performed at point A and C as shown in Figs. 3.13a and Figs. 3.13c respectively. Even worst, swiping directivity is virtually impossible to determine at position B since the Doppler signatures are similar among 4 motion segments as clearly depicted in Figs. 3.13b. Regarding the micro-Doppler effect due to the non-rigid body motion elaborately described in section 2.3.3, it can be evidently observed in terms of the spectrum spreading in these figures.

3.7 Summary

This chapter first described the significance of spatial mapping and cyclic shift diversity to the additional shift of CSI phase which needs to be removed before further analysis. Secondly, a CSI calibration method was introduced to virtually remove time-varying phase rotation while preserving original phase information. The proposed technique uses a so-called reference CSI, a time-invariant channel that experiences the same phase rotation as the target

CSI. Practically, a back-to-back channel representing a wired channel in the cable between transmit and receive antenna ports was selected as the reference CSI. Bistatic Doppler radar model was employed to describe the effect of motion as Doppler frequency in CSI.

An experiment was conducted to validate the performance of our method by comparing with a channel measured by a VNA. The result showed that phase rotation was mitigated according to our propose CSI calibration model and portrayed a similar pattern but with a higher phase variation than the channel from the VNA. Although a constant phase offset possibly due to the residual of the PLO still existed after calibration, it should have small significant for CSI-based motion analysis as any constant would result in zero Doppler frequency. For a fair validation, we statistically removed the constant phase offset from the calibrated CSI. Promisingly, the data produced high correlation to the result measured using the VNA with approximately 0.117 radians RMSE phase error.

Another experiment was carried out to observe the effect of hand waving on the calibrated CSI at three different locations. The movement profile was visualized in the time-Doppler domain after the CSI was Fourier transformed. A bell-shaped pattern of Doppler frequency caused by the hand gesture was observed where the sign of Doppler which indicates the motion direction was correctly predicted according to the bistatic Doppler model. The micro-Doppler effect during hand gesture was visibly observed in the spectrum. The thorough analysis of micro-Doppler effect for the non-rigid body motion of hand movement will be carried out in chapter 5. Doppler signature performed at different position also strongly confirmed that the Doppler characteristic is location-dependent. This impact evidently shows that Wi-Fi based hand gesture recognition will have their performance varied on the position where gesture is being performed.

To the best of our knowledge, this CSI calibration model is the first solution to practically obtain Wi-Fi CSI without phase offset and thus allowing full use of the Wi-Fi channel for further in-depth CSI-based motion analysis. In fact, this calibrated model will be used as basis for motion tracking analysis that will be covered in chapter 6

Chapter 4

Simulated Time-Variant CSI Model of Hand Gesture

4.1 Introduction

As shown in chapter 3, the micro-Doppler effect of hand gesture does not only depend on the movement direction of non-rigid body but also location where the gesture is performed. Predicting the micro-Doppler characteristic may need a bunch of measurement data to accurately construct the stochastic model given plenty of variables. In comparison, the deterministic model based prediction could be more comprehensible since the physics of hand gesture kinematic and the micro-Doppler effect have been well-established in the field of biomechanic and electromagnetic scattering theory respectively. In fact, as mentioned in [51], the deterministic approach has been widely utilized in the study of micro-Doppler effect.

In the first step to detect the hand Doppler signature for hand motion tracking with Wi-Fi channel, the study in this chapter focuses on the development of the simulated CSI model based on the deterministic motion of human limb. Specifically, the robot arm model is utilized to simulate the non-rigid body motion characteristic of the human limb. In order to generate the time-variant characteristic of CSI induced by the motion of hand gesture, the electromagnetic (EM) scattering wave theory has been utilized. In particular, physical optics (PO) approximation techniques [83] is chosen for the computation of scattering wave. The modified PO based on circular mesh has been explored and validated as the practical usage in the analysis of EM scattering wave in dynamic environment. Finally, with the incorporation between the human limb model and the modified PO, the simulated CSI model of for hand gesture can be computed. The overall procedure is summarized in Fig. 4.1. Last but not least, the applicability of the simulated CSI model will be validated with the measurement CSI in terms of micro-Doppler effect prediction.

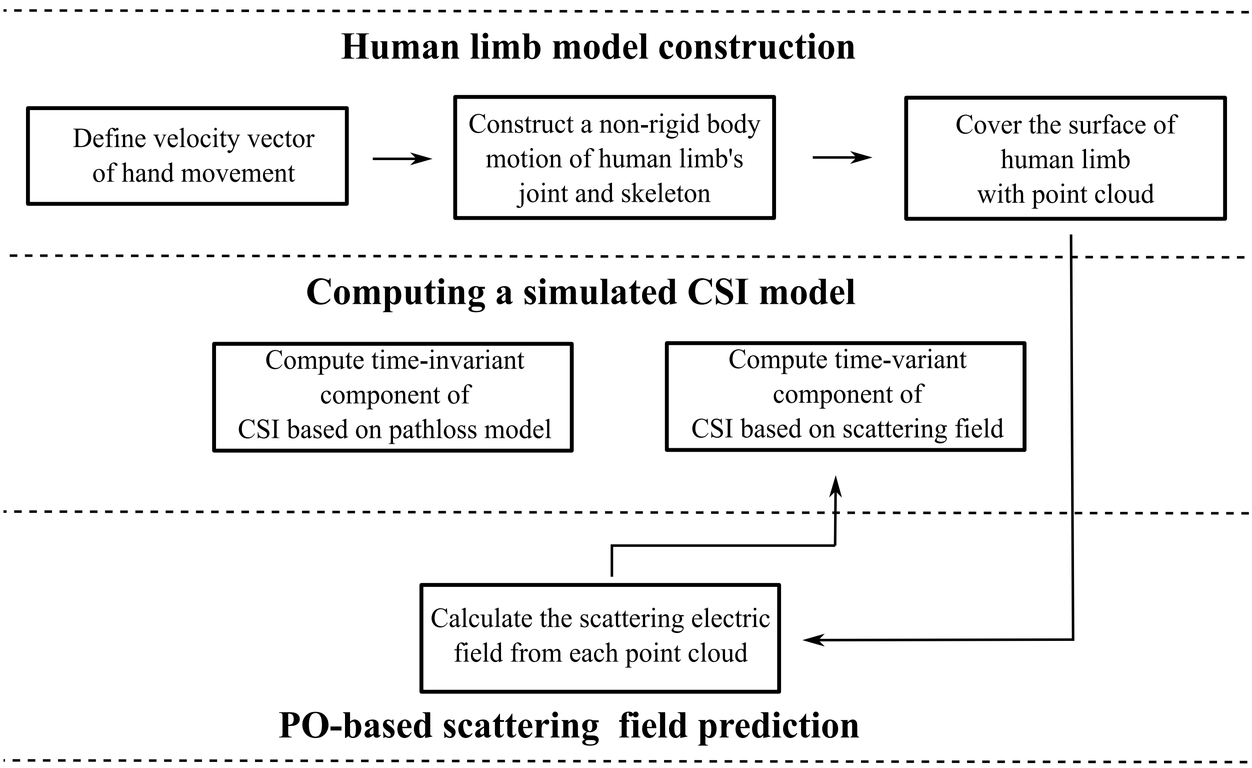

Figure 4.1: Construction flowchart of the simulated CSI model with hand gesture.

4.2 Human Limb Model of Hand Gesture

The construction of human limb model consists of three procedures as shown in Fig. 4.1. First of all, the movement characteristic of rapid hand gesture has to be defined in terms of 3D-vector velocity profile which will be covered in section 4.2.1. Based on this motion vector, we can easily derive a reference position at each timestamp of the entire hand movement. Secondly, by utilizing the robot arm model which will be explained in section. 4.2.2 together with the knowledge of the reference position, the skeleton motion of human limb can be computed in terms of position vectors. Finally in section. 4.2.3, the surface points of simplified human limb are constructed at each timestamp which is represented by four geometrical shapes. The usage of surface points will then be applied to calculate a deterministic time-variant CSI component by using PO approximation which will be discussed in section 4.4.

4.2.1 Velocity Profile of Hand Gesture

The analysis of hand movement has been widely investigated in various fields including bio-mechanics and robotics. In general, any movement can be loosely classified into either intention or spontaneous movement [78, 79]. Hand gesture motion is one of the former class since its trajectory should be intentionally predetermined. When we complete a particular gesture, for example, the latter class of motion unintentionally takes control to move our hand back to the natural position. This in fact could be regarded as a habitual motion according to the literature.

Considering a simple goal-directed motion with a straight trajectory from one position to another, the corresponding speed usually exhibits a bell-shaped profile of ballistic motion [78, 81, 124]. This temporal speed pattern of a rapid hand movement has been firstly modeled and verified under a controlled environment in [81]. Later on, comparative experiments have been conducted in [124, 125] using equipped sensors. Their results have suggested that a speed profile hand and wrist likely follow either Gaussian or Log-Gaussian function.

As clearly observed in [78, 126], the speed profile of any hand gesture can be decomposed into a short sequence of the bell-shaped profile. Suppose each motion segment of a particular gesture has a pattern of Gaussian, the boundary of the segment has to be defined because Gaussian itself is an unbounded function. In this work, the Gaussian finite window is heuristically identified based on the extreme speed the human hand can performed. The study in [79] investigated the rapid arm movement in the extreme case where the healthy adults have to quickly raise their arm to protect their head and body from the approaching object. Through their measurement with many subjects, it was found that the peak of speed profiles were around 3 m/s. Suppose the minimum detectable speed is 0.01 cm/s, the finite window can be heuristically defined within ± 3 times the Gaussian standard deviation. Accordingly, the overall velocity profile at time t can be represented by,

$$\boldsymbol{v}(t) = \begin{cases} v_{\max,u} \exp\left(-\dfrac{\left(t - (t_u + 0.5T_u)\right)^2}{2\left(T_u/6\right)^2}\right)\hat{\boldsymbol{v}} & ; \quad t_u \leq t \leq t_u + T_u \\ 0 & ; \quad \text{otherwise} \end{cases} \tag{4.1}$$

where $\hat{\boldsymbol{v}}$, T_u and t_u are given 3D unit vector of the motion followed by a period and a starting time of u-th motion segment respectively. With the defined Gaussian speed profile, standard deviation and mean of Gaussian function are equivalent to $0.5T_u$ and $\frac{T_u}{6}$ respectively. Suppose a desired distance for u-th motion segment is given by $D_{\mathrm{seg},u}$, the maximum speed can be defined as,

$$v_{\max,u} = \frac{D_{\mathrm{seg},u}}{T_u\sqrt{2\pi}} \tag{4.2}$$

This formula is derived using the integral form of Gaussian function. The velocity profile in eq. (4.1) will be applied as the basis movement of simulated hand gesture model.

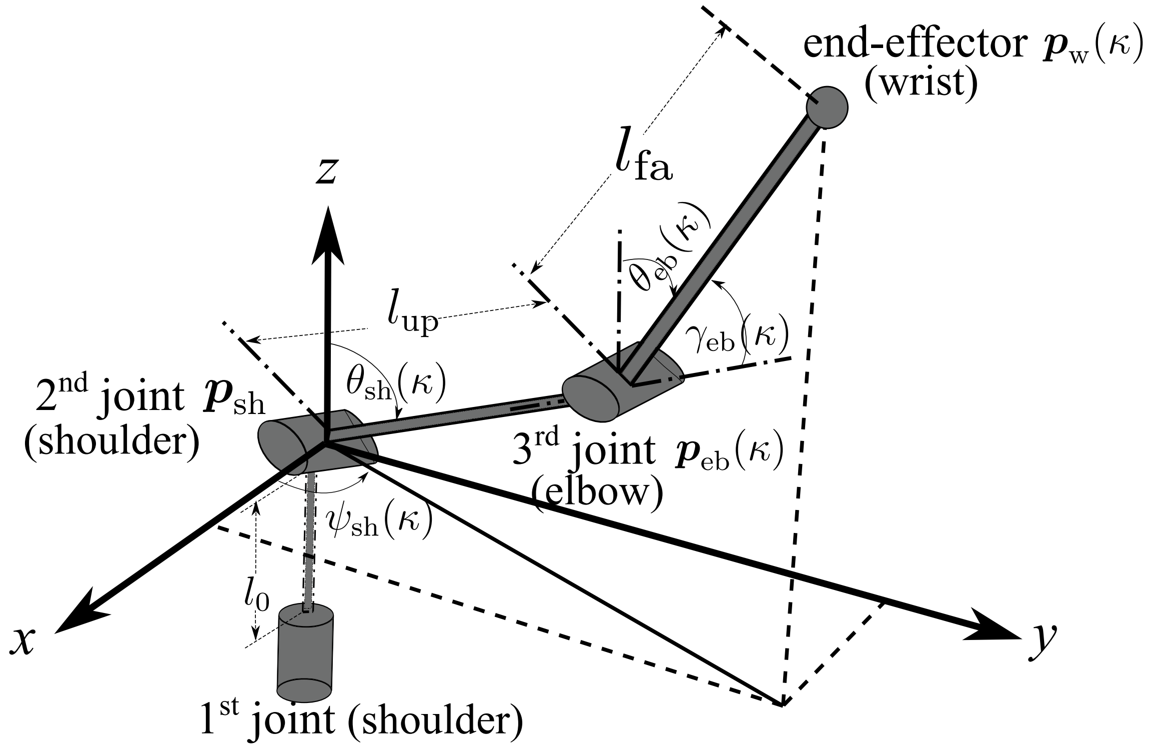

Figure 4.2: 6R-PUMA Robot arm for human limb modelling.

4.2.2 Non-Rigid Movement of Human Limb

Due to the deformation property, a movement of human limp while performing hand gesture is categorized as a non-rigid body motion [51]. Generally, human limb structure consists of three joints located at wrist, elbow, and shoulder. The incorporation between these joints then governs the position and orientation of hand, forearm, and upperarm segments. In other word, any location on the limb surface at a given time can be easily determined once joints' kinematic properties are acquired. Since the model is constructed in the discrete time, let us define κ as a time index such that $t = \kappa T_{\mathrm{s}}$ where t and T_{s} are a continuous time and time sampling respectively. considering a scenario of hand gesture in 3D space where a particular vector $\boldsymbol{p}_{(\cdot)}(\kappa) = \begin{bmatrix} p_{(\cdot)_x}(\kappa) & p_{(\cdot)_y}(\kappa) & p_{(\cdot)_z}(\kappa) \end{bmatrix}^T$ represents a position in Cartesian coordinates where the subscript denotes either human limb segment or joint. Suppose an orientation of hand segment and a position of shoulder $\boldsymbol{p}_{\mathrm{sh}}$ are fixed. A predetermined trajectory can be recursively determined as,

$$\boldsymbol{p}_{\mathrm{w}}(\kappa + 1) = \boldsymbol{p}_{\mathrm{w}}(\kappa) + \boldsymbol{v}_{\mathrm{w}}(\kappa) T_{\mathrm{s}} \tag{4.3}$$

where $\boldsymbol{p}_{\mathrm{w}}(\kappa)$ is a temporal position of wrist and a time difference between two consecutive timestamps respectively. With this definition, the reference position of the non-rigid body motion of human is the wrist position which also know as the end-effector of the robot arm. Therefore the wrist's velocity profile $\boldsymbol{v}_{\mathrm{w}}(\kappa)$ could be determined from eq. (4.1). In addition, as stated in [127], it is possible to describe a length of limb segment in terms of human height. Suppose a particular person is Λ meter tall. His length of upperarm l_{up}, forearm l_{fa}, and hand l_{hd} can be determined as 0.186Λ, 0.146Λ, 0.108Λ respectively.

Given a fixed $\boldsymbol{p}_{\mathrm{sh}}$ joint and the reference trajectory $\boldsymbol{p}_{\mathrm{w}}(\kappa)$, the only challenge left is how to estimate the elbow joint $\boldsymbol{p}_{\mathrm{eb}}(\kappa)$ such that the overall movement follows a physical motion of human limb. In comparison to the limb movement, the robot arm also has a multi-joint configuration whose model could be used to simulate the trajectory of our limb. Henceforth, the temporal position of elbow joint could be calculated based on the inverse kinematic problem in robotics [1]. the 6R-PUMA robot arm was selected for modeling the human limb due to its simplicity and configuration similarity. In fact, the applicability of this robot arm for the limb movement has been validated with the measurement in [80]

In this model, a rotation of shoulder is controlled by azimuth $\phi_{\mathrm{sh}}(\kappa)$ and co-elevation $\theta_{\mathrm{sh}}(\kappa)$ angles which is equivalent to the 1^{st} and 2^{nd} joint in 6R-PUMA given $l_0 = 0$ as depicted in Fig. 4.2. The 3^{th} joint, which can rotate vertically with the angle $\gamma_{\mathrm{eb}}(\kappa)$, represents an elbow while the wrist can be regarded as the end-effector of the robot arm. Hence, by applying the inverse kinematic solution in [1], the limb orientation parameters can be calculated as follow,

$$\gamma_{\mathrm{eb}}(\kappa) = \tan^{-1}\left(\frac{\sqrt{4l_{\mathrm{up}}^2 l_{\mathrm{fa}}^2 - \left(|\boldsymbol{p}_{\mathrm{w}}(\kappa)|^2 - l_{\mathrm{up}}^2 - l_{\mathrm{fa}}^2\right)^2}}{|\boldsymbol{p}_{\mathrm{w}}(\kappa)|^2 - l_{\mathrm{up}}^2 - l_{\mathrm{fa}}^2}\right) \tag{4.4}$$

$$\theta_{\mathrm{sh}}(\kappa) = \frac{\pi}{2} - \tan^{-1}\left(\frac{p_{\mathrm{w}_z}(\kappa)}{\sqrt{p_{\mathrm{w}_x}^2(\kappa) + p_{\mathrm{w}_y}^2(\kappa)}}\right) + \tan^{-1}\left(\frac{l_{\mathrm{fa}}\sin\gamma_{\mathrm{eb}}(\kappa)}{l_{\mathrm{up}} + l_{\mathrm{fa}}\cos\gamma_{\mathrm{eb}}(\kappa)}\right) \tag{4.5}$$

$$\phi_{\mathrm{sh}}(\kappa) = \tan^{-1}\left(\frac{p_{\mathrm{w}_y}(\kappa)}{p_{\mathrm{w}_x}(\kappa)}\right) \tag{4.6}$$

Consequently, the temporal position of elbow $\boldsymbol{p}_{\mathrm{eb}}(\kappa)$ can be easily determined by,

$$\boldsymbol{p}_{\mathrm{eb}}(\kappa) = \left[\boldsymbol{p}_{\mathrm{sh}}(\kappa) + l_{\mathrm{up}}\right]\mathbf{I}_3 \begin{bmatrix} \cos\phi_{\mathrm{sh}}(\kappa)\sin\theta_{\mathrm{sh}}(\kappa) \\ \sin\phi_{\mathrm{sh}}(\kappa)\sin\theta_{\mathrm{sh}}(\kappa) \\ \cos\theta_{\mathrm{sh}}(\kappa) \end{bmatrix} \tag{4.7}$$

where l_{fa}, l_{up}, and $\mathbf{I}_3$ represents a length of forearm, length of upperarm, and 3×3 identity matrix respectively. Having the temporal of joints known, the non-rigid body motion of human limb can be simulated in terms of the skeleton movement which is similar to the movement in Fig. 2.6a but in 3D space.

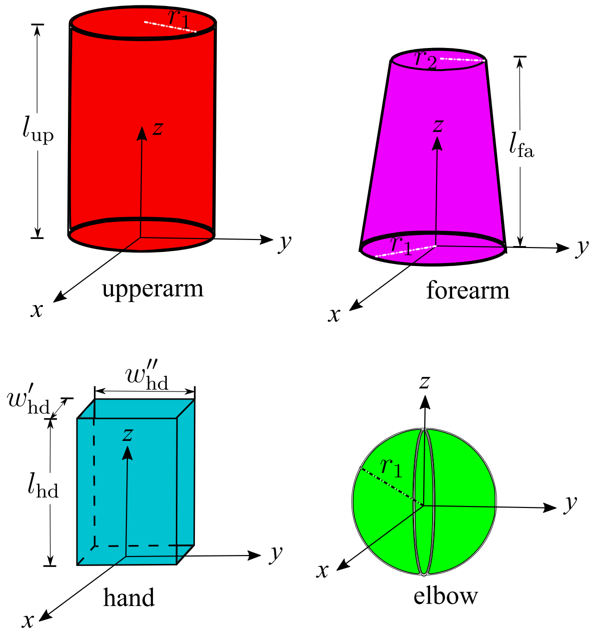

(a) Geometric components of human limb model

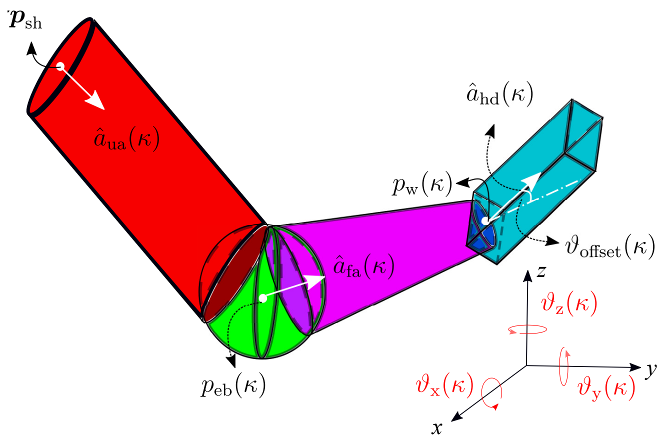

(b) Schematic of human limb model

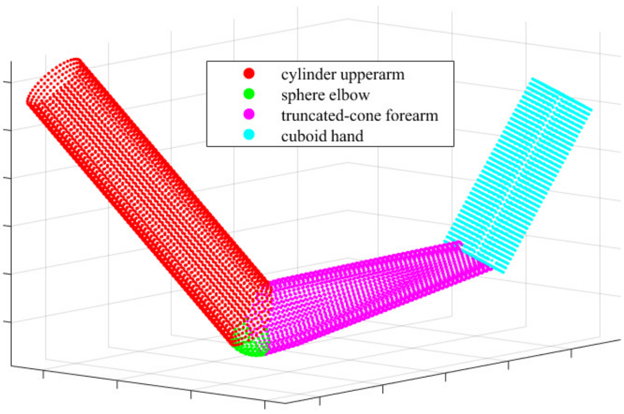

(c) Human limb model as surface points

Figure 4.3: Construction of human limb surface model based on geometric shapes

4.2.3 Simplified Surface-point based Human Limb Model

Although modeling a shape of human limb seems complicated at first glance, it becomes simpler by substituting the entire structure as a composition of simple geometrical shapes. Hence, in our model, a limb is broken down into an upperarm (ua), elbow (eb), forearm (fa), and hand (hd) segments whose shapes are simulated using a cylinder, sphere, truncated cone, and cuboid respectively as shown in Fig 4.3. The size of arm segments and elbow depends on radius r_1, r_2, and its length l_{up}, l_{fa}. Likewise, l_{hd}, w',and w'' parameters define the size of hand. For simplification, surface points are distributed along the human limb surface in the loosely-packed squared alignment.

Suppose these human limb segments are originally created at the original position depicted in Fig. 4.3a whose surface is covered by surface points. Cylinder, cone, sphere, and cuboid equations are applied to construct these surface points. In this scenario, the surface points are distributed along the surface in the loosely-packed squared alignment. In order to assemble them into the shape of human limb as shown in Fig. 4.3b, surface points require a transformation to orientate and translate into the aligned position. Fortunately, The correct orientation of each segment at a timestamp t can be calculated based on the direction of upperarm, forearm and hand segments defined accordingly in terms of unit vector,

$$\hat{\boldsymbol{a}}_{\mathrm{ua}}(\kappa) = \frac{\boldsymbol{p}_{\mathrm{eb}}(\kappa) - \boldsymbol{p}_{\mathrm{sh}}(\kappa)}{\left\|\boldsymbol{p}_{\mathrm{eb}}(\kappa) - \boldsymbol{p}_{\mathrm{sh}}(\kappa)\right\|} \tag{4.8}$$

$$\hat{\boldsymbol{a}}_{\mathrm{fa}}(\kappa) = \frac{\boldsymbol{p}_{\mathrm{w}}(\kappa) - \boldsymbol{p}_{\mathrm{eb}}(\kappa)}{\left\|\boldsymbol{p}_{\mathrm{w}}(\kappa) - \boldsymbol{p}_{\mathrm{eb}}(\kappa)\right\|} \tag{4.9}$$

$$\hat{\boldsymbol{a}}_{\mathrm{hd}}(\kappa) = \hat{\boldsymbol{a}}_{\mathrm{fa}}(\kappa) \tag{4.10}$$

Although the hand direction is presumably aligned with the forearm given this configuration, another variable will be introduced later to relax this constraint.

Let us consider the Euler rotation matrix [1] as the tool to orientate each limb segment into the proper arrangement. This matrix is a function of ϑ_{x}, ϑ_{y}, and ϑ_{z} which define the principle rotation around x, y, and z axis respectively. As depicted in Fig. 4.3b, it can be observed that ϑ_{y}, and ϑ_{z} share the same rotation direction with the co-elevation and azimuth angle supposing $\vartheta_{\mathrm{y}} \in [0, 180°]$. In this model, the orientation is controlled by these two angular variables. Therefore we set ϑ_{x} to zero to avoid the complexity of the movement model in the orientation The rotation matrix for this problem could be expressed as,

$$\begin{aligned}\mathfrak{R}_{(\cdot)}(\vartheta_{\mathrm{y}}, \vartheta_{\mathrm{z}}, \kappa) &= \mathfrak{R}_{\mathrm{z}(\cdot)}(\vartheta_{\mathrm{z}}, t)\mathfrak{R}_{\mathrm{y}(\cdot)}(\vartheta_{\mathrm{y}}, \kappa) \\ &= \begin{bmatrix} \cos\vartheta_{\mathrm{z},(\cdot)}(\kappa) & -\sin\vartheta_{\mathrm{z},(\cdot)}(\kappa) & 0 \\ \sin\vartheta_{\mathrm{z},(\cdot)}(\kappa) & \cos\vartheta_{\mathrm{z},(\cdot)}(\kappa) & 0 \\ 0 & 0 & 1 \end{bmatrix} \begin{bmatrix} \cos\vartheta_{\mathrm{y},(\cdot)}(\kappa) & 0 & \sin\vartheta_{\mathrm{y},(\cdot)}(\kappa) \\ 0 & 1 & 0 \\ -\sin\vartheta_{\mathrm{y},(\cdot)}(\kappa) & 0 & \cos\vartheta_{\mathrm{y},(\cdot)}(\kappa) \end{bmatrix}\end{aligned} \tag{4.11}$$

where $\mathfrak{R}_{z(\cdot)}(\vartheta_z, \kappa)$ and $\mathfrak{R}_{y(\cdot)}(\vartheta_y, \kappa)$ are the transformation matrix in with respect to the rotation around z and y axis respectively. the rotation matrix in x axis is omitted in the equation since it reduces to identity matrix given the condition that $\vartheta_x = 0$. Here the subscript $(\cdot)$ can be either ua, fa, and hd which represents the rotation operation for surface points of upperarm, forearm and hand respectively. The aligned orientation can be obtained by left-multiplies each surface point with the corresponding rotation matrix in eq. (4.11). Note that $\vartheta_{z,\mathrm{ua}}(\kappa)$ and $\vartheta_{z,\mathrm{fa}}(\kappa)$ are just the azimuth angles of respective arm segments and can be computed from the unit vectors in eqs.(4.8) - (4.10). Likewise, $\vartheta_{y,\mathrm{ua}}(\kappa)$ and $\vartheta_{y,\mathrm{fa}}(\kappa)$ are determined from the the co-elevation angles of their unit vectors. In case of the hand orientation, although its azimuth is angle set to be equivalent with the forearm $\vartheta_{z,\mathrm{hd}}(\kappa) = \vartheta_{z,\mathrm{fa}}(\kappa)$ to maintain the smooth alignment, the hand co-elevation angle could be computed by $\vartheta_{y,\mathrm{hd}}(\kappa) = \vartheta_{\mathrm{offset}}(\kappa) + \vartheta_{y,\mathrm{fa}}(\kappa)$ where $\vartheta_{\mathrm{offset}}(\kappa)$ is a particular angle that rotates the vertical orientation of the hand segment away from that of the forearm. Elbow segment does not need the rotation matrix due to its geometrical symmetry of the sphere.

The last procedure for the human limb alignment is to translate the surface points into their respective arrangement by offsetting these points with the reference position at each timestamp. The surface points on upperarm and hand segment can refer to the joints $\boldsymbol{p}_{\mathrm{sh}}$ and $\boldsymbol{p}_{\mathrm{hd}}$ for the translation. In a similar manner, surface points on the elbow and forearm utilize the joint $\boldsymbol{p}_{\mathrm{eb}}$. Finally, the human limb in terms of surface points can be visualized as in Fig. 4.3c.

4.3 Simulated CSI Model

Let us consider the CSI model described in eq. (2.2) consisting of time-invariant $H_{n,m}^{\mathrm{TIV}}(f_k)$ and time-variant $H_{n,m}^{\mathrm{TV}}(\kappa, f_k)$ components. For simplification, the propagation path with respect to the time-invariant component is restricted only a single component ($L_{\mathrm{TIV}} = 1$) which is the dominated component of Line-of-Sight (LoS) path visualized as a black sinusoidal wave in Fig. 4.4 and can be written as

$$H_{n,m}^{\mathrm{TIV}}(f_k) = \frac{\lambda_k}{4\pi D_{\mathrm{LoS}}} \exp\left(-\mathrm{j}\frac{2\pi}{\lambda_k} D_{\mathrm{LoS}}\right) \tag{4.12}$$

where $D_{\mathrm{LoS}} = \left\| \boldsymbol{p}_{\mathrm{T}_m} - \boldsymbol{p}_{\mathrm{R}_n} \right\|$ is the LoS propagation distance between the position of m-th Tx antenna and n-th Rx antennas denoted as $\boldsymbol{p}_{\mathrm{T}_m}$ and $\boldsymbol{p}_{\mathrm{R}_n}$ respectively.

The dynamic component $H_{n,m}^{\mathrm{TV}}(\kappa, f_k)$, on the other hand, should contains all propagation paths scattered from the surface points of the moving human limb model. Considering the geometry of human limb object with respect to the position of Tx and Rx, there exists a shadowing region on the surface whose LoS of those surface pointss are blocked. For simplicity, these surface points depicted by a black circle in Fig. 4.4 is assumed to generate

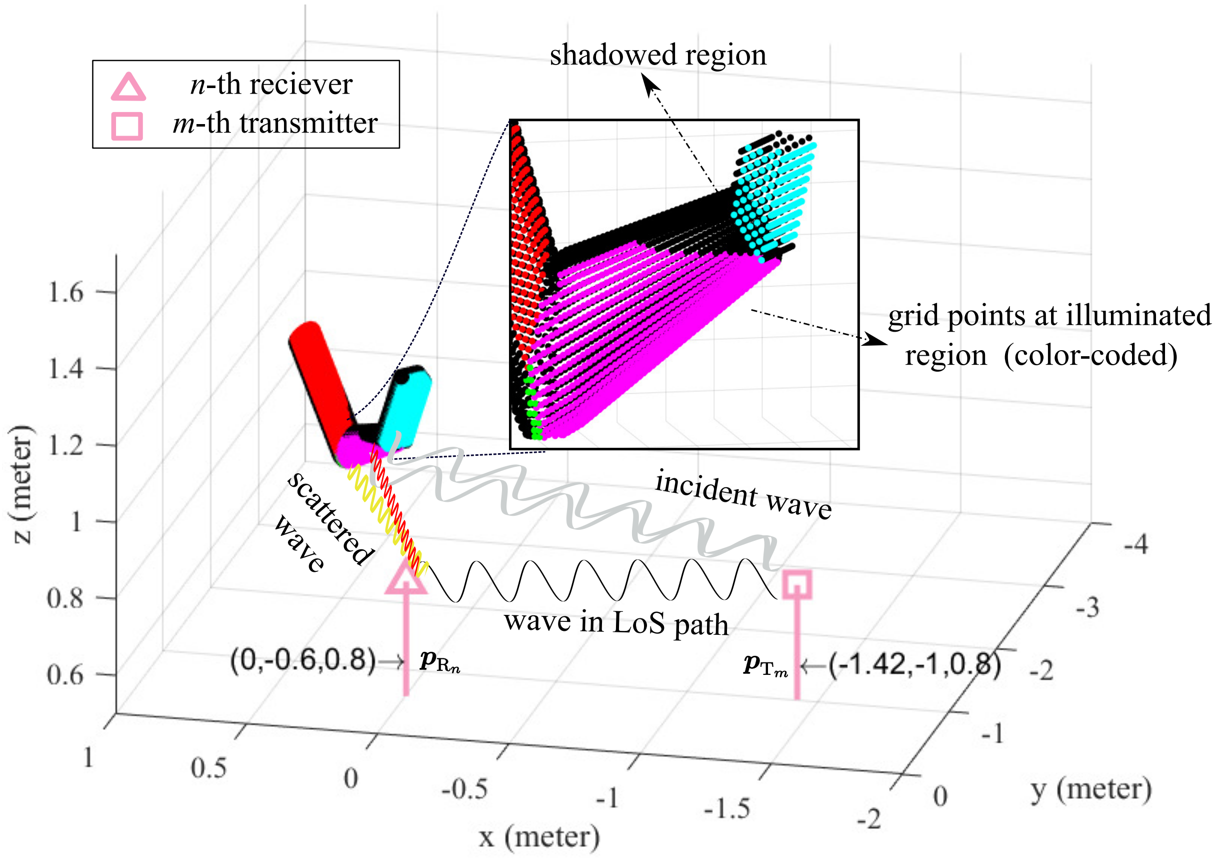

Figure 4.4: Scenario of the simulated CSI model with respect to the channel between $\boldsymbol{p}_{\mathrm{T}_m}$ Tx and $\boldsymbol{p}_{\mathrm{R}_n}$ Rx in the presence of the human limb model.

no Doppler frequency regardless of how fast it was moving. Suppose a set $\Omega(\kappa) = \{\boldsymbol{p}_\iota^{(i)}(\kappa)|i = 1, 2, \cdots, L_\iota(\kappa)\}$ consists of $L_\iota(\kappa)$ surface points located only in the illuminated region (non-shadowing) at a timestamp t which are visualized as a colored dot marker in Fig. 4.4. In other word, each $\boldsymbol{p}_\iota^{(i)}(\kappa)$ exists the LoS path with respect to both Tx and Rx and is visualized in the figure as the region where the colored sine wave can be incident to and scattered from. This condition can be easily determined by comparing the direction between a normal vector of surface points and the vector from those surface points to Tx and Rx. Geometrically, it means each illuminated point should satisfy the following geometric criteria,

- $\left\langle \boldsymbol{p}_\iota^{(i)}(\kappa) - \boldsymbol{p}_{\mathrm{T}_m},\, \boldsymbol{n}_\iota^{(i)}(\kappa) \right\rangle < 0$
- $\left\langle \boldsymbol{p}_{\mathrm{R}_n} - \boldsymbol{p}_\iota^{(i)}(\kappa),\, \boldsymbol{n}_\iota^{(i)}(\kappa) \right\rangle > 0$

where $\hat{\boldsymbol{n}}_\iota^{(i)}(\kappa)$ is a normal vector of $\boldsymbol{p}_\iota^{(i)}(\kappa)$ and $\langle\ ,\ \rangle$ denotes an inner product. It should be noted that the criteria above does not consider the shadowing between limb segments. By utilizing the concept of line-plane intersection, one can effortlessly address this type of shadowing especially for geometric shape. As a result, the dynamic component of CSI can be expressed in terms of bistatic Doppler frequency by utilizing eq. (2.2b) and eq. (2.8) as follows,

$$H_{n,m}^{\mathrm{TV}}(\kappa, f_k) = \sum_{i\in\Omega(\kappa)} \alpha_{n,m}^{\mathrm{TV},(i)}(\kappa, f) \exp\left(-\mathrm{j}\frac{2\pi}{\lambda_k} d_{\mathrm{bi}}^{\mathrm{TV},(i)}(\kappa)\right) \tag{4.13a}$$

$$\begin{aligned} d_{\mathrm{bi}}^{(i)}(\kappa) &= d_{\mathrm{T}_m}^{\mathrm{TV},(i)}(\kappa) + d_{\mathrm{R}_n}^{\mathrm{TV},(i)}(\kappa) \\ &= \lambda_k \sum_{\kappa=0}^{\kappa_{\max}} f_{\mathrm{d}}^{(\mathrm{i})}(\kappa) T_{\mathrm{s}} \\ &= \sum_{\kappa=0}^{\kappa_{\max}} v_{\mathrm{bi}}^{(i)}(\kappa) \left[\cos\theta_{\mathrm{T}_m}(\kappa) + \cos\theta_{\mathrm{R}_n}(\kappa)\right] T'_{\kappa} \end{aligned} \tag{4.13b}$$

where $\kappa_{\max}$, $d_{\mathrm{T}_m}^{(i)}(\kappa) = \left\|\boldsymbol{p}_\iota^{(i)}(\kappa) - \boldsymbol{p}_{\mathrm{T}_m}\right\|$, $d_{\mathrm{R}_n}^{(i)}(\kappa) = \left\|\boldsymbol{p}_\iota^{(i)}(\kappa) - \boldsymbol{p}_{\mathrm{R}_n}\right\|$, $\alpha_{n,m}^{\mathrm{TV},(i)}(\kappa, f_k)$, $f_{\mathrm{d}}^{(\mathrm{i})}(\kappa)$, and $v_{\mathrm{bi}}^{(i)}(\kappa)$ are the maximum time index, the distance from i-th surface point to the m-th Tx antenna and n-th Rx antenna respectively, followed by the Doppler profile, bistatic speed and the time-variant complex attenuation of i-th surface point accordingly.

Regarding the time-variant complex attenuation, this term represents the propagation loss between Tx antenna to the i-th surface point, the RF scattering loss at the surface, and the propagation loss from the surface point back to the Rx antenna. This term physically influences the power spectrum of Doppler frequency which will be explained in section 4.5. Since the scattered wave can be calculated by using the solution from the electromagnetic theory, PO approximation has been applied in this study to estimate TV-CSI [83]. In order to incorporate our limb model consisting of surface points to the PO framework, the small surface area that corresponds to $\alpha_{n,m}^{\mathrm{TV},(i)}(\kappa, f_k)$ has been constructed. Here each surface area is represented by a circular shape in order to avoid the need of surface reconstruction algorithm. The detail solution and validation of this PO based on circular mesh will be separately covered in section 4.4.2. Therefore, at each timestamp t and subcarrier frequency f_k, the term $H_{n,m}^{\mathrm{TV}}(\kappa, f_k)$ is equivalent to the total scattered electric field at the received antenna obtained from the PO solution.

4.4 Scattering Wave on The Non-Rigid Body Motion of Human Limb

As mentioned earlier, TV-CSI component can be deterministically computed from the EM theory of scattering wave since it physically represents the attenuation and distortion of the scattered signal in the wireless channel. In fact, this techniques commonly use to simulate micro-Doppler effect of the bulky moving objects as stated in [51]. In terms of scattered field prediction, PO technique has gained the reputation due to its lower complexities in comparison with other numerical techniques such as finite-difference time-domain (FDTD)

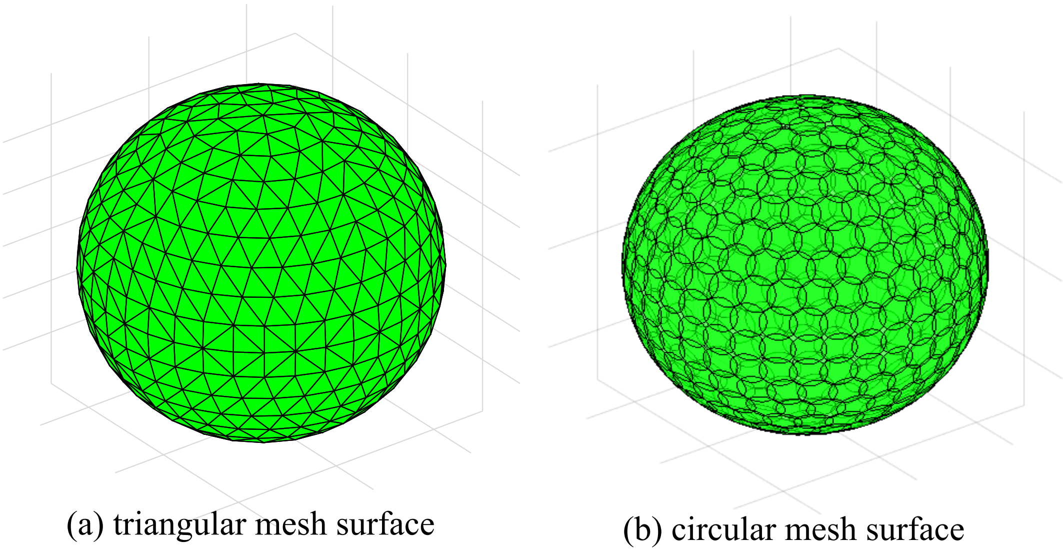

Figure 4.5: Mesh surface comparison between the (a) triangular shape widely-implemented in PO and (b) circular shape in the proposal.

and method-of-moments (MoM) [128], as well as its higher accuracy than that of geometric optics (GO). In this section, the explanation of PO-based scattering field prediction will be given as the tool to calculate the TV component of CSI as depicted in the flowchart of Fig. 4.1. Specifically, the practical usage for applying PO in the movement object is firstly explained. The modified PO framework will be investigated as an alternative and practical method to predict the scattered field.

4.4.1 Practical Usage Issue of PO with Surface Reconstruction

Conventional PO [129, 130] in general, by decomposing a target surface into small surface meshes, calculates the scattered field on the surface of meshes that has been illuminated by the EM wave with respect to source at the Tx antenna and observation at the Rx antenna [83, 131]. Typically, mesh surface is created in the triangular shape where three vertices are represented by three adjacent points as visualized in Fig. 4.5a due to its ability to enclose any surface given sufficient density of surface points. The popular implementation of PO, therefore, calculates the equivalent scattered field illuminated over triangular mesh by utilizing Ludwig integral [132, 133]. Because the inaccurate mesh geometry is also one of the reasons that degrade the performance of PO, the way of reconstructing mesh could not be taken lightly. Various complex surface reconstructions from non-uniformly distributed surface points have been introduced such as crust-based algorithm [134, 135, 136], and alpha-shaped based algorithm [137] to create triangular meshes. Considering a dynamic scenario where surface points of the moving surface gradually change with time especially in the presence of non-rigid body motion where the object surface could be gradually deformed, the surface reconstruction algorithm has to be repeatedly implemented every snapshot. Even in a solid model where surface information is given, the surface reconstruction algorithm is inevitably required to determine the vertices of each triangular mesh in every snapshot. Additionally, the reconstructed surface may not be perfect depending on the reconstruction algorithm which requires a manual examination at each snapshot.

This issue also happens in our case because the non-rigid movement of human limb gradually changes the number of illuminated area with time. Therefore, surface reconstruction is required before the computation of scattered field at each snapshot t. For the better practical usage in computing TV-CSI with PO, an alternative method that could create an equivalent scattered field of mesh surface directly from the surface point given the surface information would be highly beneficial since it does not rely on the surface reconstruction algorithm .

4.4.2 Development of Circular-mesh PO for the Analysis of Moving Scatterer

The proposed modification of PO technique is to decompose the surface area of a target object into small circular meshes. These meshes are elaborately created from a given set $\mathbb{G}$ of surface points which represents the target surface and situated at the center of the circle as shown in Fig. 4.6. The normal vector of of surface points are supposedly given which is possible when dealing with the solid model where the surface information is provided. In the object with a simple shape, a normal vector can be estimated from adjacent points [134, 138].

Previously, the analytical scattered field solution of a circular plate has been widely applied to analyze and compare the scattered and diffracted fields from large circular disk estimated from different techniques [139, 140, 141], and also to model the scattering wave from vegetation leaves [142, 143]. However, in this modification, the solution is now applied to estimate scattered fields for small circular mesh as part of a larger surface and thus does not need any surface reconstruction algorithm. For the sake of explanation, surface points with a given normal vector are supposedly arranged in a fully-packed equilateral triangle alignment. If the normal vector is not provided, the technique in [134, 138] could be applied to estimate the correspondence normal vector of m-th surface point which is effectively equivalent to the vector whose direction is approximately orthogonal to all vectors between the m-th point to its adjacent points. Regarding the notation clarification, the variables that are involved with transmitter and receiver will be subscripted with T and R notations exclusively for this section.

Let us firstly consider the local coordinate of g-th circular mesh with a_g radius governed by basis vectors $(\hat{\boldsymbol{x}}_g, \hat{\boldsymbol{y}}_g, \hat{\boldsymbol{z}}_g)$ and lied on the $\hat{\boldsymbol{x}}_m\hat{\boldsymbol{y}}_m$-plane as illustrated in Fig. 4.6. For consistency, a subscript g is added to denote variables that are constituted to the local coordinate of g-th mesh. Suppose the EM wave emitted from an infinitesimally small dipole antenna

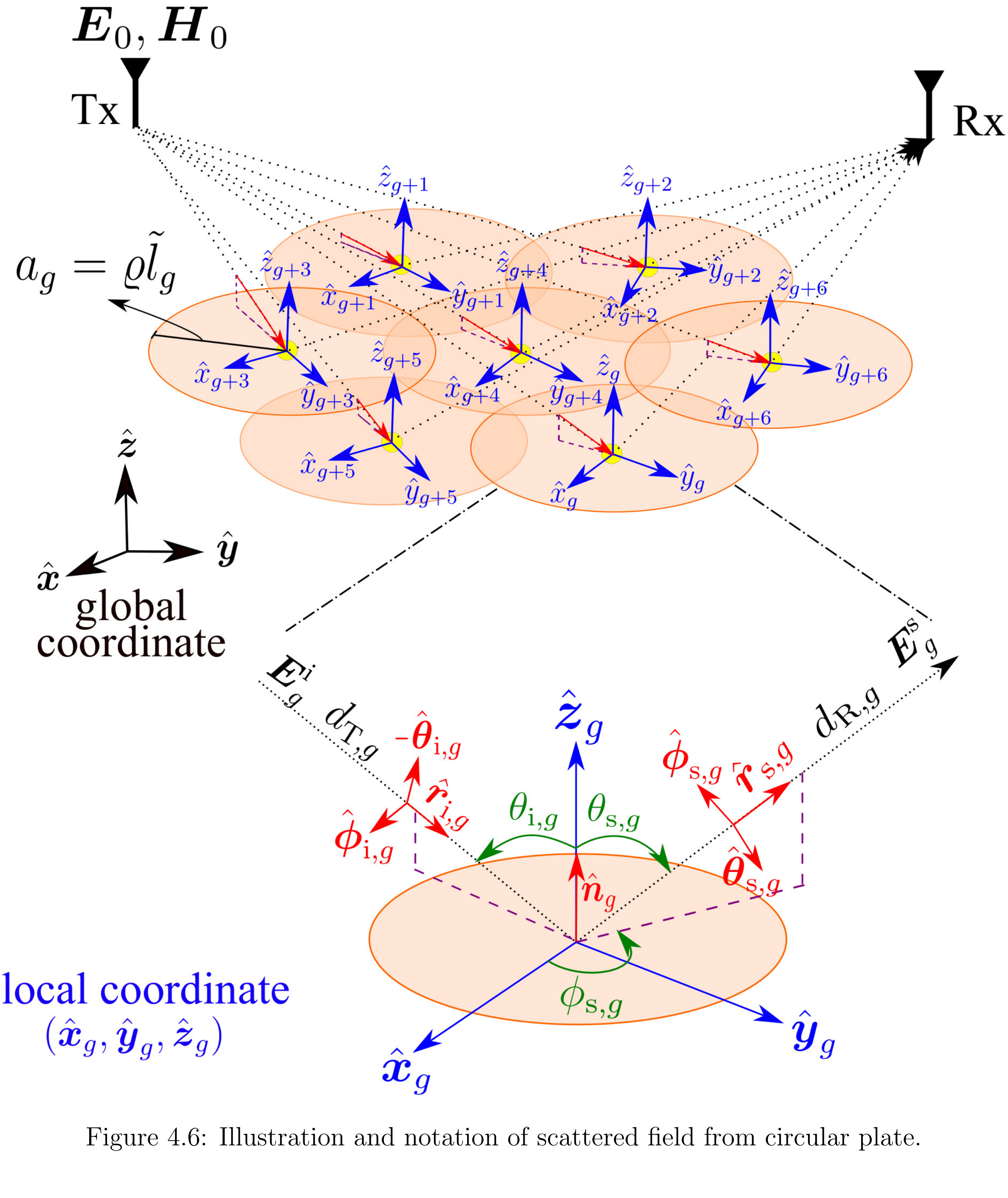

Figure 4.6: Illustration and notation of scattered field from circular plate.

(Tx) with the electric dipole moment $\boldsymbol{e}_0$ polarized in a direction of $\hat{\boldsymbol{e}}_{\mathrm{T}}$. The propagation of this wave along $\hat{\boldsymbol{y}}_g\hat{\boldsymbol{z}}_g$-plane is incident on the center of the PEC circular mesh with the direction of incident $\hat{\boldsymbol{r}}_{\mathrm{i},g}$. Geometrically, these local basis vectors can be represented by an incident azimuth vector $\hat{\boldsymbol{\phi}}_{\mathrm{i},g}$, a projection of $\hat{\boldsymbol{r}}_{\mathrm{i},g}$ onto the mesh surface, and mesh's normal vector $\hat{\boldsymbol{n}}_g$ respectively. Hence, the corresponding incident electric field can be given by

$$\boldsymbol{E}_g^{\mathrm{i}} = \frac{\lambda}{4\pi d_{\mathrm{T},g}} \exp\left(-\mathrm{j}\frac{2\pi}{\lambda} d_{\mathrm{T},g}\right) \boldsymbol{e}_{0\mathrm{r},g} \tag{4.14}$$

$$\boldsymbol{e}_{0\mathrm{r},g} = (\boldsymbol{e}_0 \cdot \hat{\boldsymbol{\theta}}_{0,g})\hat{\boldsymbol{\theta}}_{0,g} \tag{4.14a}$$

where $\hat{\boldsymbol{\theta}}_{0,g}$, $d_{\mathrm{T},g}$, λ, and k are the unit vector of angle between $\hat{\boldsymbol{r}}_{\mathrm{i},m}$ and $\boldsymbol{p}_0$, the distance from the source to the mesh, wavelength, and wave number respectively. From the observation point Rx located at a distance $d_{\mathrm{R},g}$ away from the circular mesh, the far-field scattered electric field along the scattered propagation direction $\hat{\boldsymbol{r}}_{\mathrm{s},g}$ which was derived in [83] under the configuration in Fig. 4.6 can be expressed as

$$\boldsymbol{E}_g^{\mathrm{s}} = E^{\mathrm{s}}_{\theta,g}\hat{\boldsymbol{\theta}}_{\mathrm{s},g} + E^{\mathrm{s}}_{\phi,m}\hat{\boldsymbol{\phi}}_{\mathrm{s},g} \tag{4.15}$$

where $E^{\mathrm{s}}_{\theta,g}$ and $E^{\mathrm{s}}_{\phi,g}$ are the scattered electric field components in spherical coordinates denoted by basis vectors $(\hat{\boldsymbol{r}}_{\mathrm{s},g}, \hat{\boldsymbol{\theta}}_{\mathrm{s},g}\ \hat{\boldsymbol{\phi}}_{\mathrm{s},g})$. Since the electric field in $\hat{\boldsymbol{r}}_{\mathrm{s},g}$ is approximately zero in far-field region, it is omitted from the above equation. These components are the summation of scattered electric field in parallel and perpendicular polarization with respect to the incident plane whose directions are defined by unit vectors in spherical coordinate of the incident field $-\hat{\boldsymbol{\theta}}_{\mathrm{i},g}$ and $\hat{\boldsymbol{\phi}}_{\mathrm{i},g}$ respectively and thus can be defined accordingly as,

$$E^{\mathrm{s}}_{\theta,g} = C_g\left(D_{\theta\theta,g}E^{\mathrm{i}}_{\theta,g} + D_{\theta\phi,g}E^{\mathrm{i}}_{\phi,g}\right) \tag{4.16}$$

$$E^{\mathrm{s}}_{\phi,g} = C_g\left(D_{\phi\theta,g}E^{\mathrm{i}}_{\theta,g} + D_{\phi\phi,g}E^{\mathrm{i}}_{\phi,g}\right) \tag{4.17}$$

where $E^{\mathrm{i}}_{\theta,g}$ and $E^{\mathrm{i}}_{\phi,g}$ are the components of the incident electric field in the spherical coordinates. The term $B_{op,g}$, where o and p denotes the component of the scattered and incident fields respectively and can be either θ or ϕ, are introduced for brevity in the followings,

$$B_{\theta\theta,g} = -\cos\theta_{\mathrm{s},g}\sin\phi_{\mathrm{s},g} \tag{4.18}$$

$$B_{\phi\theta,g} = -\cos\phi_{\mathrm{s},g} \tag{4.19}$$

$$B_{\theta\phi,g} = -\cos\theta_{\mathrm{i},g}\cos\theta_{\mathrm{s},g}\cos\phi_{\mathrm{s},g} \tag{4.20}$$

$$B_{\phi\phi,g} = \cos\theta_{\mathrm{i},g}\sin\phi_{\mathrm{s},g} \tag{4.21}$$

where the azimuth scattered angle, co-elevation scattered and incident angles are defined as $\phi_{\mathrm{s},g}$, $\theta_{\mathrm{s},g}$, and $\theta_{\mathrm{i},g}$ respectively. The complex constant variable C_g which also contains the phase rotation due to the overall propagation distance can be explained by,

$$C_g = \mathrm{j}\frac{2\pi a_g^2}{\lambda d_{\mathrm{R},g}}\left[\frac{J_1(\nu_g)}{\nu_g}\right]\exp\left(-\mathrm{j}\frac{2\pi}{\lambda}\left(d_{\mathrm{T},g} + d_{\mathrm{R},g}\right)\right) \tag{4.22}$$

$$\nu_g = ka_g\sqrt{A_{1,g}^2 + A_{2,g}^2} \tag{4.22a}$$

$$A_{1,g} = \sin\theta_{s,g}\cos\phi_{s,g} \tag{4.22b}$$

$$A_{2,g} = \sin\theta_{s,g}\sin\phi_{s,g} - \sin\theta_{i,g} \tag{4.22c}$$

where $J_1(\nu_g)$ is the Bessel function of the first kind of order one.

In practical standpoint, the human limb does not have PEC properties and thus the PEC solutions in eq. (4.18) - (4.22) cannot be appropriately used. Hence, the scattered field solution for dielectric material is needed in our case to calculate the simulated CSI. Fortunately, the concept of PO in dielectric material case has been discussed in [144] that the current densities could be estimated from an incident wave in both polarizations each factored by their Fresnel reflection coefficients. In this case, the reflection coefficient in parallel and perpendicular polarization derived from [83] are given as $R_{\theta,g}$ and $R_{\phi,g}$ respectively. Through mathematical manipulation, it was found that, although there is no change in C_g, terms in eqs. (4.18) - (4.21) have to be rearranged for the calculation of scattered field in dielectric material as follow,

$$B^*_{\theta\theta,g} = \frac{\sin\phi_{s,g}}{2}\left[R^+_{\theta,g}\cos\theta_{i,g} - R^-_{\theta,g}\cos\theta_{s,g}\right] \tag{4.23}$$

$$B^*_{\phi\theta,g} = \frac{\cos\phi_{s,g}}{2}\left[R^+_{\theta,g}\cos\theta_{i,g}\cos\theta_{s,g} - R^-_{\theta,g}\right] \tag{4.24}$$

$$B^*_{\theta\phi,g} = \frac{\cos\phi_{s,g}}{2}\left[R^+_{\phi,g} - R^-_{\phi,g}\cos\theta_{i,g}\cos\theta_{s,g}\right] \tag{4.25}$$

$$B^*_{\phi\phi,g} = \frac{\sin\phi_{s,g}}{2}\left[R^-_{\phi,g}\cos\theta_{i,g} - R^+_{\phi,g}\cos\theta_{s,g}\right] \tag{4.26}$$

where

$$R^-_{\{\theta,\phi\},g} = 1 - R_{\{\theta,\phi\},g}$$
$$R^+_{\{\theta,\phi\},g} = 1 + R_{\{\theta,\phi\},g}.$$

By substituting these analytical solutions in eqs. (4.18) - (4.26) into eqs. (4.16) - (4.17), the total electric field of each mesh can be computed for both PEC and dielectric cases from eq. (4.15). Hence, the electric field scattered from the surface of the target object can be equivalently calculated by accumulating meshes' electric field. However, the summation is invalid unless both $\hat{\boldsymbol{\theta}}_{s,g}$ and $\hat{\boldsymbol{\phi}}_{s,g}$ of each mesh are derived in terms of global coordinates.

There are many way to project the g-th local coordinate to the global coordinate. One method in particular is to utilize the matrix conversion between spherical and Cartesian coordinate system [83]. Suppose the basis vectors of g-th local Cartesian coordinates $\hat{\boldsymbol{x}}_g$, $\hat{\boldsymbol{y}}_g$, and $\hat{\boldsymbol{z}}_g$ have their components written in terms of global Cartesian coordinates $(\hat{\boldsymbol{x}}, \hat{\boldsymbol{y}}, \hat{\boldsymbol{z}})$. Spherical unit vectors $\hat{\boldsymbol{\theta}}_{s,g}$ and $\hat{\boldsymbol{\phi}}_{s,g}$ of the scattered electric field $\boldsymbol{E}^s_g$ can be also written in terms of the global Cartesian coordinates system as well by,

$$\hat{\boldsymbol{\theta}}_{\mathrm{s},g} = \cos\theta_{\mathrm{s},g}\cos\phi_{\mathrm{s},g}\hat{\boldsymbol{x}}_g + \cos\theta_{\mathrm{s},g}\sin\phi_{\mathrm{s},g}\hat{\boldsymbol{y}}_g - \sin\theta_{\mathrm{s},g}\hat{\boldsymbol{z}}_g \tag{4.27}$$

$$\hat{\boldsymbol{\phi}}_{\mathrm{s},g} = -\sin\phi_{\mathrm{s},g}\hat{\boldsymbol{x}}_g + \cos\phi_{\mathrm{s},g}\hat{\boldsymbol{y}}_g \tag{4.28}$$

By substituting eqs. (4.27) - (4.28) into eq. (4.15), each mesh's electric field is now derived in terms of global Cartesian coordinates and the total electric field of the entire surface on the target object can be computed by,

$$\boldsymbol{E}^{\mathrm{s}} = \sum_{g\in\mathbb{G}} \boldsymbol{E}^{\mathrm{s}}_g \tag{4.29}$$

Suppose the observation point is represented by an infinitesimally small dipole antenna with a polarization pointed toward $\hat{\boldsymbol{e}}_{\mathrm{R}}$ direction. The received electric field is then equivalent to the amount of the electric field projected on $\hat{\boldsymbol{e}}_{\mathrm{R}}$.

4.4.3 Analysis of Circular Mesh Size

Since the closed-surface could not be perfectly covered by circular meshes, the proposal inevitably introduces the prediction discrepancy onto the scattered field. Therefore, the analysis of the mesh size which depends on its radius must be addressed to optimize this discrepancy. the radius can be easily defined as $a_g = \varrho\tilde{l}_g$ where $\tilde{l}_g$ and ϱ are an averaged resolution of surface point and a size parameter of g-th mesh. Considering a fully-packed alignment as shown in Fig. 4.6, $\tilde{l}_g$ defines an average distance between the g-th surface points to its 6 neighbors. Given this alignment, the equivalent mesh's shape that can fit the surface would be a hexagon [145]. Therefore, by considering the equivalent surface area between circle and hexagon, the optimal ϱ can be computed as $\left(\frac{3}{4\pi^2}\right)^{1/4}$. Likewise, a loosely-packed alignment [145] would have a square as the equivalent shape for example. In this case, 4 adjacent points are required to estimate $\tilde{l}_g$ and the optimal ϱ becomes $\frac{1}{\sqrt{\pi}}$. These examples showed that the optimal size of circular mesh highly depends on the alignment of the surface point. With this regard, it should be noted that the proposed method requires the adaptive search technique to estimate the size parameter of g-th mesh from its local density and alignment of adjacent points when dealing with the typical point could with the highly non-uniform distribution. Therefore, this proposal is generally suitable for the solid model with the nearly-uniform surface point where the knowledge of surface points distribution is easily determined.

Since the mesh size must be tiny, the Bessel argument ν_g may vary in the range of relatively small value. Therefore, the Bessel function in C_g could be simplified into the lower-order polynomial, For instance, under the assumption that the average point resolution is around $\tilde{l}_m = 0.1\lambda$ and the optimal ϱ of equilateral triangle alignment defined previously, the argument ν is still smaller than 1. Therefore, the Bessel function could be reduced to

$$J_1(\nu) = \sum_{q=0}^{\infty} \frac{(-1)^q (0.5\nu)^{2q+1}}{q!(q+1)!}$$
$$\simeq \sum_{q=0}^{1} \frac{(-1)^q (0.5\nu)^{2q+1}}{q!(q+1)!} = \frac{\nu}{2} - \frac{\nu^3}{16} \tag{4.30}$$

By simply limit the summation of Bessel function to only the first two terms, the error from this approximation is still negligibly small which around 0.1% different from the true value within the range $0 \leq \nu \leq 1$. As a result, eq. (4.22) could be simplified in terms of C'_m as,

$$C'_g \simeq -\mathrm{j}\frac{\pi k \alpha^2 l_g^2}{8\lambda d_{\mathrm{R},g}} \left[8 - \nu_g^2\right] \exp\left(-\mathrm{j}\frac{2\pi}{\lambda}\left(d_{\mathrm{T},g} + d_{\mathrm{R},g}\right)\right). \tag{4.31}$$

It is obvious that C'_m becomes independent over incident and scattering angles when ν_m^2 approaches zero. This is similar in the case of modeling the mesh with infinitesimally small dipole [129].

4.4.4 Validation of Circular-mesh PO

In this simulation, the scattered field on the flat and round surface of a square plate and sphere calculated via the proposed method has been conducted respectively. The generated surface point was arranged in the equilateral triangle configuration as shown in Fig. 4.6. The averaged point resolution was varied in the proposed method for validation. The center of test objects was positioned at the origin with the orientation of the square plate parallel to the $\hat{\boldsymbol{x}}\hat{\boldsymbol{y}}$-plane as shown in Fig. 4.7. Tx and Rx were located $1,000\lambda$ away from the center of test objects which is supposedly in a far-field region relative to their mesh sizes. Rx position was varied along $\hat{\boldsymbol{y}}\hat{\boldsymbol{z}}$-plane to observe the scattered power in the angular domain. Other relevant simulation parameters were summarized in Table 4.1.

Table 4.1: Circular mesh based PO simulation parameters

Parameters	**Values**
$\lvert\boldsymbol{e}_0\rvert$	$4\pi/\lambda$
Center frequency	5 GHz
Averaged point resolution	λ, $\lambda/2$, $\lambda/10$, $\lambda/25$
Size of square plate	$20\lambda \times 20\lambda$
Radius of sphere	10λ
Dielectric constant (rubber) [83]	3
Tx azimuth (ϕ_{Tx}) and co-elevation (θ_{Tx})	$\phi_{\mathrm{Tx}} = 270°$, $\theta_{\mathrm{Tx}} = 45°$
Tx, Rx antenna polarization	$\hat{\boldsymbol{e}}_{\mathrm{Tx}} = \hat{\boldsymbol{e}}_{\mathrm{Rx}} = [1\ 0\ 0]$

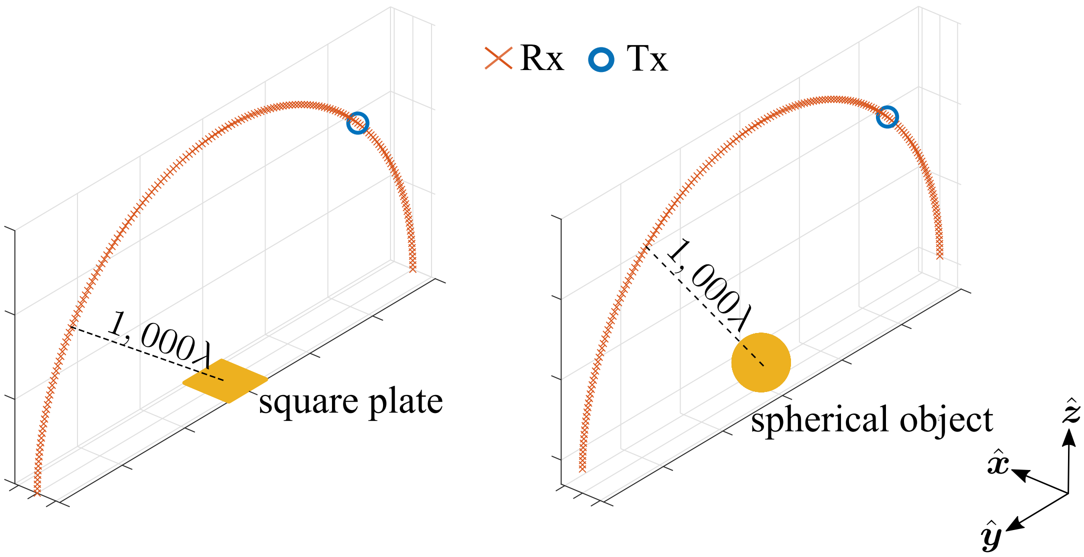

Figure 4.7: Simulation scenario.

The goal of this experiment is to investigate the acceptable averaged resolution that could asymptotically predict the scattered field by using the PO with circular mesh in terms of the electric field power at a different scattering angle. The fine-grained surface point density ($\frac{\lambda}{50}$ resolution) of widely-implemented PO with triangular mesh [131] was selected as the reference. The relative error, defined as the discrepancy from the reference normalized by the maximum power of the reference, was introduced to clarify the effect of mesh resolution to the prediction accuracy. In Fig. 4.8, it can be observed that the proposed method with $\tilde{l}_m = \lambda$ poorly predicted the scattered field from the square plate in both materials. Although the finer resolution down to $\frac{\lambda}{10}$ significantly reduced the discrepancy, the differences could still be seen when θ_s approaches 90° in the $-\hat{\boldsymbol{y}}$ region. Since these resolutions were not sufficiently fined, it could not keep up with faster phase rotation, especially at the plate square border. This discrepancy clearly mitigated when the resolution became $\frac{\lambda}{25}$. This improvement was comparatively visualized in Fig. 4.10 as the relative error gradually reduced around 5-10 dB when increasing the surface point density.

In the curvature surface of the spherical object depicted in Fig. 4.9, the agreement between the result from the proposed method and reference was observed in all angles even when the averaged resolution was $\frac{\lambda}{10}$. Its relative error depicted in Fig. 4.10 also confirmed that the error level was almost identical to those with $\frac{\lambda}{25}$ resolution. This is because the scattered power from the sphere did not suffer from the perimeter shifting and offset on the $\hat{\boldsymbol{x}}\hat{\boldsymbol{y}}$-plane caused by circular meshes. Moreover, the specular reflection can be observed for all Rx angles in the case of the sphere. Thus, faster phase rotation at higher Fresnel zones did not have a significant impact resulting in the acceptable prediction at $\frac{\lambda}{10}$ resolution.

This result has validated the applicability of circular mesh PO for the prediction of scattered power without the need for any surface reconstruction algorithm. However, the

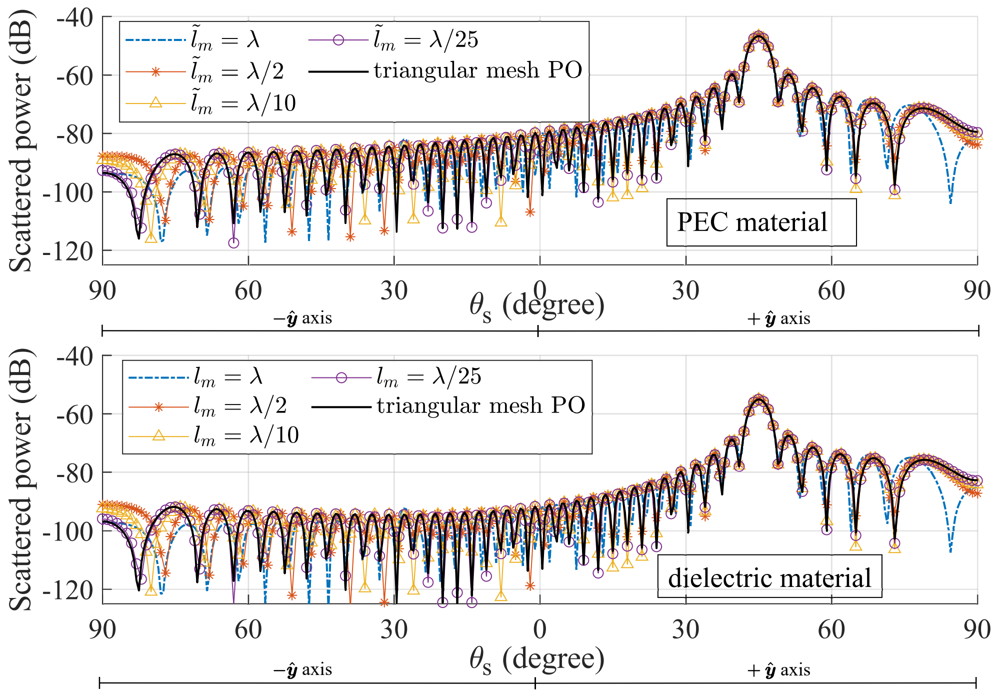

Figure 4.8: Comparison of scattered power from the square plate using the nearly-uniform circular mesh at different mesh resolution.

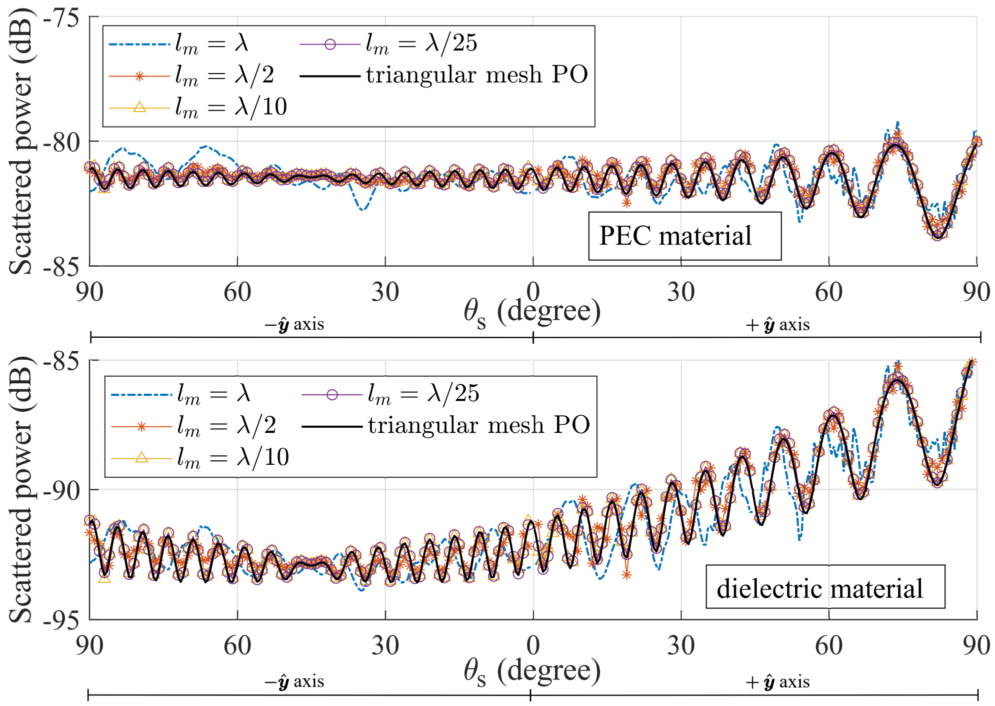

Figure 4.9: Comparison of scattered power from the spherical object using the nearly-uniform circular mesh at different mesh resolution.

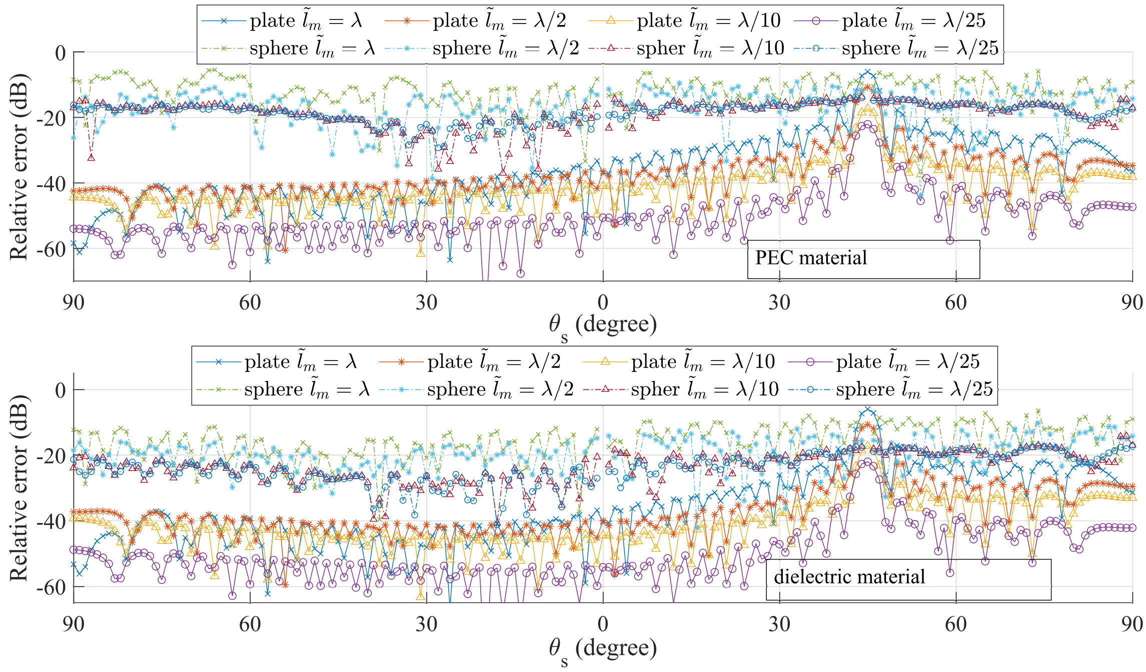

Figure 4.10: Performance of the proposed technique in terms of error normalized by the peak of reference scattered power.

surface point resolution should be fit to the applicable range which is relatively smaller than 0.1λ to apply the proposed technique in the actual case.

4.4.5 Construction of Time-Variant Component of CSI with The Circular Mesh PO

Having the performance verified in section 4.4.4, the modified PO framework with circular mesh can be applied for the prediction of the time-variant component of CSI. Considering the subcarrier frequency of Wi-Fi CSI, incident electric field is proportional to the amount of Tx signal propagated through the wireless channel at f_k subcarrier frequency. Likewise, the scattered electric field is also related to the Rx signal projected on the Rx antenna which is assumed to be an infinitesimal dipole antenna for simplification. Hence, the complex time-variant wireless channel defined in eq. (2.2b) which corresponds to the propagation between m-th Tx to the n-th Rx through the scattering from the human limb model at snapshot t and subcarrier frequency f_k could be computed in a similar manner as eq. (2.1) by,

$$\begin{aligned} H'^{,\mathrm{TV}}_{n,m}(\kappa, f_k) &= \frac{1}{I_0|\boldsymbol{e}_0|} \sum_{i \in \Omega(\kappa)} \boldsymbol{E}_i^{\mathrm{s}}(\kappa, f_k) \cdot \hat{\boldsymbol{e}}_n \\ &\simeq H^{\mathrm{TV}}_{n,m}(\kappa, f_k) \end{aligned} \tag{4.32}$$

Table 4.2: Human limb and CSI model parameters

Parameters	**Values**
Motion segment period T_i	1.2 s
Human height Λ	180 cm
Arm r_1 and wrist r_2 radius	7, 3.5 cm
Hand width w'_{hd} and height w''_{hd}	9, 18 cm
Hand elevated angle $\vartheta_{\mathrm{z,hd}}(\kappa)$	30°
Average $\boldsymbol{p}_\iota(\kappa)$ resolution	5 mm
Number of $\boldsymbol{p}_\iota(\kappa)$ (one snapshot)	7,067 - 7,115
Number of snapshot	10.000
Snapshot sampling frequency	2,500 Hz
Center frequency	5.31 GHz

where I_0 and $\hat{\boldsymbol{e}}_n$ are the constant current on an infinitesimal dipole Tx antenna and the polarization of n-th Rx antenna respectively. The scattered electric field $\boldsymbol{E}_i^{\mathrm{s}}(\kappa, f_k)$ of the i-th surface points are referred to those addressed in section 4.4.2. Here subscript (n, m) is omitted from the electric field for brevity. Finally, the simulated CSI model is estimated by substituting the dynamic component in eq. (4.32) and the static component in eq. (4.12) to the CSI model in eq. (2.2).

Given the human limb with the surface points, we can simulate the the distribution of micro-Doppler frequency for each i-th surface point by utilizing the bistatic radar model as stated in eq. (2.8). Suppose the transmission whose parameters of RF signal propagation and the size of human limb model is summarized in Table. 4.2. Assuming a simple motion of hand gesture swiping in horizontal and vertical direction respectively as depicted in Fig. 4.11, it can be observed from the figure that surface points located near shoulder produced smaller Doppler shift, indicated by gray and yellow, than those near the hand segment which are colored in red which denotes the direction of hand moving away from the bistatic baseline. This characteristic of micro-Doppler signature is reflected, after accumulated at receiver, as the broadening of the Doppler power spectrum which will be further discussed in sec. 4.5.

With the simulated CSI model, we are also able to investigate the spatial distribution of the path gain in addition to the Doppler frequency from each surface points on the human limb that are the main two factors that influences the joint time-Doppler power spectrum as mentioned in [94]. The simulation has been conducted under the same configuration with those in Fig. 4.11 given the simulation parameter denoted in Table 4.2. The complex dielectric constant of the human skin defined in [146] was applied in the dielectric scattered power prediction from the human limb. Since the the generated surface points is distributed in the nearly square alignment, circular plate size parameter ϱ was set to $\frac{1}{\sqrt{\pi}}$ according to the equi-surface between square and circle as discussed in section 4.4.3. As depicted in Fig. 4.12,

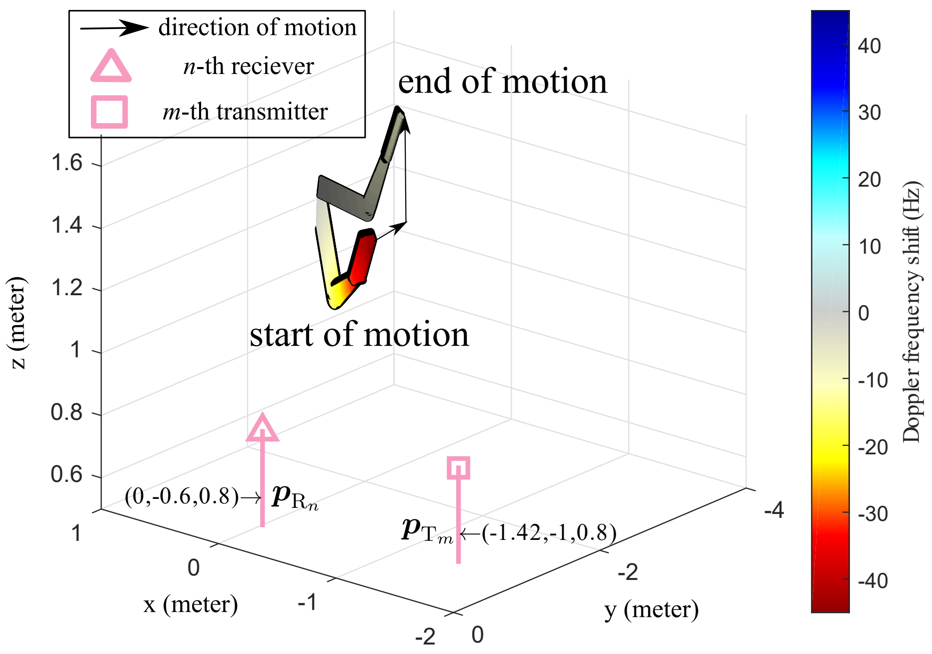

Figure 4.11: Micro-Doppler frequency corresponding to the movement of each surface point on limb surface assuming 5.31-GHz RF signal is transmitted from $\boldsymbol{p}_{\mathrm{T}_m}$ and observed at $\boldsymbol{p}_{\mathrm{R}_n}$.

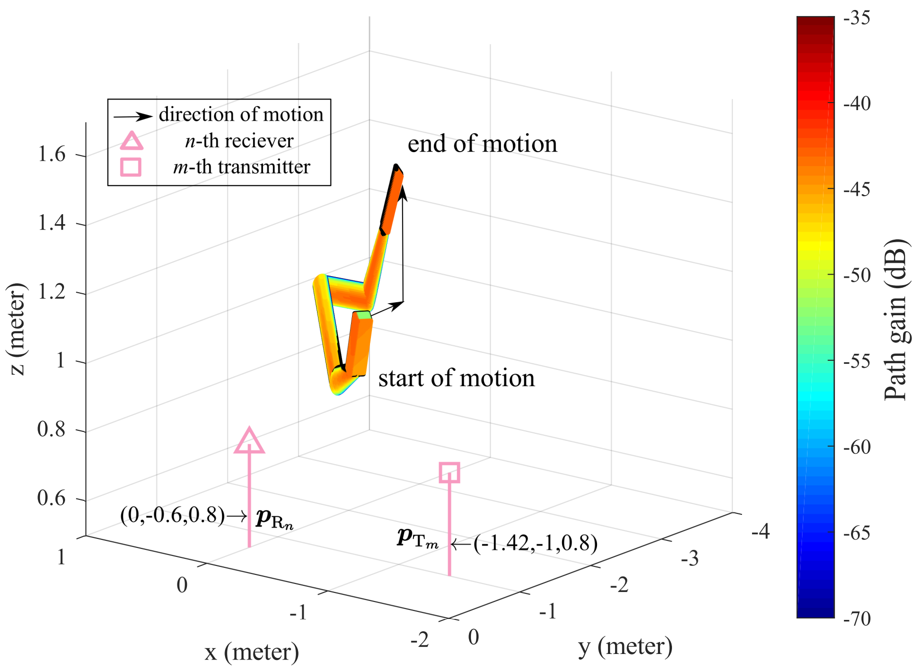

Figure 4.12: Distribution of complex attenuation scattered from each human limb surface point in terms of path gain given 5.31-GHz RF signal propagation between $\boldsymbol{p}_{\mathrm{T}_m}$ and $\boldsymbol{p}_{\mathrm{R}_n}$.

the spatial distribution of the TV-CSI complex attenuation were plotted in term of path gain $\left\|\sum_{i\in L_{\mathrm{TV}}} \alpha_i^{\mathrm{TV}}(\kappa, f_k)\right\|^2$ to visualize the the contribution of each i-th surface circular area to the overall TV-CSI. As expected, the stronger path gain is not necessary coming from a certain part of human limb but rather depending on the incident and scattered angle relative to Tx and Rx position which, in this case, could be described by eqs. (4.18) - (4.26). In the Doppler spectrum, this will translate to the variation of peak level at their respective Doppler frequency induced by each part of the human limb as depicted in Fig. 4.11.

4.5 Micro-Doppler Effect Produced by Simulated CSI

We will further investigate the micro-Doppler effect produced by the movement of human limb through the spectral analysis of the short-time Fourier transform (STFT). As mention in section 2.3.3, this transformation could decompose multiple components of Doppler frequency induced from different parts in terms of the power spectrum density. The limitation of STFT spectrum that could strongly influence the observable spectrum in the context of time-Doppler frequency uncertainty will be addressed. Finally, we then compare the micro-Doppler effect produced by the simulated CSI with those from the measurement campaign.

4.5.1 Doppler Power Spectrum of Hand Gesture and Uncertainty Trade-Off

Since the Doppler term is located at the phase of CSI, the simple way to obtain the instantaneous Doppler profile is by taking the first derivative to the phase term of CSI at each timestamp. One of famous method is through the usage of Hilbert transform (HBT) [89]. However, as stated in section 2.3.3, HBT method works when there is only a single component of Doppler frequency which is not the case for the motion of human limb. This is because, as clearly seen from eq. (4.13) and the simulation in Fig. 4.11, Doppler frequency in the phase term of TV-CSI at a certain time is a combination of various Doppler frequency components continuously spread over the limb surface. Hence, STFT with Gaussian window $g(\kappa)$ [93, 94], one of well-known joint time-frequency analysis, is applied to decompose these micro-Doppler components within a short-time window. Hence, Doppler-variant transfer function [50],

$$B_{n,m}(\delta, f_{\mathrm{d}}, f_k) = \sum_{\kappa=-\infty}^{\infty} \hat{H}_{n,m}^{\mathrm{TV}}(\kappa, f_k) g(\kappa - R\delta) \exp\left(-\mathrm{j}2\pi f_{\mathrm{d}} \kappa T_{\mathrm{s}}\right) \tag{4.33}$$

where δ, R, and $\hat{H}_{n,m}^{\mathrm{TV}}(\kappa, f_k)$ are the short-time index and the hop size between consecutive STFT, and the estimated TV-CSI terms obtained from eq. (2.2) by,

$$\hat{H}_{n,m}^{\mathrm{TV}}(\kappa, f_k) = H_{n,m}(\kappa, f_k) - \hat{H}_{n,m}^{\mathrm{TIV}}(\delta, f_k) \tag{4.34}$$

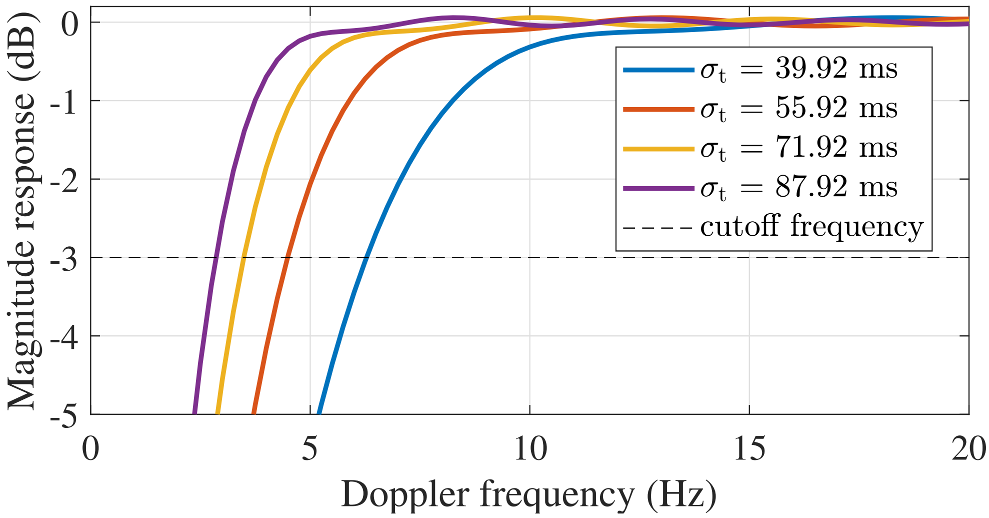

Figure 4.13: Magnitude of high-pass Gaussian filter $20\log|\mathscr{H}(f_{\mathrm{d}})|$ at different standard deviation (σ_{t}).

Since this static component can be assumed as a constant within a short period of time, $\hat{H}^{\mathrm{TIV}}_{n,m}(\delta, f_k)$ can be estimated by the weighted moving average,

$$\hat{H}^{\mathrm{TIV}}_{n,m}(\delta, f_k) = \frac{\sum\limits_{\kappa=-\infty}^{\infty} H_{n,m}(\kappa, f_k) g(\kappa - R\delta)}{\sum\limits_{\kappa=-\infty}^{\infty} g(\kappa - R\delta)} \tag{4.35}$$

This weighted average can be regarded as the special case of the low-pass Gaussian filter with frequency response $\mathscr{L}(f_{\mathrm{d}})$ [147]. Therefore, eq. (4.34) can be rewritten in terms of $H_{n,m}(\delta, f_k)$ filtered by the high-pass Gaussian filter whose frequency response can be easily determined by $\mathscr{H}(f_{\mathrm{d}}) = 1 - \mathscr{L}(f_{\mathrm{d}})$. By observing the characteristic of high-pass filter gain depicted in Fig. 4.13, it is obvious that a range of distorted Doppler frequency shift get shorten when the standard deviation (σ_{t}) of Gaussian window increases. Suppose the gain higher than 3dB is considered the passband region of this high pass filter, the cutoff Doppler frequency can be computed based on the result in Fig. 4.13 as $f_{\mathrm{d,cutoff}} = \frac{1}{4\sigma_{\mathrm{t}}}$. It should be noted that $B_{n,m}(\delta, f_{\mathrm{d}}, f_k)$ unfortunately suffers from the high pass filter at the lower Doppler frequency shift.

Doppler spectral density from eq. (4.33) can be computed by the following procedure according to [50],

$$P_B(\delta, f_{\mathrm{d}}) = \sum_{\tau\in\mathcal{T}} \left| \sum_{k=1}^{K} B(\delta, f_{\mathrm{d}}, f_k) \exp\left(\mathrm{j}2\pi f_k \Delta f \tau\right) \right|^2 \tag{4.36}$$

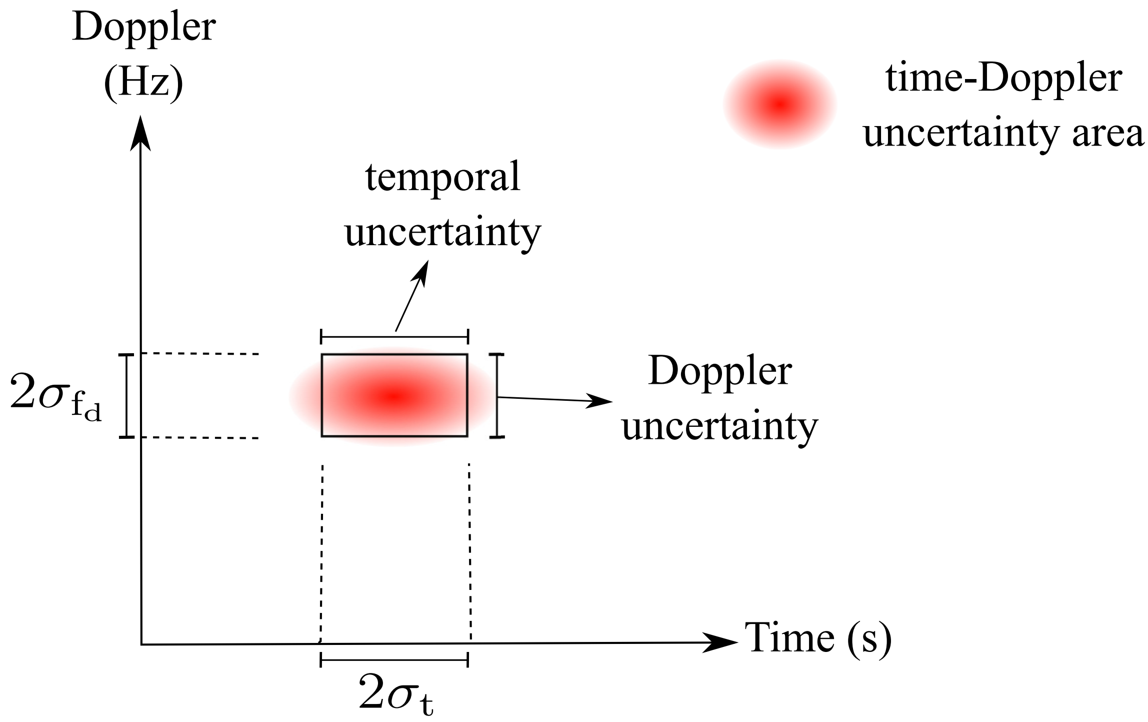

Figure 4.14: Time-Doppler frequency uncertainty area.

where τ, $\mathcal{T}$, and $\mathcal{F}$ are a propagation delay bin, a set of propagation delay within the excess delay of the TV propagation paths, and a set of subcarier frequency respectively. Here the areas with relatively higher power correspond to various components of Doppler frequency induced by the movement of each surface point on the limb. According to the closed-form solution of STFT with Gaussian window provided in [94], the Doppler power is proportional to the complex attenuation of TV-CSI in eq. (4.13) whose distribution was visualized in Fig. 4.12.

Beside the influence of attenuation from each surface surface points, this broadening of Doppler spectrum is also governed by time-frequency uncertainty trade-off [93, 94]. In general, this uncertainty stated that we can accurately localize each Doppler frequency component but with the lost of time resolution since the the longer duration is needed to resolve Doppler frequency information. Likewise, the time-series signal could be perfectly localized with a larger information in Doppler spectrum thus reducing the Doppler resolution accordingly. Therefore, STFT could localize both time and Doppler frequency information but with a lower resolution. Similar to Heisenberg's uncertainty in Quantum physics, the resolution trade-off in STFT restricts to the fact that the signal information is observable within the rectangular uncertainty area depicted in Fig. 4.14 which is equivalent to the product of time and Doppler variance. According to the Gabor limit [93], the optimal trade-off is reached by applying the Gaussian window to the STFT. Hence the uncertainty trade-off can be expressed mathematically as,

$$\sigma_{\mathrm{t}}\sigma_{\mathrm{f_d}} \geq \frac{1}{4\pi} \tag{4.37}$$

where $\sigma_{\mathrm{f_d}}$ is the standard deviation of the corresponding Gaussian in Doppler frequency domain. To visualize this effect, let us consider the STFT of human limb with the same course of motion as shown in Fig. 4.11. For comparison, two STFT spectrum with different uncertainty trade-off were illustrated in Fig. 4.15. Although both figures can manifest the micro-Doppler effect from the hand and arm segments which are depicted as the the larger and multiple stripes on the spectrum, they both additionally suffer from the resolution trade-off. Specifically at around 1 s in the spectrum, wider spread in the Doppler domain is visibly observed in Fig. 4.15a as the variation reaches -52 Hz whereas the peak at the same time in Fig. 4.15b has relatively less spread of around -42 Hz. Vice versa, The former spectrum has a better temporal resolution where the shorter spread resulting in the first motion observably completed before 1.5 s while the latter experience a longer duration.

The thoroughly understanding the effect of uncertainty trade-off is beneficial to decide a short-time period δ for the analysis of the Doppler spectrum.

4.5.2 Comparison of Doppler Power Spectrum Produced between Simulated CSI and Measurement

The applicability of our simulated CSI will be investigated with the result from the measurement campaign. The hardware configuration to obtain Wi-Fi CSI is the same as in the measurement setup of section. 3.5.1. In general, the 1×2 MIMO configuration between two laptops was employed where the novel b2b calibration proposed in chapter 3 has been implemented to mitigate the undesired phase rotation. Injection and monitor mode were enabled to control transmission parameters such as transmission rate and the number of active antennas. The location of Tx and Rx antennas as well as the hand gesture's performer location were adjusted according to the simulation scenario depicted in Fig. 4.12. two segments of hand swiping in 60-cm horizontal and vertical direction were performed accordingly which is similar to the simulation condition. For a fair comparison with the simulated CSI case, the subject was asked to complete each motion segment within 1.2 s duration and paused with the same duration before begin the motion segment. Three measurement were conducted for reproducibility. In all measurements, 2,500 Wi-Fi packets were sent every second over the 5.31 GHz frequency band with 40 MHz bandwidth OFDM signal. 30 number of subcarrier frequency was measured according to the limitation of CSI tool [35]. STFT Doppler spectrum were calculated based on eq. (4.36). CSI was additionally captured in the absence of hand gesture as the reference to calculate the spectrum noise floor.

Depicted in Fig. 4.16 were the Doppler spectrum calculated from the simulated CSI and the measured CSI with the b2b calibration. Standard deviation of Gaussian window was

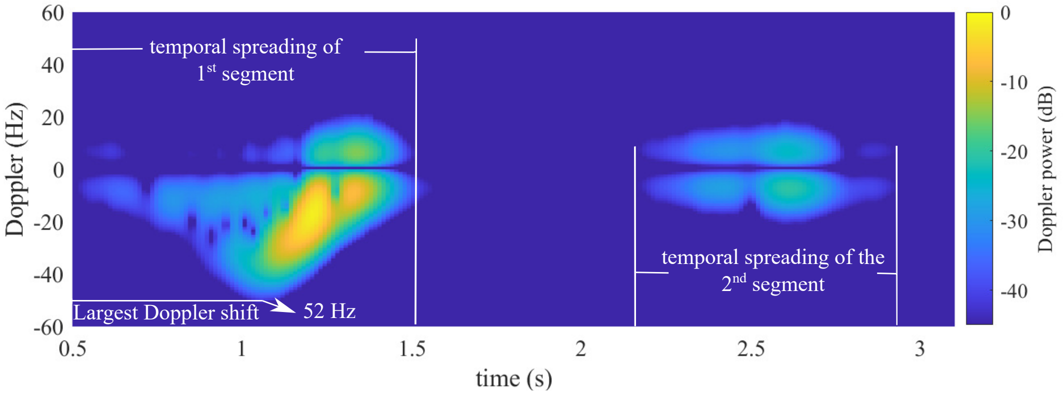

(a) Short-time spectrum with $\sigma_{\mathrm{t}} = 22.7$ ms

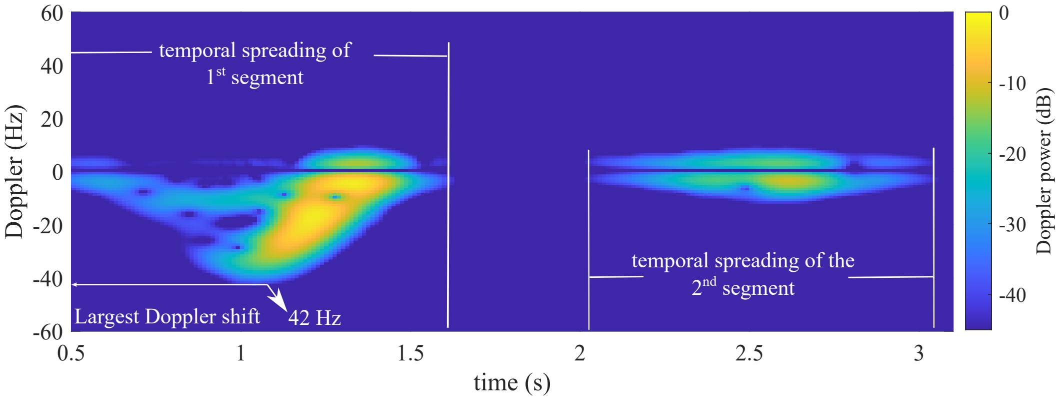

(b) Short-time spectrum with $\sigma_{\mathrm{t}} = 53$ ms

Figure 4.15: Short-time spectral density $P_B(\delta, \mathrm{f_d})$ and $f_{\mathrm{d}}^{(k)}(\kappa)$ distribution of hand swiping in horizontal and vertical direction.

arbitrarily set to 32 ms. Based on the recorded CSI in the static environment, the overall average of power spectrum is regarded as the noise floor since there is no Doppler frequency even at 0 Hz as the TIV component was already removed before applying STFT using eq. (4.35). Therefore, the noise floor in the Doppler spectrum was estimated to be around -28 dB whereas the noiseless condition was assumed for the simulation. To limit the analyzed Doppler frequency within the motion area, Lower bound and upper bound of propagation delays are determined based on the location of the hand gesture performer as $\tau_{\min} = 0$ s and $\tau_{\max} = 82.76$ ns respectively.

In comparison, it was found that the overall characteristic of micro-Doppler effect computed from the simulated CSI showed a certain agreement with all three measurements. The bell-shape Doppler profile was also produced in a similar fashion as the selected speed profile mentioned in section 4.2.1. At around $0.5 - 1$ s, both simulation and measurement results exhibits the smaller power Doppler which was spread out in the negative Doppler

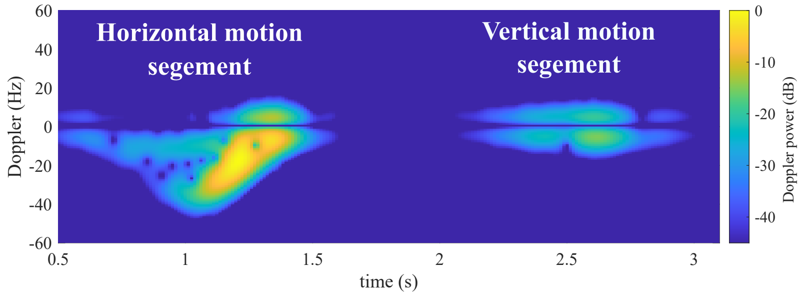

(a) Simulated CSI with 50 dB SNR

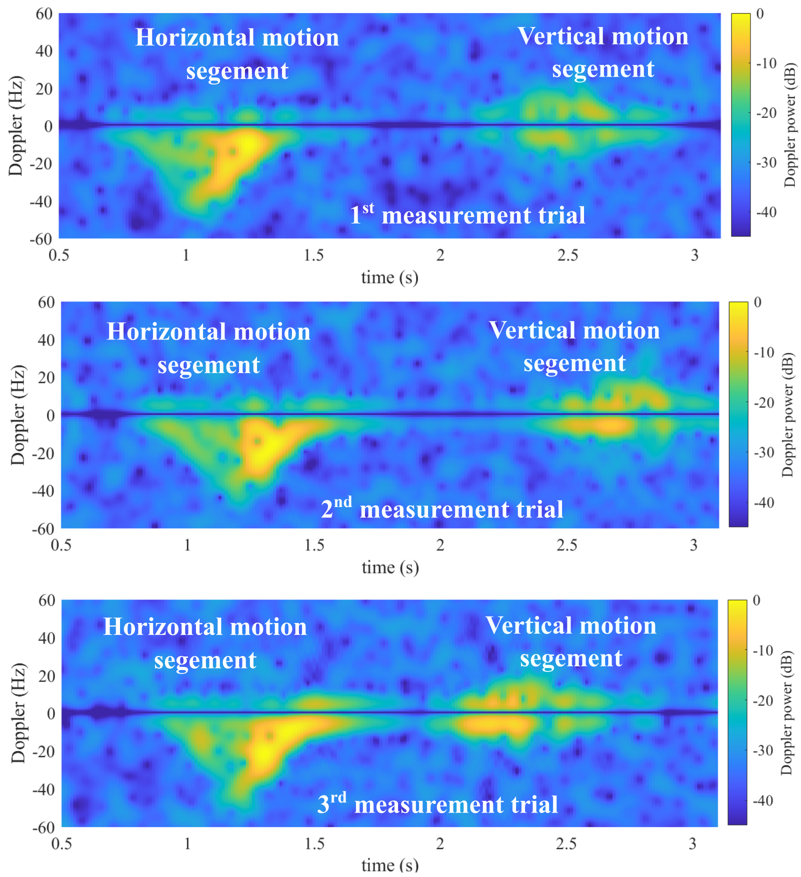

(b) 3 trials of measured CSI

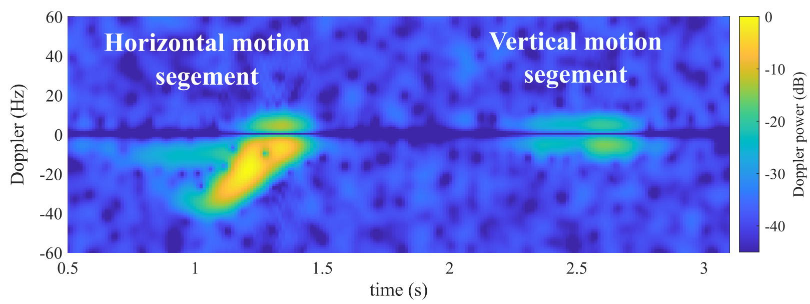

(c) Simulated CSI with 40 dB SNR

Figure 4.16: Comparison of the Doppler spectrum between the simulated and measured CSI

plane. On the other hand, the relative higher power was observed at $1 - 1.5$ s in all cases due to the influence of the complex attenuation [20, 84]. In the vertical motion, Doppler frequency shift was comparatively smaller due to the orthogonal direction of motion to the bistatic radar baseline according to eq. (2.8). Although simulated Doppler spectrum also successfully generated a similar micro-Doppler pattern, the measurement exhibited a fairly larger Doppler shift within ± 20 Hz in comparison with the ± 15 Hz spread in the simulated Doppler. This is possibly due to the inaccuracy of the non-rigid motion of robot arm that underdetermined the speed distribution along the human limb in the vertical direction. To simulate the noisy Doppler power spectrum, the simulated result with 40 dB SNR was additionally compared in Fig. 4.16c. The result could balance the simulated spectrum shape closer to the measurement in terms of the noise level.

Regarding the level of Doppler power, the result from the measurement had a shorter dynamic range of around 30 dB in comparison with the simulated Doppler of 50 dB. Since the measured CSI was normalized by internal reference of Wi-Fi chip [35], the temporal fluctuation in CSI may as well normalize which affected the dynamic range of the Doppler power spectrum. Although the further detailed examination is needed to clarify this effect, it may not introduce a strong impact on the motion tracking because the spectrum shapes are the most important factor for extracting the hand Doppler profile that will be discussed in chapter 5.

This experiment has confirmed the usability of the simulated CSI model to deterministically reproduce the micro-Doppler effect due to the motion of hand gestures in terms of joint time-Doppler spectrum.

4.6 Summary

To investigate the micro-Doppler effect during hand gesture, this chapter sought the solution through the deterministic hand movement and the EM scattering characteristic or RF signal that interacts with the moving object. It is widely known that hand gesture involves not only the hand movement but the entire human limb. Therefore, the kinematic model of 6R-PUMA robot arm was utilized to simulate the non-rigid body motion of human limb due to its simplicity and similarity to the physical motion of human limb. In general, the skeleton motion controlled by three joints of limb: shoulder, elbow, and wrist, were estimated using the robot inverse kinematic problem. The skeleton were then covered with surface points distributed over the human limb surface. For simplicity, surface of hand, forearm, elbow, and upperarm are represented by four geometric shapes of cuboid, truncated cone, sphere, and cylinder respectively. The usage of surface surface points is to compute the time variant component of CSI via PO approximation tool.

Motivated by the practical issue of surface reconstruction in the applying the PO in the dynamic scenario of human limb motion, the modified PO based on circular mesh have been introduced. The validation of the proposed PO was compared with the widely-implemented PO with triangular mesh. The simulation result confirmed the usage of circular mesh PO in both flat and curvature surface given the mesh resolution around the 10^{th} and 25^{th} of the wavelength respectively. The uneven border increased the discrepancy for the circular mesh PO when the backscattered direction is nearly parallel. In other angles, the 10^{th} of the wavelength is still acceptable.

By computing the scattered field from the moving human limb, the time-variant CSI can be calculated as the scattered field normalized by the magnitude of the EM wave emitted from the Tx antenna. With the simulated CSI, we are able to investigate the spatial distribution of micro-Doppler frequency and the path gain which are the main two influential parameters to the spectral characteristic of the joint-time time-Doppler power spectrum. It was found that the dominated path gain is not always corresponding to only hand segment nor other arm segments. In fact, the characteristic depends on the incident and scattered angles with respect to Tx and Rx position according to the EM scattering theory. Lastly, the usability of the simulated model has been comparatively confirmed with the measured CSI. STFT was introduced as the joint time-Doppler analysis tool together with addressing the drawback in the context of uncertainty trade-off. The experiment result has shown the ability of the simulated CSI to reproduce the micro-Doppler effect due to the movement of hand gesture similar to those produced from the measured CSI.

The detail analysis on the hand Doppler signature will be addressed in chapter 5 in order to develop the extraction method of the hand-only Doppler signature. As the moving features, The hand signature will be a vital part for the development of hand trajectory tracking that will be discussed in chapter 6.

Chapter 5

Temporal Profile Extraction of Hand Doppler Signature

5.1 Introduction

From the simulated CSI described in chapter 4, it opens up the possibility to investigate the contribution of each small surface area on human limb to the overall CSI at each timestamp while performing the hand gesture. Since the objective of this thesis is to track the hand motion during gesture performing, Doppler frequency signature induced exclusively for hand segment is straightforwardly important for the hand tracking problem which will be discussed in the next chapter. To fulfill this goal, the characteristic of hand Doppler signature will be examined based on the distribution of path gain and Doppler frequency produced by time-variant CSI component in section 5.2. Specifically, the time progression of hand Doppler frequency and its corresponding path gain will be compared with those from the arm segment which is treated as the interference.

Based on the findings on this investigation, the criteria for the profile extraction of hand Doppler signature will be established in section 5.3. The proposed could detect the likely hand component out of the Power Doppler spectrum separately for each short-time window considering the Doppler spread due to micro-Doppler effect and the uncertainty trade-off. Finally, the simulation will be conducted in section 5.4 to validate the performance of the proposed profile extraction technique in terms of discrepancy between the extracted profile and the reference provided directly from the human limb model. Since the extracted hand Doppler profile will be directly applied for hand gesture tracking in chapter 6 which requires multi-static radar system to derive the trajectory, the validation will be conducted under the Wi-Fi multiple-input-multiple-output (MIMO) configuration.

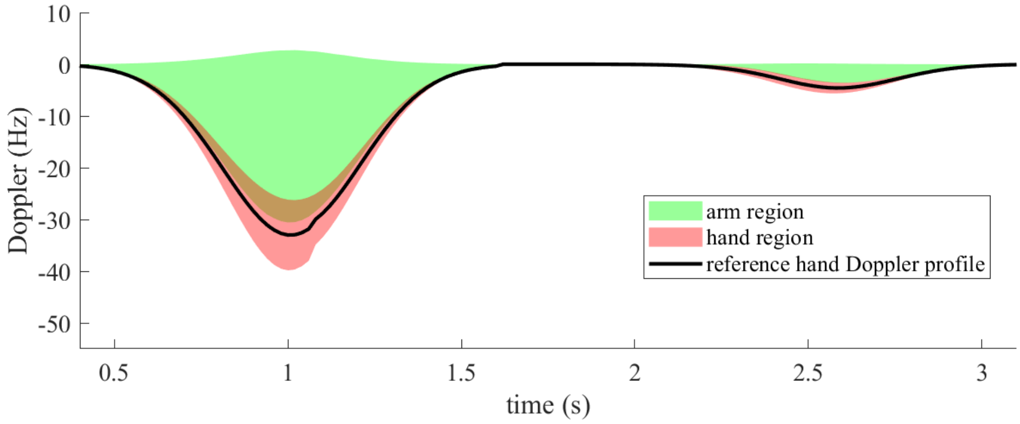

(a) Instantaneous Doppler frequency distribution

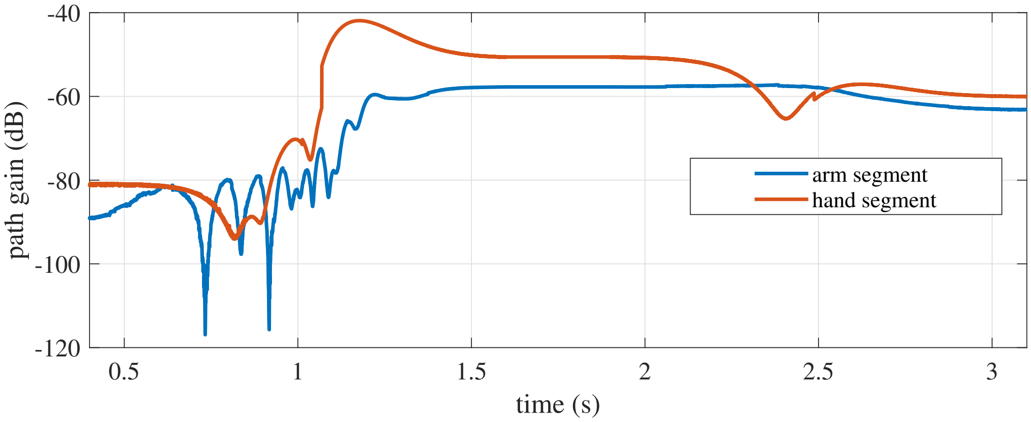

(b) Instantaneous path gain distribution

Figure 5.1: Temporal characteristic of Doppler signature and path gain co responding to hand and arm segment of human limb model.

5.2 Characteristic of Hand Doppler Signature During Hand Gesture

To estimate the Doppler profile component induced from the hand segment which will be used for tracking a hand trajectory, the first step is to investigate how the micro-Doppler effect influences the spectral shape of the Doppler power spectrum. In general, as mentioned in [94], the Doppler power level is proportional to the magnitude of complex attenuation with respect to each part on the human limb surface. In each short-time window, the radial speed of each surface point shifts the Doppler power to situate at their corresponding Doppler frequency. Regardless of position on the human limb surface, the small surface areas that exhibit similar Doppler shift will have their Doppler power superimposed in the spectrum. This is in fact the result of the Fourier-based signal decomposition in the STFT explained mathematically eq. (4.36).

To ease our analysis on the hand Doppler frequency component, the time-variant component of CSI from eq. (4.32) is re-introduced in terms of the combination between the dynamic channels corresponding to the scattered wave from the hand and arm surfaces,

$$\begin{aligned} H'^{,\mathrm{TV}}_{n,m}(\kappa, f_k) &= H'^{,\mathrm{TV,hd}}_{n,m}(\kappa, f_k) + H'^{,\mathrm{TV,arm}}_{n,m}(\kappa, f_k) \\ &\simeq \frac{1}{I_0|\boldsymbol{p}_0|}\left[\sum_{i_{\mathrm{hd}}\in\Omega_{\mathrm{hd}}(\kappa)} \boldsymbol{E}^{\mathrm{s}}_{i_{\mathrm{hd}}}(\kappa, f_k)\cdot\hat{\boldsymbol{e}}_n + \sum_{i_{\mathrm{arm}}\in\Omega_{\mathrm{arm}}(\kappa)} \boldsymbol{E}^{\mathrm{s}}_{i_{\mathrm{hd}}}(\kappa, f_k)\cdot\hat{\boldsymbol{e}}_n\right] \end{aligned} \tag{5.1}$$

where I_0, $\boldsymbol{e}_0$, $\hat{\boldsymbol{e}}_n$ are the constant current magnitude and electric dipole moment of infinitesimal small Tx dipole antenna, followed by the polarization direction of the infinitesimal small Rx dipole antenna respectively. $\Omega_{\mathrm{hd}}(\kappa)$ and $\Omega_{\mathrm{arm}}(\kappa)$ are the set of surface points on hand and arm surfaces respectively. Both sets are the subset of $\Omega(\kappa)$ which is the set of the entire surface points on the human limb model at each timestamp. With this definition, we can compute the Doppler profile induced from hand and arm segments denoted as $f^{(i_{\mathrm{hd}})}_{\mathrm{d,hd}}(\kappa)$ and $f^{(i_{\mathrm{arm}})}_{\mathrm{d,arm}}(\kappa)$ respectively by utilizing eq. (4.13b). Here subscript (n, m) is omitted from the electric field and Doppler frequency for brevity. Likewise, the total path gain scattered from hand and arm segment can be easily computed by $\left\|H'^{,\mathrm{TV,hd}}_{n,m}(\kappa, f_k)\right\|^2$ and $\left\|H'^{,\mathrm{TV,arm}}_{n,m}(\kappa, f_k)\right\|^2$ respectively.

Let us consider the STFT Doppler power of the simulated hand gesture depicted in Fig. 4.16a. With the notation in eq. (5.1), we are able to analyze the time-varying hand-only Doppler signature and its path gain. Both variables are then illustrated in Fig. 5.1 in comparison with those induced by the rest of arm segment. Regarding the Doppler signature shown in Fig. 5.1a, all Doppler frequency induced by hand surface points, $f^{(i_{\mathrm{hd}})}_{\mathrm{d}}(\kappa)$, are varied within the red region whereas those from arm surface points which are considered as the interference situated along the green region. From the area spanned by these two regions, it is discovered that the hand segment induces a larger magnitude of Doppler frequency shift than the arm segment most of the time due to faster acceleration the hand exerted. The temporal change of path gain in the time-variance of CSI can be visibly observed in Fig. 5.1b. Although the path gain caused by hand segment seems to dominate those from the arm segment, this characteristic depends on the orientation of human limb relative to both transmitter and receiver position. That is the reason the lower path gain of the hand segment can be seen during the periods of $0.7 - 0.9$ s and $2.3 - 2.5$ s. Consequently, it is challenging to pin point the micro-Doppler signature from the path gain alone without the knowledge of angular information. The revelation of micro-Doppler effect characteristic will be considered as the basic assumption for the development of the method to extract hand-only Doppler signature which will be addressed in the next section.

In addition, the time-varying path gain characteristic has also clearly confirmed the change of STFT spectrum shape depicted in Fig.4.16a. Especially, the rapid increase of path gain of around 35 dB during $1 - 1.5$ s as shown in Fig. 5.1b due to the scattered and incident angles of human limb clearly influenced the Doppler spectrum at the same period. Within $1 - 1.2$ s, the stronger Doppler is concentrated in the higher Doppler shift of the hand because the arm segment path gain is still considerably weaker. This investigation also addresses the usefulness of our simulated CSI to the deep analysis of micro-Doppler effect.

5.3 The Proposed Hand Doppler Profile Extraction Technique Based on Peak Detection Approach

According to the findings from the analysis in previous section, it could be suggested that the hand Doppler component should be likely positioned at or near the farthest peak in the spectrum with respect to the faster speed of the hand segment. Since the dominant Doppler power is not always coming from the hand movement but rather depending on the incident and scattered and angles, the Doppler power may not be a reliable feature unless the angular information of human limb is given. Considering the time-Doppler frequency uncertainty, the width of each spectrum peak may possibly contain multiple Doppler components from either or both hand and arm segments whose Doppler frequencies are indistinguishable within the time-Doppler uncertainty area. This prevents us to deterministically extract a representation of the hand Doppler component from the spectrum.

Therefore, the heuristic approach is chosen for the proposed estimation technique of hand Doppler signature. In a nutshell, the Doppler frequency induced from the hand surface is defined as the expectation value of the Doppler spectrum over the region that likely contains the hand Doppler component. Let us define this region as the hand Doppler window $\mathcal{S}_\delta$. The temporal profile of hand Doppler could be computed by,

$$\hat{f}_\mathrm{d}(\delta) = \frac{\sum\limits_{f_d \in \mathcal{S}_\delta} f_\mathrm{d} P_B(\delta, f_\mathrm{d})}{\sum\limits_{f_d \in \mathcal{S}_\delta} P_B(\delta, f_\mathrm{d})} \tag{5.2}$$

It is obvious that the criteria to determine $\mathcal{S}_\delta$ may differ at each short-time period due to the variety of the spectral shapes. Through the heuristic investigation, we are able to break down into four scenarios where the criteria to select $\mathcal{S}_\delta$ region are developed separately depending on the spectral shape. To ease the explanation, the flowchart of the proposed technique is summarized in Fig. 5.2. Specifically, we divides the spectrum shape into single and multiple peaks spectrum. The detail explanation of the selected region selection are narrated in the followings.

1. **Single-peak Doppler spectrum.**

   - **Scenario 1: One peak region**

     Although the non-rigid body movement would have usually produced multiple spectrum peaks, it is possible to have only a single peak on the spectrum. This scenario happens when there clearly exists the dominant component with a distinct high power surrounded by other components at nearby Doppler frequency shift with comparatively weaker power. For instance, the path gain and Doppler distribution at $1.6 - 1.7$ s in Fig. 5.1 also describes this case with the dominant component belongs to the scattered power from the hand surface. If the Doppler uncertainty $\sigma_{\mathrm{f_d}}$ is larger, these weaker components were then merged to the dominant component as clearly seen in the spectrum of Fig. 4.16a at the same period. The peak spectrum shape is consequently wider than $\sigma_{\mathrm{f_d}}$ as depicted in Fig. 5.3a whose area ranging from 5 to 40 Hz.

     Suppose the dominant peak depicted as the green cross marker in Fig. 5.3a is located at $f_{\mathrm{d}} = \rho_\delta^{(1)}$ Hz on the spectrum whose power is greater than noise the noise floor depicted as the black line in the figure. In this case, the region on the spectrum between two nearest valley points from $\rho_\delta^{(1)}$ represented by the magenta line is regarded as the selected region $\mathcal{S}_\delta$. As clearly depicted in the figure, the portion on the spectrum that lower than noise floor is excluded in the selected region.

2. **Multiple-peaks Doppler spectrum.**

   This is a typical spectrum shape in the presence of micro-Doppler effect. Without the influence of the dominant Doppler component, it visibly exists the spectrum with multiple peaks. Each peak width again likely contain a set of Doppler components whose Doppler frequency is smaller than the uncertainty resolution.

   Suppose it exists N_ρ peaks on the spectrum with the power stronger than the noise floor. The corresponding Doppler frequency to these peaks can be denoted in an descending order as $\rho_\delta^{(1)} > \rho_\delta^{(2)} > ... > \rho_\delta^{(N_\rho)}$. Hence, similar to the single peak case, the regions over the noise level that span between two nearest valley points of these peaks are defined as as $\mathcal{S}_\delta^{(q)}$ where $q = 1, 2, ..., N_\rho$. With respect to the distribution of $\rho_\delta^{(q)}$, the selection criteria of the region that most-likely contains hand Doppler component can be broken down into three scenarios as visualized in Fig. 5.3b-5.3d under multiple peak spectral shapes.

   - **Scenario 2: Multi-peak regions with the same sign of $\rho_\delta^{(q)}$**

     As illustrated in Fig. 5.3b, multiple peaks are situated in the same (negative)

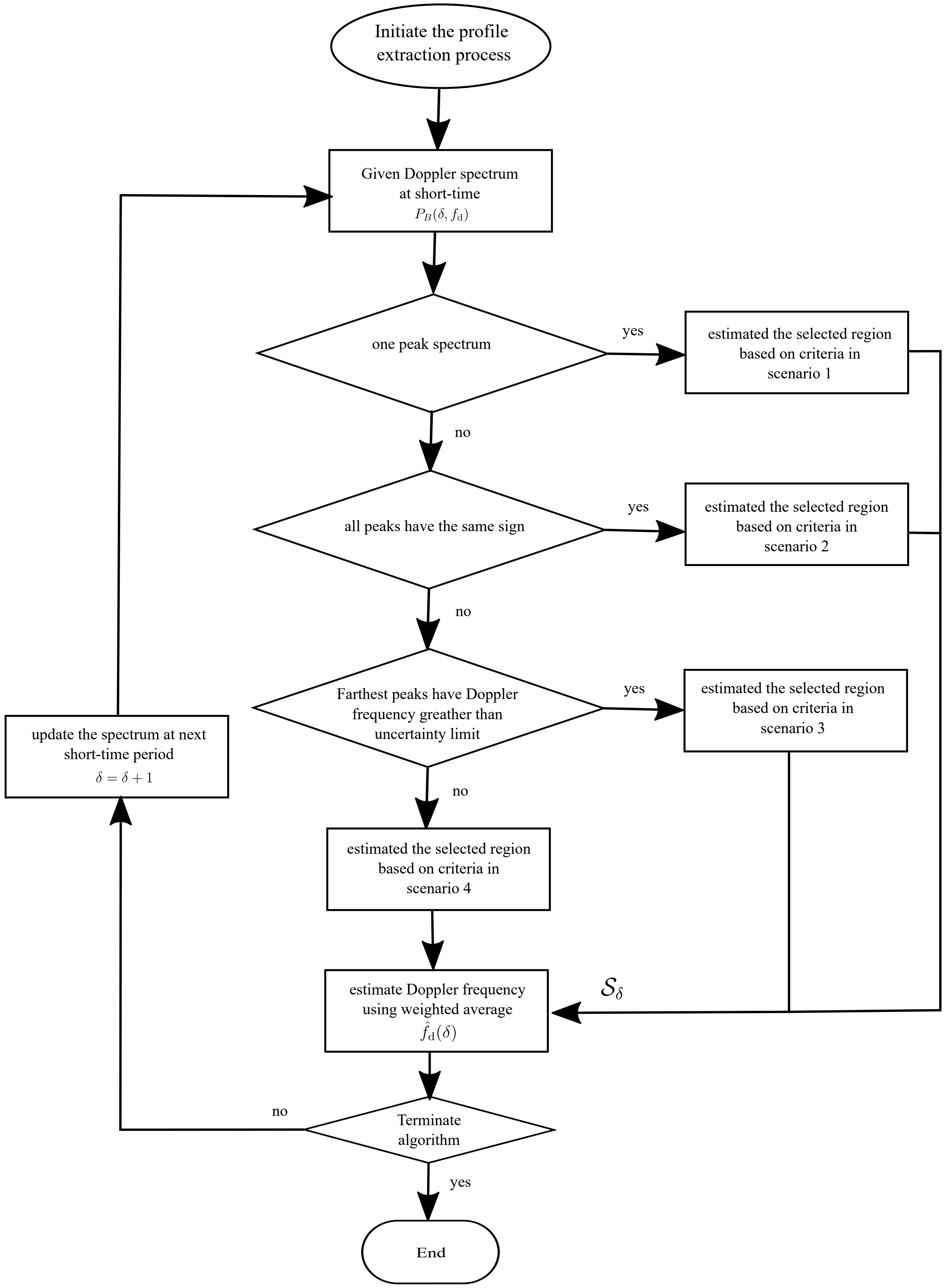

Figure 5.2: Hand Doppler profile extraction flowchart.

Doppler plane. In comparison, it is obvious that the farthest peak denoted as the green marker contains the component with the higher radial speed relative to transmitter and receiver. According to our assumption, hand Doppler profile should be within this peak region. Hence the selected region denoted as magenta line should be $\mathcal{S}_\delta^{(N_\mathrm{\rho})}$ where $N_\mathrm{\rho} = 2$. Otherwise, $\mathcal{S}_\delta^{(1)}$ region will be chosen when all $\rho_\delta^{(q)}$ are positive.

Here the selected region is marked in the magenta in Fig. 5.3b bounded between two nearest local valley whose spectrum is higher than noise floor. It should be noted in the figure that it exists another peak in opposite plane. This peak supposedly belongs to the peak in the consecutive short-time window whose Doppler power got attenuated by the Gaussian window.

- **Scenario 3: Multi-peak regions with the different sign of** $|\rho_\delta^{(q)}| \geq \sigma_{\mathrm{f_d}}$

In this scenario, we have multiple peaks distributed in both planes of Doppler spectrum. Therefore, it exist two peaks candidate that contributes to the fastest speed moving toward and away from the bistatic Doppler baseline as explained in section 2.3. Without additional information, it becomes a challenging task to determine determinisitically which components contains the desired hand Doppler component. As a result, additional assumption is introduced to solve the ambiguity.

Let us define $\rho_\delta^{(1)}$ and $\rho_\delta^{(N_\rho)}$ as the two candidate peaks located farthest in positive and negative Doppler plane respectively. Suppose a majority of limb movement within a short-time window induced the same sign of Doppler frequency. To realize this assumption, the region where Doppler component of hand is likely located can be decided based on a sign of total weighted average over the entire spectrum μ_δ. In other word, this assumption also refers that the minority of the movement in the opposite direction corresponds to a partial part of the arm segment considering the non-rigid body motion. As shown in Fig. 5.3c, $\rho_\delta^{(1)}$ is discarded and thus the selected peak goes to $\rho_\delta^{(N_\mathrm{\rho})}$ where $N_\mathrm{\rho} = 3$ since the majority of movement is away from the baseline which supposedly including the hand segment as well and so does $\mu_\delta < 0$. In a contrast, the selected region becomes $\mathcal{S}_\delta^{(1)}$ when a sign of μ_δ becomes positive.

$$\mathcal{S}_\delta = \begin{cases} \mathcal{S}_\delta^{(1)} & ; \mu_\delta > 0 \\ \mathcal{S}_\delta^{(N_\rho)} & ; \mu_\delta < 0 \end{cases}$$

Again, the selected region denoted as magenta line on the spectrum can be determined with the similar condition as the previous scenario.

- **Scenario 4: Multi-peak regions with the different sign of $|\rho_{\delta}^{(q)}| \leq \sigma_{\mathrm{f_d}}$**
  This is the special case yet difficult to estimate the hand Doppler component. In this scenario, most of Doppler components caused by hand and arm are relatively small and indistinguishable from the spectrum due to coherency. Usually, it exists only two peaks in spectrum at maximum in this case whose Doppler frequency shift is within in uncertain limit.

  Depicted in Fig 5.3d is one of examples in the scenario. This usually happens when the motion direction is nearly perpendicular to the direction from the moving object to the bistatic baseline. The simulation and measurement results in Fig. 4.16 and Fig. 3.13b also shows a similar spectrum shape. Without additionally information, therefore, the only choice to estimate the hand Doppler profile in this special case is to include regions associated with all peaks. Although this criteria may not always capture the hand Doppler component, the Doppler spread is comparatively small which may result in the smaller estimation error.

Defining $\mathcal{S}_{\delta}$ from the above spectrum-variant criteria at each short-time window, the hand Doppler profile can be statistically estimated using eq. (5.2). This temporal profile is supposed to approximately represent the speed of the entire hand although the actual Doppler frequency produced from each point on the surface of our hand consists of various magnitude as clearly seen from the simulation result in Fig. 5.1a. With respect to Doppler and spatial uncertainty, the reference Doppler frequency profile of hand motion $f_{\mathrm{d,hd}}^{\mathrm{ref}}(\delta)$ depicted as solid line in Fig. 5.1a is established for the validation of the proposed extraction method which will be validated in sec. 5.4. For brevity, the subscript (n, m) is omitted from the reference Doppler frequency. The assumption behind the reference hand Doppler profile is based on the crude statistical average within the range of hand Doppler frequency derived from the set of surface points on the surface of hand which can be computed by,

$$f_{\mathrm{d,hd}}^{\mathrm{ref}}(\delta) = \frac{1}{2}\left[\max_{i_{\mathrm{hd}} \in \Omega_{\mathrm{hd}}(\kappa)} f_{\mathrm{d,hd}}^{(i_{\mathrm{hd}})}(\delta) + \min_{i_{\mathrm{hd}} \in \Omega_{\mathrm{hd}}(\kappa)} f_{\mathrm{d,hd}}^{(i_{\mathrm{hd}})}(\delta)\right] \tag{5.3}$$

The reliability of the reference profile has been heuristically tested to produce a fine-grained hand trajectory.

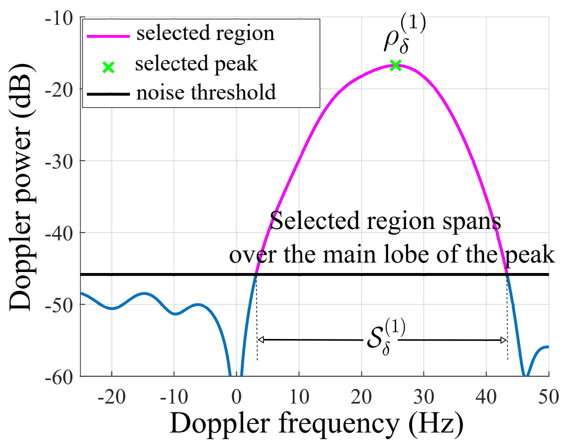

(a) Scenario 1

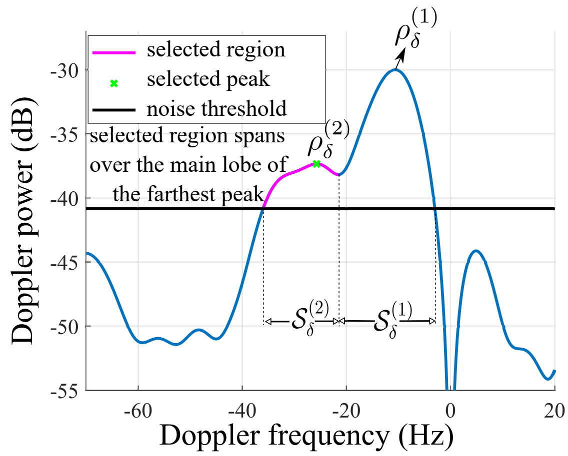

(b) Scenario 2

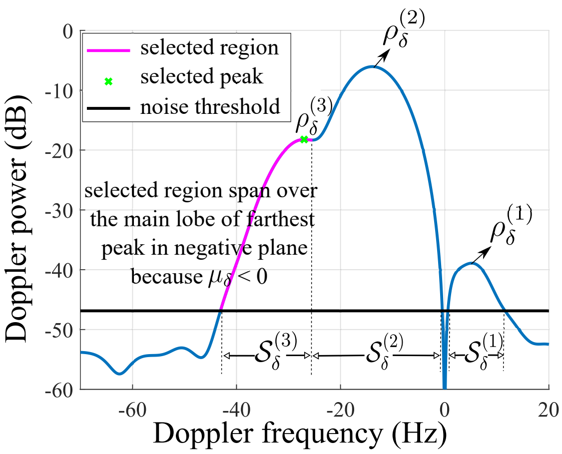

(c) Scenario 3

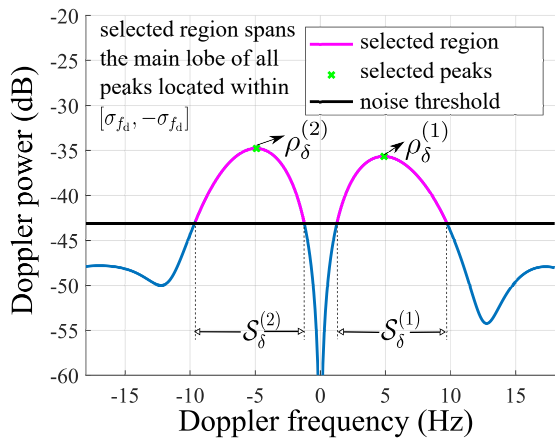

(d) Scenario 4

Figure 5.3: Criteria to select the peak region in eq. (5.2) with respect to 4 different shapes of Doppler spectrum given 5-Hz σ_{f_d}.

5.4 Simulation

The accuracy of the estimated hand Doppler profile extracted from the spectrum will be first validated. The performance of hand trajectory estimation both simulated and measured result will be evaluated and discussed in terms of relative trajectory error. The effect of the estimated initial position on the tracing performance will be also analyzed.

5.4.1 Experiment Scenario

The experiment was conducted in a simulation environment using MATLAB. Two types of hand gestures; squared shape and M shape depicted in Fig. 5.4b, were selected for evaluation of hand trajectory tracking in straight and diagonal directions with respect to yz-plane. The

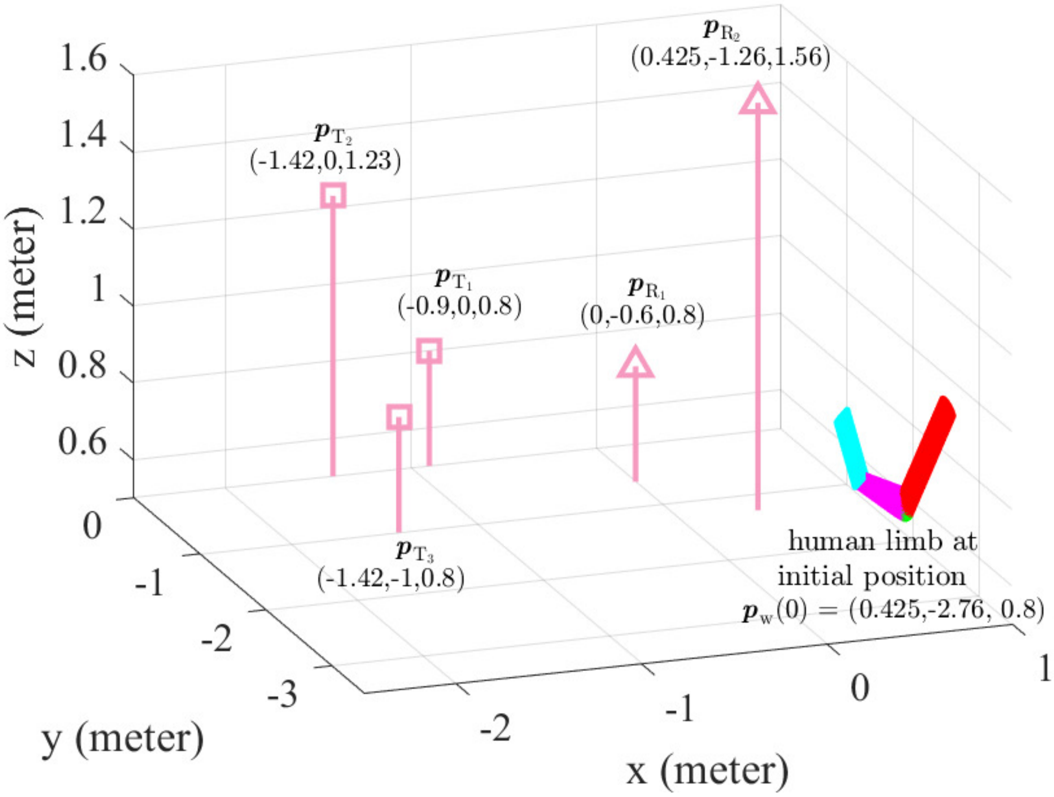

(a) Simulation scenario

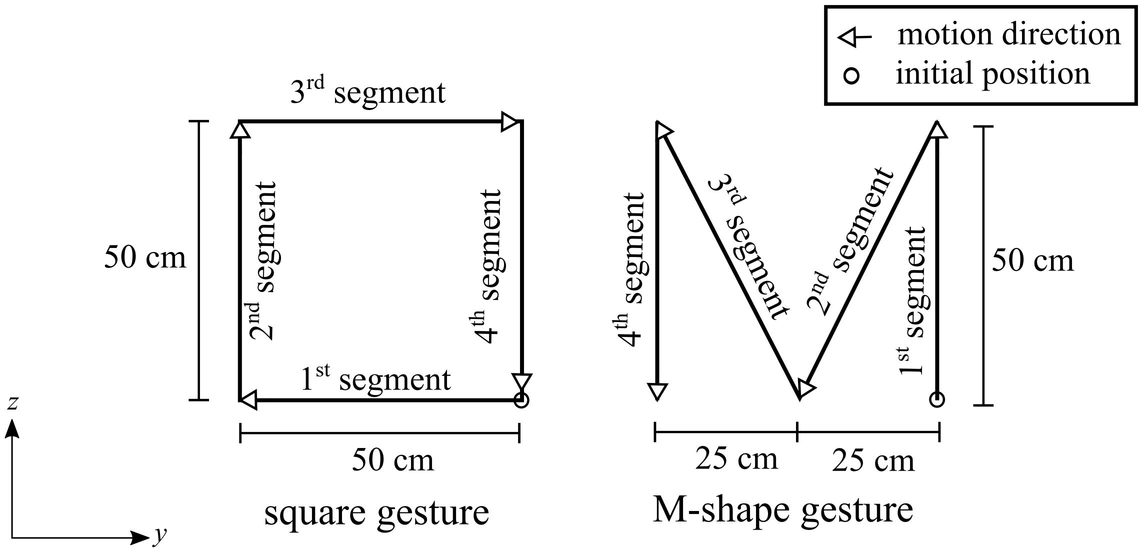

(b) Two shapes of gestures

Figure 5.4: Simulation setup of the moving human limb with 3 Tx and 2 Rx antennas.

Table 5.1: CSI model parameters

Parameters	Values
Number of snapshot	17,500
Snapshot sampling frequency	2,500 Hz
Center frequency	5.31 GHz
Bandwidth	40 MHz
Number of subcarrier frequency	30
AWGN Noise power	50 dB below CSI power
Lower bound of propagation delay τ_{min}	0 s
Upper bound of propagation delay τ_{max}	82.76 ns

simulation scenario depicted in Fig. 5.4a indicated a geometry of hand gestures together with the position of 3 transmitters and 2 receivers. The model in eq. (4.1) was applied to construct the speed profile of hand gesture. Each motion segment has the same movement period and the arbitrary halt period of 0.26 ms was added in between for segment separation. With parameters of the human limb model denoted in Table 4.2 and the Gaussian function based speed profile explained in section 4.2.1, the simulated limb model proposed in section 4.2 was constructed which then be used to simulate the time-variant CSI model that was discussed in section 4.3. Center frequency, bandwidth, and a number of subcarrier frequency of CSI listed in Table 5.1 were referred from the measurement campaign in section 3.5.2. The TV-CSI component was constructed using circular-mesh PO explained in section 4.4.2 with the dielectric constant of human limb provided in [146]. The Doppler spectrum was obtained from simulated CSI using STFT. The Gaussian window function with σ_{t} set to 33 ms.

5.4.2 Validation of Doppler Profile Estimation

The estimation technique in section 5.3 was applied to extract the hand-only Doppler profile from the Doppler spectrum. For determining the region of the selected peak, the noise power threshold was estimated as the highest noise power during a rest period. The validation of the proposed method was comparatively conducted with the reference hand Doppler profile defined using eq. (5.3). The simulation result depicted in Fig. 5.5a and Fig. 5.5b shown the similarity between estimated profiles and the reference in both gestures. In these figures, a moving average (MA) filter with 3-points windows was applied to smooth the estimated result. A small discrepancy with a few Hertz was observed at the 1$^{\mathrm{st}}$ and 3$^{\mathrm{rd}}$ motion segments for a square shape and 2$^{\mathrm{nd}}$ and 3$^{\mathrm{rd}}$ motion segments for M shape. However, our proposed estimation poorly performed with a larger magnitude of more than 5 Hz for the rest of segments.

The reason why the higher error happened locally at certain motion segments can be

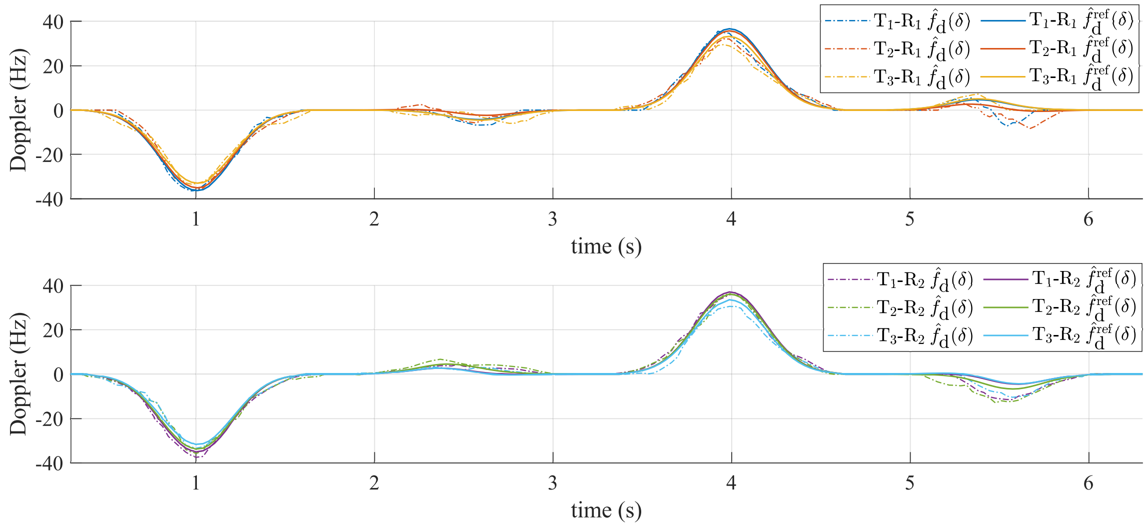

(a) Square-shape Doppler profiles with $\sigma_{f_d} = 5$ Hz

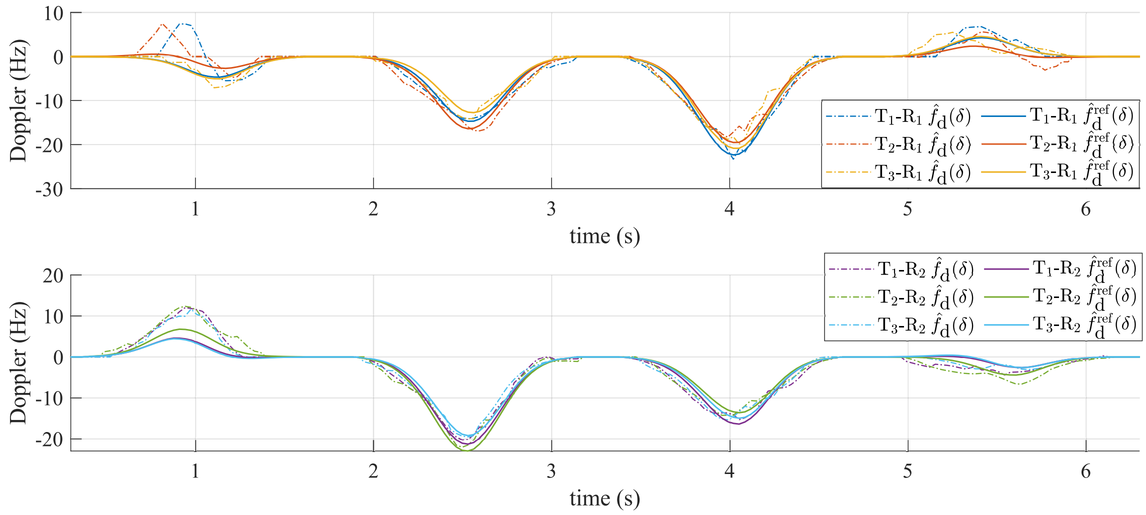

(b) M-shape Doppler profiles with $\sigma_{f_d} = 5$ Hz

Figure 5.5: Comparison of six profiles of estimated Doppler with 5-point MA filter and the reference profiles for square and M-shape gesture

explained with the main two factors in the following. First, it is clearly seen that the segment with higher discrepancy occurs at the segment where a change of Doppler profile is small. According to the time-frequency resolution trade-off with this setup, a subtle Doppler change that is smaller than temporal-Doppler uncertainty is theoretically difficult for analysis and thus resulting in a less reliable estimation. Another factor is due to the shape of the spectrum itself which can be explained by observing the sample of the Doppler spectrum in Fig. 4.15. Around 2 s in the spectrum, a small Doppler shift generally has a power spectrum spread in both negative and position Doppler plane. It is quite challenging to determine which plane on the spectrum corresponding to the hand Doppler. The estimation would wrongly

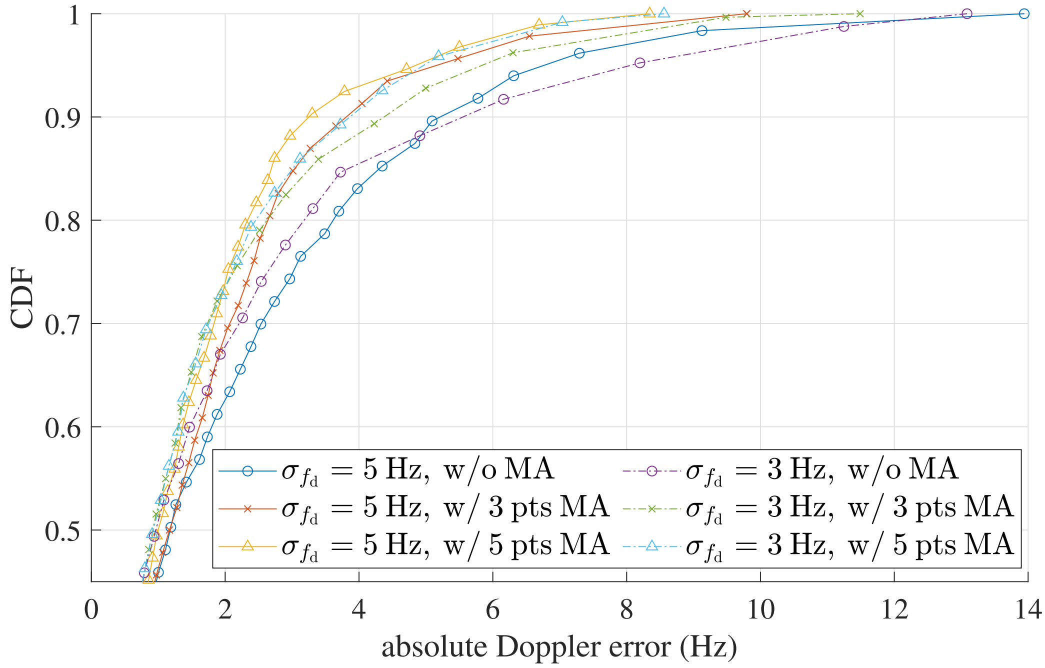

(a) Estimation error of square gesture

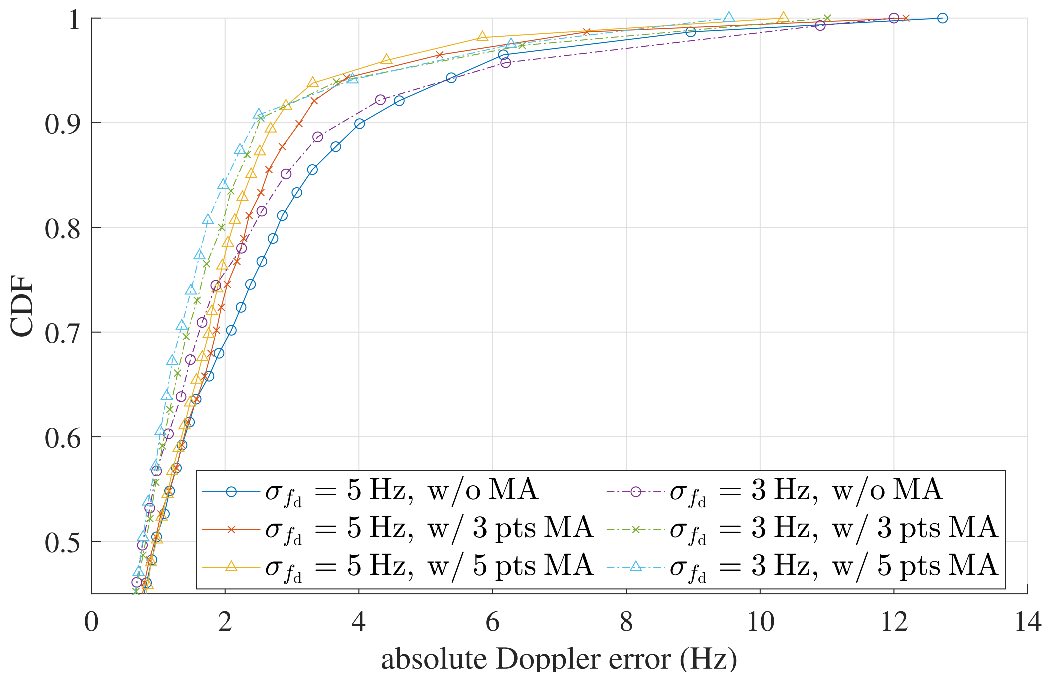

(b) Estimation error of M gesture

Figure 5.6: Comparison of the estimated Doppler profile at different MA window size and Doppler resolutions in terms of CDF of absolute Doppler error.

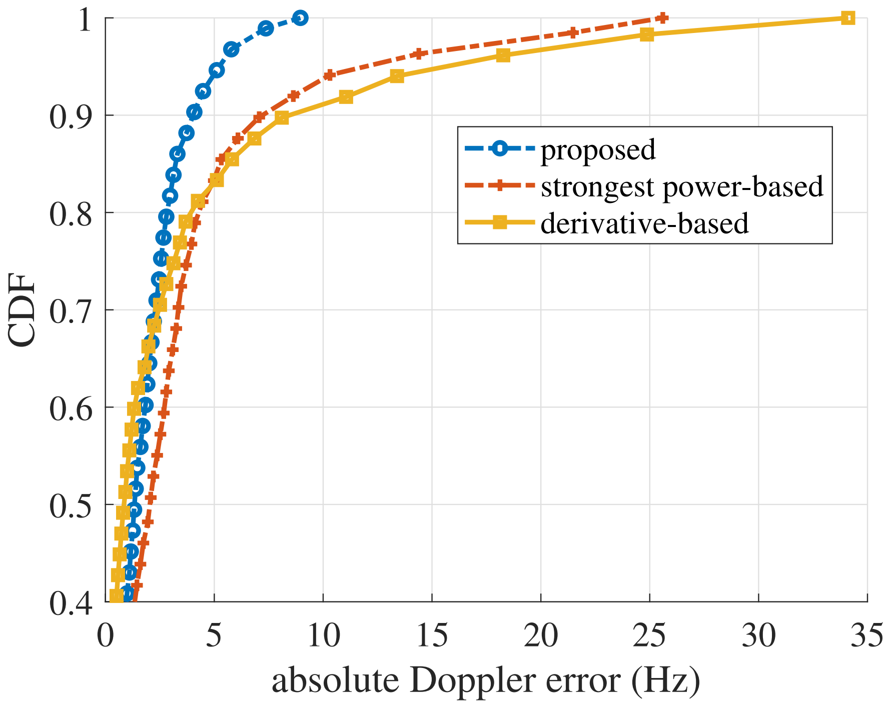

Figure 5.7: Performance comparison of proposed method with other extraction methods used in CSI-based motion tracking.

predict if the farthest peaks on a spectrum in both planes are relatively similar. Although the proposed criteria are based on weighted average as shown in Fig. 5.3d, it again can provide inaccurate prediction as long as the scattering power on the arm surface is stronger than hand. Therefore, it could be stated that the adjustment of transmitter and receiver positions plays a crucial role in the analysis of motion tracking. With a proper setup, one can mitigate the small Doppler frequency shift scenario and therefore improve the quality of the estimated Doppler profile.

Regarding the effect of MA filter and the Doppler resolution $\sigma_{\mathrm{f_d}}$ to the estimated Doppler profiles, an evaluation was depicted in Fig. 5.6 the CDF function of absolute Doppler error representing the overall discrepancy of all six estimated Doppler profiles to the reference. Although performance does not show a significant difference at the median level of 1 Hz error, MA began to gradually take effect at 90^{th} percentile with around 1 and 1.5 Hz less Doppler error with respect to 3 and 5 points MA window size respectively in both shapes. It should be addressed that there was less improvement to the estimated Doppler profile with the MA window larger than 5 points MA window. In the case of $\sigma_{\mathrm{f_d}}$, a 3-Hz resolution has a slightly less error of around 0.5 Hz in M-shape while a similar gap can be seen in the square gesture. Hence, it does not show a concrete tendency at which Doppler resolution is better. As a result, it could be assessed that the proposed profile estimation technique could extract

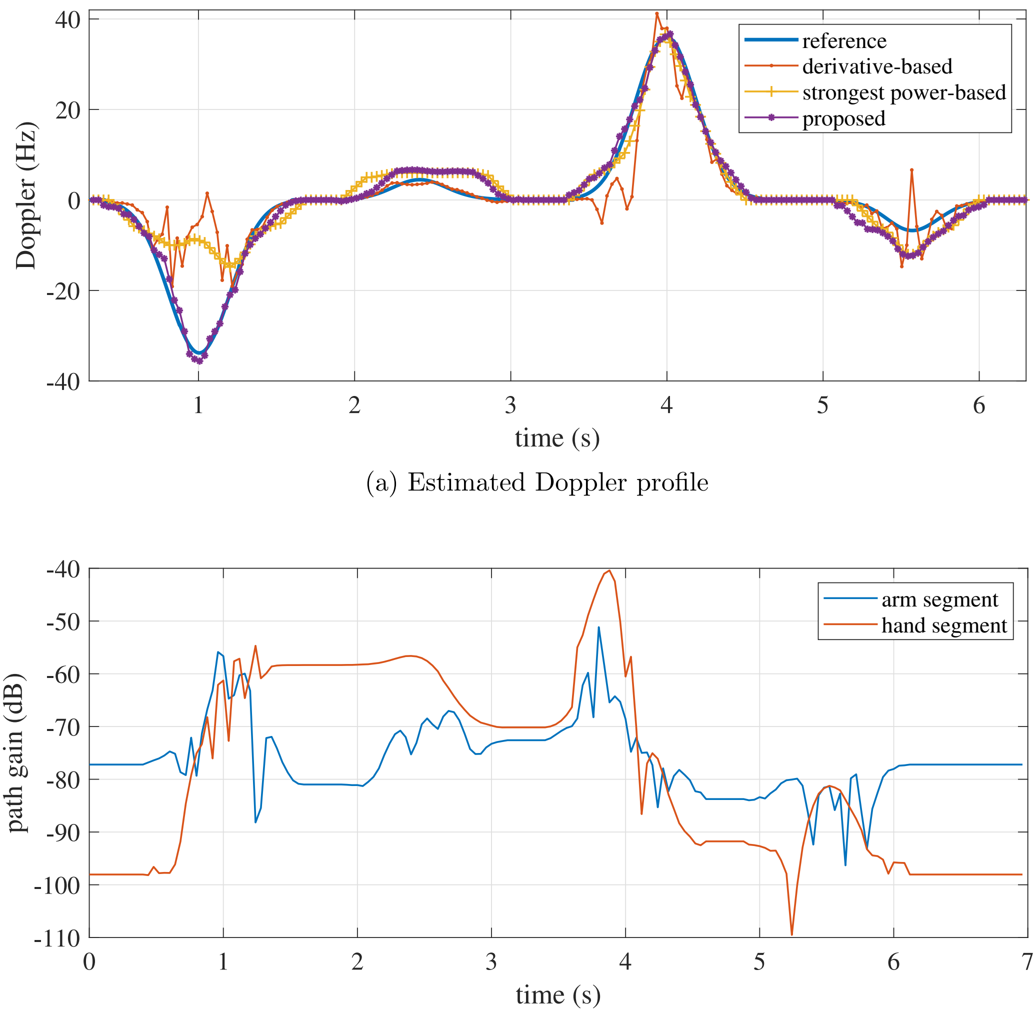

(a) Estimated Doppler profile

(b) Path gain distribution

Figure 5.8: Sample of the estimated Doppler profile between $\boldsymbol{p}_{\mathrm{T}_2}$ and $\boldsymbol{p}_{\mathrm{R}_2}$ in comparison with other extraction method and the corresponding path gain distribution.

the hand Doppler profile with the error of less than 5 Hz in most of the case. Nevertheless, the estimation performance could be worsened when the motion produces a smaller Doppler frequency shift.

Lastly, the performance of the proposed Doppler profile extraction was comparatively evaluated with other two techniques used in the CSI-based motion tracking. In the typical Time-Doppler power spectrum analysis as well as the application in human tracking [55, 54], they usually estimate the strongest in the spectrum as the target features. Mathematically, the target Doppler profile at each short-time window δ in this method can be calculated from

$$\hat{f}^{\max}_{\mathrm{d},(n,m)}(\delta) = \arg\max_{f_\mathrm{d}} P_{\mathrm{B},(n,m)}(\delta, f_\mathrm{d}) \tag{5.4}$$

Another extraction method was applied to track 2D hand gesture trajectory in horizontal plane [58]. In this work, they utilize the path length change derived from Doppler frequency to iteratively trace the 2D hand gesture. Conceptually, they did not utilize the time-Doppler spectrum analysis but rather the phase derivative which is similar to the Hilbert transform (HBT) based analysis described in section 2.3 to estimate the principle Doppler component. Since this method is based on derivative, the extracted Doppler profile does not requires the short-time period. Therefore, the instantaneous Doppler profile can be computed directly from the time-variant component of CSI as

$$\hat{f}^{\mathrm{dev}}_{\mathrm{d},(n,m)}(\kappa) = \frac{1}{2\pi}\frac{d}{dt}\angle H^{\mathrm{TV}}_{n,m}(\kappa, f_k) \tag{5.5}$$

Since the instantaneous Doppler estimation obvious suffers from the multi-component Doppler, data pre-processing technique such as low-pass filter and averaging TV-CSI component along subcarrier was introduced. The estimation result depicted in Fig. 5.7 was evaluated in terms of absolute Doppler error. Overall, our method depicted as blue line distinctly outperformed the estimated profile based on the strongest peak, $\hat{f}^{\mathrm{max}}_{\mathrm{d}}(\delta)$, depicted as red line. The derivative-based estimated depicted as yellow line in the figure, on the other hand, also contributed to the significantly large error up to 34 Hz. The reason of their significantly large error could be described by investigating the sample Doppler profile between 2$^{\mathrm{nd}}$ Tx and 2$^{\mathrm{nd}}$ Rx as depicted in Fig. 5.8a together with the path gain distribution in Fig. 5.8b. As clearly seen within $0.6 - 1.2$ s period of the 1$^{\mathrm{st}}$ motion segment, these two methods failed to estimate the temporal profile of hand gesture when the dominant path gain does not correspond to the hand segment. Since these methods did not consider the micro-Doppler effect, it straightforwardly could not handle such scenario. Our method, in contrast, is more robust to handle this effect thus minimizing the estimated Doppler error.

5.5 Summary

With the establishment of simulated CSI and the human limb model, The effect of micro-Doppler effect on the movement of hand gesture was investigated. The characteristic of STFT-based Doppler power spectrum in the presence of micro-Doppler was analyzed by comparing with the Doppler and path gain distribution. Here the Doppler signature of only-hand movement is considered the target whereas those induced by arm segments are regarded as the interference. The study was concluded that the Doppler of hand motion is likely located at the farthest peak on the Doppler power spectrum due to the faster speed hand segment produced. Since The Doppler power level is highly depended on the incident and scattered angle, the stronger power can correspond to either hand or arm Doppler components.

Based on the findings on the micro-Doppler characteristic from the model, A novel technique for extracting the temporal profile of a hand-only Doppler signature from the spectrum has been developed. Due to the uncertainty trade-off between time and Doppler, the deterministic approach cannot be applied. Therefore, the statistical-based estimation technique was introduced by utilizing the peak detection method.

The experiment was conducted to validate the performance of Doppler profile extraction. It was revealed that the error from the extracted Doppler profile was fairly small with less than 4-Hz offset at 90^{th} percentile of CDF. However, the discrepancy could go up to 10 Hz when the movement direction was approaching the orthogonality with the relative direction from hand to transmitter and receiver accordingly. In comparison with other profile estimation technique, the performance of our proposed has relatively smaller error while others could introduce the higher error in the magnitude of 30 Hz. This is because those techniques have not taken account the effect of micro-Doppler. As a result, the ability to extract Doppler profile depends on the the position of gesture performer relative to the transmitter and receiver.

This extracted Doppler profile will then be applied to reconstruct the hand trajectory whose detail explanation is covered in chapter 6.

Chapter 6

Utilizing Doppler Frequency for Hand Motion Trajectory Tracking

6.1 Introduction

Motion trajectory tracking is the core feature of radar application. Since Wi-Fi based motion sensing is considered the special case of OFDM radar as mentioned in chapter 2, hand motion trajectory tracking should be theoretically possible. In general, motion tracking in radar is commonly done by tracing temporal position of the target at each short-time period. However, this approach cannot be realized in our Wi-Fi based system because the range information is unreliable with the narrowband CSI. Therefore, the practical Wi-Fi based tracking system can only relies on the Doppler information.

with the presence of micro-Doppler effect induced by the non-rigid body motion of human limb, The proposed Doppler signature extraction technique was proposed in chapter 5 to statistically detach the temporal profile of hand Doppler component from the joint time-Doppler frequency power spectrum. This target profile contains information of temporal speed in a direction relative to the position of transmitter and receiver as detailed in chapter 2. In order to perceive the motion characteristic, we must be able to accurately draw out the velocity information embedded in this Doppler profile.

In this chapter, the well-established bistatic Doppler radar model is utilized for the trajectory estimation of the hand gesture. Since Doppler frequency only provides the movement information in radial direction, multiple transmitter (Tx) receiver (Rx) antennas were employed in the system to reconstruct the 3D trajectory of the hand gesture. The trajectory framework will be firstly detailed in section 6.2.1. To validate this tracking performance, the simulation will be conducted in section 6.3 by utilizing the simulated CSI and the human limb model explained in chapter 4. To confirm the motion tracking applicability, we further conducted the experiment using the CSI captured from commodity Wi-Fi devices installed on two laptops. Before applying the measured CSI to the tracking framework, CSI data is pre-processed with the proposed calibration technique explained in chapter 3 to filter out the undesired phase rotation thus improving the quality of measured Doppler frequency.

6.2 Trajectory Estimation

In this tracking framework, the trajectory is recursively estimated using a set of Doppler frequency information collected from a pairs of M Tx antennas and N Rx antennas. Unavoidably, the iterative process accumulate the estimation error. To handle this issue, Kalman filter (KF) [148] is applied to mitigate the cumulative noise from the trajectory estimation model. Since the initial condition is required to imitate the dynamic model based trajectory tracking, the justification of initial value estimation will be additionally discussed in section 6.2.3.

6.2.1 Trajectory Estimation Method Based on Multi-static Doppler Radar

Since the hand trajectory is estimated based on the Doppler information, the output temporal position and velocity are both corresponding to the temporal profile of hand Doppler signature. As mention in chapter 5, this profile does not physically represent any particular point on the surface of the moving hand. Instead, the extracted Doppler frequency profile is validated to be statistically similar of those produced from the hand surface. Therefore, the trajectory estimation with this extracted profile could supposedly represent the hand motion.

Suppose the temporal position and velocity of the tracking target (hand) within a short-time period δ are represented by the following 3D vectors,

$$\boldsymbol{v}_{\mathrm{hd}}(\delta) = \begin{bmatrix} \hat{v}_{\mathrm{hd,x}}(\delta) \\ \hat{v}_{\mathrm{hd,y}}(\delta) \\ \hat{v}_{\mathrm{hd,z}}(\delta) \end{bmatrix}, \qquad \boldsymbol{p}_{\mathrm{hd}}(\delta) = \begin{bmatrix} \hat{p}_{\mathrm{hd,x}}(\delta) \\ \hat{p}_{\mathrm{hd,y}}(\delta) \\ \hat{p}_{\mathrm{hd,z}}(\delta) \end{bmatrix} \tag{6.1}$$

where the additional subscript x, y, and z represents the vector components in Cartesian coordinates system. With the representation in eq. (6.1), the bistatic radar Doppler described in eq. (2.8) can be re-written in terms of Cartesian coordinates vector in the following with respect to a pair of m-th Tx and n-th Rx antennas,

$$\begin{aligned} f_{\mathrm{d},(n,m)}(\delta) &= \frac{1}{\lambda}\left[\frac{\boldsymbol{p}_{\mathrm{T}_m} - \boldsymbol{p}_{\mathrm{hd}}(\delta)}{d_{\mathrm{T}_m}(\delta)} + \frac{\boldsymbol{p}_{\mathrm{R}_n} - \boldsymbol{p}_{\mathrm{hd}}(\delta)}{d_{\mathrm{R}_n}(\delta)}\right]^T \boldsymbol{v}_{\mathrm{hd}}(\delta) \\ &= \boldsymbol{u}_{n,m}^T(\delta)\boldsymbol{v}(\delta) \end{aligned} \tag{6.2}$$

where $d_{\mathrm{T}_m}(\delta)$ and $d_{\mathrm{R}_n}(\delta)$ denotes the temporal distance from the hand to the m-th Tx and n-th Rx antennas respectively. For brevity, $\boldsymbol{u}_{n,m}(\delta)$ vector is additionally introduced which represents the relative direction between the motion direction and the direction from hand position to Tx and Rx. This vector can be expressed by,

$$\boldsymbol{u}_{n,m}(\delta) = \frac{1}{\lambda}\left[\frac{\boldsymbol{p}_{\mathrm{T}_m} - \boldsymbol{p}_{\mathrm{hd}}(\delta)}{d_{\mathrm{T}_m}(\delta)} + \frac{\boldsymbol{p}_{\mathrm{R}_n} - \boldsymbol{p}_{\mathrm{hd}}(\delta)}{d_{\mathrm{R}_n}(\delta)}\right] \tag{6.3}$$

It should be noted that only one Doppler profile is not sufficient to resolve three components of $\boldsymbol{v}_{\mathrm{hd}}(\delta)$ through the linear equation in eq. (6.2). The simplest way to resolve such underdetermined linear system is to increase number of observation. Having multiple M Tx and N received antennas placed at different positions, we then have NM set of Doppler profiles $f_{\mathrm{d}_{n,m}}(\delta)$ as well as the relative direction $\boldsymbol{u}_{n,m}(\delta)$ vectors. These variables and vectors can be stacked up as the Doppler vector and the relative direction matrix respectively,

$$\boldsymbol{f}_{\mathbf{d}}(\delta) = \begin{bmatrix} \hat{f}_{\mathrm{d},(1,1)}(\delta) \\ \hat{f}_{\mathrm{d},(2,1)}(\delta) \\ \vdots \\ \hat{f}_{\mathrm{d},(N,1)}(\delta) \\ \vdots \\ \hat{f}_{\mathrm{d},(N,M)}(\delta) \end{bmatrix}, \qquad \mathbf{U}(\delta) = \begin{bmatrix} \boldsymbol{u}_{1,1}^T(\delta) \\ \boldsymbol{u}_{2,1}^T(\delta) \\ \vdots \\ \boldsymbol{u}_{N,1}^T(\delta) \\ \vdots \\ \boldsymbol{u}_{N,M}^T(\delta) \end{bmatrix} \tag{6.4}$$

Due to the matrix properties, we can directly substitute $\boldsymbol{f}_{\mathbf{d}}(\delta)$ and $\mathbf{U}(\delta)$ into eq. (6.2) for the generalization of multi-static radar system as depicted in Fig. 6.1. Suppose the number of observable Doppler profile NM is larger than three, the multi-static Doppler radar becomes the overdetermined system. Therefore, the hand velocity can be estimated from the least square (LS) approach as,

$$\boldsymbol{v}_{\mathrm{hd}}(\delta) = \mathbf{U}^{\dagger}(\delta)\boldsymbol{f}_{\mathbf{d}}(\delta) \tag{6.5}$$

where $[\cdot]^{\dagger}$ represents Moore-Penrose pseudoinverse operation. However, the least square solution in eq. (6.5) assumes a given $\mathbf{U}(\delta)$ which is unfortunately impractical since it consists of the unknown temporal position $\boldsymbol{p}_{\mathrm{hd}}(\delta)$. Therefore, a simple approach for a prediction of hand trajectory, a path at which the temporal position vector is moving toward, can be done recursively by using kinematic equation,

$$\boldsymbol{p}_{\mathrm{hd}}(\delta + \Delta\delta) = \boldsymbol{p}_{\mathrm{hd}}(\delta) + \boldsymbol{v}_{\mathrm{hd}}(\delta)\Delta\delta \tag{6.6}$$

where $\Delta\delta = RT_{\mathrm{s}}$ is a time difference between two consecutive short-time window. Likewise, the predicted trajectory $\boldsymbol{p}_{\mathrm{hd}}(\delta+\Delta\delta)$ is substitute into $\mathbf{U}(\delta)$ to recursively estimate $\boldsymbol{v}(\delta+\Delta\delta)$. Depending on the quality of Doppler profile $\hat{f}_{\mathrm{d}_{n,m}}(\delta)$ estimated from eq. (5.2) and the initial position $\boldsymbol{p}_{\mathrm{hd}}(0)$, the trajectory performance may suffer from the error accumulated from this recursive process which could be mitigated by applying KF to the system. The formulation of KF in the trajectory framework will be explained in the next section.

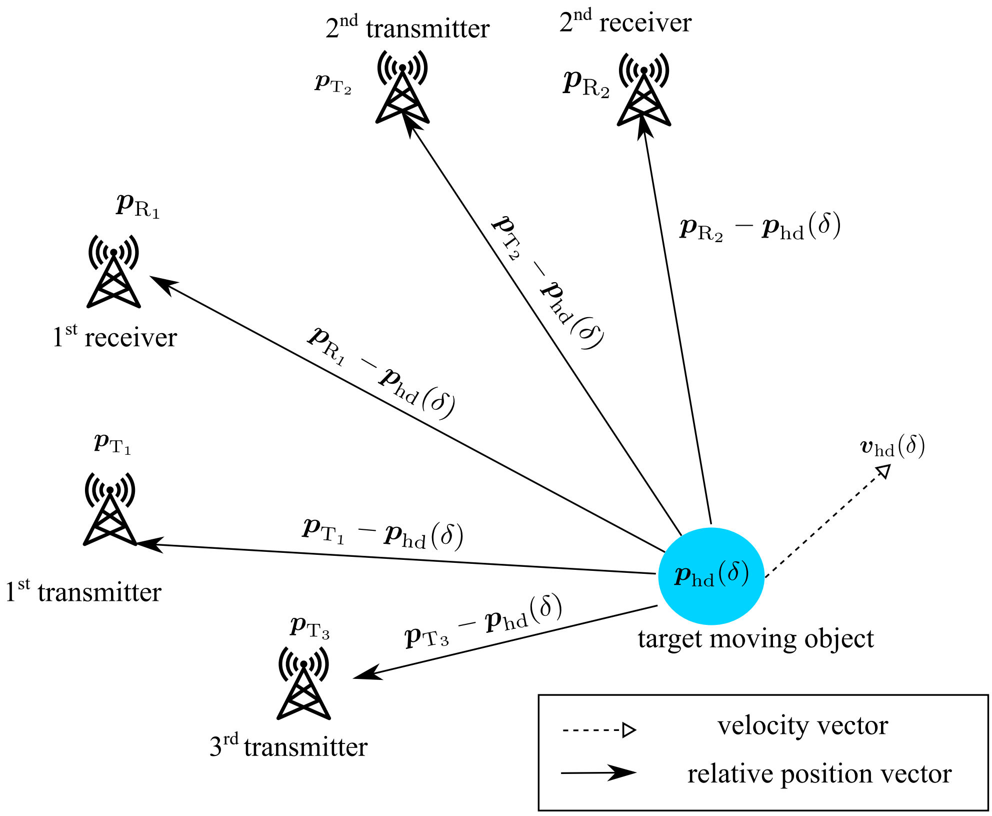

Figure 6.1: Multi-static Doppler radar for hand gesture trajectory tracking.

Issue with The Widely-Separated Antenna to The Trajectory Estimation

As clearly seen in eq. (6.5), the rank of $\mathbf{U}(\delta)$ should be greater than three for the velocity estimation in 3D space. It means that, if two pair of antennas are nearby such that $\|\boldsymbol{p}_{m+1} - \boldsymbol{p}_m\| \to 0$ and $\|\boldsymbol{p}_{n+1} - \boldsymbol{p}_n\| \to 0$, the matrix $\mathbf{U}(\delta)$ will have rank reduces by 1 since $\boldsymbol{u}_{n,m}(\delta) \simeq \boldsymbol{u}_{n+1,m+1}(\delta)$ and therefore the measured Doppler profile will exhibit similar frequency shift such that $f_{\mathrm{d,n,m}}(\delta) \simeq f_{\mathrm{d,n+1,m+1}}(\delta)$. Let us consider the multi-static Doppler radar with three Txs and Rxs in Fig. 6.1. Suppose the the hand position $\boldsymbol{p}_{\mathrm{hd}}(\delta)$ is positioned quite far from radar sensors, each pair of either two Tx or Rx is perceived as the same position which resulting in losing spatial incoherency between these pair of Doppler frequency.

This explanation obviously states that each Tx and Rx should be widely separated relative to the distance from the hand position in order to increase the incoherency between Doppler measurement. In fact, the widely-separated Doppler radar has been studied and summarized in [86]. Although MIMO antennas of single Wi-Fi station are typically a few centimeters apart, the widely-spaced antenna for hand tracking could be implemented for the practical use of Wi-Fi system by considering each Tx and Rx as an independent Wi-Fi station. For instance, five Wi-Fi stations with MIMO antennas are utilized for hand motion tracking in

Fig. 6.1. It should be noted from eq. (6.2) that the slower movement would result in the similar Doppler profiles regardless of which transmitter and receiver it belongs to since they are all factored by speed or the magnitude of $\left\|\boldsymbol{v}_{\mathrm{hd}}(\delta)\right\|$. Therefore, higher trajectory error is expected in terms of direction error. However, this impact is miniature since the trajectory progression within a short-time δ is tiny owing to the slower speed.

Let us consider Doppler frequency produced by a pair of $\boldsymbol{p}_{\mathrm{T}_1}$ and $\boldsymbol{p}_{\mathrm{R}_1}$ and in Fig. 6.1. When the object moves downward with respect to the figure's orientation, it visibly produces the negative Doppler frequency with a certain frequency shift. If we flip the moving object horizontally such that it swaps to the left of the same pair of antenna, the same Doppler frequency shift will be produced with the same motion. This explains the ambiguity in the Doppler measurement since it represents only 1D movement characteristic. Although supplying multiple antennas could resolve the velocity component, the ambiguity still persist if all antennas are arranged only in certain direction. For example, if all antennas are aligned vertically, the system cannot tell whether the object is located on the left or right side relative to antennas. Henceforth, It can be assessed that the tracking system would fail to estimate the trajectory in a certain axis if there is no antenna placed separately along that axis's direction. In conclusion, not only the trajectory estimation requires the widely separation between antenna, they should be distributed along three main axes as well in case of 3D trajectory tracking.

Effect of Tracking Error to The Overall Trajectory

Since the trajectory is govern by the temporal velocity, there should exist two types of impact to the trajectory: orientation and scaling offset. Considering the extreme case where each estimated Doppler profile were offset from the reference with the same quality Δf_{d}, the LS solution of eq. (6.5) should also experience only the scaling offset Δv_{hd} such that the movement path is either shorter or longer than the original motion. This impact, despite alter the size, could still preserve the overall shape. In practical, the offset is likely different among a pair of antennas such that $\Delta f'_{\mathrm{d},(n,m)}$. This should unfortunately affects both orientation and scaling offset together.

6.2.2 Minimizing Trajectory Error with Kalman Filter

Regarding the dynamic model in previous section, velocity vector and temporal position in eq. (6.5) and eq. (6.6) could be treated as measurement and predicted variables respectively. Hence, it is possible to formulate this problem into the KF framework [148] where the state vector $\boldsymbol{x}(\delta)$ and measurement vector $\boldsymbol{z}(\delta)$ are defined as

$$\boldsymbol{x}(\delta) = \begin{bmatrix} \tilde{\boldsymbol{p}}_{\mathrm{hd}}(\delta) \\ \tilde{\boldsymbol{v}}_{\mathrm{hd}}(\delta) \end{bmatrix}, \qquad \boldsymbol{z}(\delta) = \boldsymbol{v}_{\mathrm{hd}}(\delta) \tag{6.7}$$

Parameters with tilde symbol represents the state estimate variables. From above vectors, the state and measurement model of KF can be written respectively in the following dynamic model,

$$\boldsymbol{x}(\delta+1) = \mathbf{A}\boldsymbol{x}(\delta) + \boldsymbol{\epsilon}(\delta) \tag{6.8}$$

$$\boldsymbol{z}(\delta) = \mathbf{C}\boldsymbol{x}(\delta) + \boldsymbol{y}(\delta) \tag{6.9}$$

Assuming the constant velocity within a short-time period $\Delta\delta$, the state matrix $\mathbf{A}$ can be modelled in this problem based on the kinematic equation with zero acceleration. Since only velocity vector is observable, the measurement matrix can be simply constructed in the way that neglects the position vector from $\boldsymbol{z}(\delta)$. With this conditions both matrices can be defined as,

$$\mathbf{A} = \begin{bmatrix} \mathbf{I}_3 & \Delta\delta\mathbf{I}_3 \\ \mathbf{0}_3 & \mathbf{I}_3 \end{bmatrix}, \qquad \mathbf{C} = \begin{bmatrix} \mathbf{0}_3 & \mathbf{I}_3 \end{bmatrix} \tag{6.10}$$

where $\mathbf{0}_3$ is a 3×3 zero matrix. the zero-mean Gaussian noise is assumed for both process and measurement noise in Kalman filter and are denoted by vectors $\boldsymbol{\epsilon}(\delta)$ and $\boldsymbol{y}(\delta)$ respectively. The corresponding variance of process and measurement noise are defined accordingly as σ_ϵ^2 and σ_{y}^2.

Suppose this kinematic model is perturbed by the variation of velocity caused by different pace of movement on the hand surface within a short-time period, the noise covariance matrices corresponding to $\boldsymbol{\epsilon}(\delta)$ and $\boldsymbol{y}(\delta)$ can be defined accordingly by,

$$\mathbf{E} = \sigma_\epsilon^2 \begin{bmatrix} (\Delta\delta)^2\mathbf{I}_3 & \Delta\delta\mathbf{I}_3 \\ \Delta\delta\mathbf{I}_3 & \mathbf{I}_3 \end{bmatrix}, \qquad \mathbf{Y} = \sigma_{\mathrm{y}}^2\mathbf{I}_3 \tag{6.11}$$

By observing the measurement and predicted values in eq. (6.7), KF sequentially estimates position and velocity in $\boldsymbol{x}(\delta)$ using Kalman gain [148] which is in turn computed based on covariance matrices in eq. (6.11). Since KF state model described in eq. (6.8) assumes zero acceleration, the σ_ϵ^2 could be related to the velocity uncertainty due to an actual non-zero acceleration. This is possible in the case of a wider short-time window such that the constant speed assumption is not valid given the rapid movement of hand gesture. This effect has been explained mathematically in [46]. In contrast, σ_{y}^2 is clearly proportional to the estimated Doppler profile where the velocity is estimated from LS of eq. (6.5).

Since KF is a recursive estimation process, the initialization value of state vector $\boldsymbol{x}(0)$ is necessarily needed. Any motion should start from rest so it is straightforward to set $\tilde{\boldsymbol{v}}_{\mathrm{hd}}(0)$ with a null vector. In contrast, it is quite a challenging task for defining the initial position $\tilde{\boldsymbol{p}}_{\mathrm{hd}}(0)$ since the range information is not reliable for the position estimation. This issue will be discussed in the next section.

6.2.3 Initial Position Estimation Based on Least Square residual

Having Only Doppler profile information, it is virtually difficult to obtain a precise absolute initial position. Generally, localization of any position requires either fine-grained angular or delay information estimated from array antenna or with a wideband signal respectively [50]. High accuracy and precision of these variables are not easy to obtain with the restriction of the narrowband Wi-Fi signal captured by the off-the-shelf Wi-Fi devices such as laptops and access points. As a consequence, resolving this issue with only Doppler frequency requires additional constraints and assumptions.

Since the trajectory estimation is the concern of this study, it can be argued that any arbitrary initial position is acceptable as long as the hand trajectory is correctly estimated. Although the trajectory is a temporal sequence of position as mentioned previously, velocity itself which is proportional to the Doppler profile dictates the direction of motion. In other words, the estimated velocity in eq. (6.5) that yields the smallest residual during the entire motion given arbitrary initial position could implicitly represent the existence of an overall trajectory. Hence, this condition can be expressed in terms of optimization problem as,

$$\underset{\boldsymbol{p}_{\mathrm{hd}}(0)}{\arg\min} \quad \sum_{\delta \in \mathcal{L}} \varepsilon_{\mathrm{LS}}(\delta) \tag{6.12a}$$

$$\text{subject to} \quad \varepsilon_{\mathrm{LS}}(\delta) = \left\| \boldsymbol{f}_{\mathrm{d}}(\delta) - \mathbf{U}(\delta)\boldsymbol{v}_{\mathrm{hd}}(\delta) \right\|, \tag{6.12b}$$

$$\boldsymbol{p}_{\mathrm{lower}} \leq \boldsymbol{p}_{\mathrm{hd}}(0) \leq \boldsymbol{p}_{\mathrm{upper}} \tag{6.12c}$$

where $\mathcal{L}$, $\epsilon(\delta)$, $\boldsymbol{p}_{\mathrm{a}}$, and $\boldsymbol{p}_{\mathrm{b}}$ are a set of short-time window within a single gesture motion, the least square residual at each windowed snapshot, the lower and upper search boundaries of initial position respectively.

To incorporate this optimization to the trajectory estimation framework, a set of initial position candidates is randomly generated within the range defined in eq. (6.12c). By subjecting them to the KF model described in section. 6.2.2 in parallel, the same set of candidate trajectories can be recursively estimated up to κ_{δ} snapshots. The only initial position that satisfies the optimization problem denoted in eq. (6.12a) is supposed to produce the similar trajectory to those of the original hand gesture.

6.3 Validation of Trajectory Estimation in Simulation

In this simulation, the scenario and configuration are the same as those conducted in section 5.4.1. In general, the human limb model described in chapter 4 were constructed based on the configuration summarized in Table 4.2 to perform the square and M-shape hand gestures. Listed in Table 5.1 is the CSI parameters used in this simulation which was based on the measured CSI obtained from the CSI extraction tool [35]. Regarding the validation in the section 5.4.2, six estimated Doppler profiles depicted in Fig. 5.5 were chosen for estimating the trajectory of square and M-shape hand gestures. By applying these profiles on to the trajectory framework and KF explained in section. 6.2, both gesture trajectories were recursively reconstructed. The standard deviation of the velocity process, σ_ϵ, and measurement noise, σ_{y}, were then heuristically set to 0.1 and 1 m/s respectively. As the baseline, the trajectory reference was estimated by applying the reference Doppler profiles in eq. (5.3) to the same trajectory framework. KF was not applied during trajectory reconstruction in this case since the reference Doppler is supposed to be error-free.

Regarding the performance evaluation, the term trajectory error was used to describe the discrepancy of the estimated trajectory to the reference path. As mentioned earlier that a path of motion was governed by velocity, we defined two trajectory error quantities based on the motion velocity. Temporal magnitude error denoted as $v_{\mathrm{error}}(\delta)$ measures the speed offset at each snapshot. On the other hand, temporal direction error represented by $\psi_{\mathrm{v,error}}(\delta)$ defines the direction in which the estimated trajectory was being offset from the reference trajectory. Here both variables of trajectory error could be expressed as

$$v_{\mathrm{error}}(\delta) = \left\|\boldsymbol{v}_{\mathrm{hd}}(\delta)\right\| - \left\|\boldsymbol{v}_{\mathrm{hd}}^{\mathrm{ref}}(\delta)\right\| \tag{6.13}$$

$$\psi_{\mathrm{v,error}}(\delta) = \cos^{-1}\frac{\boldsymbol{v}_{\mathrm{hd}}^{T}(\delta)\boldsymbol{v}_{\mathrm{hd}}^{\mathrm{ref}}(\delta)}{\left\|\boldsymbol{v}_{\mathrm{hd}}(\delta)\right\|\left\|\boldsymbol{v}_{\mathrm{hd}}^{\mathrm{ref}}(\delta)\right\|} \tag{6.14}$$

Here the positive sign of magnitude error means the speed is overestimated resulting in the longer distance offset and vice versa for the negative sign. The direction error ranges from no direction offset at 0° to the maximum of 180° where the estimated trajectory is completely opposite with the reference.

In the fist validation, the initial position was supposedly known in order to mitigate the impact of trajectory error due to the initial position estimation. The initial position of wrist $\boldsymbol{p}_w(0)$ was given since it was defined as the reference movement of the entire human as stated in section 4.2. In Fig. 6.2, the result of trajectory estimation for both gestures depicted as yellow line was comparatively visualized with the reference trajectory plotted with blue line. In order to investigate the effect of KF to the overall trajectory, Another trajectory depicted in red line was estimated without applying KF model. The ordering of motion segment in each gesture was denoted in Fig. 5.4b. In general, the vertical motion ($\pm z$ direction) of the square gesture correspond to the 2$^{\mathrm{nd}}$ and 4$^{\mathrm{nd}}$ segments whereas the horizontal motion ($\pm y$ direction) is for 1$^{\mathrm{nd}}$ and 3$^{\mathrm{rd}}$ segments. In case of M-shape gesture, the vertical motion belongs to 1$^{\mathrm{nd}}$ and 3$^{\mathrm{rd}}$ segments while the diagonal motion are 2$^{\mathrm{nd}}$ and 4$^{\mathrm{nd}}$ segments.

Despite the imperfection of estimated Doppler profiles, reconstructed hand trajectories were able to preserve the overall square and M gestures even without applying KF model as shown in the orange solid line of Fig. 6.2a and Fig. 6.2b respectively. In the case of the estimated trajectory without KF model, both vertical movements of the square gesture seem to experience larger distortion than the horizontal path resulting in a longer height. This

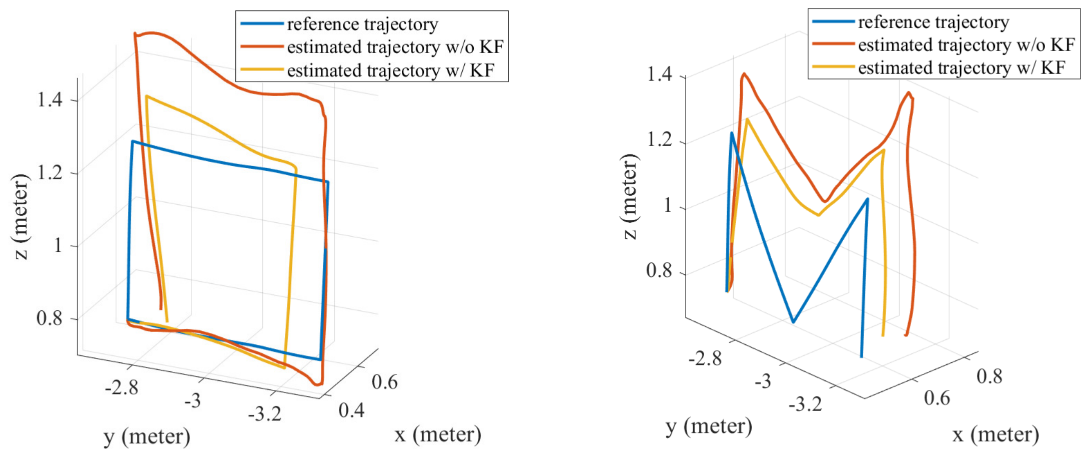

(a) Square gesture (b) M gesture

Figure 6.2: Comparison of trajectory estimation result with and without KF using estimated Doppler profiles with 5 point MA window and 5-Hz σ_{f_d}

is a consequence of the larger absolute Doppler error localized in these motion segments as explained in section. 5.4.2. It also clearly reflects on the trajectory error depicted in Fig. 6.3a as the higher magnitude error frequently appeared on the vertical motion segments which could go up to 0.6 m/s. As the magnitude error is positive most of the time, the cumulative summation which is proportional to the distance clearly contributes to the longer movement offset. On the other hand, the horizontal motion has relatively smaller error on average which cumulatively resulted in the less trajectory distortion. By observing the characteristic of trajectory error in Fig. 6.3c, the same magnitude error also manifests in the vertical movement of the M-shape gestures resulting in the comparatively larger distance offset in the 1$^{\text{st}}$ and 4$^{\text{th}}$ motion segments. The diagonal motion, however, has the magnitude error fluctuated between positive and negative plane and therefore contribute to the lesser magnitude offset.

In terms of direction error, a distinct pattern of larger offset with more than 90° was seen through all segments of both gestures at the position near the beginning and end of each motion segment. This was likely caused by the inaccuracy of the estimated Doppler profile when the magnitude of the Doppler frequency shift was fairly small in the realm of uncertainty. Although a tremendous offset in direction would have sabotaged the tracking result, this effect to the overall trajectory was miniature because the distance the estimated trajectory has progressed within this periods was insignificantly short owning to a tiny magnitude offset. Therefore, it should be assessed that the orientation offset is mainly contributed to a moderate direction error at the center of motion segments which were varied between 5 and 40 degrees.

Let us move the attention to the the estimated trajectory after applying KF. One could immediately find out the promising improvement on the estimated trajectory as depicted in a solid yellow line on Fig. 6.2a and Fig. 6.2b for both hand gestures. The distance offset in the vertical motion significantly shrunk down from those without KF in the square gesture. However, this effect contributed to the horizontal motion where distance was shorter than the reference path. In a good side, this also slightly reduced the orientation offset between the junction of the first and second motion segment as the example. The similar effect visibly showed in the M-shape gesture especially the shortening of the vertical movement. The overall orientation offset significantly improved from those without KF as can be seen from the better alignment of yellow line to the reference trajectory in comparison with those without KF.

In terms of trajectory error depicted in Fig. 6.3b and Fig. 6.3d for square and M-shape gesture respectively, it is clearly seen that the directional error has been drastically subjugated and smoothed especially in the M-shape gesture where the direction mismatch was fairly stable within 10-20 degrees in most of the time. Although a huge direction offset at both sides of the motion segment could still be observed, the corresponding magnitude offset has been vastly mitigated particularly at this period thus minimizing trajectory distortion further. The sinusoidal-like pattern of magnitude depicted in Fig. 6.3b and Fig. 6.3d is the result of KF recursively mitigating the cumulative noise. In contrast, the pattern of those without KF causes a monotonically increase in the cumulative summation of magnitude error resulting in a larger scale distortion as the time progress.

To clearly see the importance of the extracted Doppler profile to the overall trajectory, we also evaluated the trajectory tracking performance to those applied other Doppler estimation methods described in section 5.4.2. The strongest power-based Doppler profile extracted using eq. (5.4) generally applies to tracking human walking in indoor using the similar multi-static radar model [55]. Therefore, these profiles were then subjected to our tracking framework for trajectory comparison. The derivative-based Doppler extraction used in [58], on the other hand, does not support the hand tracking in vertical direction unless the antennas are situated in the same vertical plane. Nevertheless, the tracking technique is conceptually similar such that they recursively estimate the next position using Doppler frequency in terms of path length change. Our tracking framework again traced the motion based on the derivative-based profiles. The result in Fig. 6.4 confirmed that the inaccuracy of Doppler profile significantly reduced the trajectory quality for the strongest-based and derivative-based where the absolute Doppler error could go up to 30 Hz as mentioned in section. 5.4.2. Their gestures experienced higher distortion in the horizontal movement in comparison with the vertical one as clearly depicted in case of square gesture of Fig. 6.4a. With respect to the position of transmitter and receiver in this setup, the Doppler spectrum in horizontal motion suffers greatly from micro-Doppler effect in terms of spreading

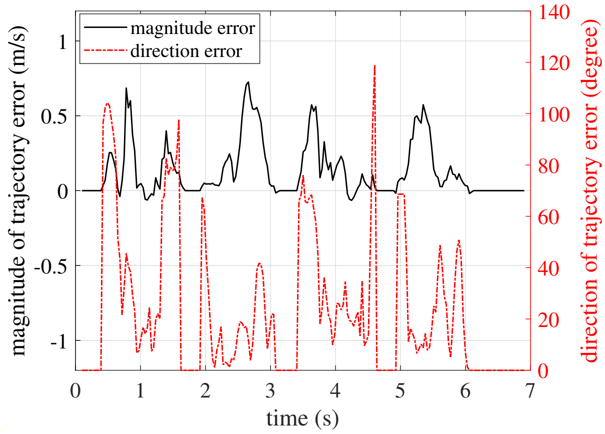

(a) Error of trajectory estimation (square gesture)

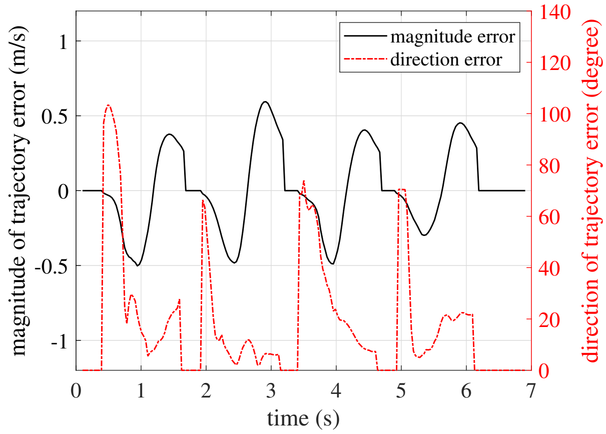

(b) Error of KF-based trajectory estimation (square gesture)

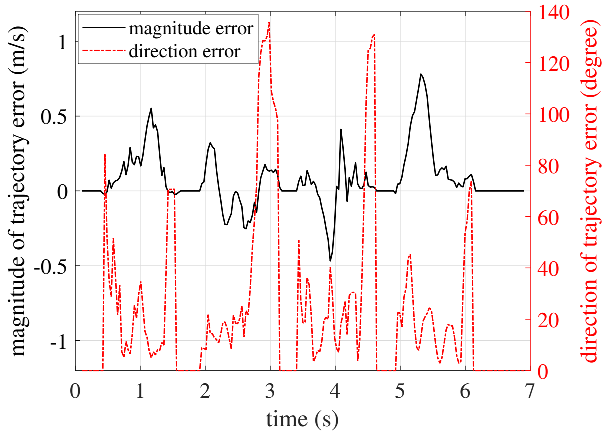

(c) Error of trajectory estimation (M gesture)

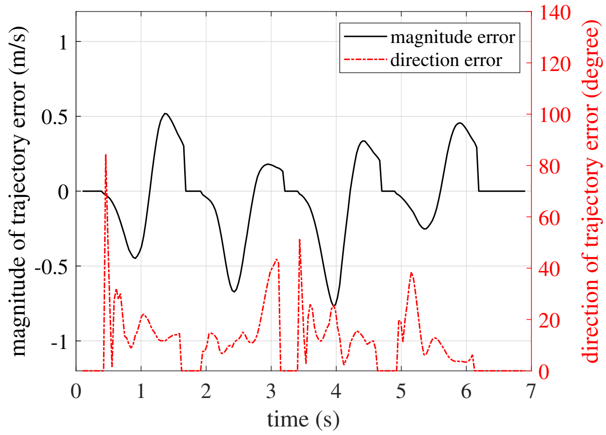

(d) Error of KF-based trajectory estimation (M gesture)

Figure 6.3: Performance of trajectory estimation of Fig. 6.2 in terms of magnitude and angle trajectory error

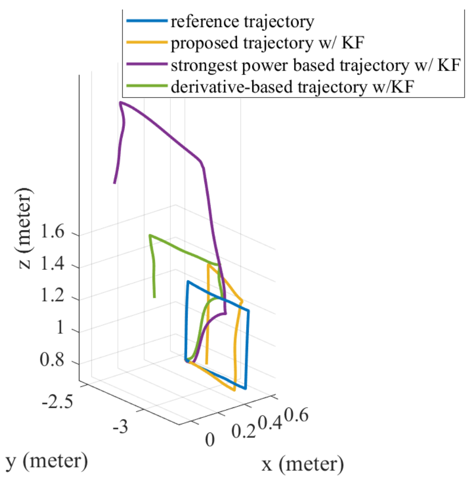

(a) Square gesture

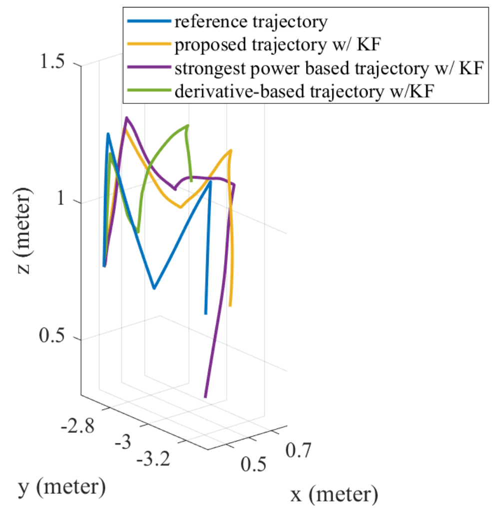

(b) M gesture

Figure 6.4: Trajectory comparison between the Doppler profile from the proposed method with other methods in CSI-based motion tracking.

as evidently shown in Fig. 5.1a. Since the dominant Doppler component was not always corresponding to the hand segment, these two methods which aims to capture the principle components failed to cope with the spreading spectrum. The vertical motion, however, has a small variance in Doppler shift since the radial speed was comparatively small for the entire human limb movement. Therefore, it resulted in the less distortion owing to lesser Doppler error in these segments. The same explanation also valid for M-shape gesture depicted in Fig. 6.4b. The beginning of gesture started significantly in the diagonal direction since the spectrum spread was larger than the vertical movement. This findings confirmed the robustness of our extracted Doppler technique to the micro-Doppler effect given the trajectory framework described in section. 6.2.1.

6.3.1 Effect of Initial Position to The Estimated Hand Trajectory

At this point, the trajectory estimation was computed under the assumption that the initial hand position was given. However, the initial state is typically unknown in practical scenario. Therefore, the optimization problem denoted in section. 6.2.3 was applied to estimate the initial position based on the cumulative LS residual. this optimization solution should implicitly represent the construable hand trajectory given estimated Doppler profiles. The search boundary could be easily determined through the analysis of the joint delay-Doppler spectrum [46] among 6 streams of CSI in this simulation. Although the position uncertainty could span a few meters in a magnitude due to a coarse-grained delay resolution in the narrowband signal, it was sufficient to determine the search region. Given the 8-meter

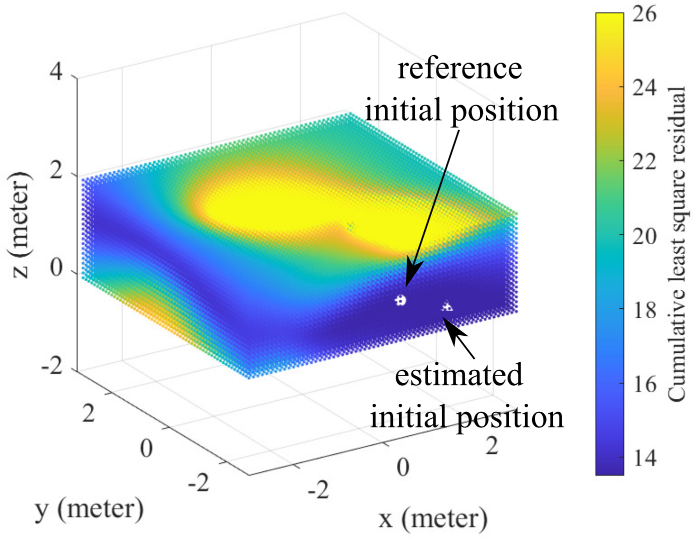

(a) Square gesture

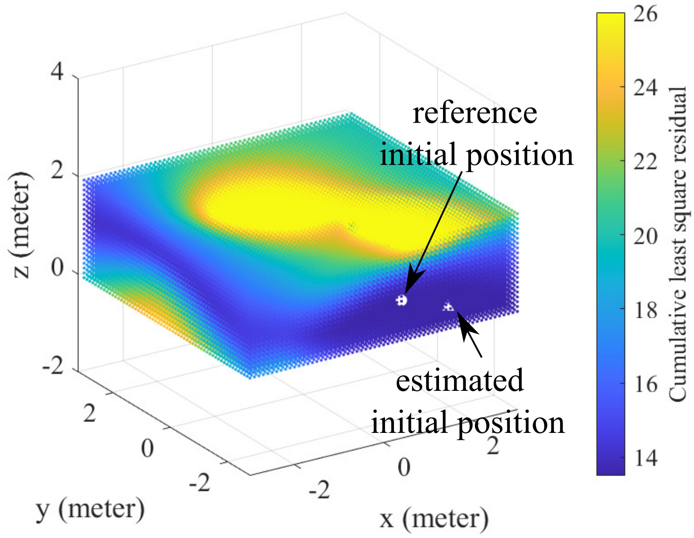

(b) M gesture

Figure 6.5: Spatial distribution of cost function for the initial position estimation

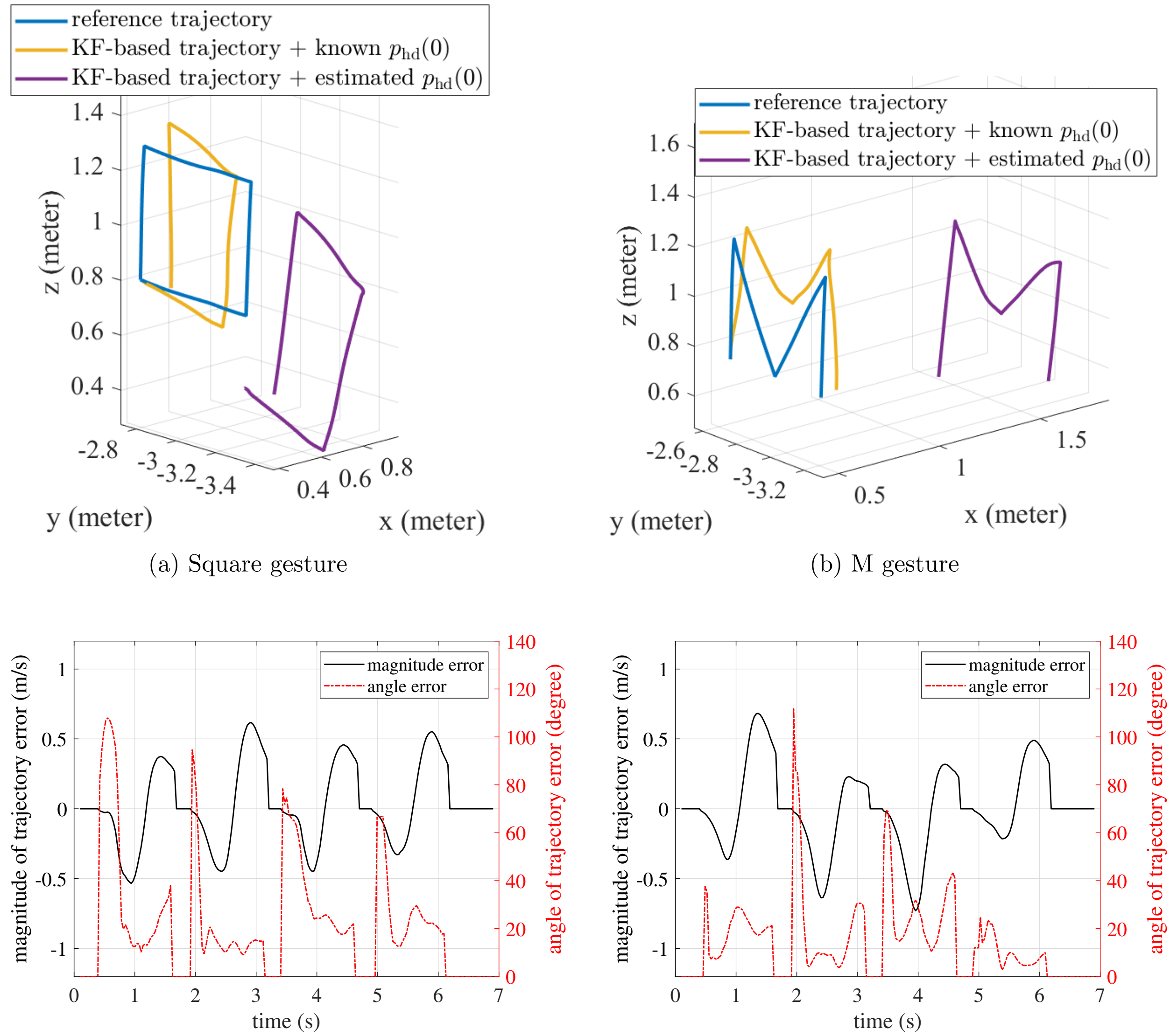

(a) Square gesture

(b) M gesture

(c) Error of trajectory estimation (square gesture)

(d) Error of trajectory estimation (M gesture)

Figure 6.6: Result and performance of trajectories with the estimated initial position

uncertainty derived from the bandwidth, $\boldsymbol{p}_{\mathrm{lower}}$ and $\boldsymbol{p}_{\mathrm{upper}}$ has been set to (-4, 4, 0) and (4, 4, 2) respectively. The 2-meter in z-direction was arbitrary chosen based on the human height indicated in Table 4.1. In Fig. 6.5, the distribution of cost function in eq. (6.12a) was illustrated in a function of initial position candidate for both gestures' trajectory. Due to the error in the estimated Doppler profile and the spatial uncertainty on the hand surface, the optimal initial position under the optimization criteria was clearly offset from the reference position of wrist which acted as the reference motion of the human limb model described in section. 4.2. In fact, it is obvious from the spatial cost function distribution that multiple local optimal points exist. Therefore, the optimization could produce different initial position depending on a boundary search condition. Since the assumption behind was not to find the absolute initial state but rather the position that could sustain its trajectory, it is not unexpected to have an arbitrary position as the solution.

To assess the performance of trajectory tracking in the presence of the estimated initial position, its trajectory result was comparatively plotted together with the trajectory with a given initial position as described in the previous validation. Shown in Fig. 6.6a - 6.6b are the trajectory comparison of square and M-shape gestures respectively. It is apparent that their trajectories depicted in magenta line were still produced the recognizable shapes despite a meter-level difference in the initial position for both gestures. Nonetheless, the difference in initial position was explicitly manifested in terms of scale and orientation offset. Only through the visual inspection, one can obviously saw the effect of initial position offset results in the the higher constant rotation and shifting away from the reference. In fact, the impact could be explained by analyzing the magnitude and direction error as depicted in Fig. 6.6d - 6.6b for both gestures. Fortunately, the amount of trajectory distortion was relatively stable which could be validated from a similar pattern of trajectory error between Fig 6.3 and Fig 6.6 for a given and estimated initial position cases respectively. The reason for trajectory offset could be explained by considering the geometric of multi-static Doppler model used in the tracking framework as explained in section 6.2.1. Given the estimated Doppler profile, the proportion of velocity components will be altered to accommodate the change of $\boldsymbol{U}^{\dagger}(\delta)$ because of the different initial positions. The change of velocity vector contributed to the orientation and scale offset. Nonetheless, this evaluation has confirmed that the trajectory is less sensitive to the initial position than the accuracy of Doppler profile derived from the spectrum.

6.3.2 Effect of Doppler Power to the Estimated Trajectory Performance

As discussed in previous section, the quality of Doppler profile strongly influences the performance of the estimated trajectory. The proposed Doppler profile extraction explained in chapter 5 is obtained from Doppler power spectrum. In other word, the extraction technique would not be able to retrieve Doppler profile at certain time if Doppler power was undetectable. This situation may happens when Doppler power level is smaller than the noise level and thus undetectable which likely occurs in the actual measurement.

In the previous simulation, the scenario could be regarded as noise-free since the SNR level was insignificantly small. In this section, noisy environment will be taken into account in order to verify the effect of the noise power to the overall performance of hand trajectory tracking. In general, the simulation condition is the same as in section 6.3.1 but varying SNR of CSI from 50 dB, which is the approximated dynamic range of the Doppler power induced by the motion given the proposed deterministic CSI model, to 30 dB. In each SNR level, 100

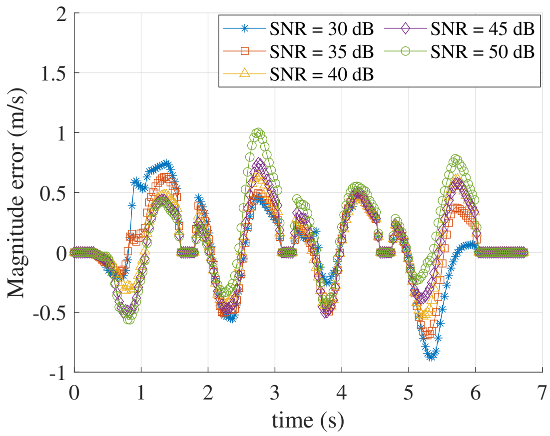

(a) Magnitude error of square gesture

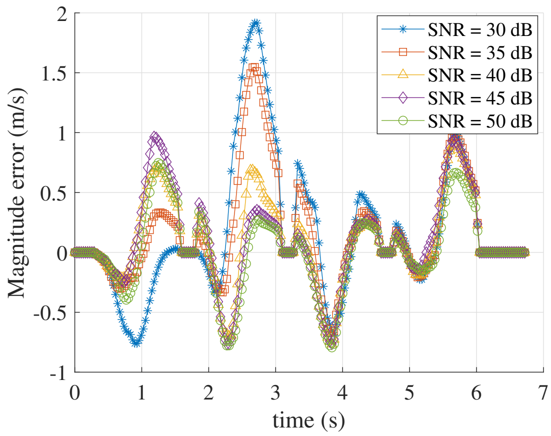

(b) Magnitude error of M gesture

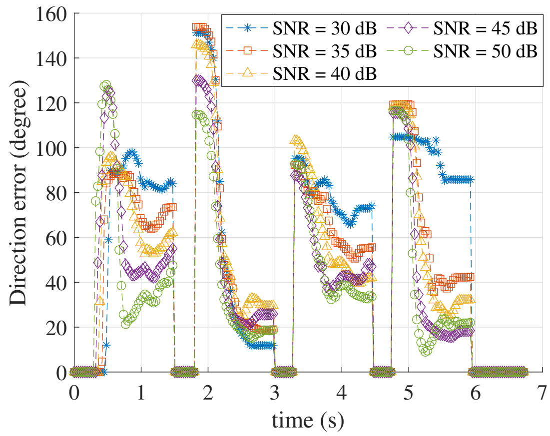

(c) Direction error of square gesture

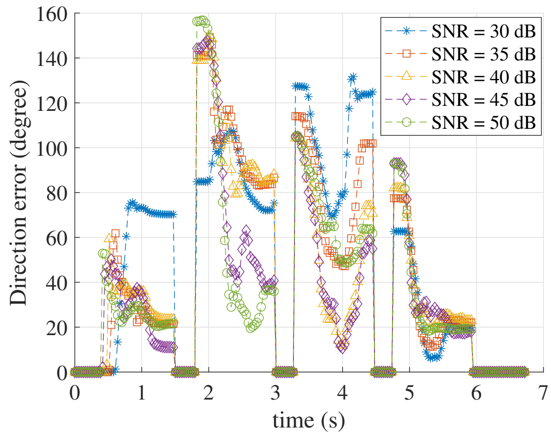

(d) Direction error of M gesture

Figure 6.7: Performance of the estimated trajectory at different SNR level

trials of simulation have been conducted and the result was compared in terms of an average of magnitude and direction trajectory error respectively for both gesture as visualized in Fig. 6.7. While SNR level was gradually reduced, the figures clearly indicated the degradation of trajectory performance as the direction offset relative to the reference trajectory increased. In square gesture depicted in Fig. 6.7c, the improvement at the horizontal motion (first and third motion segments) was astonishing as the direction offset has been mitigated from 65-85 to 20-40 degrees. In the vertical motion, relatively smaller direction error was observed from 35-50 dB whereas the transit between 30 to 35 dB showed a huge decrease of direction error which was indicated in the remaining segments of square as well as in Fig. 6.7d of M gesture's vertical motion (first and forth motion segment). The similar trend could be observed in the magnitude error especially in the second segment of M gesture as depicted in Fig 6.7b where the huge decreased of averaged direction error was observed around 1 m/s when SNR changed from 35 dB to 40 dB. In particular, estimated trajectory with a higher SNR tended to have a balance level of magnitude error between negative and position values at each segment which minimized the cumulative trajectory error in terms of overall distance. As comparatively discussed in Fig. 6.3, this benefit is the result of KF which effectively controlled the abrupt change in the movement speed. In contrast, this characteristic is gradually disappeared in the case of the estimated trajectory with lower SNR especially in 30-35 dB cases. This validation has confirmed that the estimated trajectory is sensitive to the decreased of SNR level since only partial of Doppler information could be extracted from the noisy Doppler spectrum.

For further visual analysis, Fig. 6.8 showed a sample of estimated trajectory at different SNR level. In general, the size of estimated gestures are relatively larger than the reference. However, the consistency in the size and orientation offset between the estimated trajectory at higher SNR of 45 and 50 dB were clearly shown in Fig. 6.8b and Fig. 6.8d for square and M gestures respectively. Beside. they are closely-positioned in the space since Doppler profiles could be obtained with less impact from the noise power and thus converging the optimal initial position. In the case of lower SNR depicted in Fig. 6.8a and Fig. 6.8c, although some trajectories could maintain the original shapes of square and M gesture, its orientation was clearly diverse which depended on the estimated initial position. This is because a partial of Doppler spectrum was hindered by the noise level which consequently reduced Doppler information to be extracted as Doppler profiles. To clarify this issue, Fig. 6.9 compared the noise-free Doppler power spectrum to those at 30-dB SNR for the case of square gesture as the example. In this figure, Doppler information in the the second and forth segments is totally undetectable in the sampled spectrum between T_1 and R_1 at lower SNR as depicted in Fig. 6.9c despite observable in the noise-free spectrum as visualized in Fig. 6.9a. Although another pair of Doppler spectrum between T_1 and R_1 shown in Fig. 6.9d could barely detect the Doppler power of the second motion segment, the forth segment is obscured by the

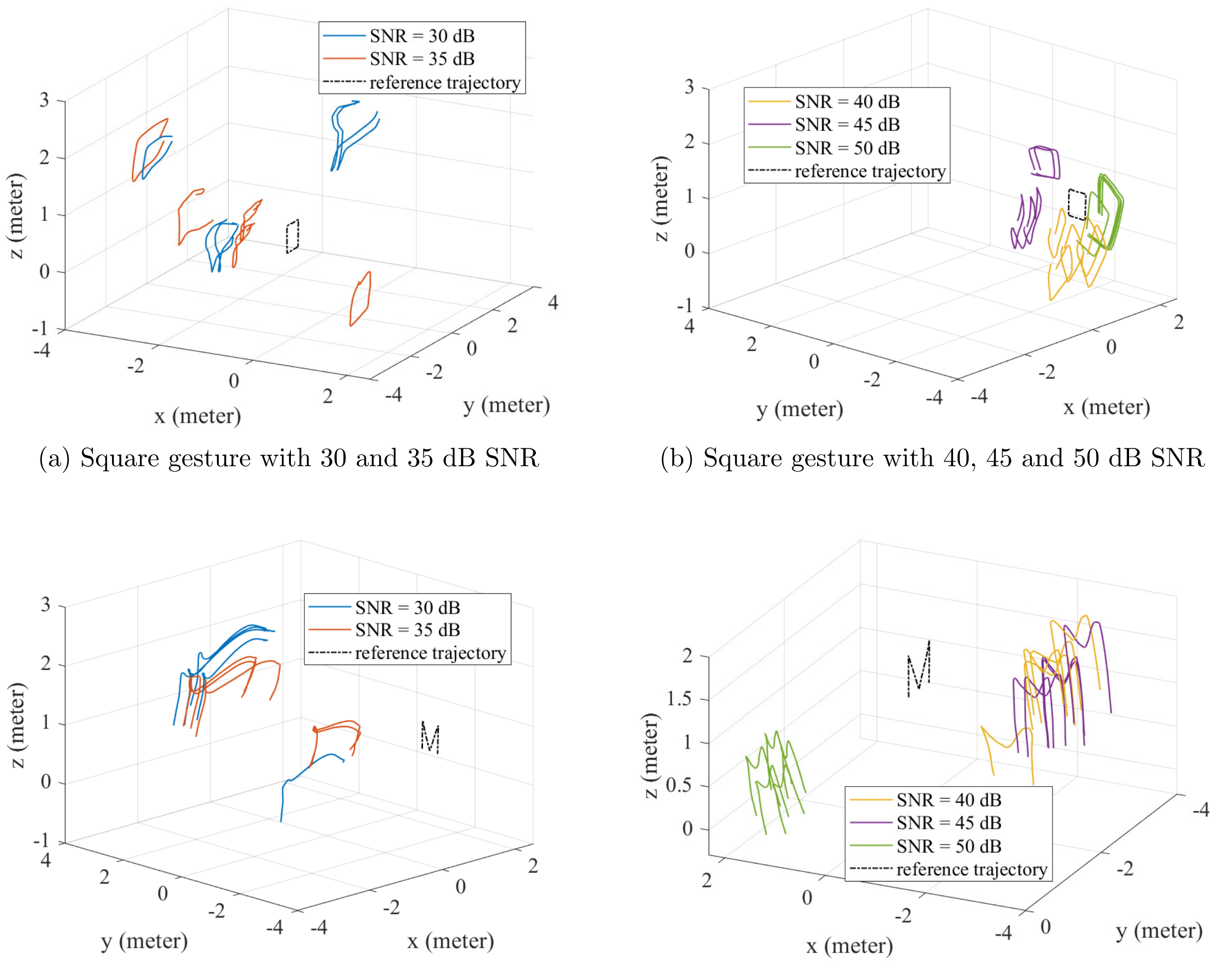

(a) Square gesture with 30 and 35 dB SNR

(b) Square gesture with 40, 45 and 50 dB SNR

(c) Square gesture with 30 and 35 dB SNR

(d) M gesture with 40, 45 and 50 dB SNR

Figure 6.8: Result comparison of trajectory estimation in noisy scenario with difference SNR level

noise in comparison with those in noise-free shown in Fig. 6.9b. This characteristic clearly justify the distorted shape in Fig. 6.8a at lower SNR. If the majority of Doppler information was nearly contaminated, trajectory may not be able to reconstructed as seen in the vertical motion of 30-dB SNR for both gestures. Additionnally, depending on the obtainable profiles, the optimal trajectory that minimized LS residual in eq. (6.12a) could be differed which results in the diverse trajectory orientation.

In conclusion, this analysis shed the light on the limitation of this framework when dealing with the noisy CSI in terms of orientation offset. At SNR level falls below 35 dB, quality of Doppler profiles were not sufficient to fully reconstruct the shape of hand gesture. In a bright side, the analysis also described that the estimated trajectory in the actual environment may preserve the overall gesture shape but unfortunately represent itself in the the different frame-of-reference from those of actual gesture.

6.3.3 Effect of Antenna Position Uncertainty to Hand Trajectory

The positions of Tx and Rx antennas in previous simulations are assumed to be point source and observation located at certain position. In the actual scenario, antenna has a particular dimension and thus hardly to be defined by a particular point in the space. Moreover, the measurement uncertainty such as equipment precision could be the uncontrollable source of antenna position uncertainty.

To investigate the effect of antenna position uncertainty, the performance of hand trajectory tracking given the estimated initial position is simulated under the assumption that the estimated Tx and Rx antennas defined as $\hat{\boldsymbol{p}}_{\mathrm{T}_m}$ and $\hat{\boldsymbol{p}}_{\mathrm{R}_n}$ accordingly are suffered from the measurement uncertainty,

$$\hat{\boldsymbol{p}}_{\mathrm{T}_m} = \hat{\boldsymbol{p}}_{\mathrm{T}_m} + \mathscr{N}_{\mathrm{TR}}(0, \sigma_{\mathrm{TR}}) \tag{6.15}$$

$$\hat{\boldsymbol{p}}_{\mathrm{R}_n} = \hat{\boldsymbol{p}}_{\mathrm{R}_n} + \mathscr{N}_{\mathrm{TR}}(0, \sigma_{\mathrm{TR}}) \tag{6.16}$$

where $\mathscr{N}_{\mathrm{TR}}(0, \sigma_{\mathrm{TR}})$ is the zero-mean Gaussian noise with standard deviation σ_{TR}. The validation is conducted by comparing the estimated trajectory of the uncertain antenna positions with those without antenna position uncertainty (reference) depicted in purple line of Fig. 6.6a. Monte-Carlo simulation with 1,000 trial was conducted to estimate the trajectory of the square gesture at different level of uncertainty controlled by σ_{TR}.

Root-mean-squared error (RMSE) with respect to number of simulation trials were comparatively validated in Fig. 6.10 in terms of magnitude and direction error. It was quantitatively shown that the estimated trajectories with the antenna uncertainty level below $\sigma_{\mathrm{TR}} \leq 5$ cm produced relatively small discrepancy with the magnitude and direction error less than 0.1 m/s and 10 degree. On the other hand, the discrepancy significantly when $\sigma_{\mathrm{TR}} \geq 12$ cm in both error metrics. Therefore, it implicitly indicates that the tracking system could handle the uncertainty of antenna position if the deviation is in the magnitude

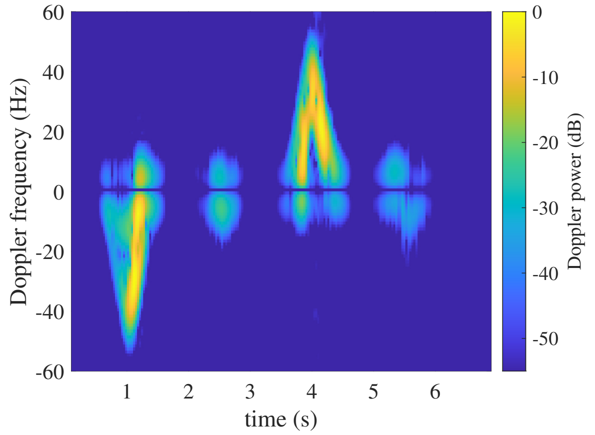

(a) Noise-free Doppler spectrum between $T_1 - R_1$

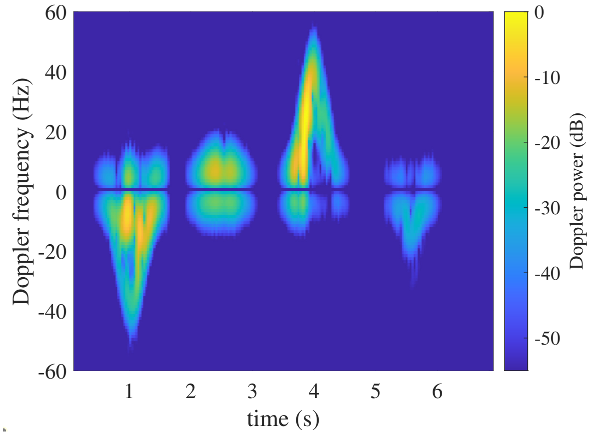

(b) Noise-free Doppler spectrum between $T_2 - R_2$

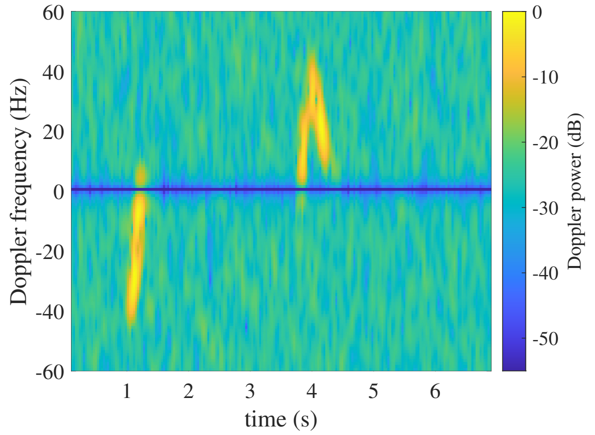

(c) 30-dB SNR Doppler spectrum between $T_1 - R_1$

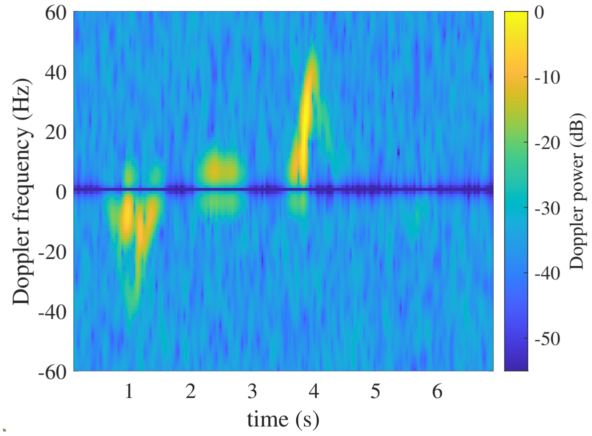

(d) 30-dB SNR Doppler spectrum between $T_2 - R_2$

Figure 6.9: Sampled Doppler power spectrum at lower SNR in comparison with those without noise

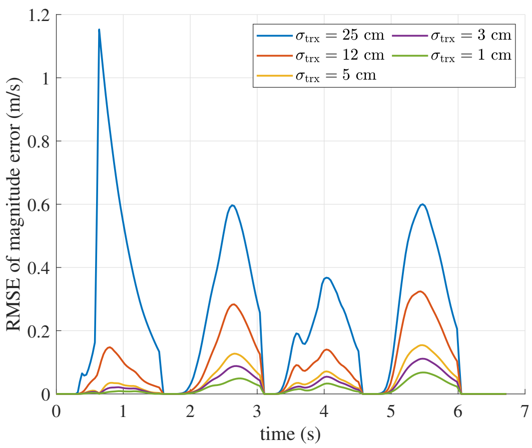

(a) RMSE of magnitude error

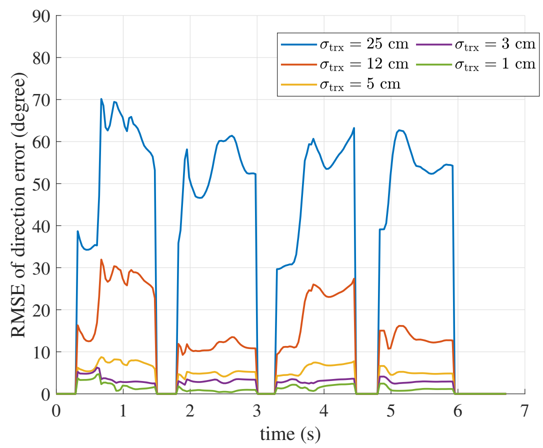

(b) RMSE of direction error

Figure 6.10: Discrepancy of the gesture trajectory with antenna position uncertainty at different σ_{TR} relative to those with the certain antenna position in terms of RMSE

of a few centimeters. The simulation in the case of M-shape gesture was omitted since it produced a similar result to the square gesture. Considering eq. (6.1), it should be noted that the tolerable range of antenna position uncertainty is subject to the distance of the moving object relative to the position of Tx and Rx. The farther the distance is, the tolerable range would increase and vice versa for the shorter distance.

6.4 Measurement Campaign for Trajectory Estimation

In this section, our tracking framework will be testes with the measurement CSI conducted in the meeting room. Wi-Fi system with 3x2 MIMO configuration was set up using two commercial laptops where the 6 dBi-omnidirectional Wi-Fi antennas were externally connected through a coaxial cable with 0.77 velocity factor and U.FL-to-SMA adapter cables. Each antenna was placed in the different position as depicted in Fig. 6.11. These positions can be translated to the relative position frame of reference with respect to the simulation setup in Fig. 5.4a. The Linux 802.11n CSI Tool [24] was installed on both laptops to collect CSI data while performing square and M-shape gesture respectively. The Undesired phase rotation that obscured Doppler frequency was mitigated using the proposed b2b calibration technique explained and evaluated in chapter 3. The schematic connection with b2b calibration setup is the same as the one depicted in Fig. 3.6. Specifically, a Mini-Circuits ZFSC-2-10G 2-way RF power splitter/combiner was applied at the first Tx antenna for dividing the signal into the b2b channel at the first Rx antenna. A 40dB-attenuator was inserted between the b2b channel to prevent the damage caused by power surge to the Wi-Fi chip as well as avoid the

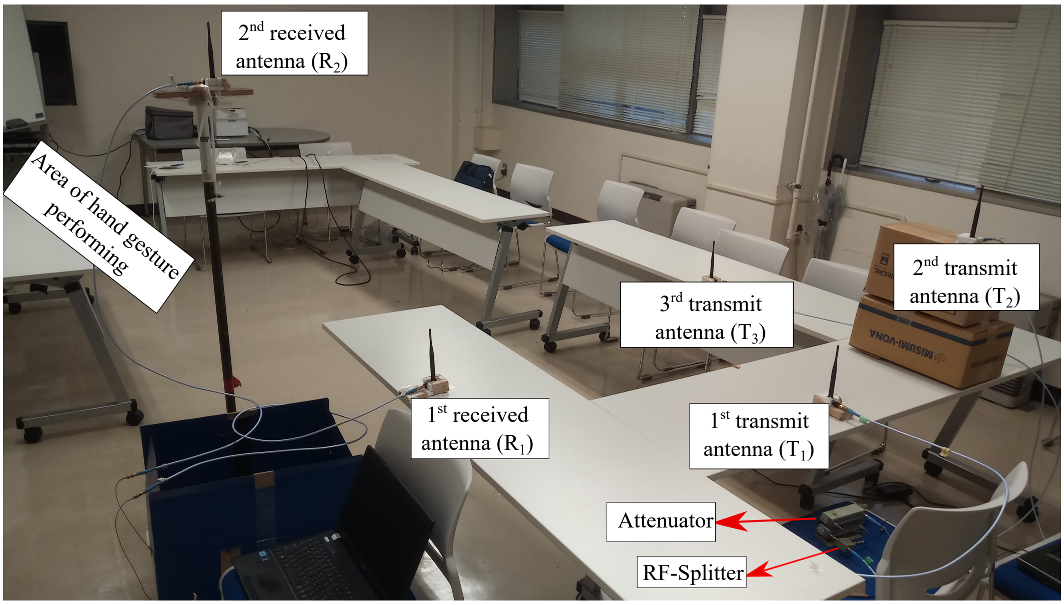

Figure 6.11: Measurement scenario for the hand gesture trajectory tracking.

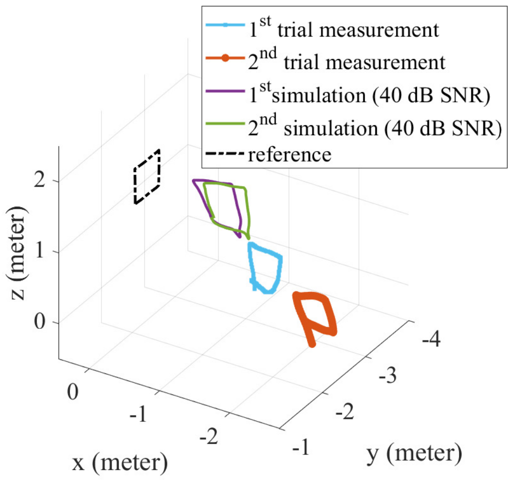

(a) Square gesture

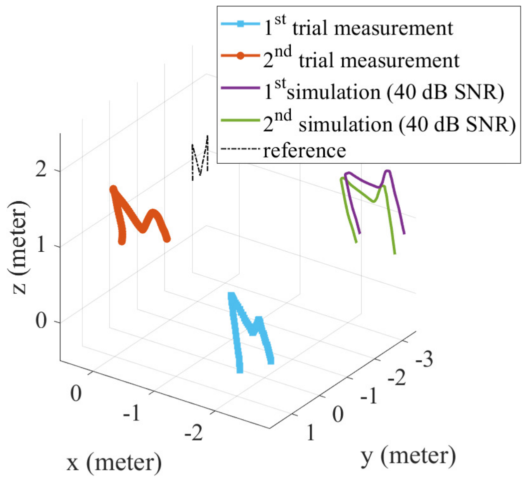

(b) M gesture

Figure 6.12: Comparison of the estimated trajectory of hand gestures between actual and simulated CSI

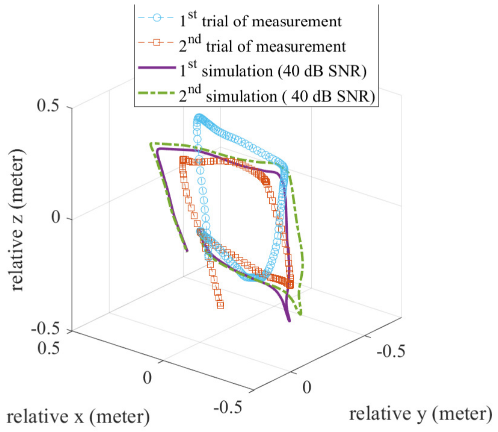

(a) Square gesture

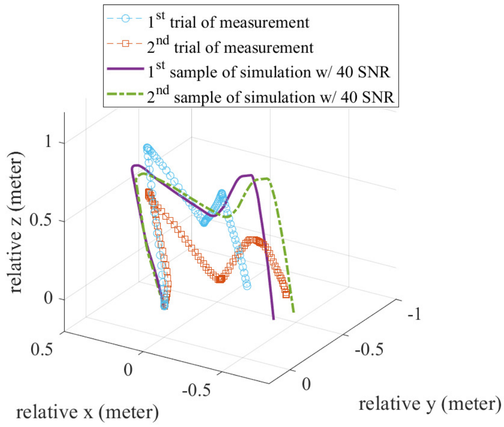

(b) M gesture

Figure 6.13: Comparison of estimated gesture trajectory between the simulation and measurement result under the relative frame of reference

power saturation due to the power difference between b2b and the wireless channel at the Rx antenna ports. Consequently, three Tx and two Rx antennas are usable in this setup whereas another received antenna is sacrificed for calibration purposed. The 40-MHz bandwidth Wi-Fi signal were sent with the sampling frequency of 2,500 Hz at Wi-Fi channel number 62 (5.31 GHz center frequency). 30 subcarriers equally sampled every four subcarriers from a total of 114 were obtained at the receivers which follows the CSI grouping number 4 according to standard [3] covering 36.25 MHz bandwidth. In this measurement, each square and M gesture was performed twice at the same position while CSI was being captured for reproducibility. The trajectory and initial position were estimated offline in MATLAB using the same proposed technique explained in section 6.2.1.

As depicted in Fig. 6.12, the estimated trajectories could resemble the square and M gestures in both trials in comparison with the simulation the reference albeit the orientation offset. With the discussion in section 6.3.2, this is the result of the quality of Doppler profiles that was deteriorated from the lower level of Doppler power which strongly influences the distortion of reconstructed shapes as well as its orientation. Beside, various uncertainty factors during the measurement such as the difference in speed profile, non-rigid movement, initial orientation and position of human limb may also affects the difference in gesture size relative to the trajectory reference. In terms of algorithm, the optimization problem in eq. (6.12a) could produce multiple optimal values, thus the the initial positions in these measurements were different. As discussed in section 6.3.2, this usually happens under lower SNR where extracted Doppler profiles are incomplete. Since the simulation results showed that the tracking framework is more robust to the initial position, it does not strongly affect the overall trajectory.

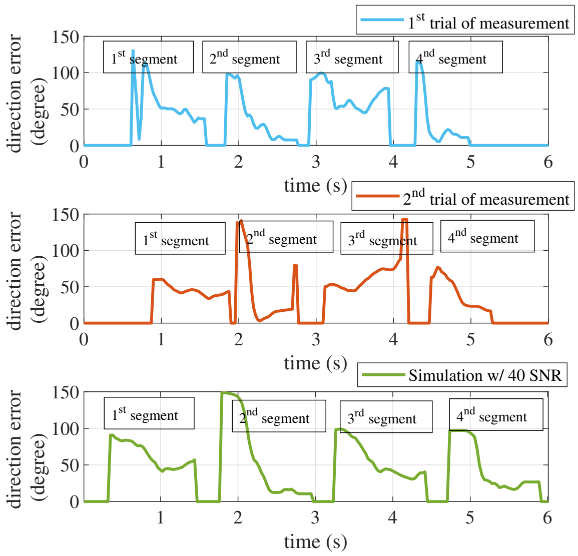

(a) Square gesture

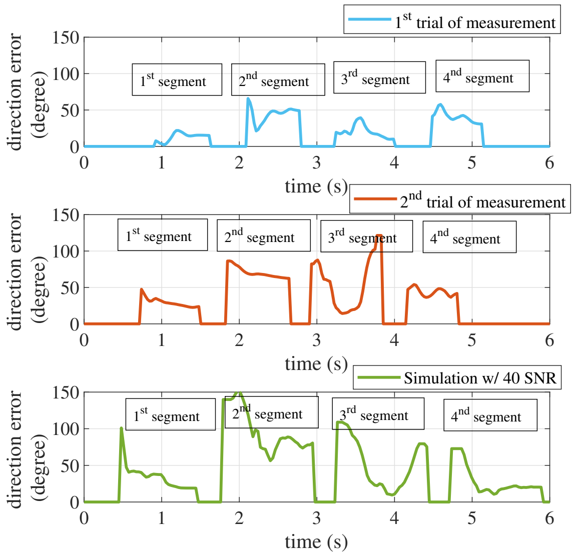

(b) M gesture

Figure 6.14: Performance of the estimated trajectory in terms of direction trajectory error of measurement and simulation results from Fig. 6.12

For a clear visual comparison with the simulation result, initial position of estimated trajectories in both measurements and simulation are normalized to the origin in Fig. 6.13. Here the simulated result with 40-dB SNR was selected since it has shown a similar spectrum distortion due to the noise contamination as shown in Fig. 4.16c. It was found that the simulation at 40-dB SNR produced relatively similar trajectory degradation similar to those of measurements especially in the square gesture as depicted in Fig. 6.13a. Noting that the 2nd simulation was included for reproducibility purpose. However, the visible difference could be observed in the vertical motion segment. A slight difference in size and shape between two trials was probably due to the measurement uncertainty during performing hand gesture. Additional experiment with the reproducible instrument such as robot arm may be needed to control and clarify this inconsistency. The distortion of the hand trajectory in measurement was likely a result of a higher noise power that conceals the Doppler spectrum. This consequently contributed to the quality of the estimated Doppler profile which is the main source of trajectory error. In the case of M-gesture as visualized in Fig. 6.13b, both trials obviously had a larger discrepancy from the simulation result in comparison with the square gesture. This characteristic is expected since square gesture produced a stronger Doppler power during horizontal segment thus improving the overall trajectory. Despite distortion, this measurement successfully confirmed the usability of tracing hand trajectory from commodity Wi-Fi devices.

Since the fined-grained information of hand movement during the actual measurement could not be obtained, magnitude trajectory error was not able to validate. Fortunately, the experiment used the simple square and M-shape hand gesture whose direction movement can be easily known. Therefore, only direction error was applied to quantitatively compare the performance of trajectory tracing result as depicted in Fig, 6.14. In this figure, the direction error is a relative orientation offset from the reference direction shown in Fig. 6.12 as a black dotted-line. The direction error of both measurement in general contained a similar pattern as the result in simulation especially in the vertical motion of square gesture (second and forth motion segment). In particular, the higher direction error was usually situated at the beginning of motion segment and gradually reduced as the movement speed increased. Although a higher orientation offset in the horizontal motion (first and third motion segment) of around 50 degrees, it does not strongly influence the overall trajectory as depicted in Fig. 6.13a because the estimated trajectory produced the rotation offset relative to the reference. The same characteristic could be seen for the diagonal movement of M-shape gesture (second and third motion segment) in the measurement as shown in Fig. 6.14b. Recognizingly, vertical motion of the 2^{nd} trial produced almost identical direction offset in the first and third motion segment. This comparison indirectly showed the applicability of the trajectory framework for the hand gesture tracing with the actual off-the-shelf Wi-Fi devices.

In conclusion, our work is able to successfully perform the 3D trajectory with a few number of antennas requirement whereas the hand gesture trajectory tracking system in [57] needed more than 30 antennas to resolve the hand tracking that should be performed less than a meter from the receiver. In comparison with the trajectory estimation system in [58], their system is limited to the horizontal hand gesture while ours can work gesture in any orientation. Moreover, considering the Doppler tracking method, their gesture tracking performance highly depends on the orientation of the gesture performer relative to the transmitter and receiver as mentioned in Fig. 5.4.2 since micro-Doppler effect was not taking into account.

6.5 Summary

Restricted by the narrowband Wi-Fi signal, temporal position of hand gesture could not be directly obtained through the range information. On the other hand, the temporal profile of hand Doppler signature could be obtained by the proposed extraction technique explained in previous chapter. Therefore, the alternative tracking technique that requires only the knowledge of Doppler frequency is necessarily needed. Specifically, we sought to utilize the velocity information with the goal to trace hand gesture trajectory.

Accordingly, the trajectory estimation framework is formulated based on the multi-static

Doppler radar model. This framework recursively calculates both velocity and temporal position of hand gesture given a set of Doppler profiles captured from multiple Txs and Rxs. As the recursive process generates the cumulative error as the tracking progress, Kalman filter is applied to mitigate the trajectory error from the recursive model. Unfortunately, this system requires the given initial position which is practically difficult to accurately obtain due to the poor resolution in range information. Therefore, the optimization problem was applied to estimate the arbitrary initial position that could maintain the overall trajectory.

In the simulation, the trajectory of both square and M-shape gestures could successfully be reconstructed even without applying KF model. the scale and orientation offset obviously could be mitigated with the help of KF model. The correctness of trajectory is highly sensitive to the extracted Doppler profile. On the other hand, the quality of the overall trajectory is more robust to the initial position. Even though the estimated trajectory was far away from the reference, the shape of trajectory could still be preserved. Nevertheless the impact of the initial position offset manifests in terms of additional orientation offset but does not contribute much to the shape distortion. The measurement campaign using commodity Wi-Fi devices also provided the promising results in the trajectory tracking of hand gestures in all trials. This experiment therefore confirmed the applicability of our tracking framework in practical.

Chapter 7

Conclusion

7.1 Summary

The RF-based motion sensing has been addressed to enable the sensing capability in the scenarios where the commercial vision-based sensing system finds it difficult to operate. This thesis proposed the novel non-intrusive hand gesture trajectory tracking framework by utilizing commodity Wi-Fi devices. The non-intrusive capability allows the tracking possible without relying on the body-equipped sensors that could be inconvenient and may be impractical for the applications in elderly care, and intrusion detection. Utilizing Wi-Fi motion sensing is considered the application of OFDM radar which conceptually allows the system to estimate position and velocity from the radial range and Doppler information provided by Wi-Fi CSI. The main challenge of the Wi-Fi-based hand motion tracking is the inability to trace accurately the absolute position of the hand movement from the range information due to the Wi-Fi narrowband restriction. Most literature, therefore, utilized the movement characteristic embedded in Doppler information. However, there exists two issues when dealing with Doppler frequency in CSI: phase non-synchronization and micro-Doppler effect.

The former challenge introduced the undesired phase rotation which obscures Doppler frequency in the phase term of CSI. Many mitigation techniques have been proposed to handle this synchronization issue in their respective applications. But alas, to the best of the author's knowledge, no previous study has successfully resolve the non-synchronization issue without sacrificing a portion of Doppler information. In this thesis, the novel calibration technique was introduced. Practically, a back-to-back channel representing a wired channel in the cable between transmit and receive antenna ports was selected as the reference channel to solve the non-synchronization issue thus removing the undesired phase rotation in the process. The performance of the proposed calibration was confirmed by comparing the calibrated CSI with those channel measured by vector network analyzer

Another issue in micro-Doppler effect introduces multiple Doppler components caused by a bulky composite object such as the movement of human limb. This effect makes it difficult to choose the Doppler frequency signature that corresponds to the target movement which is the hand motion in this study. To understand how the micro-Doppler effect is generated during hand gesture, surface point cloud based human limb model was developed. The non-rigid motion of limb was simulated by the model of robot arm. In this work, simulated CSI was computed based on EM scattering from surface points on the human limb. The modified physical optics was introduced as the practical usage to compute the time-variant component of the simulated CSI. This approach enables us to obtain the deterministic micro-Doppler signatures induced by each segment on a human limb. the applicability of the simulated CSI model to produce micro-Doppler was confirmed with the result from measurement

By analyzed the hand Doppler characteristic, the novel Doppler profile estimation technique based on peak detection was established to extract a portion of hand micro-Doppler signatures from the spectrum. It was revealed that the error from the extracted Doppler profile was fairly small with less than 4-Hz offset at 90^{th} percentile of CDF in comparison with the larger error from the previous extraction methods used in CSI-based motion sensing analysis.

Our hand motion tracking framework is based on multi-static radar system. The trajectory was reconstructed by recursively estimating velocity and temporal position from the extracted Doppler profiles. KF was applied to subjugate the accumulated noise from the recursive tracking process. With simulation, the trajectory of both square and M-shape gesture were successfully traced albeit moderate scale and orientation distortion. The result also shows the robustness of the proposal to the micro-Doppler effect induced by human limb since the Doppler profile is extracted based on the analysis of micro-Doppler, and the performance is not depended on the user position in contrast to recognition approach. Last but not least, it was found that the quality of the overall trajectory is robust to the initial position but highly sensitive to the extracted Doppler profile. The measurement has been conducted to verify the applicability of this trajectory tracking framework. CSI was captured from commodity Wi-Fi devices installed on two laptops. The trajectory of hand gestures was successfully reconstructed with promising results in all trials.

7.2 Applicability to The Future Motion Sensing System

In this section, the discussion of how the findings in this thesis can contribute to the future motion sensing. With respect to the novel b2b calibration, it could be used as a low-cost reference signal for the modelling of the undesired phase rotation. With further research on the phase rotation issue, it is possible to develop the CSI calibration that does not require hardware modification. This discovery could have made the Wi-Fi based motion sensing more practical than our b2b calibration since no wired cable connection required in the sensing system. Even without improving the calibration technique, our calibrated CSI can improve the study in Wi-Fi based motion analysis in various applications such as intrusion detection, vital signal detection, activity and gesture recognition, and object tracking since the information of Doppler frequency is now fully obtainable.

Although our simulated CSI model was purposedly developed for the study of micro-Doppler effect during hand gesture, one can adopt our model to study the characteristic of micro-Doppler in their target motions such as human activity. This can be applied by simply subjecting the target object model with the PO-based scattered prediction to construct the deterministic CSI model. Moreover, the usage of this model could be extended further for the prediction of micro-Doppler signatures at different configuration. For example, in case of gesture recognition, a bunch of motion features can be obtained directly from simulation. This effectively could reduce the labored work during the construction the recognition database. In case of hand motion trajectory tracking, the findings showed that higher distortion happens when Doppler shift is small in the realm of uncertainty. Therefore, further study could be focused on the optimization position of the transmit and received antennas to minimize this issue. Another possibility of future research worth mentioning is the orientation offset of the estimated hand trajectory in the actual environment with noisy CSI. In particular, the development of mathematical model to describe the mechanism behind this trajectory rotation would be beneficial to predict the possible set of trajectories given the degraded Doppler profiles at lower SNR. In case of applying the trajectory tracking into gesture recognition framework, the study of coordinate alignment would be helpful to match the given trajectory with the trained gesture database.

In terms of industrial availability, it will be mostly beneficial for the motion sensing technology related company which involves in the development of low-cost and ubiquitous contactless interface such as smart devices, Internet-of-Things (IoT) devices, as well as virtual reality and augmented reality devices. It could assist the optical-based motion sensing to enable the sensing capability in the non-LoS scenario, private locations. In addition, the wireless communication related business could have a solution to integrate the motion sensing functionality into the home-scale Wi-Fi router enabling them to work as IoT gadgets rather than simply data communication.

Bibliography

[1] Kevin M. Lynch and Frank C. Park, *Modern Robotics: Mechanics, Planning, and Control*. Cambridge University Press, 2017, no. May.

[2] M. Speth, S. Fechtel, G. Fock, and H. Meyr, "Optimum Receiver Design for Wireless Broad-Band Systems Using OFDM – Part I," *IEEE Trans. Commun.*, vol. 47, no. 11, pp. 1668–1677, 1999.

[3] IEEE, "IEEE Standard for Information technology– Local and metropolitan area networks– Specific requirements– Part 11: Wireless LAN Medium Access Control (MAC)and Physical Layer (PHY) Specifications Amendment 5: Enhancements for Higher Throughput," *IEEE Std 802.11n-2009*, pp. 1–565, 2009.

[4] Q. Pu, S. Gupta, S. Gollakota, and S. Patel, "Whole-Home Gesture Recognition UsingWireless Signals," in *Proc. 19th Annu. Int. Conf. Mob. Comput. Netw. - MobiCom '13*, 2013, pp. 27–38.

[5] K. Qian, C. Wu, Y. Zhang, G. Zhang, Z. Yang, Y. Liu, and Y.-H. Liu, "Widar2.0: Passive Human Tracking with a Single Wi-Fi Link," in *Proc. 16th Annu. Int. Conf. Mob. Syst. Appl. Serv.* Munich, Germany: Association for Computing Machinery, 2018, p. 12.

[6] M. A. Aide Al-Qaness and F. Li, "WiGeR:Wifi-based gesture recognition system," *ISPRS Int. J. Geo-Information*, vol. 5, no. 6, pp. 1–17, 2016.

[7] G. Wang, Y. Zou, Z. Zhou, K. Wu, and L. M. Ni, "We Can Hear You with Wi-Fi!" *IEEE Trans. Mob. Comput.*, vol. 15, no. 11, pp. 2907–2920, 2016.

[8] K. Qian, C. Wu, Z. Zhou, Y. Zheng, Z. Yang, and Y. Liu, "Inferring Motion Direction using Commodity Wi-Fi for Interactive Exergames," in *CHI '17 Proc. 2017 CHI Conf. Hum. Factors Comput. Syst.*, 2017, pp. 1961–1972.

[9] X. Wang, C. Yang, and S. Mao, "PhaseBeat: Exploiting CSI Phase Data for Vital Sign Monitoring with Commodity WiFi Devices," in *2017 IEEE 37th Int. Conf. Distrib. Comput. Syst.*, 2017, pp. 1230–1239.

[10] S. Yousefi, H. Narui, S. Dayal, S. Ermon, and S. Valaee, "A Survey on Behavior Recognition Using WiFi Channel State Information," *IEEE Commun. Mag.*, vol. 55, no. 10, pp. 98–104, 2017.

[11] X. Liu, J. Cao, S. Tang, and J. Wen, "Wi-sleep: Contactless sleep monitoring via WiFi signals," in *Proc. - Real-Time Syst. Symp.*, 2014, pp. 346–355.

[12] H. Wang, D. Zhang, J. Ma, Y. Wang, Y. Wang, D. Wu, T. Gu, and B. Xie, "Human respiration detection with commodity wifi devices," in *Proc. 2016 ACM Int. Jt. Conf. Pervasive Ubiquitous Comput. - UbiComp '16*, 2016, pp. 25–36.

[13] D. Wu, D. Zhang, C. Xu, H. Wang, and X. Li, "Device-Free WiFi Human Sensing : From Pattern-Based to Model-Based Approaches," *IEEE Commun. Mag.*, vol. 55, pp. 91–97, oct 2017.

[14] Y. Ma, G. Zhou, and S. Wang, "WiFi sensing with channel state information: A survey," *ACM Comput. Surv.*, vol. 52, no. 3, 2019.

[15] F. Adib, Z. Kabelac, and D. Katabi, "Multi-Person Localization via RF Body Reflections," *Proc. 12th USENIX Symp. Networked Syst. Des. Implement. (NSDI 15)*, pp. 279–292, 2015.

[16] F. Adib, H. Mao, Z. Kabelac, D. Katabi, and R. C. Miller, "Smart Homes that Monitor Breathing and Heart Rate," *Proc. 33rd Annu. ACM Conf. Hum. Factors Comput. Syst. - CHI '15*, pp. 837–846, 2015.

[17] B. Kellogg, V. Talla, and S. Gollakota, "Bringing Gesture Recognition To All Devices," in *Proc. 11th USENIX Symp. Networked Syst. Des. Implement. (NSDI 14)*, 2014, pp. 303–316.

[18] S. Archasantisuk, T. Aoyagi, T. Uusitupa, M. Kim, and J.-i. Takada, "Human Motion Classification Using Radio Signal Strength in WBAN," *IEICE Trans. Commun.*, vol. E99.B, no. 3, pp. 592–601, 2016.

[19] H. Abdelnasser, M. Youssef, and K. A. Harras, "WiGest: A Ubiquitous WiFi-based Gesture Recognition System," in *Proc. - IEEE INFOCOM*, vol. 26, 2015, pp. 1472–1480.

[20] N. Patwari, L. Brewer, Q. Tate, O. Kaltiokallio, and M. Bocca, "Breathfinding: A wireless network that monitors and locates breathing in a home," *IEEE J. Sel. Top. Signal Process.*, vol. 8, no. 1, pp. 30–42, 2014.

[21] R. M. Sandoval, A. J. Garcia-Sanchez, and J. Garcia-Haro, "Improving RSSI-based path-loss models accuracy for critical infrastructures: A smart grid substation case-study," *IEEE Trans. Ind. Informatics*, vol. 14, no. 5, pp. 2230–2240, 2018.

[22] G. Lui, T. Gallagher, B. Li, A. G. Dempster, and C. Rizos, "Differences in RSSI readings made by different Wi-Fi chipsets: A limitation of WLAN localization," in *2011 Int. Conf. Localization GNSS, ICL-GNSS 2011*, 2011, pp. 53–57.

[23] C. A. Boano, H. Wennerström, M. A. Zúñiga, J. Brown, C. Keppitiyagama, F. J. Oppermann, U. Roedig, L.-Å. Nordén, T. Voigt, and K. Römer, "Hot Packets: A Systematic Evaluation of the Effect of Temperature on Low Power Wireless Transceivers," in *Extrem. Conf. Commun.* Association of Computing Machinery, 2013, pp. 7–12.

[24] D. Halperin, W. Hu, A. Sheth, and D. Wetherall, "Tool Release: Gathering 802.11n Traces with Channel State Information," *ACM SIGCOMM Comput. Commun. Rev.*, vol. 41, no. 1, p. 53, 2011.

[25] Y. Xie, Z. Li, and M. Li, “Precise Power Delay Profiling with Commodity WiFi,” in *Proc. 21st Annu. Int. Conf. Mob. Comput. Netw. - MobiCom ’15*, 2015, pp. 53–64.

[26] W. Wang, A. X. Liu, M. Shahzad, K. Ling, and S. Lu, “Device-Free Human Activity Recognition Using Commercial WiFi Devices,” *IEEE J. Sel. Areas Commun.*, vol. 35, no. 5, pp. 1118–1131, 2017.

[27] S. Sen, B. Radunovic, R. R. Choudhury, and T. Minka, “You are Facing the Mona Lisa: Spot Localization using PHY Layer Information Souvik,” in *Proc. 10th Int. Conf. Mob. Syst. Appl. Serv. - MobiSys ’12*, 2012, p. 183.

[28] J. Zhang, B. Wei, W. Hu, and S. S. Kanhere, “WiFi-ID : Human Identification using WiFi signal,” in *2016 Int. Conf. Distrib. Comput. Sens. Syst.*, 2016, pp. 75–82.

[29] X. Zheng, J. Wang, L. Shangguan, Z. Zhou, and Y. Liu, “Smokey: Ubiquitous smoking detection with commercial WiFi infrastructures,” in *Proc. - IEEE INFOCOM*, 2016, pp. 1–9.

[30] H. Li, W. Yang, J. Wang, Y. Xu, and L. Huang, “WiFinger: Talk to Your Smart Devices with Finger-grained Gesture,” in *Proc. 2016 ACM Int. Jt. Conf. Pervasive Ubiquitous Comput. - UbiComp ’16*, 2016, pp. 250–261.

[31] K. Ali, A. X. Liu, W. Wang, and M. Shahzad, “Keystroke Recognition Using WiFi Signals,” in *Proc. 21st Annu. Int. Conf. Mob. Comput. Netw. - MobiCom ’15*. Paris, France: ACM, 2015, pp. 90–102.

[32] S. Tan and J. Yang, “WiFinger: Leveraging commodity WiFi for fine-grained finger gesture recognition,” in *17th ACM Int. Symp. Mob. Ad Hoc Netw. Comput. MobiHoc 2016*. Paderborn, Germany: Association for Computing Machinery, 2016, pp. 201–210.

[33] C. Wu, Z. Yang, Z. Zhou, K. Qian, Y. Liu, and M. Liu, “PhaseU: Real-time LOS Identification with WiFi,” in *Proc. - IEEE INFOCOM*, 2015, pp. 2038–2046.

[34] L. Gong, W. Yang, D. Man, G. Dong, M. Yu, and J. Lv, “WiFi-based real-time calibration-free passive human motion detection,” *Sensors*, vol. 15, no. 12, pp. 32 213–32 229, 2015.

[35] D. C. Halperin, “Simplifying the Configuration of 802.11 Wireless Networks with Effective SNR,” Ph.D. dissertation, University of Washington, 2012.

[36] J. Liu, Y. Wang, Y. Chen, J. Yang, X. Chen, and J. Cheng, “Tracking Vital Signs During Sleep Leveraging Off-the-shelf WiFi,” in *Proc. 16th ACM Int. Symp. Mob. Ad Hoc Netw. Comput. - MobiHoc ’15*, 2015, pp. 267–276.

[37] Y. Wang, X. Jiang, R. Cao, and X. Wang, “Robust Indoor Human Activity Recognition Using Wireless Signals,” *Sensors*, vol. 15, no. 7, pp. 17 195–17 208, 2015.

[38] X. Wang, L. Gao, and S. Mao, “CSI Phase Fingerprinting for Indoor Localization with a Deep Learning Approach,” *IEEE Internet Things J.*, vol. 3, no. 6, pp. 1113–1123, 2016.

[39] L. Gong, D. Man, J. Lv, G. Shen, and W. Yang, "FRID: Indoor Fine-Grained Real-Time Passive Human Motion Detection," in *Proc. - 2015 IEEE 12th Int. Conf. Ubiquitous Intell. Comput. 2015 IEEE 12th Int. Conf. Adv. Trust. Comput. 2015 IEEE 15th Int. Conf. Scalable Comput. Commun. 20.* IEEE, 2016, pp. 308–311.

[40] D. Zhang, H. Wang, Y. Wang, and J. Ma, "Anti-fall: A non-intrusive and real-time fall detector leveraging CSI from commodity WIFI devices," *Lect. Notes Comput. Sci. (including Subser. Lect. Notes Artif. Intell. Lect. Notes Bioinformatics)*, vol. 9102, pp. 181–193, 2015.

[41] X. Wang, C. Yang, and S. Mao, "TensorBeat: Tensor Decomposition for Monitoring Multi-Person Breathing Beats with Commodity WiFi," *ACM Trans. Intell. Syst. Technol.*, vol. 9, no. 1, pp. 1–28, 2017.

[42] Z. Tian, J. Wang, X. Yang, and M. Zhou, "WiCatch: A Wi-Fi Based Hand Gesture Recognition System," *IEEE Access*, vol. 6, pp. 16 911–16 923, 2018.

[43] W. He, K. Wu, Y. Zou, and Z. Ming, "WiG: WiFi-based gesture recognition system," in *Proc. - Int. Conf. Comput. Commun. Networks, ICCCN*, vol. 2015-Octob, 2015, pp. 1–7.

[44] M. I. Skolnik, *Radar Handbook.* McGraw-Hill Education, 2008.

[45] Y. C. Xiao, P. Wei, and T. Yuan, "Observability and performance analysis of Bi/multi-static Doppler-only radar," *IEEE Trans. Aerosp. Electron. Syst.*, vol. 46, no. 4, pp. 1654–1667, 2010.

[46] Z. Solatzaheh and A. Zaimbashi, "Accelerating target detection in passive radar sensors: Delay-doppler-acceleration estimation," *IEEE Sens. J.*, vol. 18, no. 13, pp. 5445–5454, 2018.

[47] B. J. Donnet and I. D. Longstaff, "Combining MIMO radar with OFDM communications," *Proc. 3rd Eur. Radar Conf. EuRAD 2006*, no. September, pp. 37–40, 2006.

[48] C. Sturm, T. Zwick, and W. Wiesbeck, "An OFDM system concept for joint radar and communications operations," in *IEEE Veh. Technol. Conf.*, no. 4. IEEE, 2009, pp. 1–5.

[49] S. Sen, G. Tang, and A. Nehorai, "Designing OFDM radar waveform for target detection using multi-objective optimization," *IEEE Trans. Signal Process.*, vol. 59, no. 2, pp. 639–652, 2011.

[50] A. Molisch, *Wireless Communications*, 2nd ed. Wiley-IEEE Press, 2005.

[51] V. C. Chen, *The Micro-Doppler Effect in Radar.* Artech House, 2011.

[52] M. G. Amin, Z. Zeng, and T. Shan, "Hand gesture recognition based on radar micro-doppler signature envelopes," *2019 IEEE Radar Conf. RadarConf 2019*, 2019.

[53] Z. Zeng, M. G. Amin, and T. Shan, "Arm motion classification using time-series analysis of the spectrogram frequency envelopes," *Remote Sens.*, vol. 12, no. 3, pp. 1–20, 2020.

[54] X. Li, D. Zhang, S. Li, Y. Zhang, H. Mei, Q. Lv, J. Xiong, X. Li, D. Zhang, S. Li, Y. Zhang, H. Mei, and J. Xiong, "IndoTrack: Device-Free Indoor Human Tracking with Commodity Wi-Fi," in *Proc. ACM Interact. Mob. Wearable Ubiquitous Technol*, vol. 1, no. 72. New York, NY, USA: ACM, 2017, pp. 72:1—-72:22.

[55] K. Qian, C. Wu, Z. Yang, Y. Liu, and K. Jamieson, "Widar : Decimeter-Level Passive Tracking via Velocity Monitoring with Commodity Wi-Fi," in *Proc. 18th ACM Int. Symp. Mob. Ad Hoc Netw. Comput.* Chennai, India: ACM, 2017, pp. 6:1—-6:10.

[56] K. Saho, M. Fujimoto, M. Masugi, and L.-S. Chou, "Gait Classification of Young Adults, Elderly Non-Fallers, and Elderly Fallers Using Micro-Doppler Radar Signals: Simulation Study," *IEEE Sens. J.*, vol. 17, no. 8, pp. 2320–2321, 2017.

[57] L. Sun, S. Sen, D. Koutsonikolas, and K.-H. Kim, "WiDraw: Enabling Hands-Free Drawing in the Air on Commodity WiFi Devices," in *Proc. 21st Annu. Int. Conf. Mob. Comput. Netw.* Paris, France: Association for Computing Machinery, 2015, pp. 77–89.

[58] L. Wang, H. Dai, A. X. Liu, and X. Wang, "WiTrace : Centimeter-Level Passive Gesture Tracking Using WiFi Signals," in *2018 15th Annu. IEEE Int. Conf. Sensing, Commun. Netw.* IEEE, 2018, pp. 1–9.

[59] B. G. Lee and S. Choi, *Broadband Wireless Access and Local Network: Mobile WiMax and WiFi.* Artech House, 2008.

[60] E. Dahlman, S. Parkvall, and J. Sköld, *4G LTE/LTE-Advanced for Mobile Broadband.* Elsevier, 2011.

[61] European Telecommunications Standard Institute, "ETSI EN 300 744 v1.2.1," *Digital Video Broadcasting (DVB); Framing structure, channel coding and modulation for digital terrestrial television*, 1999.

[62] European Telecommunications Standard Institute , "ETSI EN 300 401," *Radio Broadcasting Systems; Digital Audio Broadcasting (DAB) to mobile, portable and fixed receivers*, 2016.

[63] Y. Li, L. J. Cimini, and N. R. Sollenberger, "Robust channel estimation for OFDM systems with rapid dispersive fading channels," *IEEE Trans. Commun.*, vol. 46, no. 7, pp. 902–915, 1998.

[64] M. Morelli and U. Mengali, "A comparison of pilot-aided channel estimation methods for OFDM systems," *IEEE Trans. Signal Process.*, vol. 49, no. 12, pp. 3065–3073, 2001.

[65] S. Coleri, M. Ergen, A. Puri, and A. Bahai, "Channel estimation techniques based on pilot arrangement in OFDM systems," *IEEE Trans. Broadcast.*, vol. 48, no. 3, pp. 223–229, 2002.

[66] H. Minn and V. K. Bhargava, "An investigation into time-domain approach for OFDM channel estimation," *IEEE Trans. Broadcast.*, vol. 46, no. 4, pp. 240–248, 2000.

[67] A. Borhani and M. Patzold, "A Non-Stationary Channel Model for the Development of Non-Wearable Radio Fall Detection Systems," *IEEE Trans. Wirel. Commun.*, vol. 17, no. 11, pp. 7718–7730, 2018.

[68] F. Adib and D. Katabi, "See through walls with WiFi!" in *SIGCOMM 2013 - Proc. ACM SIGCOMM 2013 Conf. Appl. Technol. Archit. Protoc. Comput. Commun.*, 2013, pp. 75–86.

[69] Ettus Research, "USRP Software Defined Radio Device," Santa Clara, CA, USA, 2010. [Online]. Available: https://www.ettus.com

[70] Y. Xie, J. Xiong, M. Li, and K. Jamieson, "xD-Track: Leveraging multi-dimensional information for passive Wi-Fi tracking," *Proc. Annu. Int. Conf. Mob. Comput. Networking, MOBICOM*, pp. 39–43, 2016.

[71] T. Tsao, M. Slamani, P. Varshney, D. Weiner, H. Schwarzlander, and S. Borek, "Ambiguity function for a bistatic radar," *IEEE Trans. Aerosp. Electron. Syst.*, vol. 33, no. 3, pp. 1041–1051, 1997.

[72] N. Levanon, "Multifrequency radar signals," in *IEEE Natl. Radar Conf. - Proc.*, vol. 0, 2000, pp. 683–688.

[73] G. E. Franken, H. Nikookar, and P. Van Genderen, "Doppler tolerance of OFDM-coded radar signals," in *Proc. 3rd Eur. Radar Conf. EuRAD 2006*, vol. 9, no. September, 2006, pp. 108–111.

[74] D. Garmatyuk and J. Schuerger, "Conceptual design of a dual-use radar/communication system based on OFDM," in *MILCOM 2008 - 2008 IEEE Mil. Commun. Conf.*, San Diego, CA, 2008, pp. 1–7.

[75] S. Sen and A. Nehorai, "Adaptive design of OFDM radar signal with improved wideband ambiguity function," *IEEE Trans. Signal Process.*, vol. 58, no. 2, pp. 928–933, 2010.

[76] J. Fink and F. K. Jondral, "Comparison of OFDM radar and chirp sequence radar," in *2015 16th Int. Radar Symp.*, Dresden, 2015, pp. 315–320.

[77] K. M. Braun, "OFDM Radar Algorithms in Mobile Communication Networks," Ph.D. dissertation, Karlsruhe Institute of Technology, 2014.

[78] E. B. Torres, "Two classes of movements in motor control," *Exp. Brain Res.*, vol. 215, no. 3-4, pp. 269–283, 2011.

[79] K. M. DeGoede, J. A. Ashton-Miller, J. M. Liao, and N. B. Alexander, "How quickly can healthy adults move their hands to intercept an approaching object? Age and gender effects," *Journals Gerontol. - Ser. A Biol. Sci. Med. Sci.*, vol. 56, no. 9, pp. 584–588, 2001.

[80] T. Kashima, K. Yanagihara, and M. Iwaseya, "Trajectory formation based on a human arm model with redundancy," in *Conf. Proc. - IEEE Int. Conf. Syst. Man Cybern.*, 2012, pp. 959–963.

[81] T. Flash and N. Hogans, "The Coordination of Arm Movements : An Experimentally Confirmed Mathematical Model," *J. Neurosci.*, vol. 5, no. 7, pp. 1688–1703, 1985.

[82] M. I. Skolnik, "An Analysis of Bistatic Radar," *IRE Trans. Aerosp. Navig. Electron.*, vol. ANE-8, no. 1, pp. 19–27, 1961.

[83] C. A. Balanis, *Advanced Engineering Electromagnetics, 2nd edition.* John Wiley & Sons, 2012.

[84] A. Abdelgawwad, A. Borhani, and M. Pätzold, "Modelling, analysis, and simulation of the micro-doppler effect in wideband indoor channels with confirmation through pendulum experiments," *Sensors*, vol. 20, no. 4, 2020.

[85] N. H. Lehmann, E. Fishler, A. M. Haimovich, R. S. Blum, D. Chizhik, L. J. Cimini, and R. A. Valenzuela, "Evaluation of transmit diversity in MIMO-radar direction finding," *IEEE Trans. Signal Process.*, vol. 55, no. 5 II, pp. 2215–2225, 2007.

[86] A. M. Haimovich, R. S. Blum, and L. J. Cimini, "MIMO radar with widely separated antennas," *IEEE Signal Process. Mag.*, vol. 25, no. 1, pp. 116–129, 2008.

[87] A. Baccigalupi and A. Liccardo, "The Huang Hilbert Transform for evaluating the instantaneous frequency evolution of transient signals in non-linear systems," *MEASUREMENT*, vol. 86, pp. 1–13, 2016.

[88] M. S. Gupta, "Definition of instantaneous frequency and frequency measurability," *Am. J. Phys.*, vol. 43, no. 12, pp. 1087–1088, 1975.

[89] N. E. Huang, Z. Shen, S. R. Long, M. C. Wu, H. H. Snin, Q. Zheng, N. C. Yen, C. C. Tung, and H. H. Liu, "The empirical mode decomposition and the Hubert spectrum for nonlinear and non-stationary time series analysis," *Proc. R. Soc. A Math. Phys. Eng. Sci.*, vol. 454, no. 1971, pp. 903–995, 1998.

[90] D. Labate, F. L. Foresta, G. Occhiuto, F. C. Morabito, A. Lay-Ekuakille, and P. Vergallo, "Empirical mode decomposition vs. wavelet decomposition for the extraction of respiratory signal from single-channel ECG: A comparison," *IEEE Sens. J.*, vol. 13, no. 7, pp. 2666–2674, 2013.

[91] E. Deléchelle, J. Lemoine, O. Niang, E. Deléchelle, J. Lemoine, and O. Niang, "Empirical mode decomposition : an analytical approach for sifting process," *IEEE Signal Process. Lett.*, vol. 12, pp. 764–767, 2005.

[92] Y. Gao, G. Ge, Z. Sheng, and E. Sang, "Analysis and solution to the mode mixing phenomenon in EMD," *Proc. - 1st Int. Congr. Image Signal Process. CISP 2008*, vol. 5, pp. 223–227, 2008.

[93] Mallat Stéphane, *A Wavelet Tour of Signal Processing: The Sparse Way.* Academic press, 2009.

[94] M. Pätzold and C. A. Gutierrez, "Enhancing the resolution of the spectrogram of non-stationary mobile radio channels by using massive MIMO techniques," *IEEE Veh. Technol. Conf.*, vol. 2017-Septe, pp. 1–7, 2018.

[95] S. Yun, Y.-C. Chen, and L. Qiu, "Turning a Mobile Device into a Mouse in the Air," in *Proc. 13th Annu. Int. Conf. Mob. Syst. Appl. Serv. - MobiSys '15*, 2015, pp. 15–29.

[96] D. Gabor, "A Theory of Communication," *J. Inst. Electr. Eng. - Part I Gen.*, vol. 94, no. 73, pp. 429–457, 1947.

[97] D. Jordan, R. W. Miksad, and E. J. Powers, "Implementation of the continuous wavelet transform for digital time series analysis," *Rev. Sci. Instrum.*, vol. 68, no. 3, p. 1484, 1997.

[98] Y. J. G. Steven E. Noel, Harold H. Szu, "Doppler frequency estimation with wavelets and neural networks," in *SPIE Proc. Wavelet Appl.*, 1998, pp. 150–157.

[99] N. Aydin and H. S. Markus, "Wavelet Analysis of Quadrature Doppler Ultrasound Signals," in *2000 First Int. Conf. Adv. Med. Signal Inf. Process. (IEE Conf. Publ. No. 476)*, 2000, pp. 251–256.

[100] A. Matani, O. Oshiro, and K. Chihara, "Doppler Signal Processing of Blood Flow Using a Wavelet Transform," *Jpn. J. Appl. Phys.*, vol. 35, no. Part 1, No. 5B, pp. 3131–3134, 1996. [Online]. Available: http://iopscience.iop.org/1347-4065/35/5S/3131

[101] H. L. V. Trees, *Optimum Array Processing: Part IV of Detection, Estimation, and Modulation Theory.* John Wiley & Sons, 2002.

[102] R. O. Schmidt, "Multiple emitter location and signal parameter estimation," *Adapt. Antennas Wirel. Commun.*, no. 3, pp. 190–194, 2009.

[103] R. Roy, "ESPRIT-estimation of signal parameters via rotational invariance techniques - Acoustics, Speech and Signal Processing [see also IEEE Transactions on Signal Processing], IEEE Tr," *IEEE Trans. Acoust.*, vol. 37, no. 7, pp. 984–995, 1989.

[104] W. Chen, G. Zhou, and G. B. Giannakis, "Velocity and acceleration estimation of Doppler weather radar/lidar signals in colored noise," *ICASSP, IEEE Int. Conf. Acoust. Speech Signal Process. - Proc.*, vol. 3, no. 1, pp. 2052–2055, 1995.

[105] C. Yunhe, "Joint estimation of angle and Doppler frequency for bistatic MIMO radar," *Electron. Lett.*, vol. 46, no. 2, pp. 170–172, 2010.

[106] P. J. Vaitkus, R. S. Cobbold, and K. Wayne Johnston, "A new time-domain narrowband velocity estimation technique for doppler ultrasound flow imaging. part ii: comparative performance assessment," *IEEE Trans. Ultrason. Ferroelectr. Freq. Control*, vol. 45, no. 4, pp. 955–971, 1998.

[107] D. Zhang, H. Wang, and D. Wu, "Toward centimeter-scale human activity sensing with wi-fi signals," *Computer (Long. Beach. Calif).*, vol. 50, no. 1, pp. 48–57, 2017.

[108] Y. Zhuo, H. Zhu, and H. Xue, "Identifying a New Non-linear CSI Phase Measurement Error with Commodity WiFi Devices," in *Proc. Int. Conf. Parallel Distrib. Syst. - ICPADS*, Wuhan, China, 2017, pp. 72–79.

[109] J. Lv, D. Man, W. Yang, X. Du, and M. Yu, "Robust WLAN-Based Indoor Intrusion Detection Using PHY Layer Information," *IEEE Access*, vol. 6, pp. 30 117–30 127, 2017.

[110] J. Lv, D. Man, W. Yang, L. Gong, X. Du, and M. Yu, "Robust device-free intrusion detection using physical layer information of WiFi signals," *Appl. Sci.*, vol. 9, no. 1, 2019.

[111] E. Ding, X. Li, T. Zhao, L. Zhang, and Y. Hu, "A robust passive intrusion detection system with commodity WiFi devices," *J. Sensors*, vol. 2018, 2018.

[112] B. Y. Su, K. C. Ho, M. J. Rantz, and M. Skubic, "Doppler radar fall activity detection using the wavelet transform," *IEEE Trans. Biomed. Eng.*, vol. 62, no. 3, pp. 865–875, 2015.

[113] A. Borhani and M. Patzold, "A Non-Stationary Channel Model for the Development of Non-Wearable Radio Fall Detection Systems," *IEEE Trans. Wirel. Commun.*, vol. 17, no. 11, pp. 7718–7730, 2018.

[114] Y. Wang, K. Wu, and L. M. Ni, "WiFall: Device-Free Fall Detection by Wireless Networks," *IEEE Trans. Mob. Comput.*, vol. 16, no. 2, pp. 581–594, 2017.

[115] B. Erol, M. Amin, F. Ahmad, and B. Boashash, "Radar fall detectors: a comparison," *Radar Sens. Technol. XX*, vol. 9829, no. May 2016, p. 982918, 2016.

[116] C. Wu, Z. Yang, Z. Zhou, X. Liu, Y. Liu, and J. Cao, "Non-invasive detection of moving and stationary human with WiFi," *IEEE J. Sel. Areas Commun.*, vol. 33, no. 11, pp. 2329–2342, 2015.

[117] F. Adib, C.-Y. Hsu, H. Mao, D. Katabi, and F. Durand, "Capturing the human figure through a wall," *ACM Trans. Graph.*, vol. 34, no. 6, pp. 1–13, 2015.

[118] Y. Wang, J. Liu, Y. Chen, M. Gruteser, J. Yang, and H. Liu, "E-eyes: Device-free location-oriented activity identification using fine-grained wifi signatures," in *Proc. 20th Annu. Int. Conf. Mob. Comput. Netw. - MobiCom '14*. Maui, Hawaii, USA: ACM, 2014, pp. 617–628.

[119] M. Li, Y. Meng, J. Liu, H. Zhu, X. Liang, Y. Liu, and N. Ruan, "When CSI Meets Public WiFi," in *Proc. 2016 ACM SIGSAC Conf. Comput. Commun. Secur. - CCS'16*, 2016, pp. 1068–1079.

[120] M. N. Mahfoudi, T. Turletti, T. Parmentelat, F. Ferrero, L. Lizzi, R. Staraj, W. Dabbous, M. N. Mahfoudi, T. Turletti, T. Parmentelat, F. Ferrero, L. Lizzi, R. Staraj, and W. Dabbous, "ORION: Orientation Estimation Using Commodity Wi-Fi," in *2017 IEEE Int. Conf. Commun. Work. (ICC Work.*, 2017, pp. 1033–1038.

[121] D. Vasisht, S. Kumar, and D. Katabi, "Decimeter-Level Localization with a Single WiFi Access Point," in *Proc. 13th Usenix Conf. Networked Syst. Des. Implement.* Santa Clara, CA: USENIX Association, 2016, pp. 165–178.

[122] M. Kotaru, K. Joshi, D. Bharadia, and S. Katti, "SpotFi: Decimeter Level Localization Using WiFi," in *Proc. 2015 ACM Conf. Spec. Interes. Gr. Data Commun. - SIGCOMM '15*, vol. 45, 2015, pp. 269–282.

[123] K. Qian, C. Wu, Z. Yang, Z. Zhou, X. Wang, and Y. Liu, "Tuning by turning: Enabling phased array signal processing for WiFi with inertial sensors," in *Proc. - IEEE INFOCOM*, 2016, pp. 1–9.

[124] R. Plamondon, A. M. Alimi, P. Yergeau, and F. Leclerc, "Modelling velocity profiles of rapid movements: a comparative study," *Biol. Cybern.*, vol. 69, no. 2, pp. 119–128, 1993.

[125] L. Vaisman, L. Dipietro, and H. I. Krebs, "A comparative analysis of speed profile models for wrist pointing movements," *IEEE Trans. Neural Syst. Rehabil. Eng.*, vol. 21, no. 5, pp. 756–766, 2013.

[126] V. B. Zordan and J. K. Hodgins, "Tracking and Modifying Upper-body Human Motion Data with Dynamic Simulation," in *Comput. Animat. Simul. '99.* Milano, Italy: Springer, 1999, pp. 13–22.

[127] D. A. Winter, *Biomechanics and Motor Control of Human Movement: Fourth Edition.* John Wiley & Sons, 2009.

[128] C. Uluisik, G. Cakir, M. Cakir, and L. Sevgil, "Radar cross section (RCS) modeling and simulation, part 1: a tutorial review of definitions, strategies, and canonical examples," *IEEE Antennas Propag. Mag.*, vol. 50, no. 1, pp. 115–126, 2008.

[129] N. Lertsirisopon, G. S. Ching, M. Ghoraishi, J.-I. Takada, I. Ida, and Y. Oishi, "Investigation of non-specular scattering by comparing directional channel characteristics from microcell measurement and simulation," *IET Microwaves, Antennas Propag.*, vol. 2, no. 8, pp. 913–921, 2008.

[130] P. Hanpinitsak, K. Saito, W. Fan, J. Hejselbaek, J. I. Takada, and G. F. Pedersen, "Frequency Characteristics of Geometry-Based Clusters in Indoor Hall Environment at SHF Bands," *IEEE Access*, vol. 7, pp. 75 420–75 433, 2019.

[131] E. Yamashita, *Analysis Methods for Electromagnetic Wave Problems.* Artech House Inc., 1990.

[132] N. Dos Santos, MLX and Rabelo, "On the ludwig integration algorithm for triangular subregions," *Proc. IEEE*, vol. 74, no. 10, pp. 1455–1456, 1986.

[133] A. C. Ludwig, "Computation of Radiation Patterns Involving Numerica1 Double Integration," *IEEE Trans. Antennas Propag.*, vol. 16, no. 6, pp. 767–769, 1968.

[134] H. Hoppe, T. DeRose, T. Duchamp, J. McDonald, and W. Stuetzle, "Surface reconstruction from unorganized points," *Comput. Graph.*, vol. 26, no. 2, pp. 71–78, 1992.

[135] N. Amenta, S. Choi, and R. K. Kolluri, "The power crust, unions of balls, and the medial axis transform," *Comput. Geom. Theory Appl.*, vol. 19, no. 2-3, pp. 127–153, 2001.

[136] N. Amenta, M. Bern, and D. Eppstein, "The Crust and the β-Skeleton: Combinatorial Curve Reconstruction," *Graph. Model. Image Process.*, vol. 60, no. 2, pp. 125–135, 1998.

[137] F. L. Bernardini Chandrajit Bajaj, "Sampling and Reconstructing Manifolds Using Alpha-Shapes," in *Proc. 9th Can. Conf. Comput. Geom*, 1997, pp. 193–198.

[138] N. J. Mitra, A. Nguyen, and L. Guibas, "Estimating surface normals in noisy point cloud data," *Int. J. Comput. Geom. Appl.*, vol. 14, no. 4-5, pp. 261–276, 2004.

[139] T. ANDO, Makoto and KINOSHITA, "Accuracy comparison of PTD and PO for plane wave diffraction from a large circular disk," *Trans. IEICE*, vol. 72, no. 11, pp. 1212–1218, 1989.

[140] D. W. Duan, Y. Rahmat-Samii, and J. P. Mahon, "Scattering From A Circular Disk: A Comparative Study Of Ptd And Gtd Techniques," *Proc. IEEE*, vol. 79, no. 10, pp. 1472–1480, 1991.

[141] S. Nomura , Yûkichi and Katsura, "Diffraction of Electromagnetic Waves by Circular Plate and Circular Hole," *J. Phys. Soc. Japan*, vol. 10, no. 4, pp. 285–304, 1955.

[142] M. A. Karam and A. K. Fung, "Scattering from randomly oriented circular discs with application to vegetation," *Radio Sci.*, vol. 18, no. 4, pp. 557–565, 1983.

[143] M. A. Karam, A. K. Fung, and Y. M. Antar, "Electromagnetic Wave Scattering from Some Vegetation Samples," *IEEE Trans. Geosci. Remote Sens.*, vol. 26, no. 6, pp. 799–808, 1988.

[144] J. G. Meana, J. Á. Martínez-Lorenzo, F. Las-Heras, and C. Rappaport, "Wave scattering by dielectric and lossy materials using the Modified Equivalent Current Approximation (MECA)," *IEEE Trans. Antennas Propag.*, vol. 58, no. 11, pp. 3757–3761, 2010.

[145] K. Stephenson, "Circle packing: a mathematical tale," *Not. AMS*, vol. 50, no. 11, pp. 1376–1388, 2003.

[146] M. Yamagishi, T. Hikage, M. Sasaki, M. Nakamura, and Y. Takatori, "FDTD-Based Numerical Estimation of Human Body Blockage Characteristics in 26GHz Band Indoor Propagation," *2018 48th Eur. Microw. Conf. EuMC 2018*, pp. 878–881, 2018.

[147] R. B. Staszewski and P. T. Balsara, *All-digital frequency synthesizer in deep-submicron CMOS*. John Wiley & Sons, 2006.

[148] R. E. Kalman, "A new approach to linear filtering and prediction problems," *J. Fluids Eng. Trans. ASME*, vol. 82, no. 1, pp. 35–45, 1960.

Publications

Journal Papers

1. **N. Keerativoranan**, A. Haniz , K. Saito, J. Takada, "Mitigation of CSI Temporal Phase Rotation with B2B Calibration Method for Fine-Grained Motion Detection Analysis on Commodity Wi-Fi Devices," *Sensors*, vol. 18, no. 11, pp. 3795, Nov. 2018.

2. **N. Keerativoranan**, P. Hanpinitsak, K. Saito, J. Takada,"Circular Mesh based Physical Optics for Scattered Field Prediction on Point Cloud Surface," *IEEE Antennas and Wireless Propagation Letters., [submitted].*

3. **N. Keerativoranan**, P. Hanpinitsak, K. Saito, J. Takada,"Analysis of Non-Intrusive Hand Trajectory Tracking by Utilizing Micro-Doppler Signature Obtained from Wi-Fi Channel State Information," *IEEE Access., [submitted]*

International Conference

1. **N. Keerativoranan**, K. Saito, J. Takada, "A Comparative Study of Doppler Frequency Profile from Hand Gestures for Device-free Motion Sensing using Wi-Fi Channel State Information," in *2019 URSI Asia Pacific Radio Science Conf. (URSI AP-RASC 2019)*, New Delhi, India, Mar. 2019.

2. **N. Keerativoranan**, K. Saito, J. Takada, "Utilizing Doppler Frequency of Wi-Fi Channel State Information to Trace Trajectory of Hand Gesture," in *2019 URSI-Japan Radio Science Meeting Conf. (URSI-JRSM 2019)*, Tokyo, Japan, Sep. 2019.

3. **N. Keerativoranan**, K. Saito, J. Takada, " A Study of Hand Motion Trajectory Tracking by Utilizing Channel State Information of off-the-shelf Wi-Fi Devices," in *40th Progress in Electromagnetics Research Symposium (PIERS 2018)*, Toyama, Japan, Aug. 2018. [Poster]

4. **N. Keerativoranan**, K. Saito, J. Takada, "Calibration of Wi-Fi Channel State Information for Motion Analysis," in *2018 Asia-Oceania Top University League on Engineering Conf. (AOTULE 2018)*, Chennai, India, Nov. 2018.

Domestic Conference

1. **N. Keerativoranan**, K. Saito, J. Takada, "Tracking 1D Hand Motion Directivity by Estimating Doppler Frequency of CSI information from Commodity Wi-Fi Devices," IEICE Tech. Rep., vol. 117, no. 366, MW2018-145, pp. 19-24, Dec. 2017.

2. **N. Keerativoranan**, K. Saito, J. Takada, "Development of Doppler CSI model for Wi-Fi based hand gesture detection application.," IEICE Tech. Rep., vol. 118, no. 468, ASN2018-111, pp. 175-180, Mar. 2019.

Workshop

1. **N. Keerativoranan**, K. Saito, J. Takada, "The study of Wi-Fi based Hand Gesture Trajectory Estimation by Utilizing the Doppler Frequency shift, " in *11th Multi-disciplinary International Student Workshop*, Tokyo Institute of Technology, Tokyo, Japan, Aug. 2019.

2. **N. Keerativoranan**, K. Saito, J. Takada, "Calibration of Wi-Fi Phase Channel State Information for Dynamic Motion Analysis, " in *10th Multi-disciplinary International Student Workshop*, Tokyo Institute of Technology, Tokyo, Japan, Aug. 2018.

3. **N. Keerativoranan**, K. Saito, J. Takada, "RFID-based Virtual Touchscreen by Micro-Doppler Effect, " in *9th Multi-disciplinary International Student Workshop*, Tokyo Institute of Technology, Tokyo, Japan, Aug. 2018. [Poster]